

A self-referenced single-electron current source

Von der Fakultät für Mathematik und Physik
der Gottfried Wilhelm Leibniz Universität Hannover
zur Erlangung des Grades

Doktor der Naturwissenschaften
- Dr. rer. nat. -

genehmigte Dissertation
von

Dipl.-Phys. Lukas Fricke
geboren am 16.09.1985 in Celle

2015

Referent: Prof. Dr. Rolf J. Haug
Korreferent: PD Dr. Frank Hohls

Tag der Promotion: 28.01.2015

Abstract

This thesis addresses the experimental realisation of a self-referenced current source. Such a device, consisting of a combination of single-electron pumps and single-electron detectors, makes the redefinition of the electric unit "ampere", based on constants of nature, feasible by relaxing the requirements on the individual building blocks.

Based on a AlGaAs/GaAs heterostructure, a chain of dynamic quantum dots has been formed using standard techniques of nanotechnology, like electron-beam lithography, wet-chemical etching and metalization by thermal evaporation. Between two neighbouring quantum dots, metallic single-electron transistors have been placed by two-angle evaporation of aluminium, being capable of detecting changes in the occupation number of the interconnecting nodes by one electron.

After discussing the functioning of the elements based on measurements using conventional direct-current techniques, electron counting is employed to investigate clocked single-electron transfer on the level of individual transfer events. Detailed insights into the dynamics of single-electron capture by a dynamic quantum dot are gained. Furthermore, a generalisation of the decay-cascade model is developed to account for varying decoupling times of the different quantum dot states.

Finally, the series operation of dynamic quantum dots with intermediate charge detection is presented and analysed. Besides the reduction in uncertainty of the number of emitted electrons as compared to the operation of an individual quantum dot, interaction effects between dynamic quantum dots via the forming potential in-between as well as the operation at higher repetition rates are discussed.

Keywords: Single-electron pump, Dynamic quantum dot, Counting statistics, charge detection, Quantum Ampere

Kurzzusammenfassung

Diese Arbeit beschreibt die experimentelle Entwicklung einer selbst-referenzierten Stromquelle. Diese besteht aus einer Kombination von Elektronen-Pumpen und Detektoren und erleichtert die Neudefinition der elektrischen Einheit "Ampere" auf der Basis von Naturkonstanten, indem die Anforderungen an die einzelnen Elemente gesenkt werden.

Aufbauend auf einer AlGaAs/GaAs Heterostruktur wurde eine Serie von dynamischen Quantenpunkten mittels Standardverfahren der Nanotechnologie wie Elektronenstrahlolithographie, nasschemischem Ätzen und Metallisierung durch thermisches Verdampfen hergestellt. Zwischen benachbarten Quantenpunkten wurden hochsensitive Transistoren platziert, die fähig sind Änderungen in der Besetzungszahl auf diesen Zwischeninseln von der Größe eines Elektrons zu detektieren.

Nach einer Diskussion der einzelnen Bauteile auf Grundlage konventioneller Strommessungen wird das Elektronen-Zählen benutzt, um den getakteten Elektronen-Transfer auf Basis individueller Ereignisse zu untersuchen. Dabei konnten detaillierte Einblicke in den Einfangprozess des dynamischen Quantenpunkts gewonnen werden. Weiterhin wurde eine Verallgemeinerung des Zerfallskaskaden-Modells entwickelt, um abweichende Entkopplungszeitpunkte für verschiedene Zustände zu berücksichtigen.

Zuletzt wird die serielle Verschaltung von dynamischen Quantenpunkten zusammen mit einer Ladungsdetektion an den Zwischeninseln gezeigt und analysiert. Neben einer Verringerung der Unsicherheit über die Zahl emittierter Elektronen verglichen mit der eines einzelnen dynamischen Quantenpunkts werden Wechselwirkungseffekte zwischen den Quantenpunkten durch das sich aufbauende Potential als auch der Betrieb bei höherer Repetitionsrate diskutiert.

Stichworte: Einzel-Elektronen-Pumpe, Dynamischer Quantenpunkt, Zählstatistik, Ladungsdetektion, Quanten-Ampere

Contents

List of Figures	ix
List of Symbols	xv
List of Abbreviations	xxii
1 Introduction	1
2 Basics of single-charge transfer	11
2.1 Electrons in a confining potential	11
2.1.1 The two-dimensional electron gas	11
2.1.2 One-dimensional electron gas	16
2.2 Quantum mechanical tunneling	18
2.3 Static quantum dots	20
2.4 Adiabatic electron turnstiles and pumps	29
2.4.1 Single-electron turnstile	29
2.4.2 Adiabatic single-electron pump	32
2.5 Non-adiabatic single-electron pumping using a dynamic QD	36
2.5.1 Illustrative description of the charge transfer mechanism	38
2.5.2 The charge-capturing process	47
2.6 Series operation of non-adiabatic dynamic QDs	53
2.6.1 Mesoscopic feedback	53
2.7 Metrological context: Quantum metrological triangle	57

3	Experimental methods	63
3.1	Sample fabrication	64
3.2	Introduction of the processed chip	71
3.3	Low-temperature environment	74
3.3.1	Electric wiring	77
3.3.2	Sample holder	78
3.4	Laboratory setup	79
3.4.1	Voltage sources	79
3.4.2	Amplifiers	80
3.4.3	Waveform generators and digitizers	83
3.4.4	Software	85
4	Conventional device characterization	89
4.1	Basic device characterization	90
4.1.1	Resistance during cool-down	90
4.1.2	Gate-dependence of the channel's conductance	90
4.1.3	Coulomb-blockade: Estimating capacitances	95
4.2	Charge transfer by the non-adiabatic dynamic QD (cw drive)	98
4.2.1	Finding the region of quantized-charge transfer	98
4.2.2	Investigation of the transfer characteristics (cw) of the individual dynamic QDs	100
4.2.3	Effect of the amplitude of the driving waveform	105
4.3	The dc-coupled single-electron transistor	107
4.3.1	Introduction to the superconducting SET . .	107
4.3.2	Optimal working point of the SETs operated as charge detectors	118

5	Dynamic quantum dots investigated by charge detection	121
5.1	Non-invasive charge detection on the dynamic dot . . .	122
5.1.1	Data analysis	130
5.1.2	Results	133
5.1.3	Continuous charging experiments beyond barrier characterization	142
5.2	Microscopic insight into dynamics of single-electron capture	147
5.2.1	Data evaluation	151
5.2.2	Counting statistics of charge transfer by a dynamic quantum dot	157
5.2.3	Detailed analysis of the capture mechanism	165
5.2.4	Analysis of entrance-gate voltage dependence by counting	170
5.2.5	Qualification of dots QD2 and QD4 by counting	172
5.2.6	Summary	175
6	The self-referenced current source	177
6.1	Introduction to series pumping and error accounting	178
6.2	Description of the measurement	182
6.3	Details of the counting algorithm	188
6.4	Results and discussions	195
6.4.1	Error accounting	196
6.4.2	Counting the number of transferred electrons	201
6.5	Conclusion	207
7	Series operation: Feedback and MHz repetition rates	209
7.1	Introduction to feedback during series operation . . .	210

7.2	Parameter dependence of transfer fidelity in series operation	213
7.2.1	Evaluation of transfer probabilities	216
7.2.2	Evaluation of charge built-up on the node	219
7.2.3	Break-down of unidirectional charge transfer	224
7.2.4	Summary	227
7.3	Series operation of dynamic QDs with MHz repetition rate	227
8	Summary and outlook	237
	Bibliography	241
	Curriculum vitae	263
	List of publications	265
	Danksagung	267

List of Figures

1.1	System of units and defining constants for redefinition	3
2.1	Two-dimensional density of states.	16
2.2	One-dimensional density of states.	17
2.3	tunneling across a potential barrier.	19
2.4	Density of states of a zero-dimensional system.	21
2.5	Simple model of a quantum dot.	23
2.6	Coulomb-Blockade in a Quantum dot.	26
2.7	Sketch of turnstile operation.	30
2.8	Sketch of adiabatic pump operation.	33
2.9	Precision measurement of the adiabatic pump.	35
2.10	SEM image of a typical pump structure.	37
2.11	Illustration of the charge capture process of the dynamic quantum dot.	40
2.12	Three-dimensional plot of the pumped current and its derivative.	43
2.13	Two-dimensional plot of the pumped current.	44
2.14	One-dimensional plots of the pumped current for fixed exit gate voltages.	46
2.15	One-dimensional plot of the pumped current for fixed entrance gate voltage.	48
2.16	Time-dependences of back-tunneling rate and the dot's chemical potential during charge capture.	50

List of Figures

2.17	Change of plateau transition as a function of bias potential.	55
2.18	Series operation of pumps illustrating mesoscopic feedback.	57
2.19	Quantum metrological triangle experiment.	60
3.1	Wafer layer stacking and band diagram	65
3.2	Sample processing: Mesa etching	66
3.3	Sample processing: Metallization	67
3.4	Sample processing: SET fabrication	68
3.5	SEM image of a processed SET	70
3.6	SEM image of the processed chip	72
3.7	Labelled image of the sample under investigation	74
3.8	Photography of the dry dilution cryostat	76
3.9	Photography of the sample holder	79
3.10	The 3-stage current amplification circuit	81
3.11	Photography of the PXI frame equipped with digitizers and waveform generators	84
4.1	Evolution of device resistances during cool-down	91
4.2	Pinch-off of current across channel by topgates	92
4.3	Coulomb diamond measurement of node 1	96
4.4	Location of the main pumping plateau of QD4 relative to dc characteristic	99
4.5	Quantized charge transfer by QD4, operated with cw driving signal	101
4.6	QD2 dc current measurement with continuous pulse train	102
4.7	QD1 dc current measurement with continuous driving signal	104

4.8	QD2 dc current measurement with continuous rf signal, comparison of different V_{ac}	106
4.9	Density of states of a superconductor in the semiconductor model	108
4.10	Quasi-particle tunneling across an all superconducting double junction	109
4.11	Coulomb diamond measurement of an all superconducting SET	111
4.12	Derivative of Coulomb diamond measurement of an all superconducting SET	112
4.13	Illustration of the Josephson-quasi-particle (JQP) cycle	114
4.14	Illustration of the double Josephson-quasi-particle cycle (DJQP)	116
4.15	SET modulation envelope as a function of bias voltage	117
4.16	Determination of SETs' optimal working point	119
5.1	Circuitry used for continuous node-charging	123
5.2	Gate-voltage patterns for continuous node-charging	123
5.3	Evaluation of continuous node-charging by QD1	126
5.4	Illustration of evaluation of continuous node-charging	132
5.5	Transfer fidelity in continuous charging experiment for combined detectors	135
5.6	Analysis of hold errors	137
5.7	Number of electrons stored on the node	139
5.8	Detection efficiency for single detectors and the combination of both	141
5.9	Analysis of coupling capacitances	143
5.10	Detector responses to continuous loading by QD2 from an open source reservoir	146
5.11	Setup and raw detector signals at pulsed electron transfer with intermediate reset	149

5.12	Histograms derived from pulsed electron transfer with intermediate reset	152
5.13	Counting signals derived from pulsed electron transfer with intermediate reset	154
5.14	Gate dependence of SET current before pulsed charge transfer and the position of the histograms' maxima under gate variation during pulsed transfer	156
5.15	Gate dependence of probabilities contributing to single-charge transfer	158
5.16	Number of correlated events per working point . . .	161
5.17	Calculated current derived from counting	162
5.18	Histogram of change of node's electron number due to reset pulse	164
5.19	Comparison between thermal and athermal modelling of counting data	168
5.20	Results from counting under variation of entrance barrier voltage	171
5.21	Probability distributions of charge transfer derived by counting for QD2 and QD4	173
6.1	Colored SEM-Image of the self-referenced current source	183
6.2	Pulse pattern, expected detector signals and raw detector signals in ideal series charge transfer	185
6.3	Raw detector signals indicating errors in series charge transfer	187
6.4	Evaluation of the SETs' response to the marker sequence	190
6.5	Raw detector traces together with counting and error signals	193
6.6	Exemplary demonstration of error accounting	198
6.7	Resulting probability distributions after accounting .	203
6.8	Resulting probability distributions after accounting .	205

7.1	Introductory example of feedback in series operation of dynamic quantum dots	211
7.2	Sketched detector signals and corresponding counting signals in sequential-transfer mode	214
7.3	Detector signals and corresponding counting signals in sequential transfer mode	215
7.4	Evaluation of transfer probabilities in series operation (sequential-transfer mode) as a function of working point of QD4	218
7.5	Evaluation of charge accumulation on the nodes in series operation (sequential-transfer mode)	221
7.6	Mesoscopic feedback using QD1 and QD4 with cw drive observed by detector D2	223
7.7	Evaluation of transfer probabilities in series operation (sequential-transfer mode) as a function of working point of QD4 on logarithmic scale	225
7.8	Pulse pattern used in series charge transfer of two dynamic quantum dots with MHz repetition rate	228
7.9	Time trace of series charge transfer of two dynamic quantum dots with MHz repetition rate	231
7.10	Histogram of difference in detector D2 current in response to pulses	232
7.11	Diagrams showing the resulting probabilities under variation of working points	234
7.12	Comparison of success probability of three frequent pulses with the single transfer success probability	236

List of Symbols

α_{II}	Amplitude of propagating wave in area II
α_V	Fitting parameter
$\alpha_{V \rightarrow E}$	Voltage-to-energy conversion factor
$\alpha_{X,n}$	Fitting parameter, decay cascade limit
$\alpha_{\mu,n}$	Fitting parameter, grand canonical limit
β_{II}	Amplitude of counter-propagating wave in area II
β	Temperature coefficient (equal to $(k_B T)^{-1}$)
β_d	Coupling to drain lead
β_s	Coupling to source lead
Δ	Difference
$\delta_{x,y}$	Kronecker Delta
$\Delta_{X,n}$	Fitting parameter, decay cascade limit
$\Delta_{\mu,n}$	Fitting parameter, grand canonical limit
$\Delta\nu(^{133}\text{Cs})_{\text{HFS}}$	Hyperfine splitting of ^{133}Cs (equal to 9.192631770 GHz)
Δ_s	Superconducting gap
ε	Subband energy (Optional superscript defines dimension)
ε_0	Vacuum permittivity (equal to $8.854 \times 10^{-12} \text{ Fm}^{-1}$)
ε_J	ε -correction of Josephson constant
ε_K	ε -correction of von Klitzing constant

List of Symbols

ε_p	ε -correction of charge
ε_r	Relative permittivity (≈ 13 for GaAs)
Γ	Total transition rate
Γ_d	Detector bandwidth
γ_d	Slope of line corresponding to a resonance with drain
Γ_{err}	Rate of transfer errors
γ_s	Slope of line corresponding to a resonance with source
κ_{II}	Wave number in area II
μ	Electrochemical potential (Optional subscript marks the corresponding state)
μ_0	Vacuum permeability (equal to $4\pi \times 10^{-7} \text{ Vs(Am)}^{-1}$)
μ_{ch}	Chemical potential
μ_d	Drain's electrochemical potential
μ_{node}	Electrochemical potential of the node
μ_s	Source's electrochemical potential
$\tilde{\mu}$	Generalized energies, used as fitting parameters for grand-canonical limit
Ω	Thermodynamic grand potential
ω_y	Angular frequency of a potential in y -dimension
Φ	Electrostatic contribution to the electrochemical potential
ϕ	Separated component of the electron's wave function
φ	Phase of the transfer pulse
π	3.14159265359 . . .
ψ	Electron wave function
σ	Width of a Gaussian distribution

τ	Time interval
Θ	Heaviside step function
\vec{A}	Vector potential
A	Fitting parameter (amplitude)
a	Spatial extension
Al	Aluminium
As	Arsenic
Au	Gold
B	Magnetic field
b	Spatial extension
C	Capacitance
c	Speed of light in vacuum (equal to $299792458 \text{ ms}^{-1}$)
C_d	Capacitance to drain
C_{fg}	Capacitive coupling via FG from node to detector
CF_4	Carbon monofluoride
C_g	Capacitance to gate
$C_{\Sigma}^{\text{node1}}$	Capacitance of node 1
C_{Σ}^{node}	Capacitance of whole node
$C_{\Sigma}^{\text{node2}}$	Capacitance of node 2
^{133}Cs	Caesium isotope with 133 u
C_s	Capacitance to source
C_{Σ}^{SET}	Overall capacitance of the SET
C_{Σ}	Overall capacitance
d_1	State of detector D1
d_2	State of detector D2
$D(E)$	Density of states
d	Diameter
E	Energy

List of Symbols

e	Elementary charge (equal to 1.602×10^{-19} C)
E_b	Energy of a barrier
E_C	Charging energy
E_c	Conduction band energy
E_f	Fermi energy
E_{th}	Thermal energy
exp	Exponential function
F	Force
f_p	Charge transfer frequency
$f(E)$	Fermi function
$\bar{f}(E)$	Inverse Fermi function, $\bar{f}(x) = 1 - f(x)$
f_j	Microwave frequency to induce Josephson effect
\mathcal{F}	Canonical free energy
f_s	Sampling frequency
G	Conductance
Ga	Gallium
Ge	Germanium
H	Hydrogen
h	Planck constant (equal to 6.626×10^{-34} Js \equiv 4.136×10^{-15} eVs)
He	Helium
\hbar	Reduced Planck constant (equal to $h/2\pi$)
I	Electric current
i	Integer number
I_c	Current with accounting
\vec{k}	Reciprocal wave vector, $\vec{k} = (k_x, k_y, k_z)$
k_B	Boltzmann constant (equal to 8.617×10^{-5} eVK $^{-1}$)

K_{cd}	Spectral luminous efficacy of a monochromatic Terahertz light source
k_f	Fermi wave number
K_{J-90}	Conventional unit of voltage
K_J	Josephson constant (equal to $\frac{2e}{h}$)
L	Length scale
l	Integer number
l_j	Number of the Josephson voltage step
\ln	Natural logarithm
m	Mass
m_e	Mass of an electron, (equal to 9.109×10^{-31} kg)
m^*	Effective mass of an electron
M_n	Number of successful events involving n electrons
$m0$	Missing cycle event during marker sequence
N	Dot's occupation number
n	Integer
N_A	Avogadro constant (equal to 6.022×10^{23} mol ⁻¹)
∇	Vector differential operator (Nabla)
Nb	Niobium
\overline{N}_{corr}	Average number of correlated events
n_c	Number of captured electrons
N_d	Donor density
$N(E)$	Number of states
N_e	Total number of emitted electrons
n_e	Number of emitted electrons
Ni	Nickel
N_{node}	Number of electrons stored on the node
N_0	Equilibrium occupation number

List of Symbols

N_{ser}	Number of pumps in series
n_s	carrier density in the 2DEG
O	Oxygen
P	Probability of electron capture (Optional superscript refers to the appropriate QD, subscript to the number of electrons)
Q	Charge
$Q_{\text{p-90}}$	Conventional unit of charge
Q_p	Charge transferred per cycle
\mathcal{R}	Reflection coefficient
r	Amplitude of the reflected component
\vec{r}	Position vector, $\vec{r} = (x, y, z)$
R_{F}	Feedback resistor
R_{H}	Hall resistance
$R_{\text{K-90}}$	Conventional unit of resistance
R_{K}	Von Klitzing constant (equal to $\frac{h}{e^2} = 25812.807 \Omega$)
R_{T}	Tunnelling resistance
Ru	Ruthenium
S	Sulfur
$s1$	Event not uniquely to attribute
$s0$	Missing cycle event during series operation
\mathcal{T}	Transmission coefficient
t_{III}	Amplitude of the transmitted component
t	Time
t^b	Time corresponding to onset of back-tunnelling
t^c	Time corresponding to full decoupling from source
t^e	Time of emission
T	Temperature

Ti	Titanium
t^∞	Point in time with complete decoupling from source
t^0	Arbitrary initial point in time
U	Electrostatic potential
u_c	Relative uncertainty after accounting
u	Uncertainty
U_J	Josephson voltage
V_{ac}	Voltage amplitude (peak) of the charge-transfer pulse
V_{G1}	Entrance gate voltage (Optional superscript identifies corresponding QD)
V_{G2}	Exit gate voltage (Optional superscript identifies corresponding QD)
V_{G3}	Third gate voltage (Optional superscript identifies corresponding QD)
V_g	Voltage applied to the gate of a 0-d structure
V_0	Offset voltage, used as fitting parameter
V_{sd}	Voltage difference applied between source and drain contact
W^-	Instantaneous rate to remove an electron
W^+	Instantaneous rate to add an electron
X	Integrated decay rates, used as fitting parameters for the generalized decay cascade limit
x	Spatial coordinate
$y(x)$	Fitting function
y	Spatial coordinate
z	Spatial coordinate

List of Abbreviations

ac	alternating current
ADC	Analog-to-Digital Converter
a.u.	arbitrary units
AWG	Arbitrary Waveform Generator
cw	continuous wave
D1,D2	Detector D1 and D2, respectively
DAC	Digital-to-Analog Converter
dc	direct current
DJQP	Double Josephson quasi-particle cycle
FG	Gate with floating potential for enhanced coupling
JQP	Josephson quasi-particle cycle
NI	National Instruments
NIST	National Institute of Standards and Technology
PCI	Peripheral Component Interconnect
pfi	pantheon file for instruments
pfp	pantheon file for parameters
PMMA	Polymethyl methacrylate
PTB	Physikalisch-Technische Bundesanstalt
PXI	PCI eXtensions for Instrumentation
QD i	(Dynamic) Quantum dot $i = 1, 2, 4$
rf	radio frequency
SAW	Surface acoustic wave
SEM	Scanning Electron Microscope
SET	Single Electron Transistor
SMA	SubMiniature version A, high-frequency connector



Introduction

But a molecule, say of hydrogen, if either its mass or its time of vibration were to be altered in the least, would no longer be a molecule of hydrogen.

If, then, we wish to obtain standards of length, time, and mass which shall be absolutely permanent, we must seek them not in the dimensions, or the motion, or the mass of our planet, but in the wave-length, the period of vibration, and the absolute mass of these imperishable and unalterable and perfectly similar molecules.

James C. Maxwell in "Address to the Mathematical and Physical Sections of the British Association", 1870 [1, p. 225]

Quite remarkably, Maxwell envisioned the concept of universal absolute units already in the middle of the nineteenth century, and only three years after in 1873, he proposed universal units for the meter, the second, and the mass [2]. This concept has been extended in 1900 by Max Planck to a system of "natural units" for length, time, mass and temperature based on thermodynamic principles (here, the theory of the entropy of radiation) which is detached from specific elements or certain realizations and which is therefore valid for all times and even "extraterrestrial or non-human cultures" [3]. Both concepts express the strong need in science for a common unit system which allows quantification of results, the estimation of uncertainties and the possibility for comparison between different laboratories or physical systems, for example. As a consequence of these aspects, every unit system should fulfil the following conditions [4]:

- Readily available to all
- Constant throughout time and space
- Easy to realize with high accuracy

Nowadays, the International System of Units (the SI, "Système international d'unités") is well established, providing a system of seven base units (kilogram, meter, second, ampere, kelvin, mol, candela as shown in Fig. 1.1) from which every physical quantity can be derived in terms of a product of powers of these base units using laws of physics [4, 5]. In contrary to Maxwell's vision, the current definition of the SI is only partly of this universality: The second, for example, is fundamentally defined via the radiation frequency corresponding to the hyperfine energy splitting of the ground state of ^{133}Cs (i.e., based on an atomic property). Together with this definition, also the meter can be defined by fixing the speed of light in vacuum. On the opposite, e.g., the kilo-

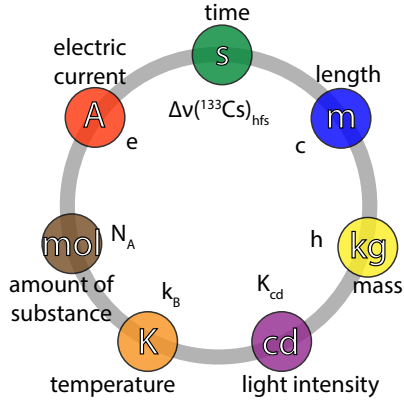


Figure 1.1:

System of units and defining constants for redefinition. Nowadays, the SI consists of seven base units (outer circle), while at the time of redefinition the values of seven fundamental, defining constants will be fixed.

gram is represented by an artefact (there is by definition no second realization) made of Platinum and Iridium which is stored in a safe near Paris (therefore, only indirectly accessible using a hierarchical procedure employing copies traced back to the international prototype) and, most importantly, comparisons suggest that the artefact might not remain stable over time [6, 7].

Turning the focus to the electric representative in the system of units, the ampere, let us have a look at its current definition [4]:

The ampere is that constant current which, if maintained in two *straight parallel* conductors of *infinite length*, of *negligible circular cross-section*, and placed 1 metre apart in vacuum, would produce between these conductors a force equal to $F = 2 \times 10^{-7}$ newton per metre of length.

Emphasized by italic formatting are those aspects which constitute idealizations for proper theoretical description but which cannot be realized straightforward experimentally. Equivalent to previous definitions, this one fixes the value of the vacuum permeability to $\mu_0 = 4\pi \times 10^{-7} \text{ kg m s}^{-2} \text{ A}^{-2}$ directly evidencing the link to the mechanical units in the SI, the kg, m, and s. [4]. This example demonstrates quite remarkably one of the main points of criticism of the currently used system of units: Not always the constant and its value fixed by the definition are readily apparent [5].

With the advent of the "new SI", the transition towards a fundamental system based on natural constants will be completed whose explicit values will directly fix the whole system of units [8–10]. Although there is still some ongoing discussion [11, 12], I will discuss the current proposal of this redefinition [9] shortly: The fundamental constants chosen consist of the Cs hyperfine splitting $\Delta\nu(^{133}\text{Cs})_{\text{HFS}} = 9\,192\,631\,770 \text{ Hz}$, the speed of light c , Planck's constant h , the elementary charge e , Boltzmann's constant k_{B} , Avogadro's constant N_{A} and the luminous efficacy K_{cd} of a monochromatic light source at 540 THz. Exemplary, the Ampere will be defined by stating that $e = 1.602\,176\,565 \times 10^{-19} \text{ A s}$ (assuming here the adjusted Codata value of e from 2010 [13]) and will thus only be linked to the unit of time which may be realized in a laboratory with lowest relative uncertainty of the order of 10^{-16} [14]. Inverting this relation, one obtains for the ampere A [9]:

$$1 \text{ A} = \left(\frac{e}{1.602\,176\,565 \times 10^{-19}} \right) \text{ s}^{-1} \quad (1.1)$$

$$= 6.789\,687 \dots \times 10^8 \Delta\nu(^{133}\text{Cs})_{\text{HFS}} e, \quad (1.2)$$

independent of any specific realization. Of course, this way of definition might be a bit abstract, but it directly reflects the physical picture

of electric current: The equations state that one ampere equals the flow of $(1.602\,176\,565 \times 10^{-19})^{-1}$ electrons per second.

Although the quantization of electric charge and its value could have been assessed in the famous experiments of Millikan on charged oil drops already in 1913 to $e = (4.774 \pm 0.009) \times 10^{-10}$ [esu] [15] (equivalent $e = (1.592 \pm 0.003) \times 10^{-19}$ C in SI units), the first observation of single-electron charging effects in a designed solid-state system has been reported only in 1987 [16].

Generally speaking, the single-charge devices aiming for a direct realization of the ampere may be divided into two groups, of which one relies on the active manipulation of electrons while the other one is based on a passive approach referred to as electron counting.

The former devices were initially fabricated in both metallic and semiconducting systems and employed the tunnelling effect, but were operated adiabatically only [17–20] leading to the relation

$$I = e \cdot f_p, \quad (1.3)$$

where the electric current I is realized by the periodic transfer of single electrons with charge e at a repetition frequency f_p .

It is important to mention that in contrast to macroscopic quantum effects observed in solid-state systems like the quantum Hall effect [21] or the Josephson effect [22, 23], the output current of any known single-electron device is not exactly quantized but scales with the average number $\langle n_e \rangle$ of transferred electrons per cycle:

$$I = \langle n_e \rangle e \cdot f_p, \quad (1.4)$$

where the deviation of the generated current $|1 - \langle n_e \rangle|$ results from the underlying statistics of single-electron manipulation.

Practical aspects require a current level of a few 100 pA accompanied by a relative uncertainty of 10^{-8} [24]. These two requirements have

not yet been met simultaneously in any device, e.g. metallic pumps yielded the required uncertainty [25–27], but only at the expense of low repetition rates leading to currents of the order of 1 pA, due to the RC time constant of the barriers confining the structure. On the opposite, surface-acoustic-wave driven devices [28–30] can be operated at high frequencies of several Gigahertz (leading to currents in the nA-range) since here the tunnelling barriers are modulated by the surface wave (leading to much lower RC time constants), but, most probably due to heating effects, the precision was rather limited to about 10^{-4} [31]. Recently, a complimentary concept of massive parallelization using optically-driven self-assembled quantum dots has been reported [32], demonstrating high current generation at low repetition frequencies, but several fundamental questions have to be solved on the way towards metrological precision. In the following chapter 2 I will discuss some of these realizations and their principles of operation in more detail.

However, among different other realizations recently developed [33–37], the so-called non-adiabatic single-electron pump implemented in a GaAs-AlGaAs heterostructure [38, 39] is considered as one of the most promising candidates [40], employing a semiconductor quantum dot driven by an external voltage source. This device is sufficiently robust [41] to operate in complex circuits (e.g., parallel [42] or serial [43] arrangements have been demonstrated) and has additionally shown promising precision of $|1 - \langle n_e \rangle| \lesssim 10^{-6}$ at current levels of about 150 pA [44]. These dynamic quantum dots form one of the building blocks of the device investigated in this thesis.

Although metrological aspects are definitely the driving force within this development, all these devices touch fundamental aspects of quantum transport, since detailed understanding of the operation principles is necessary to, e.g., derive the dominating sources of errors [45–48]. Additionally, by employing these single-electron sources one ob-

tains a tool for triggered single-electron emission, opening the access to study single-electron wavepackets in time and energy [49], perform interference experiments using two on-demand electron sources [50] or the splitting of electron pairs emitted by a single clocked source at a barrier [51] mimicking fundamental quantum optics experiments in solid-state systems.

However, all single-electron (or Cooper-pair [52–54]) devices are based on the manipulation of individual particles. Thus, the current generated $I = n_e e f_p$ may not be given by an exact integer n_e but by a stochastic average $\langle n_e \rangle$ due to the nature of the underlying principles. As a second path towards the realization of the Ampere based on single electron effects, the passive charge counting has therefore been investigated: In these experiments, electrons passing a constriction are monitored using a detector which is only capacitively coupled [55]; therefore, electrons remain in the system under observation. Shortly after the first real-time counting experiment [56] as a practical application of the development of the radio-frequency single-electron transistor [57], two concepts involving either a chain of metallic tunnelling junctions [58] or a double quantum dot structure [59] have been demonstrated. Compared to conventional real-time counting experiments [60, 61], the main achievement in these experiments is to ensure the direction of electron transfer, i.e. from which lead electrons enter or to which one electrons leave the constriction. However, the maximum current level achievable is limited by the detector's bandwidth.

Only recently, the late Michael Wulf proposed the combination of both concepts in a more complex circuit [62], combining the possibility of triggered charge transfer employing single-electron sources with the ability of passive charge detectors to monitor single electrons. In a series of synchronously operating quantum current sources, the number of electrons in-between, given by the difference of incoming and outgoing

electrons, changes only in the rare case of a transfer error by one of the neighbouring sources. Thereby, the requirements on both, the transfer fidelity of the sources as well as the bandwidth of the detectors, can be relaxed. Using this concept, the uncertainty in the output current may be reduced by orders of magnitude compared to the individual current sources. This proposal is sometimes regarded as an extension of the original qualification of the metallic single-electron pump on the level of single electrons by shuttling carriers back and forth [25]. However, this type of device allows to validate the output current directly *during* its generation [63].

The results shown in this thesis can be divided into two parts, depending on the combination of single-electron transfer devices and single-electron detectors. On the one hand, the precision of single-charge detection will be employed to investigate the transfer mechanisms underlying the clocked transfer of electrons by an individual dynamic quantum dot. Using only single transfer pulses, the outcome of each transfer operation can be reliably determined using single-charge detectors. Thus, these measurements allow to assess the precision of the capture mechanism on the level of single electrons. On the other hand, using a series combination of dynamic QDs with charge detectors coupled to the interconnecting nodes, the error accounting scheme is experimentally demonstrated. By applying statistical analysis to the events detected, the uncertainty in the output current is reduced compared to an individual dynamic quantum dot. Furthermore, interaction effects between serially connected dynamic dots are addressed.

The thesis is outlined as follows: **Chapter 2** is devoted to the theoretical basis and the presentation of competing concepts. This covers the concept of density of states and the two- and one-dimensional electron gas, the properties of (static) quantum dots as zero-dimensional structures and selected realizations of single-electron current sources (early pumps and turnstiles) to give an introduction to single-electron transfer

devices. Afterwards, the theoretical description of the semiconducting dynamic quantum dot acting as quantized-current source will be presented. In particular, two different models for single-charge capture will be discussed as well as aspects necessary to understand effects in series operation of these structures, namely the mesoscopic feedback [43, 64]. Final remarks on the significance of these devices in the context of metrology and the discussion of the so-called metrological triangle [65, 66] conclude this chapter.

In the following **chapter 3**, technical aspects of this work will be covered. Starting with the sample layout and aspects of device processing, a short introduction to low-temperature measurements and electric wiring to connect the device with the room-temperature electronics will be given. Furthermore, the instruments and concepts employed to electrically control the structure will be presented together with a short description of the software used for remote control.

Subsequently, the first experimental results obtained will be shown in **chapter 4**. The focus here is on the introduction of the individual building blocks and verifying/discussing proper operation using conventional direct-current measurements only. Initially, the operation of the semiconducting elements is presented, followed by the discussion of quantized-current generation using continuous driving signals. The gate-dependence of all individual structures is shown for fixed driving signals in order to serve as a reference for the following experiments. The chapter is concluded by the general introduction of the all-superconducting single-electron transistor. Here, the parameter dependence of the current is discussed and features specific to the coexistence of quasi-particles and Cooper-pairs in transport are presented.

In the following **chapter 5**, the pulsed operation of a dynamic quantum dot investigated by charge detection will be introduced. Main aspects within this section are the investigation of transfer fidelity as well as the occurrence of hold-errors or the enhancement of dynamic

range by combining several detectors. The second part of this chapter addresses the first experimental investigation of this type of dynamic quantum dot by single-electron counting, being not only limited to the extraction of the full transfer probabilities, but also giving access to a deeper understanding of the underlying physical phenomena in dynamic single-charge capture, derived from the interplay of transfer rates.

The succeeding **chapter 6** discusses the experimental realization of operating dynamic quantum dots in series with intermediate highly-sensitive charge detectors, a concept which is referred to as the self-referenced current source. Here, we put emphasis on the discussion of the underlying error-accounting scheme. Moreover, the specific pulse pattern used will be outlined: This allows simultaneous operation of the dynamic quantum dots in series while calibrating at the same time the intermediate charge detectors on the level of single electrons and extracting the individual full counting statistics of the dynamic quantum dots involved. The concept of error accounting is finally demonstrated by comparing the resulting probability distribution over the number of electrons transferred using the compound device with the distribution expected for an individual dynamic quantum dot.

In the last experimental **chapter 7**, the analysis of the interaction of dynamic quantum dots operated in series is presented. Here, we investigate the series charge transfer probabilities under variation of the individual points of operation. Experiments shown cover the series operation of two dynamic quantum dots at higher repetition rates (≈ 800 kHz) as well as the investigation of feedback by charge accumulation employing three dynamic quantum dots in series.

The thesis is concluded with **chapter 8**, containing a summary of the results obtained as well as the presentation of strategies for further development.



Basics of single-charge transfer

2.1 Electrons in a confining potential

2.1.1 The two-dimensional electron gas

The charge transport in a metal may be described using the so-called Drude-Sommerfeld model. There, electrons may flow freely in all directions in space, leading to the dispersion relation

$$E = \left(\frac{\hbar^2}{2m^*} \right) (k_x^2 + k_y^2 + k_z^2), \quad (2.1)$$

with $\vec{k} = (k_x, k_y, k_z)$ the reciprocal wave vector and m^* the effective mass of an electron in the crystal. The concept of an effective mass accounts for the interactions of electrons with the lattice potentials. In general, this mass is a tensor, but for GaAs (as used in this thesis) it simplifies to $m^* \approx 0.067m_e$ at low temperatures [67], with m_e

2 Basics of single-charge transfer

the mass of a free electron. Following the argumentation in [68], the electron dynamics may be written using the Schrödinger equation as

$$\left(E_c + \frac{1}{2m^*} \left(i\hbar\nabla + e\vec{A} \right)^2 + U(\vec{r}) \right) \psi(\vec{r}) = E\psi(\vec{r}), \quad (2.2)$$

with $U(\vec{r})$ the potential energy, caused by e.g. space-charge, \vec{A} the vector potential and E_c the conduction band energy, because in the structures under discussion transport takes place through electrons in the conduction band. Neglecting the lattice potential (being included only in the electron's effective mass), the resulting wave functions $\psi(\vec{r})$ have the form of plane waves instead of Bloch waves [67, 68]:

$$\psi(\vec{r}) = \exp(i\vec{k} \cdot \vec{r}). \quad (2.3)$$

In artificially created heterostructures (for a review, e.g. see [69]) inhibiting a 2-dimensional electron gas (2DEG), the electrons may propagate freely in two dimensions but are confined by some potential $U(z)$ in the third one chosen here as the growth direction (z-axis). Thus, the wave function can be rewritten (excluding a magnetic field, thereby $\vec{A} = 0$) as:

$$\psi(\vec{r}) = \phi_n(z) \exp(ik_x x) \exp(ik_y y). \quad (2.4)$$

The corresponding dispersion relation reads as

$$E_n(k_x, k_y) = E_c + \varepsilon_n^z + \frac{\hbar^2}{2m^*} (k_x^2 + k_y^2) \quad (2.5)$$

with n indicating the different subbands and with

$$\varepsilon_n^z = \frac{n^2 \pi^2 \hbar^2}{2m^* L_z^2} \quad (2.6)$$

the quantized eigenenergies in the approximation of a indefinitely deep quantum well of width L_z . Obviously, the energy separation increases

with smaller dimension L_z . The phase-coherence length sets the upper limit of the dimension L_z : In excess of this length scale electrons will loose their "phase memory" and behave bulk-like [70].

The first signature of quantization in such a structure was reported in 1966 using a metal-oxide-semiconductor (MOS) field-effect transistor in Si [71]. For a true two-dimensional system, only the first subband may be occupied. This requires in turn, that all other energy scales must be much smaller than the energy difference $\varepsilon_2^z - \varepsilon_1^z$ between the first two subbands. Especially the thermal energy $E_{\text{th}} \approx k_B T$ has to be sufficiently low ($E_{\text{th}} \approx 350 \mu\text{eV}$ at $T = 4 \text{ K}$, but $E_{\text{th}} \approx 25 \text{ meV}$ at $T = 300 \text{ K}$). According to the simulations for the wafer used in this thesis (see chapter 3.1), the energy difference of the two states equals about $\varepsilon_2^z - \varepsilon_1^z \approx 20 \text{ meV}$. Therefore, one can exclude that thermal broadening allows occupation of the second subband in this experiment, being conducted at nominally $T = 25 \text{ mK}$.

Using periodic boundary conditions to determine allowed values for k_x, k_y , one obtains

$$\vec{k}_{x,y} = \frac{2\pi}{L}(n_x, n_y) \quad (2.7)$$

with L the dimensions of the crystal in x and y . Obviously, the allowed states form an equidistant square lattice in k -space with distance $2\pi/L$. Thus, each state occupies an area $4\pi^2/L^2$ in k -space. On the other hand, states with energy E will be contained in a disk of radius k (and area πk^2) where

$$E = E_c + \varepsilon_1^z + \frac{\hbar^2 k^2}{2m^*}. \quad (2.8)$$

Therefore, the total number of states N , given as the ratio of the disk's area to the area of each state in k -space, equals

$$N = 2 \cdot \frac{\pi k^2}{(4\pi^2)/L^2} = \frac{m^* L^2}{\pi \hbar^2} (E - E_c - \varepsilon_1^z). \quad (2.9)$$

2 Basics of single-charge transfer

The factor of 2 accounts for the spin degeneracy. Finally, the density of states per area and energy is calculated as

$$D(E) = \frac{1}{L^2} \frac{d}{dE} N(E) = \frac{m^*}{\pi \hbar^2}. \quad (2.10)$$

According to this expression, the density of states is constant and can be extended in case of the occupation of several subbands to

$$D(E) = \frac{m^*}{\pi \hbar^2} \sum_n \Theta(E - E_c - \varepsilon_n). \quad (2.11)$$

with Θ the Heaviside step function.

In transport measurements, not only the number of states and their distribution in energy is of importance, but also whether these states are occupied or not. The occupation probability of states is given under the condition of thermal equilibrium by the Fermi function

$$f(E) = \frac{1}{1 + \exp\left(\frac{E - E_f}{k_B T}\right)} \quad (2.12)$$

with E_f the Fermi energy. This expression may be simplified in two limits (for energies E far from E_f), one being the high-temperature limit where $\exp\left(\frac{E - E_f}{k_B T}\right) \gg 1$:

$$f(E) \approx \exp\left(-\frac{E - E_f}{k_B T}\right). \quad (2.13)$$

In the opposite limit at low temperatures, called the degenerate limit, the Fermi energy may be approximated by

$$f(E) \approx \Theta(E_f - E). \quad (2.14)$$

The electron density at equilibrium is now given as the sum over all energies of the product of states available times its occupation probabilities, yielding

$$n_s = \int dE D(E)f(E), \quad (2.15)$$

which equals in the case of a degenerate Fermi function

$$n_s = \frac{m^*}{\pi \hbar^2} (E_f - E_c - \varepsilon_1^z) \quad (2.16)$$

with the expression $(E_f - E_c - \varepsilon_1^z) = (\hbar k_f)^2 / 2m^*$ defining the associated Fermi wave number k_f . By finally combining these two expressions, the Fermi wave number can be directly related to the electron density n_s [68, 72] via

$$k_f = \sqrt{2\pi n_s}. \quad (2.17)$$

In case of the occupation of more than one subband, one speaks of a quasi two-dimensional system. The resulting 2d density of states is shown in Fig. 2.1a) together with a realistic confining potential in b) as obtained by simulating the heterostructure used in this thesis. Sketched also are the energetic positions of the first two subbands as well as the Fermi energy.

Inserting the experimentally derived carrier density of $n_s = 2.77 \times 10^{15} \text{ m}^{-2}$ into the expression (2.17), one obtains a Fermi energy relative to the energy of the first subband ε_1^z of $E_f \approx 10 \text{ meV}$. In conclusion, the first subband is filled almost halfway to the onset of the second subband ($\varepsilon_2^z - \varepsilon_1^z \approx 21 \text{ meV}$ according to the simulations of the employed heterostructure), i.e. the electron gas can be regarded as a true two-dimensional system.

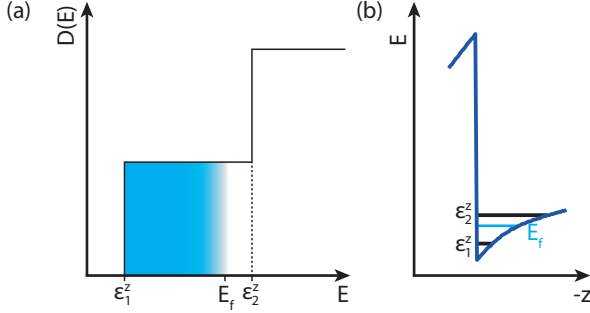


Figure 2.1:

Two-dimensional density of states (a) and a real confining potential in a heterostructure as used in this thesis (b). Shown as blue line is the conduction band at the interface between AlGaAs and GaAs where the 2DEG is located. Additionally, the lowest two discrete energy states and the location of the Fermi energy are sketched.

2.1.2 One-dimensional electron gas

If now also the lateral propagation of electrons is confined in another dimension to a one-dimensional channel, e.g. by etching the heterostructure or applying electrostatic potentials using gates, quantization of energies and the formation of subbands is also observed in this dimension (y-axis here and assuming a harmonic potential $U(y) = \frac{1}{2}m^*\omega_y^2y^2$):

$$E = E_c + \varepsilon_n^z + \varepsilon_l^y + \frac{\hbar^2}{2m^*}k_x^2 \quad (2.18)$$

with

$$\varepsilon_l^y = \hbar\omega_y\left(l - \frac{1}{2}\right), \quad (l = 1, 2, 3, \dots). \quad (2.19)$$

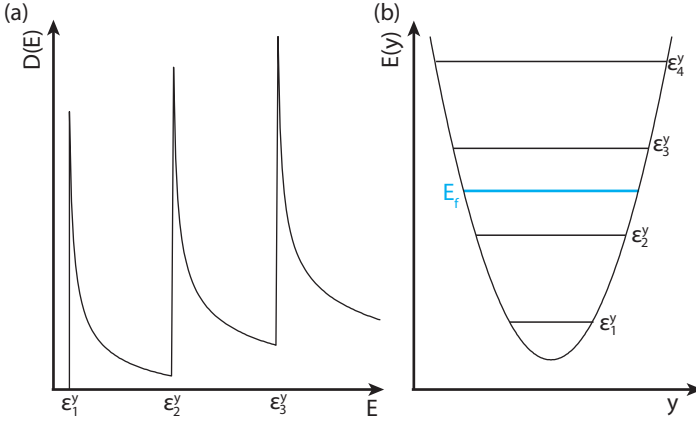


Figure 2.2:

Quasi one-dimensional density of states (a) and a harmonic confining potential (b). In this sketch, the lowest two subbands are occupied, providing four transport channels in case of spin degeneracy.

The resulting density of states $D(E)$ equals

$$D(E) = \frac{\sqrt{2m^*}}{\pi\hbar} \sum_{n,l} (E - E_{n,l})^{-1/2} \Theta(E - E_{n,l}), \quad (2.20)$$

i.e. the density of states is proportional to the inverse square-root of the energy in the case of a one-dimensional system.

Thus, electrons may flow freely in x -direction while being confined in y and z dimensions which is the regime of one-dimensional transport. Although Ohm's law is valid even for wires of the diameter of a few atoms in the diffusive regime [73], remarkable effects are observed when the probability of scattering is strongly reduced. This is the regime of ballistic transport which can be achieved if the mean free path is much larger than typical sample dimensions. Here, the conductance

takes quantized values only in multiples of $2e^2/h$ (in case of spin degeneracy), yielding an achievable lower limit of the conductance of about $G = 77.5 \mu\text{S}$ even for the most-perfect contacts. First experimental observations of this effect have been reported in 1988 by van Wees [74] and Wharam [75], studying the charge transport of point contacts inhibited in a AlGaAs-GaAs heterostructure. This phenomenon can be described using the formalism proposed by Landauer [76, 77] and extended to the multi-terminal case in magnetic fields by Büttiker [78] (for an introduction, see e.g. [68, 79]) which is referred to as "Landauer-Büttiker-formalism". Instead of regarding current flow as a system's response to an applied electric field, it is described here using transmission \mathcal{T} and reflection \mathcal{R} coefficients of individual channels (the subbands in y -direction). But where does the finite conductance, even in case of perfect transmission $\mathcal{T} = 1$, come from? This effect is attributed to the interface between the contacts (providing an infinite number of transverse modes) and the channel (only a few modes) which requires that the current-carrying electrons have to be redistributed here, giving rise to the finite resistance.

2.2 Quantum mechanical tunneling

In classical physics, a particle with energy E may not pass a barrier characterized by an energy $E_b > E$ and width $2a$. Instead, it will be reflected at the barrier. But in quantum mechanics, there is a probability that a particle may overcome such a barrier as depicted in Fig. 2.3. Additionally, even a particle with energy $E > E_b$ may be reflected at such a barrier in contradiction to classical physics. The particle, in our case an electron of mass m^* incident from the left and propagating to the right, is described by the wave function $\psi(x)$ which has been normalized to one for simplicity. As a consequence of the barrier, the wave will be partly reflected leading to a counter-propagating wave of

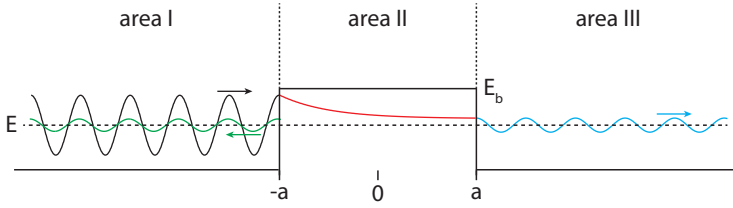


Figure 2.3:

Tunneling across a barrier of height E_b and width $2a$. The incoming wave is coloured black, the reflected one green and the transmitted wave blue. Inside the barrier, the wave (red) decays exponentially.

amplitude r in area I while the transmitted wave in area III is described by a wave of amplitude t_{III} . Conservation of particles requires that $|t_{\text{III}}|^2 + |r|^2 = 1$. Inside the barrier in area II, the particle wave is decaying, thus leading to the following ansatz for the electron's wave function [80]:

$$\psi(x) = \begin{cases} \exp(ikx) + r \exp(-ikx) & x < -a \quad (\text{area I}) \\ \alpha_{\text{II}} \exp(-\kappa_{\text{II}}x) + \beta_{\text{II}} \exp(\kappa_{\text{II}}x) & |x| < a \quad (\text{area II}) \\ t_{\text{III}} \exp(ikx) & x > a \quad (\text{area III}) \end{cases} \quad (2.21)$$

where the wave numbers k and κ_{II} are defined as

$$k = \sqrt{\frac{2m^*}{\hbar^2} E}, \quad \kappa_{\text{II}} = \sqrt{-\frac{2m^*}{\hbar^2} (E - E_b)}, \quad (2.22)$$

respectively. All three functions need to match with boundary conditions, especially $\psi(x)$ needs to be continuous at the interfaces, i.e.

$$\frac{1}{\psi(x)} \frac{d\psi(x)}{dx} \Big|_{x=-a,a} \quad (2.23)$$

must be continuous. The probability of transmitting the electron through the barrier is then given by the energy dependent transmission coefficient $T(E) = |t_{\text{III}}|^2$ which shows the following approximate dependence (in the limit of a large barrier) on the parameters of the barrier:

$$\ln(T(E)) \simeq -4a\sqrt{\frac{2m^*}{\hbar^2}(E_b - E)} \quad (2.24)$$

In summary, the transmission probability depends exponentially on the effective barrier given as the difference of the electron's energy to the barrier height as well as the barrier's length. In a physical system, the barriers are not simple square functions and additionally, in transport experiments also the density of states on both sides of the barrier has to be taken into account. But this rather simple example demonstrates the concept of energy-dependent transmission coefficients or, in other words, tunneling rates.

2.3 Static quantum dots

The previously increased confinement of electrons from one to two dimensions lead to quantization of energies in these coordinates, but still the energy in the remaining, free directions was continuous. In the case of quantum dots, the confinement is extended to all spatial directions, resulting in a (quasi) zero-dimensional system which is described by a discrete density of states

$$D(E) = 2 \sum_j \delta(E - \varepsilon_j), \quad (2.25)$$

as shown in Fig. 2.4. These confinement energies may be reasonably large in semiconductor systems due to which quantum dots are discussed as a solid-state analogon of an atom, including effects compa-

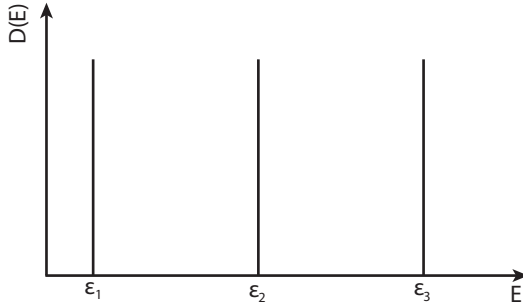


Figure 2.4:

Density of states of a zero-dimensional system showing a discrete spectrum, representing the quantum dot energy levels ε_j .

rable to filling of orbitals and shells [81, 82]. In contrast, metallic systems behave almost bulk-like due to the larger electron densities so that in mesoscopic metallic devices excitation effects are typically not observed [70]. Only for ultrasmall metallic grains of the size $\lesssim 10$ nm, coupled via oxide barriers to source and drain contacts, also quantum transport effects could have been studied in metals [83].

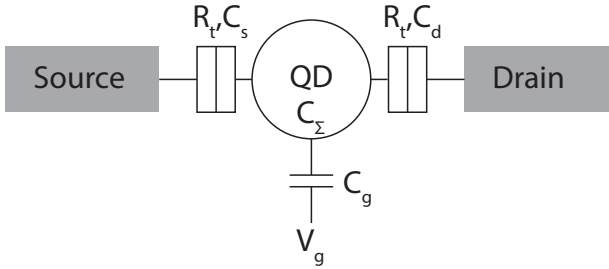
Until now, specific properties of electrons like the electric charge e , leading to interaction effects, have been neglected. To further discuss the transport properties of static quantum dots, we will use a model known as "constant-interaction model" [84–86]. The basic electric circuit is depicted in Fig. 2.5. The QD in the center, characterized by a capacitance C_Σ , is coupled to electron reservoirs, called source and drain. This coupling is achieved via tunneling barriers, formed e.g. by electrostatic potentials or small oxide layers, which are described via a tunneling resistance, R_T , and a capacitance, C_s and C_d , respectively. The size of the QD is so small that the granular nature of the electric charge becomes visible: The charge stored on the island is allowed to

change only in integer multiples of the elementary charge. This imposes a certain requirement on the tunneling resistance, which must be sufficiently large in order to ensure this quantization (as discussed later in this section). Additionally sketched is a pure capacitively coupled gate (via the capacitance C_g) which may be used to tune the potential of the QD by applying a voltage V_g . However, electrons may enter or leave the dot only via the tunneling barriers to source and drain leads. These leads are characterized by electrochemical potentials μ_s and μ_d , which may be tuned by applying an external voltage difference between the two. For simplicity, we assume $\mu_s > \mu_d$ in the following. If now one also attributes an electrochemical potential to the dot μ_n being occupied by n electrons, then charge transport is energetically allowed at low temperatures only if

$$\mu_s > \mu_n > \mu_d. \quad (2.26)$$

Here, we exclude higher-order tunneling effects like co-tunneling. Obviously, the electrochemical potential of the dot therefore plays a major role in transport experiments involving quantum dots. Thus, we will explain next how to determine this parameter and its dependence of, e.g., the number of electrons on the dot or the external gate voltage V_g .

Along with the constant-interaction model, two implicit assumptions are being made: This is on the one hand the approximation that the interaction between electrons on the dot and a surplus electron can be parameterized by the dot's capacitance C_Σ . This parameter will be discussed at the end of this section. On the other hand, one assumes that the discrete single-particle energy spectrum of the dot remains unchanged for interacting electrons. Hence, the dot's ground state energy,


Figure 2.5:

Simple model of a quantum dot, coupled via tunneling barriers to source and drain leads. Its electrostatic potential may be influenced using a capacitively coupled gate.

being occupied by n electrons, is given [82] by

$$U_n = \frac{(en - C_g V_g)^2}{2C_\Sigma} + \sum_{i=1}^n \varepsilon_i, \quad (2.27)$$

neglecting any residual electrons on the dot at $V_g = 0$ (which would lead to a transformation of $n \rightarrow n - N_0$ only). The two assumptions previously stated become obvious by the simple summation of the electrostatic (first) term including the interaction via the capacitance and the gate potential and the second, chemical term summing up the single-particle energies. For simplicity, this term will be abbreviated in the following via E_n .

The difference of the two energies U_n and U_{n-1} defines the electrochemical potential $\mu_n = U_n - U_{n-1}$. Inserting the definition (2.27) yields

$$\mu_n = \underbrace{\left(n - \frac{1}{2} \right) \frac{e^2}{C_\Sigma} - e \frac{C_g}{C_\Sigma} V_g}_{=e\Phi_n} + \varepsilon_n. \quad (2.28)$$

Here, the factor

$$E_C = \frac{e^2}{C_\Sigma} \quad (2.29)$$

is called the charging energy, depending only on the capacitance of the QD. Thus, the electrochemical potential may be regarded as the sum of the chemical potential $\mu_{\text{ch}} = \varepsilon_n$, depending on the confining potential only, and an electrostatic contribution $e\Phi_n$ [86]. The latter in turn consists of a discrete element $(n - 1/2)e^2/C_\Sigma$ (resulting from the interaction of the electrons on the dot) and a continuous contribution $\frac{C_g}{C_\Sigma}V_g$ in response to the electrostatic environment. In case of the occupation of a state with ε_i with $i > n$ during transport, tunneling does not take place via the lowest possible energy state and therefore, one speaks of transport via an excited state.

The addition energy finally, which equals the amount of energy necessary to change the dot's occupation number from n electrons to $n+1$, is given as the difference of the contributing electrochemical potentials:

$$\Delta\mu_{n+1} = \mu_{n+1} - \mu_n = \frac{e^2}{C_\Sigma} + \Delta E, \quad (2.30)$$

with $\Delta E = \varepsilon_{n+1} - \varepsilon_n$. In summary, the energy required to change the occupation of the quantum dot by one electron is constant and equals the charging energy E_C provided the difference in the single-particle energies ΔE is negligible small. Most-importantly, the charging energy is also independent of the number of electrons on the dot, leading finally to an equidistant spacing of energy states in case of negligible quantum energy differences. Moreover, μ_n may be continuously varied by applying a gate voltage V_g , according to equation (2.28). Figure 2.6a) shows the resulting potentials in the regime of Coulomb blockade. The tunneling barriers separating the source and drain leads (characterized by μ_s and μ_d , respectively) from the QD are sketched as white squares. The difference $\mu_s - \mu_d = eV_{\text{sd}}$ opens a transport

window (sketched as the grey area in the quantum dot) which allows charge transport if any of the dot's electrochemical potentials μ_n lies within. In the situation depicted, the state μ_n is always occupied, since $\mu_s > \mu_n$ (i.e., occupation from source is energetically allowed), but tunneling to drain is energetically forbidden because all states at the energy μ_n in the drain lead are occupied ($\mu_d > \mu_n$). The next available, empty state μ_{n+1} (sketched as the lowest dashed line) is separated in energy by the addition energy and may not be occupied from either source or drain since $\mu_{n+1} > \mu_s, \mu_d$. Therefore, Coulomb blockade suppresses the flow of electrons from source to drain.

However, as discussed above, the gate voltage may be adjusted such that the electrostatic contribution $e\Phi_n$ shifts the electrochemical potential μ_{n+1} below μ_s and therefore into the transport window. This situation is shown in Fig. 2.6b) where tunneling of electrons from source becomes energetically favourable. The occupation number of the dot changes in consequence from n to $(n + 1)$. In the small bias regime, as depicted, tunneling of another electron is now forbidden due to the separation of the next level in energy due to the charging energy. The electrostatic term $e\Phi_n$ changes in consequence by the charging energy leaving the situation depicted in Fig. 2.6c). Subsequent tunneling of the surplus electron to drain then returns the QD occupation number back to n and the cycle may start again.

Its experimental signature is shown in Fig.2.6d) where the conductance G peaks at gate voltages corresponding to quantum dot states within the transport window. As outlined above, transport is suppressed in-between by the electrostatic repulsion in response to another electron, i.e. the system is "Coulomb blocked". Coupling of the states of the dot to source and drain reservoirs leads to a slight broadening of the peaks [87]. The transport window may be tuned by changing the voltage difference $V_{sd} = e^{-1}(\mu_s - \mu_d)$. The parameter dependence of the conductance across the quantum dot as a function of both ex-

2 Basics of single-charge transfer

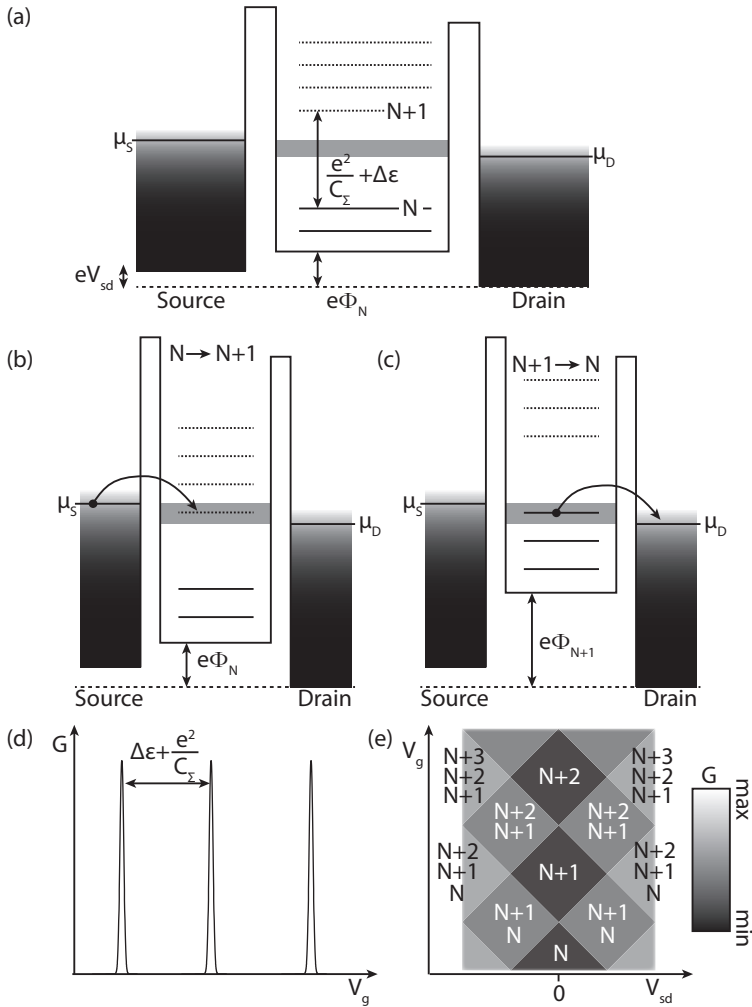


Figure 2.6: Coulomb-Blockade in a Quantum dot. Depicted are the general model in the blocking regime (a), sequential charge tunneling at constant gate voltage V_g (b,c) and the dependence of the conductance across the QD as a function of gate voltage (d) and of gate and bias voltages (e). For details see text.

ternal parameters, gate and bias voltage, is shown as a two-dimensional plot in Fig. 2.6e). The transport window determines the number of transport channels (each separated in energy by the charging energy), leading to a step-wise increase in the conductance with increasing bias voltage difference. The dark regions in the center mark the suppression of transport due to Coulomb blockade (only one charge state on the dot is energetically allowed). The charge state of the dot in the center region is therefore well defined and constant, leading to the term "stability diagram" for this kind of graph. The plot shown in Fig. 2.6d) corresponds to a vertical line in the regime $V_{sd} \approx 0$. Both plots contain additional information about the device parameters since the charging energy or contributing capacitances may be derived from the data. E.g., the peak distance ΔV_g in Fig.2.6d) yields the gate capacitance $C_g = e/\Delta V_g$. Additionally, the extent of the blockaded region in Fig.2.6e) along the source-drain voltage axis gives the charging energy and thereby the total capacitance, C_Σ :

$$e\Delta V_{sd} = E_C = e^2/C_\Sigma. \quad (2.31)$$

Finally, from the transitions between the stable regions one can derive the capacitances of the tunnel junctions. Lines with positive slope γ_s correspond to resonances with the source lead, yielding

$$\gamma_s = (C_\Sigma - C_s)/C_g, \quad (2.32)$$

while negative slopes γ_d correspond to resonances with drain, leading to

$$\gamma_d = -C_s/C_g. \quad (2.33)$$

Detailed descriptions of these derivations may be found in, e.g., Refs. [88, 89].

Let us finally discuss the requirements to observe single-charging effects in quantum dots. As outlined above, the charging energy is parameterized by the overall capacitance C_Σ (see eq.(2.29)). At room-

2 Basics of single-charge transfer

temperature conditions and assuming a capacitor of $C = 1$ pF, this effect can be neglected since $E_C \approx 160$ neV while the thermal energy equals already $E_{\text{th}} \approx 25$ meV therefore being about five orders of magnitude larger. In quantum dots, the capacitance may be approximated geometrically by a disk of diameter d :

$$C = 4\epsilon_r\epsilon_0d \quad (2.34)$$

with the dielectric constant $\epsilon_r \approx 13$ in GaAs. Assuming further a disk of diameter $d = 500$ nm, equation (2.34) yields $C \approx 230$ aF. This number should be regarded as a lower limit of the dot's capacitance only since all neighbouring capacitances of e.g. the tunneling barriers or gates will increase the value of $C_\Sigma = C_s + C_d + C_g$. However, inserting this number in equation 2.29, one obtains $E_C \approx 700$ μ eV. At low temperatures, this energy may exceed the thermal energy which equals $E_{\text{th}} \approx 100$ μ eV at about 1 K. In conclusion, small sizes (leading to small capacitances and thereby high charging energies, according to eq. (2.34)) and low temperatures are necessary requirements to observe single-charging effects.

Additionally, there is another requirement resulting from quantum mechanics onto the quantum dots, foreshadowed in the beginning of this section: Heisenberg's uncertainty principle states $\Delta E \Delta \tau > h$. To observe single-charging effects, the electron's wave function must be sufficiently localized on the dot. The average time on the dot $\Delta \tau$ is approximately given by the RC -time constant of the tunneling barriers. Thus, the uncertainty principle yields

$$\Delta E \Delta \tau \approx \frac{e^2}{C_\Sigma} R_T C_\Sigma = e^2 R_T > h, \quad (2.35)$$

superimposing the condition $R_T \gg h/e^2$ onto the tunneling resistance R_T .

2.4 Adiabatic electron turnstiles and pumps

Although the granular nature of electric current due to the electrostatic energy of an additional electron on the island has played already a major role in the discussion of the quantum dot, current through such a device has not been quantized on the level of single electrons at all until now: As soon as a state becomes available in the transport window opened by the bias voltage, a flow of randomly tunneling electrons sets in whose amplitude is determined by the tunneling constants attributed to the barriers. However, only a few years after the first single-electron transistor created by Fulton and Dolan [16] the first devices being able to transfer a specific number of carriers per unit time interval have been reported, realized in metallic [17] and semiconductor systems [18]. These first implementations were all based on the "turnstile" operation mode which is introduced in the following section. All devices under discussion in this section operate adiabatically, i.e. the frequency is sufficiently low in order to allow the system to follow the energetic ground state.

2.4.1 Single-electron turnstile

In order to deterministically control the tunneling of electrons through a quantum dot system, one necessarily needs to be able to control the tunneling barriers and their transparency in time. In metallic systems, however, these barriers are fixed which in turn requires the usage of a chain of quantum dots (three in series are required for the turnstile operation [90]). Effectively, the outermost series dots act as additional tunneling barriers [19]. The device's operation principle is shown in Fig. 2.7a) for a metallic system. After correction of background offset charges using additional gates, the directed charge transfer is achieved by using one oscillating signal applied to the central island and a bias

2 Basics of single-charge transfer

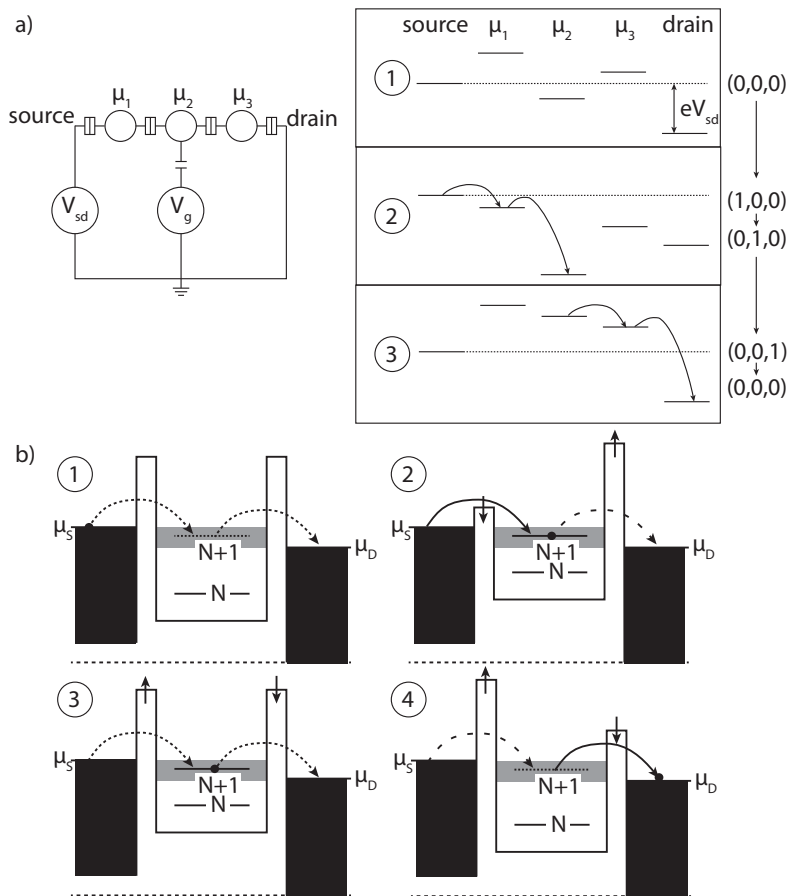


Figure 2.7:

Sketch of turnstile operation for a metallic, fixed-barrier system (upper panel a), adapted from [19]) and for a semiconductor, tunable-barrier realization (lower panel b), adapted from [18]).

potential $\mu_s - \mu_d$ across the series array. The former does not only shift the central electrochemical potential μ_2 , but also modulates via cross-coupling the outer chemical potentials μ_1, μ_3 in the same direction but with smaller amplitude. If initially tuned as shown in panel ①, the left island exceeds the right one in energy throughout the cycle which defines the unidirectional transfer of electrons from left (source) to right (drain). tunneling of electrons from either lead onto one of the islands is prohibited in panel ① since the outermost energy levels are energetically unfavourable. By lowering the central island, the left island's state is simultaneously lowered in energy, until in situation ② its state is below the source's electrochemical potential, leading to the tunneling of one electron from source via the left to the central island. Afterwards, as shown in ③, the central level is raised again in energy while back-tunneling to source is always suppressed by the left-most island, even in the case that μ_2 exceeds μ_s since $\mu_1 > \mu_2$. Only if level $\mu_3 > \mu_d$, tunneling from the center island to drain is allowed. In summary, one electron has been transferred from source to drain during this cycle.

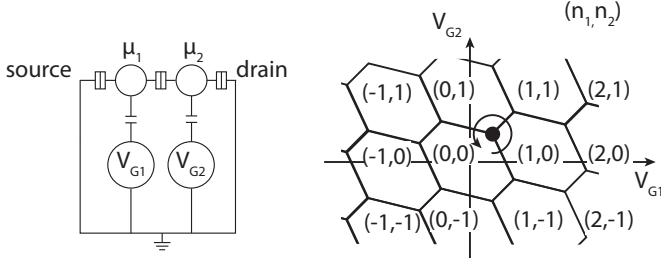
Using a semiconductor turnstile, as shown in Fig. 2.7b), the device itself can be reduced in complexity, since the tunneling barriers may be modulated directly using topgates. However, then two driving signals, one for each barrier, are necessary. By applying a phase-shift of π to both signals at the same amplitude, both contributions to the dot's energy level cancel out and the level remains constant while the barriers are modulated. Opening initially the barrier to source, one electron can occupy the energetically lower empty dot state. But, it cannot leave the dot to drain since this barrier is at its maximum. After another half-period, the drain barrier is sufficiently low to allow tunneling of the surplus electron to drain. Again, the bias potential $\mu_s - \mu_d$ is essential to determine the direction of charge transfer. In general, this type of device should allow higher transfer frequen-

cies due to the possibility of lifting the barrier completely as compared to the metallic counterparts. However, operation frequencies beyond $f_p > 20$ MHz have not been reported. Remarkably, also non-adiabatic single-parameter charge pumping has been observed in these devices already in 1991 [91], but this direction of research has not been further pursued.

The advantage of the turnstile is its rather simple operation mode, employing only one rf signal in the metallic realization (of course, at the expense of a more complex device compared to the semiconductor realization). However, due to the necessity of the bias potential to achieve unidirectional single-charge transfer, energy is dissipated in the structure which leads to heating and thereby to an increasing probability of higher-order tunneling events (co-tunneling). Therefore, this type of device has not been studied for metrological precision experiments.

2.4.2 Adiabatic single-electron pump

This disadvantage of energy dissipation in the circuit due to the applied bias has been overcome by the concept of the adiabatic pump. Although also in semiconducting systems adiabatic pumping operation has been demonstrated [18] by applying different modulation amplitudes to both gates (thereby lifting and lowering the electrochemical potential of the dot during the cycle), these systems have not been employed in metrological applications. Only recently, adiabatic pumping in semiconductor systems has returned into focus again when being implemented using state-of-the-art Silicon fabrication techniques and operation at GHz frequencies [92]. However, we will focus here on metallic adiabatic pumps which set the benchmark in accuracy of single-electron charge transfer. Schematically, such an adiabatic pump is shown for a metallic system in Fig. 2.8a). Such device consists of a


Figure 2.8:

Sketch of adiabatic pump operation for a metallic system (adapted from [20]), consisting of two islands whose electrochemical potentials are tunable by gate voltages V_{G1} and V_{G2} (a). Stability diagram of the charge states occupied by the system. The encircled triple point exemplarily defines the range of modulation of gate voltages for single-charge transfer. The sense of the rotation, experimentally accessible via the relative phase of both modulation signals, defines the direction of charge transfer, independently of applied bias voltages.

series arrangement of three tunneling junctions, separating source and drain leads from the two center islands. Both electrochemical potentials can be adjusted by gate voltages V_{G1} and V_{G2} . The system's charge state is characterized by the tuple (n_1, n_2) corresponding to the occupation number of the islands 1 and 2. Their dependence on gate voltages is shown in Fig. 2.8b) with an arbitrary definition of $n_i = 0$. Inside the hexagonal areas, the charge states are stable while lines correspond to transitions between charge states. The intersections between three hexagons are called triple points of which one is marked by the black dot. Encircling this point, the system changes its state in the order

$$(n_1, n_2) \rightarrow (n_1 + 1, n_2) \rightarrow (n_1, n_2 + 1) \rightarrow (n_1, n_2) \quad (2.36)$$

with $n_1 = 0, n_2 = 0$ in the beginning for this point. Obviously, this sequence exactly matches the sequential transfer of one electron

from source via the two islands to drain. The direction of charge transfer is then given only by the relative phase between both voltage signals and is therefore independent of the bias voltage. The frequency of operation is limited by the requirement of adiabaticity. However, the highest frequency in such device reported (employing a 3-junction metallic pump with additional chromium resistors in series, referred to as "R-pump" [93]) is $f_p = 100$ MHz, yielding a current of about $I \approx 16$ pA [94].

There are several sources of errors in these devices which lead to deviations from perfect single-charge transfer, e.g. missing cycle events (in case of operating too fast), thermally activated errors, photon-assisted tunneling and co-tunneling [45, 90]. Co-tunneling is regarded as the limiting source of errors and describes a quantum mechanical effect in which several electrons tunnel in a coherent manner. This process can be suppressed by either increasing the tunneling resistance (leading to higher tunneling time constants) or by increasing the number of tunneling barriers (thereby enhancing device complexity). The most-precise single-electron transfer device has been reported in 1996 [25], using a seven-junction adiabatic pump which is shown schematically in Fig. 2.9a). The achieved deviation from single-electron transfer was 15×10^{-9} at a frequency of $f_p = 5.05$ MHz, however, theoretical considerations suggested an even lower deviation.

Besides this measurement still being the benchmark with respect to the precision achieved, the underlying ideas of how the error rates are determined are of even higher importance for the understanding of this thesis since this concept will be reused in the framework of error accounting (see chapter 6). As previously discussed, the direction of single-charge transfer can be switched in an adiabatic pump by simply changing the phase between the driving gate voltages. With the depicted needle switch open, the (large) external island is charged by the transfer of an electron. This is reflected by a jump in the signal of a ca-

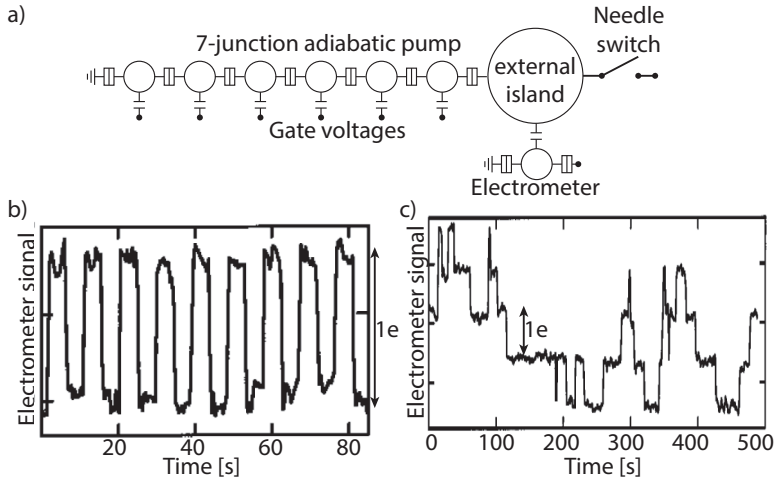


Figure 2.9:

Precision measurement of the adiabatic pump. a) Sketch of the basic device, containing a seven-junction pump and a switch to select between charging a capacitor (to determine the precision of operation) and delivering a quantised current. In a slow shuttling experiment, one electron is transferred onto and off the capacitor whose charge state is monitored by an electrometer (b). If the shuttling frequency is increased above the detector's bandwidth, the average charge on the capacitor is monitored which changes only in case of a transfer error (c). (adapted from [25])

capacitively coupled electrometer. After removing the electron again by the inverse process, the system switches back to its initial state as shown in Fig. 2.9b). In the graph, two transfer events are delayed by several seconds which is sufficiently slow to be resolved by the electrometer. However, if the frequency of this shuttling operation is much faster than the electrometer's bandwidth, only the *average* charge state of the external island is monitored which remains constant after completing the shuttling back and forth. Only in the rare case of transfer errors,

the charge state changes by one electron until the next error occurs. Provided a sufficiently low error rate, this deviation from perfect single-electron transfer can be detected, as shown in Fig. 2.9c). Each jump of height $\approx 8 \mu\text{V}$ in the detector signal corresponds to the deviation by one electron.

Following this characterization, the needle switch is closed and the unidirectional single-electron current is delivered to an external circuit. However, this method is based on the assumption that the transfer probabilities in the shuttle experiment (which has been assessed in the measurement in Fig. 2.9c)) and in the unidirectional current generation (which is unknown) equal. The deviation from the nominally quantized current corresponding to $I = ef_p$ cannot be simultaneously confirmed when the cryogenic needle switch is closed, i.e. during current generation.

2.5 Non-adiabatic single-electron pumping using a dynamic QD

In this thesis, the clocked charge transfer will be accomplished by using the non-adiabatic single-parameter pump, which basically is a quantum dot in an etched semiconductor wire defined by topgates of which one gate is driven by an additional rf voltage signal. A sketch of such a structure is shown in Fig. 2.10.

The quasi-one-dimensional wire, etched out of a two-dimensional electron gas and about 800 nm wide below the gates, can be locally depleted by applying negative potentials to the gates. Just recently, non-adiabatic charge pumping has also been demonstrated in an all gate-defined quantum dot [95]. In all experiments, the third electrode is grounded and therefore does not affect the underlying electron system. A similar structure, consisting of an etched semiconductor channel and

2.5 Non-adiabatic single-electron pumping using a dynamic QD

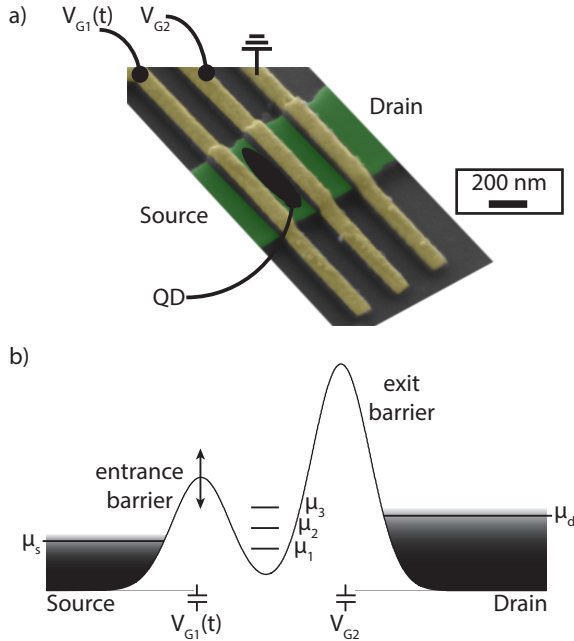


Figure 2.10:

False-color SEM image of a typical pump structure (a). By inducing negative potentials V_{G1} and V_{G2} onto the metallic gates (coloured yellow) crossing an etched semiconductor wire (green), a quantum dot (QD) is formed in-between. The third gate electrode is grounded throughout this thesis. Also shown is a sketch of the induced electrostatic potential (b). Only the entrance gate voltage $V_{G1}(t)$ is modulated by an external rf signal, leading to periodic coupling/decoupling of the dot's electrochemical potentials (labelled $\mu_1 \dots \mu_3$ for the first three charge states) with the source lead. The leads are characterized by the electrochemical potentials μ_s and μ_d , respectively. Because of acting as a pump, the condition $\mu_s > \mu_d$ for charge transfer from source to drain is not required. Instead, the direction of charge transfer is given by the arrangement of modulated and constant gate.

additional metallic topgates defining a QD, has been also employed as a turnstile by Nagamune et al. [96] in 1994, following the operation principle sketched in Fig. 2.7b). However, in the realization used here both barriers are tuned far beyond pinch-off and thus strongly suppress tunneling of electrons between source and drain leads in the static case without any rf signal applied. Between the first two gates, a quantum dot is formed in the electron system below. The electrostatic potential inside the wire is depicted as a sketch in Fig. 2.10b). By modulating the entrance barrier, the QD is periodically coupled and decoupled to/from the source lead which leads to charging the dot with electrons from source or defining an exact integer number of electrons on the dot, respectively. The electrochemical potentials of the dot are labelled $\mu_1 \dots \mu_3$ for the first three electron states located on the dot. Both leads are parametrized by the electrochemical potentials μ_s (source) and μ_d (drain lead), respectively. The exit barrier, which is held at constant potential, forms a large tunneling barrier between dot and the drain lead, suppressing any direct tunneling of electrons between source and drain while the entrance barrier is lowered in order to charge the dot with electrons. Only if electrons are excited in energy (during the emission phase), they may overcome this potential barrier.

2.5.1 Illustrative description of the charge transfer mechanism

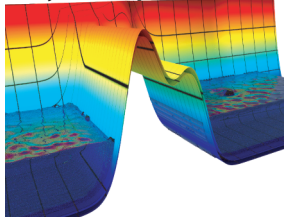
Before providing the mathematical description of charge transfer by a dynamic quantum dot, I will first give an illustrative depiction of the working principles. The inset in Fig. 2.11 shows the time dependence of the modulated potential applied to the entrance gate. In order to maintain equivalence with the barrier formed by this gate, $-V_{G1}(t)$ is plotted, i.e. the entrance barrier is at its maximum when the function $-V_{G1}(t)$ reaches its maximum. It is worth noting at this point that

2.5 Non-adiabatic single-electron pumping using a dynamic QD

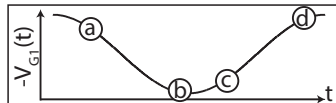
the action of the applied potentials to both of the topgates defining the quantum dot is two-fold: On the one hand, any potential applied controls the height of the barrier, i.e. the rate of tunneling from either side of the barrier to the other. On the other hand, it also couples capacitively to the electrochemical potentials of the dot formed in-between, labelled μ_n (thereby acting as a plunger gate). In summary, by applying a more negative potential (in order to increase the barrier), also the electrons on the dot are lifted in energy (reducing the effective barrier compared to the case of negligible plunger action). The ratio of these two effects is a critical parameter for the working of this type of device.

At point (a), the empty ground state of the dynamic quantum dot is high in energy and well isolated from source and drain leads. Therefore, tunneling onto the dot from either lead is suppressed. After a half cycle, reaching point (b), the barrier to source has become transparent, enabling exchange of electrons between source and the dot. Due to the capacitive coupling of the barrier potentials to the quantum dot's electrochemical potentials μ_n , occupation of those states is energetically allowed for which $\mu_n < \mu_s$ holds. Consecutively, by increasing the negative potential on this gate again (marked by (c)), the above-mentioned interplay of the gate acting as barrier (controlling the transparency to source) and as plunger (lifting the electrochemical potentials of the dot) leads to a finite number of electrons being isolated (or captured) on the dot. This is accomplished by a cascade of electrons tunneling back to source which sets in as soon as the corresponding state μ_n is lifted above the source's electrochemical potential μ_s . The exact number of electrons finally captured is defined mainly (of course, only in the case of fixed slew rates of the rf signal) by the potential of the static exit gate which controls the height of the dot's energy levels at the moment of decoupling. The more positive this potential, the lower are the quantum dot's electrochemical potentials. This leads to a higher occupation of electrons on the dot since the barrier is already more opaque at the

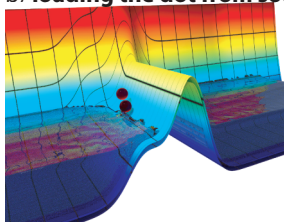
a) dynamic quantum dot isolated



The entrance barrier is held high, tunneling onto the dot from either side is suppressed. The dot's ground state is well above the chemical potential of both, source and drain, leads.

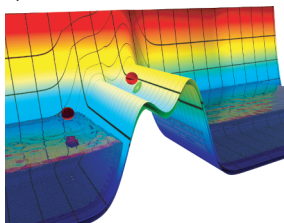


b) loading the dot from source ("initialization")



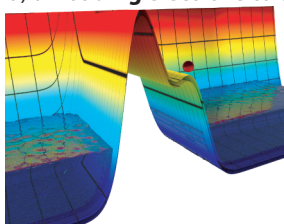
The entrance barrier is lowered below the source's chemical potential by applying a more positive voltage to the gate, thereby allowing electrons to enter the dot ("initialization"). The exit barrier remains high, preventing electrons from tunneling from/to drain.

c) define the number of electrons on the dot ("capture")



The entrance barrier is raised again, thereby also lifting the electrons on the dot in energy. This leads to an increased back-tunneling rate to source when the corresponding dot's energy state is above the source's fermi level. Finally, a well-defined number of electrons (controlled by the exit gate voltage) remains on the dot, being decoupled from both leads.

d) unloading electrons to drain ("emission")



The entrance barrier is raised further, lifting the isolated electrons on the dot in energy. This yields an increase in the tunneling rate to drain since that barrier becomes effectively lower. Provided a sufficient amplitude of modulation, all electrons are unloaded to the drain lead, leaving an empty dot.

Figure 2.11:

Illustration of the charge capture process of the dynamic quantum dot, for details see text. Inset depicts the applied rf signal $-V_{G1}(t)$.

2.5 Non-adiabatic single-electron pumping using a dynamic QD

point of beginning of back-tunneling, defined by $\mu_n > \mu_s$. Finally, depicted in situation (d), the electrons isolated on the dot are raised in energy such that the effective barrier height imposed by the potential of the exit gate is sufficiently small to allow tunneling to drain at an excess energy given by $\mu_n(t^e) - \mu_d$ with $\mu_n(t^e)$ the electrochemical potential of the n th electron on the dot at the time of its emission to drain, t^e .

One further comment on the electrochemical potentials of source and drain lead, μ_s and μ_d , respectively: Due to the driving scheme, electrons are only allowed to enter the dot from source across the modulated tunneling barrier. Electrons tunneling back to source at the phase of initialization and capture do not contribute to the average current. Since also tunneling from drain is suppressed, only those electrons which are lifted over the exit barrier to drain define the average current in this transfer period. Therefore, the potential difference $\mu_s - \mu_d$ does not define the direction of charge transfer as in the turnstile devices. Moreover, due to the large barrier to drain, this specific pump is even able to act against a reasonably large potential difference $\mu_s - \mu_d$, making it an ideal candidate for series operation.

After the completion of one period, the dot is empty again, equalling the initial situation marked (a). In the course of this thesis, also single pulses will be applied instead of a continuous wave. In such cases, the most-negative gate-voltage setting will be kept until the next pulse is applied, i.e. the scheme in the inset in Fig. 2.11 is extended by constantly repeating the initial/final value. There are two reasons for this choice: First, if the barriers are held constant at their respective maxima, tunneling across the QD, even at high electron energies, is very unlikely. Additionally, with the phase chosen this way, all dynamic processes (loading, capturing and emission) are as undisturbed as possible. Imagine, as an example, a phase of π was chosen: Then, the initialization would last as long as the delay between two subsequent

pulses. If the duration of coupling to source (enabling the initialization of the dot) is the limiting process, then the phase shift of π might lead to deviations from the behaviour observed using a cw signal.

One key ingredient of the working principle is the non-adiabaticity: While in devices operating in the adiabatic limit it is important to allow for tunneling times in order to maintain the system in the energetically lowest state (which imposes an *upper* limit onto the operation frequency), the non-adiabatic dynamic QD has a *lower* limit in frequency. If the source barrier does not become opaque sufficiently fast, all electrons on the dot will tunnel back to the source reservoir after being lifted above μ_s .

However, there exists also an upper limit in operation frequency for these devices. This is given by, e.g., the occupation of excited states in the dot during the capture process (either by excitations during the lifting of states in energy or by insufficient relaxation times when being initially loaded into an excited state). These states couple stronger to the source (being at higher energies) which leads to a reduction in the capture probability and decreasing fidelity of single-charge transfer as observed in [97].

After this general discussion, let us turn towards the parameter dependence of the quantized current. A typical plot of the current I generated by a dynamic quantum dot, operating at fixed rf parameters (frequency f_p and amplitude V_{ac}), is shown in Fig. 2.12 under variation of its static gate parameters. At the bottom of this graph the derivative is depicted, indicating the flat plateaus in multiples of ef_p (white) and sharp transitions in-between (dark grey). Typically, the dynamic quantum dots are operated on the main plateau which is marked by the red arrow. Additionally, a magnetic field has been applied, leading to an additional confinement of the electrons on the dot and therefore to sharper transitions between neighbouring plateaus. However, this aspect is beyond the scope of this thesis and is discussed in, e.g., [44,

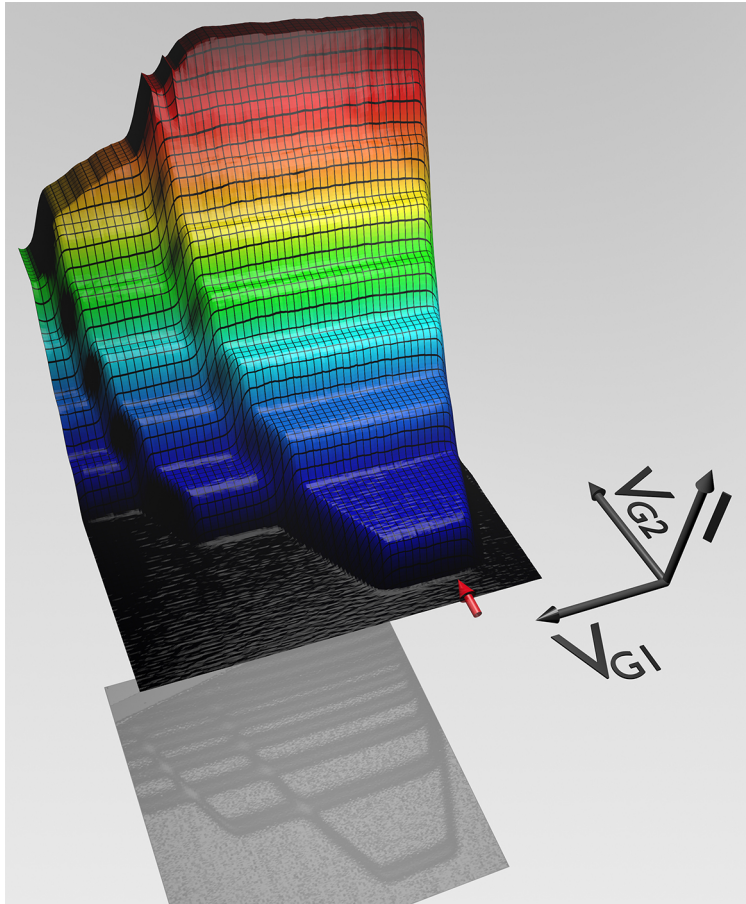


Figure 2.12:

Direct-current measurement of the single-electron pump showing a three-dimensional plot of the output current I (top) and its derivative (bottom) as a function of control gate voltages V_{G1} , V_{G2} . Frequency $f_p = 50$ MHz, amplitude $V_{ac} = 180$ mV, magnetic field $B = 9$ T. Color represents the amplitude of the current in the range of zero to $8ef_p$, the dark regions in the derivative represent transitions between plateaus. The main plateau is marked by the red arrow.

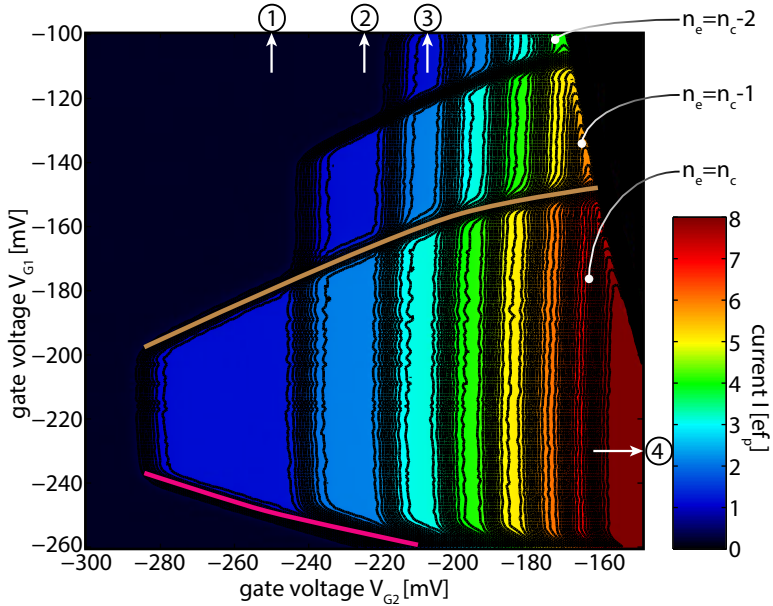


Figure 2.13:

Direct-current measurement of the single-electron pump showing a two-dimensional plot of the pumped current I as a function of control gate voltages V_{G1} , V_{G2} for same conditions (rf , B) as in Fig. 2.12. The white, labelled arrows mark traces shown in Fig. 2.14 and 2.15, respectively. The color-scale represents the amplitude of the pumped current in the range of zero to $8ef_p$, the black contour lines mark the transitions between the plateaus in steps of $0.1ef_p$. The magenta line represents the limit of pump operation due to insufficient coupling to source during initialization, the brown one incomplete unloading to drain during emission.

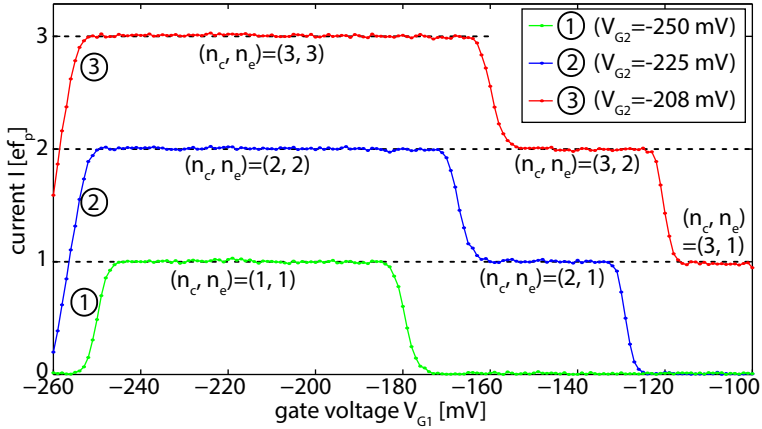
97–104].

The dependence of the formation of plateaus in multiples of ef_p on the entrance gate voltage V_{G1} can be seen more clearly in Fig. 2.13

2.5 Non-adiabatic single-electron pumping using a dynamic QD

which is a two-dimensional colour plot of the same data as in Fig. 2.12. The plateau region is limited towards most negative gate voltages V_{G1} by insufficient loading of electrons from source (marked by the magenta line). If the barrier formed by that gate is too large, the modulation does not open the contact to the source reservoir. In turn, by increasing the amplitude V_{ac} of the rf signal, this border can be shifted towards more negative values. Above, for more positive values of V_{G1} , the main plateau is formed. Here, the number n_c of electrons isolated (or captured) on the dot during the cycle equals the number of electrons emitted to drain n_e at the end of the cycle. Therefore, the dot is empty at the end of the cycle, so that any further increase in amplitude of the rf signal does not increase the number of carriers emitted. By further increasing the gate voltage V_{G1} towards more positive values, the quantum dot's ground states are lowered in energy. This leads at some point to insufficient unloading of electrons to drain, since the modulation does not lift the electrons isolated on the dot strongly enough to overcome the drain barrier formed by V_{G2} (marked by the light brown line). Thus, the integer number of electrons emitted to drain n_e is lower than the number of electrons isolated on the dot in this region, $n_e < n_c$.

Numbered white arrows mark line cuts for constant exit gate voltages V_{G2} , labelled ①, ② and ③ and shown in Fig. 2.14, respectively. As already discussed, the current I , given as the average number of emitted electrons n_e per period, is at its maximum at the main plateau ($n_e = n_c$) since for all side plateaus the condition $n_e < n_c$ holds. Even a further increase of rf amplitude (allowing to operate the dynamic quantum dot at more negative gate settings) will not increase the number of transferred electrons since the number of emitted electrons cannot exceed the amount of captured electrons, $n_e \leq n_c$. Therefore, one can derive from a line cut as shown in Fig. 2.14, at which parameter range (e.g., after an increase of amplitude if the extent of the main


Figure 2.14:

Cuts along the marked positions in Fig. 2.13 for different exit gate voltages (①: $V_{G2} = -250$ mV, ②: $V_{G2} = -225$ mV, ③: $V_{G2} = -208$ mV) showing cross-sections through the main plateau as well as the first (②) and the first two side-plateaus (③), respectively. Additionally, the number of captured electrons n_c and the number of emitted electrons n_e are depicted. The pumping parameters are the same as in Fig. 2.12.

plateau is comparable to the first side plateau) the dynamic dot is operated on the main plateau. To conclude, the accuracy of the whole transfer cycle of the dynamic quantum dot is not limited by the initialization or emission process, provided the applied rf amplitude allows operation on the main plateau, i.e. at entrance gate voltages inside the region defined by the magenta and light brown lines.

In contrast, the number of electrons transferred for a fixed entrance gate voltage (say, tuned to the main plateau), as a function of exit gate voltage V_{G2} is dominated by the capturing (isolation) process at the formation of the dynamic quantum dot, following the initialization. There are basically two limits describing the mechanisms of charge cap-

2.5 Non-adiabatic single-electron pumping using a dynamic QD

ture in tunable-barrier devices discussed in literature [47, 48], either a frozen grand-canonical distribution or a rate-driven athermal limit, also known as the decay-cascade model [46, 105]. The latter is sometimes applied as a figure of merit to benchmark the operation of a device based on its gate dependence [44]. Within this context, it is important to understand the applicability of the underlying concepts. Furthermore, depending on the mechanism dominating the charge capture process, different strategies for further optimization should be followed as discussed at the end of section 5.2.

A typical current-dependence on the exit gate voltage V_{G2} is shown in Fig. 2.15, illustrating the step-like increase in multiple integers of elementary charge times driving frequency with increasing gate voltage V_{G2} . This plot corresponds to the arrow marked ④ in Fig. 2.13. The inset demonstrates the flatness of the $n = 1$ plateau as a function of V_{G2} which corresponds to a current of about $I \approx 8$ pA at these operating conditions ($f_p = 50$ MHz). Roughly speaking, the exit gate voltage predominantly acts as plunger gate at this part of the cycle which controls the depth of the quantum dot during the capturing process: The lower the dot (i.e., the more positive the gate voltage V_{G2}), the more electrons can be isolated on the dot and subsequently emitted to the drain lead [41], leading to the experimentally observed step-wise increase of emitted electrons n_e with lower exit gate voltage V_{G2} . The detailed theoretical framework will be given in the next section, following the discussion outlined in [47].

2.5.2 The charge-capturing process

In the description of static quantum dots (see section 2.3), the relevant parameters for a proper understanding of those structures have been introduced. The main difference in this section is the time-dependence of the energy states of the dot and of the tunnel-coupling to the source

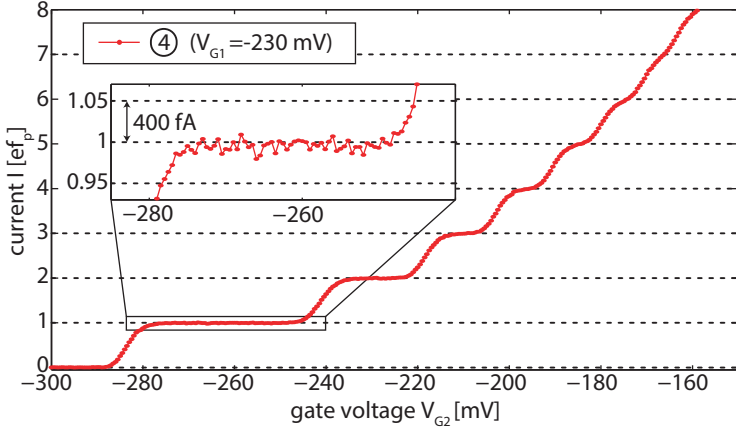


Figure 2.15:

Cut at the position marked ④ in Fig. 2.13 ($V_{G1} = -230$ mV) showing the step-like increase in current I as a function of the exit gate voltage V_{G2} . In absolute measures, the steps appear at multiples of 8 pA. The current is normalized to ef_p , the pumping parameters are the same as in Fig. 2.13. The inset shows a magnification of the $I = 1ef_p$ -plateau with the arrow's length resembling $\Delta I = 400$ fA.

lead, both affected by the modulated gate. If this modulation is sufficiently slow, excitations of electrons on the dot [97] can be neglected. Only transitions between neighbouring occupation numbers of the dot are allowed (i.e., we use a sequential tunneling model). The general master equation to describe the decoupling dynamics reads as follows [47, 106]:

$$\dot{P}_n = P_{n-1}W_{n-1}^+ - P_nW_n^- + P_{n+1}W_{n+1}^- - P_nW_n^+ \quad (2.37)$$

with W_n^\pm the instantaneous rates for adding and removing an electron to/from the dot. The total transition rate between the states $n-1$ and n can thus be defined by $\Gamma_n(t) = W_n^- + W_{n-1}^+$. The electrochemical

2.5 Non-adiabatic single-electron pumping using a dynamic QD

potentials $\mu_n(t)$ are defined additionally by

$$\exp(\beta\mu_n(t)) = \frac{W^-_n(t)}{W^+_{n-1}(t)} \quad (2.38)$$

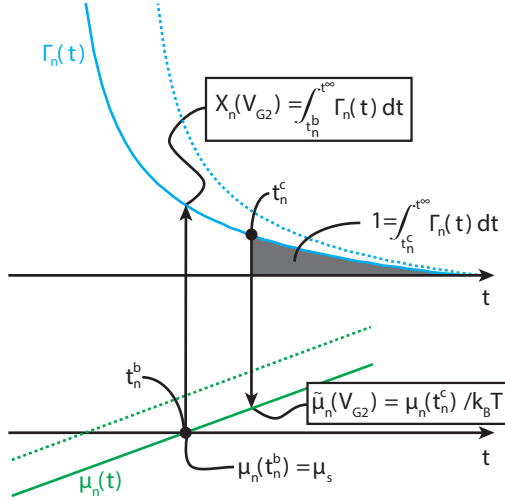
with $\beta = 1/k_B T$ the inverse product of Boltzmann constant and temperature T . Additionally, if the time dependence of rates $W^\pm_n(t)$ is quasi-static, then the equation (2.38) expresses detailed balance and the electrochemical potential μ_n equals the difference in thermodynamic grand potentials $\mu_n = \Omega_n - \Omega_{n-1}$ with $\Omega_n = \mathcal{F}_n + \Phi_n - nE_f$ [106] where \mathcal{F}_n corresponds to the canonical free energy and Φ_n to the electrostatic interaction energy. Setting $E_f = 0$, equation (2.37) can be rewritten as

$$\begin{aligned} \dot{P}_n = & -\Gamma_n [\bar{f}(\mu_n)P_n(t) - f(\mu_n)P_{n-1}(t)] \\ & + \Gamma_{n+1} [\bar{f}(\mu_{n+1})P_{n+1}(t) - f(\mu_{n+1})P_n(t)] \end{aligned} \quad (2.39)$$

where $f(E)$ equals the Fermi distribution (i.e., the occupation of states) and $\bar{f}(E) = 1 - f(E)$ (corresponding to free states in the lead). The first line treats the transitions $n \leftrightarrow n - 1$, i.e. the tunneling of an electron into a free state in the lead (first element), reducing the probability of the state n being occupied, and, as the second element, the addition of an electron from an occupied state in the lead if only $n - 1$ electrons are currently located on the dot. The second line in equation (2.39) describes these processes accordingly for transitions $n + 1 \leftrightarrow n$.

The decoupling process, already outlined in the previous paragraphs, is characterized by an isolated state n at some point in time, say t^∞ , i.e. $\Gamma_n(t^\infty) = 0$. Although the exact time dependences of neither $\mu_n(t)$ nor $\Gamma_n(t)$ are precisely known, one can identify two distinct points in time: These are on the one hand the onset of back-tunneling, labelled t^b_n , as soon as the state of the dot characterized by μ_n crosses the source's electrochemical potential, i.e.

$$\mu_n(t^b_n) = \mu_s. \quad (2.40)$$


Figure 2.16:

Time-dependences of back-tunneling rate and the dot's chemical potential during charge capture. The same process is also depicted for a more negative gate voltage of V_{G2} to show the dependence of critical time moments as a function of this tuning parameter.

On the other hand, there is a point in time t_n^c at which decoupling is achieved (equivalent to the breakdown of detailed balance), i.e. the average number of remaining tunneling events is of the order of one:

$$\int_{t_n^c}^{t_n^{\infty}} \Gamma_n(t) dt = 1. \quad (2.41)$$

These definitions are sketched in Fig. 2.16 for two settings of V_{G2} . We assume a linear dependence of the dot's energy levels $\mu_n(t)$ on the gate voltages $V_{G1}(t)$ and V_{G2} while the tunneling rates presumably depend on gate voltages exponentially. Due to the (positive) charging

2.5 Non-adiabatic single-electron pumping using a dynamic QD

energy and the raising of the dot after initialization ($\dot{\mu}_n(t) > 0$), states with larger n will switch between loading and unloading earlier, i.e. $t_{n+1}^b < t_n^b$. Furthermore, the effective barrier will be smaller for higher states, leading to a lower stability of those states: $\Gamma_{n+1}(t) > \Gamma_n(t)$ (at least for $t > t_n^b$). A more negative voltage V_{G2}' shifts the same dot state towards higher energies (raising the potential well defining the dot), which causes an earlier crossing of the (constant) source's electrochemical potential μ_s , leading to $t_{n+1}^{b'} < t_n^b$. However, the same argument as for the discussion of states $n + 1$ and n and their respective coupling to source, parametrized by $\Gamma(t)$, holds, implying $t_{n+1}^{c'} > t_n^c$.

Initially, provided sufficiently large $\Gamma_n(t)$, the distribution $P_n(t)$ follows the instantaneous equilibrium:

$$P_n(t) \approx \exp(\beta\mu_{n+1}(t))P_{n+1}(t). \quad (2.42)$$

Depending on the specific time-dependence of $\Gamma_n(t)$ and $\mu_n(t)$, one can identify two universal limits of equation (2.39): One is the thermal limit, obtained in the case of sudden decoupling, meaning that $\Gamma_{n+1}(t)$ drops that fast to zero that eq. (2.42) holds until the characteristic decoupling time t_{n+1}^c while at times $t > t_{n+1}^c$ the right-hand side of equation 2.39 becomes zero, i.e. $P_n(t) = \text{const}$.

One can show - assuming that the charging energy is large compared to temperature (implying a well-pronounced Coulomb blockade) - that in this thermal limit the occupation distribution follows the expression

$$P_n = \bar{f}(\mu_{n+1}(t_{n+1}^c)) \prod_{i=1}^n f(\mu_i(t_i^c)), \quad (2.43)$$

i.e. the probability distribution is given by a set of numbers $\tilde{\mu}_n = \beta\mu_n(t_n^c)$ and is narrowly dispersed in case of $\dots \gg \tilde{\mu}_{n+1} \gg \tilde{\mu}_n \gg \dots$

In the opposite limit, corresponding to a generalized decay-cascade model [46, 105, 107], the time-scale for switching between loading $f(\mu_n(t)) \approx 1$ (i.e., corresponding states in the source are occupied) and unloading $f(\mu_n(t)) \approx 0$ (empty states in the source lead) may become much shorter than the change in coupling, represented by $\Gamma_n(t)$. The Fermi functions are then replaced by sharp steps, i.e. $f(\mu_n) \rightarrow \Theta(t - t_n^b)$, parametrized by the back-tunneling times t_n^b . The set of equations 2.39 reduces (assuming sharp initial equilibrium at t^0 with $t_{N+1}^b < t^0 < t_N^b$ and $P_n(t^0) = \delta_{n,N}$) to

$$\dot{P}_n(t) = \begin{cases} 0 & t > t_{n+1}^b \\ \Gamma_{n+1}P_{n+1}(t) & t_{n+1}^b < t < t_n^b \\ -\Gamma_n P_n(t) + \Gamma_{n+1}P_{n+1}(t) & t_n^b < t \end{cases} \quad (2.44)$$

The solution to this system of equations [46] is given by

$$P_n = \exp(-X_n) \prod_{i=n+1}^N (1 - \exp(-X_i)), \quad (2.45)$$

with the generalized decay rates X_n extended here by the specific points in time at which back-tunneling sets in:

$$X_n = \int_{t_n^b}^{t^\infty} \Gamma_n(t) dt \stackrel{T \rightarrow 0}{=} \int_{t^0}^{t^\infty} W_n^-(t) dt \quad (2.46)$$

The two limits (2.43) and (2.45) can be experimentally distinguished due to their differing dependence on external parameters, like e.g. the exit gate voltage V_{G2} (see Fig. 2.16):

$$\tilde{\mu}_n = -\alpha_{\mu,n} V_{G2} + \Delta_{\mu,n} \quad (2.47)$$

$$\ln X_n = -\alpha_{X,n} V_{G2} + \Delta_{X,n}. \quad (2.48)$$

Another possibility to distinguish both limits is by performing frequency-dependent measurements, as proposed in [47]. As a consequence of the approximation of sudden decoupling made in order to obtain the thermal limit, $\tilde{\mu}_n$ should be independent of the driving frequency. However, $W_n^\pm(t)$ is expected to scale with $W_n^\pm(t) \rightarrow W_n^\pm(t)/x$ in case of $f_p \rightarrow x f_p$ [34].

2.6 Series operation of non-adiabatic dynamic QDs

When operating dynamic quantum dots in series, a charge Q will build up on the interconnecting node in case of differing transfer rates. Assume, e.g., the first dynamic dot QD1 to be tuned to transfer two electrons per cycle and the following one, say QD2, to about one electron per cycle. In consequence, the node will be charged by one electron per cycle leading to an effect that we call "mesoscopic feedback" [43].

2.6.1 Mesoscopic feedback

Modelling the above-mentioned example by charging a capacitor, it is obvious that the process is limited by the potential created by the surplus carriers. Although the dynamic quantum dots are remarkably robust against a potential applied from drain (due to the electrostatically defined barrier and the accordingly high emission energy of up to 100 meV [49, 51]), the node's potential acts as an additional plunger onto the dot's energy levels. Therefore, we model the effect of the intermediate charge node as an additional gating [43]:

$$I(V_{G2}, \Delta\mu_s, \Delta\mu_d) = I(V_{G2} + \beta_s\mu_s - \beta_d\mu_d) \quad (2.49)$$

with $\Delta\mu_{s,d}$ the change in electrochemical potentials of the source or drain lead, respectively, and $\beta_{s,d}$ coupling constants. Please note the

opposite sign of $\beta_{s,d}$ in equation (2.49) which can be understood in the picture outlined in the previous section 2.5.2: An increase in the electrochemical potential of the source lead ($\Delta\mu_s > 0$) will lead to a delayed onset of back-tunneling (or decoupling in the grand-canonical limit), thereby strongly enhancing the probability of capturing electrons on the isolated dot, while only weakly raising the dot's energy levels. In contrast, a change in the drain's electrochemical potential μ_d does typically not influence the dynamic processes in charge emission due to the high emission energy but only acts as an additional gate voltage, thereby influencing only weakly the dot's electrochemical potentials. In conclusion, these considerations suggest $|\beta_s| \gg |\beta_d|$.

The effect of a change in source or drain bias onto the dynamic quantum dot can already be modelled using only one QD and change the respective lead potential by applying an external voltage to source or drain, respectively, and maintaining the other one at fixed bias. The linear shift of the transfer characteristics then observed is plotted in Fig. 2.17. Here, we analyse the transitions between plateaus of quantized charge transfer (operating on the main plateau region) as a function of both, bias potential and gate voltage.

Circles correspond to the measurements with variation of source potential, squares to a change in drain potential. Data points correspond each to the position of $I = 0.5ef_p$ (red), $I = 1.5ef_p$ (green), $I = 2.5ef_p$ (blue) in the two-dimensional parameter space. The dependence of gate parameters on the bias potential is approximated by a linear function. The slope thereby derived directly corresponds to $\beta_{s,d}$. Both previously discussed properties of this parameter are evident: First, β_s is positive while β_d carries the opposite sign. Second, the effect of a source potential is much larger than the one of the variation of the drain potential, leading to an average ratio of $\beta_s/\beta_d \approx 10$.

These aspects are also of fundamental relevance to the series operation because they lead to a stabilization of the series quantum dots:

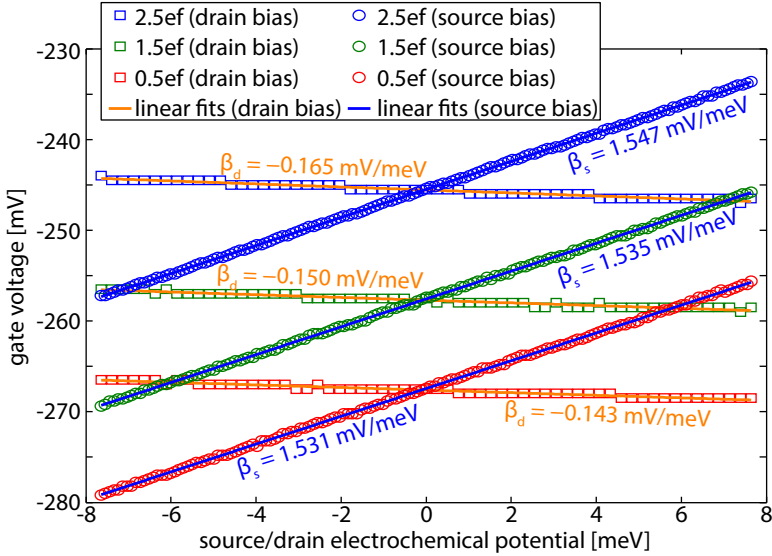


Figure 2.17:
Change of plateau transition as a function of bias potential.

Assuming the first QD again to transfer more than one electron, this will lead to a raising drain potential for the first quantum dot and an increasing source potential for the second dot. Due to the opposite sign of $\beta_{s,d}$, this causes a reduction of the capture probability of QD1 with a simultaneous increase in capture probability of QD2. Taking into account the large ratio β_s/β_d , one expects QD2 to be affected much stronger than QD1, leading to an increase of the average number of transferred electrons across the whole device. Experiments of the series current as a function of the average intermediate potential under different scenarios of detuning in the respective points of operation are discussed in [43, 108].

One measurement of this kind is exemplary shown in Fig. 2.18 using the device sketched in the inset, consisting of two serially connected dynamic quantum dots with capacitively coupled charge detector. In this measurement, the first dynamic quantum dot QD1 is operated at nominally $n_e = 2$ on its main plateau while the working point of QD2 is varied by changing its exit barrier voltage V_{G2}^{QD2} . The black dashed line (corresponding to the left axis) gives the parameter dependence of the individual device showing the step-like increase in transferred electrons per cycle. When operating in series, the charge state of the intermediate node is monitored by the detector (red open squares), revealing the charge-driven feedback mechanism which additionally leads to a five-fold increase in plateau width of the serially generated current (blue dots) compared to the $n_e = 2$ -plateau for QD2 individually. Therefore, the current is dominated by QD1 over a wide range of gate voltage. However, towards very negative control gate voltages V_{G2}^{QD2} the current is suppressed due to feedback onto QD1. In addition, this type of feedback manifests itself also at gate voltages $-280 \text{ mV} < V_{G2}^{QD2} < -250 \text{ mV}$ where an increase in series current is observed due to the positively charged intermediate node, leading to an increase in the number of transferred electrons per cycle across QD1. Solid lines indicate fits to a theoretical model based on (2.49) and charge conservation from which a coupling ratio of about $\beta_s/\beta_d \approx 7$ is derived, in proper agreement with theoretical considerations and the static characterization discussed above (cf. Fig. 2.17).

The feedback mechanism in such system is a realization of quantum feedback proposed by Brandes [64], representing in this case an integral feedback loop, acting predominantly onto QD2 in case of deviations of the momentary current $\Delta I(t) = I^{QD2}(t) - I^{QD1}(t)$ via the charge accumulation $Q = -\int_0^t \delta I(t') dt'$, leading to an expected suppression in the fluctuations of the output current as shown in [43].

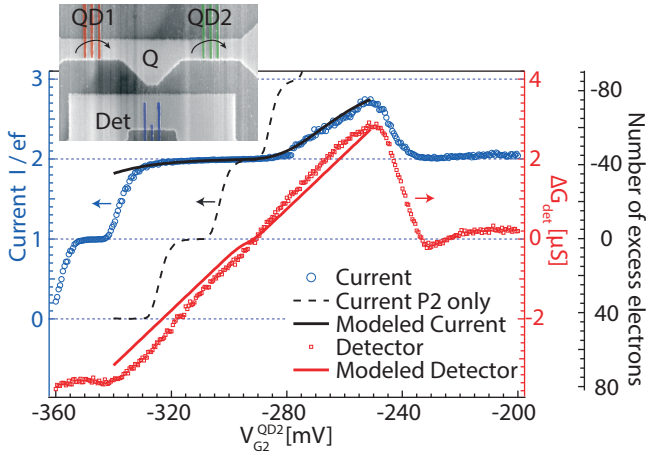


Figure 2.18:

Series operation of pumps illustrating mesoscopic feedback, the device is depicted in the inset. The black dashed line represents the parameter dependence of QD2 operated individually while the blue open dots correspond to the series current when operating QD1 at $n_e = 2$. The charge state of the interconnecting node is monitored by a capacitively coupled detector reflecting the feedback mechanism. Adapted from [43]

2.7 Metrological context: Quantum metrological triangle

As pointed out in the introduction, the envisioned redefinition of the system of units in terms of fundamental constants, like e.g. the elementary charge e or Planck's constant h , is the main driving force in the development of quantized-charge transfer devices. Concomitant with the ambition of obvious realizations of these constants, the single-electron transfer devices have been chosen as the realization of the Ampere, relating the electric current to the elementary charge by $I = n_e Q_p f_p$

with f_p the external driving frequency and $n_e Q_p$ the charge transferred per cycle. However, omitting the aspect of an illustrative realization, the elementary charge could be also represented using Ohm's law by combining a quantized voltage and a quantized resistance to

$$I = \frac{U_J}{R_K}. \quad (2.50)$$

This voltage can be obtained employing the Josephson effect and is then given by

$$U_J = \frac{l_J f_J}{K_J} \quad (2.51)$$

with

$$K_J = \frac{2e}{h} \quad (2.52)$$

the theoretical prediction of the frequency-to-voltage conversion factor (Josephson constant), f_J the frequency of the irradiated microwave and l_J the number of the voltage step. On the other hand, the Quantum Hall resistance is given by the relation

$$R_H = \frac{R_K}{i} \quad (2.53)$$

where i is an integer and R_K the von-Klitzing's constant, theoretically predicted to equal

$$R_K = \frac{h}{e^2}. \quad (2.54)$$

Both effects have been reproduced in different material systems with a very low relative standard uncertainty: For the Josephson effect, uncertainties below 10^{-11} [109] or even of the order of 10^{-19} [110, 111] regarding the frequency-to-voltage ratio have been reported. Also, the Quantum Hall resistance is well known with a relative uncertainty of

about 10^{-9} in metrological comparison studies [112, 113] and has recently been reported with an uncertainty of the order of 10^{-11} for intercomparisons in the same material system [114] or even between conventional AlGaAs/GaAs and graphene devices [115], evidencing the universality of this effect. Theoretically, corrections of the order of only 10^{-20} are predicted [116].

Although these effects have played a major role in metrology after adapting the so-called conventional units for resistance and voltage based on the fixed values of K_{J-90} and R_{K-90} [117, 118], their usage is inconsistent with the current definition of the SI [66].

However, if one employs a single-electron pump yielding a current depending only on the number of carriers emitted per cycle n_e , the driving frequency of charge transfer f_p and the value of the charge transferred per cycle $n_e Q_p$, then equation (2.50) becomes

$$n_e f_p Q_p = \frac{l_J f_J}{K_J} \frac{i}{R_K}, \quad (2.55)$$

or, by re-ordering

$$Q_p K_J R_K = \frac{l_J i}{n_e} \frac{f_J}{f_p}, \quad (2.56)$$

where the dimensionless right-hand side is given as a ratio of integers times a frequency ratio of the irradiated microwave and the pump frequency. The relation (2.56) constitutes the basis of a quantum metrological triangle experiment [65]. A sketch of the underlying concepts is shown in Fig. 2.19, indicating the relations between the quantum effects. Since frequencies can be measured with negligible uncertainties on the targeted uncertainty of such an experiment (which is of the order of 10^{-8}), one can determine the product of the phenomenological constants on the left-hand side with high precision.

Depending on the assumptions being made, one can draw some conclusion from such an experiment (see also [90, 119, 120]):

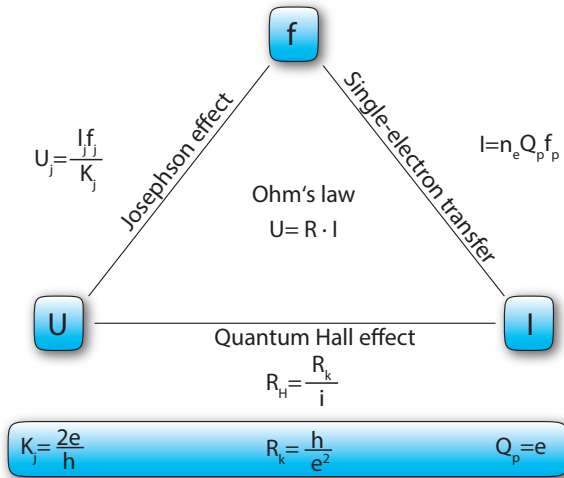


Figure 2.19:

Sketch of a quantum metrological triangle experiment, relating the quantum effects via Ohm's law to the universal constants e and h via integers n_e , l_j and i and a driving frequency f . By combining all effects, a consistency check can be performed.

- Since the right-hand side of equation (2.56) is dimensionless, the product on the left is independent of the system of units chosen.
- Assuming that the relations (2.52,2.54) are exact and further that $Q_p = e$ as expected for a single-charge device, equation (2.56) realizes the form $1 = 1$ which, if confirmed by experiments, would give strong arguments that the initial assumptions (i.e., the expression of K_j , Q_p and R_k in terms of fundamental constants) are correct (after having ruled out that conceivable deviations exactly cancel each other).
- If in a redefinition of the SI the Planck constant h is exactly

known (related to the kilogram by the Watt balance experiment) as well as the elementary charge e , realized by a single-electron source, then also K_J and R_K are exactly known, provided the relations (2.52,2.54) are valid.

- By extending equations (2.52,2.54) and $Q_p = e$ by epsilon-correction terms (i.e., $Q_p = e(1+\varepsilon_p)$, $K_J = (2e/h)(1+\varepsilon_J)$ and $R_K = (h/e^2)(1+\varepsilon_K)$), one can express the level of consistency of the initial assumptions in terms of these epsilon-corrections, which yields in first order

$$Q_p K_J R_K = 2 \frac{I_J^i}{n_e} \frac{f_J}{f_p} (1 + \varepsilon_p + \varepsilon_J + \varepsilon_K). \quad (2.57)$$

- Moreover, by replacing K_J and R_K in equation (2.56) by the values K_{J-90} and R_{K-90} , one can also define Q_{p-90} in terms of the conventional units.
- Finally, the outcome of such an experiment directly affects the so-called Watt balance [121] which provides a link $m \propto h$ [122] between a mass m and Planck's constant h assuming that relations (2.52,2.54) hold [66].

Experimentally, the realization can be obtained as follows: The single-electron device generates a quantized current, which is fed into a Hall bar placed in a high magnetic field (thereby operated at integer filling factor), leading to a quantized Hall voltage perpendicular to the direction of current flow (already experimentally demonstrated for an all-semiconductor device in [123]). This voltage can then be compared to the voltage obtained by a Josephson array voltage standard [120].

In conclusion, a precise single-electron current standard is needed to perform this experiment with sufficiently low uncertainty so that robust

2 Basics of single-charge transfer

conclusions on the questions addressed above can be drawn on a level of uncertainty of 10^{-8} .



Chapter 3

Experimental methods

In this chapter, I will briefly discuss the conditions under which the following experiments have been conducted, starting with the description of the process to fabricate the sample under investigation, followed by the presentation of the cryostat necessary to reach low temperatures, ending up finally with the depiction of the electric wiring, the instruments and the software concepts used to remotely control the structure.

3.1 Sample fabrication

The design and fabrication of samples is one major aspect during the preparation of an experiment. The recipe for the semiconducting part forming the dynamic quantum dots is from a processing point of view equivalent to standard techniques as described in detail in e.g. [104]. Therefore, I will focus here on design considerations differing from the general layout. The processing of the semiconducting elements was performed in conjunction with and under supervision of B. Kaestner and P. Mirovsky while the metallic single-electron transistors have been created by B. Mackrodt and R. Dolata.

The basis of the device forms a wafer processed by K. Pierz and H. Marx using molecular beam epitaxy (MBE) as shown in Fig. 3.1. Using molecular beam epitaxy, almost arbitrary layer stackings may be formed with atomic precision [124, 125]. The figure contains on the left hand side the stacking of the wafer together with the energy dependence of valence and conduction band on the right hand side. The black line labelled $|\psi|^2$ represents the electron's wave function in the two-dimensional electron gas. The wafer consists of a stacking of GaAs and $\text{Al}_{0.33}\text{Ga}_{0.67}\text{As}$ which have a small lattice mismatch but a large difference in the band gap. This allows stacking of layers with different concentrations in Al (resulting in differing band gaps) without any defects due to the almost perfect lattice match. The result of proper stacking is a conduction band minimum below the Fermi energy on a very small extension in vertical direction, leading to a confinement of electrons in one direction in space combined with free motion in the other two directions (the "two-dimensional electron gas"). Using the remote doping technique with a spacer layer between electron gas and dopants (Si here), very high mobilities can be achieved by maximizing the distance between dopants (acting as scatterers if ionized) and the electron gas [72]. The characterization of the wafer yields a mobility of

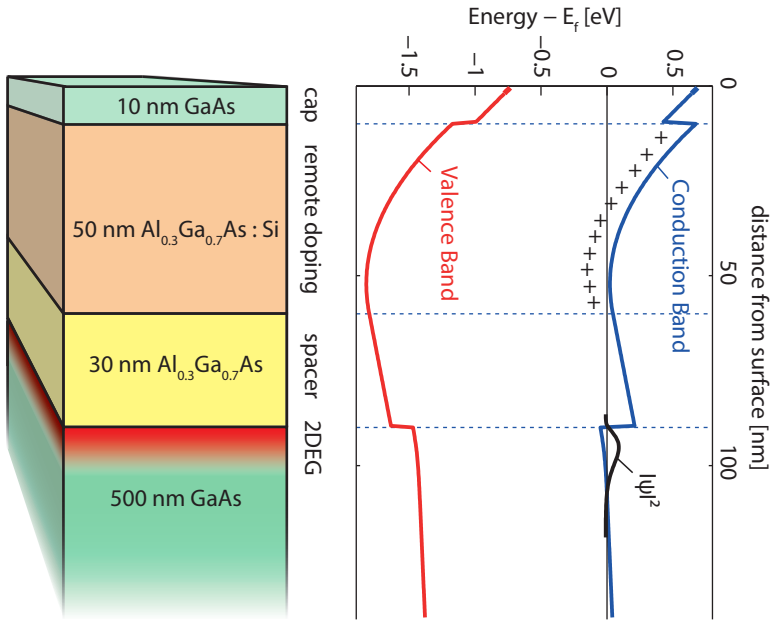


Figure 3.1:

Wafer layer stacking (left) and band diagram (right). The wafer was grown using molecular beam epitaxy (MBE) by K. Pierz and H. Marx and consists (from top to bottom) of the cap layer (10 nm), a 50 nm AlGaAs layer which is n-doped with Si (density about 10^{18} cm^{-3}), followed by the spacer layer (30 nm AlGaAs) and the interface to the GaAs layer (500 nm) where the 2DEG is formed at low temperatures. The wafer consists further of a superlattice of GaAs/AlGaAs (2 nm each, 50 times) and a buffer GaAs layer of 500 nm (both not shown). The band diagram on the right hand-side was calculated using a one-dimensional Poisson and Schrödinger solver (courtesy of Prof. G. Snider, University of Notre Dame [126]). For modelling purposes, an effective donor density of $N_d = 4.9 \cdot 10^{17} \text{ cm}^{-3}$ has been chosen to obtain a carrier density in the 2DEG of $n_s \approx 2.7 \cdot 10^{15} \text{ m}^{-2}$.

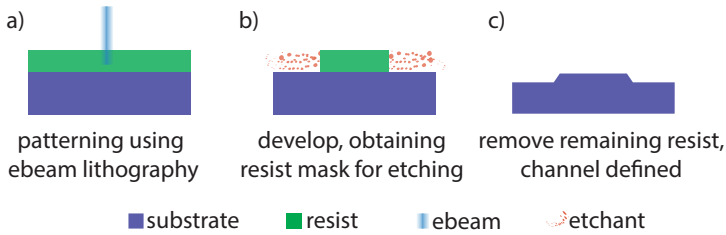


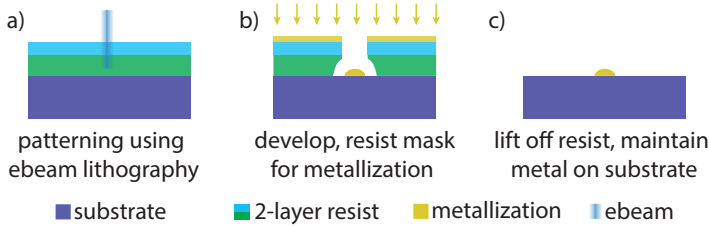
Figure 3.2:

Mesa etching. First, after spinning a negative resist onto the substrate with subsequent curing on a hot plate, the pattern for the semiconducting channel is created using electron-beam lithography (a). After developing, only the resist exposed remains, covering the underlying substrate. The commonly used etchant [100, 104, 127] which consists of H_2SO_4 (96%), H_2O_2 (30%) and deionized H_2O in a ratio of 1:8:1600 then removes uncovered substrate (b) at a rate of about 0.5 nm s^{-1} . The low rate is chosen to warrant isotropic etching profiles. Finally, the etch is stopped and the resist is removed, leaving the etched channel (c). The etch is targeted at a depth of about 55 nm and yielded a depth for this sample of about 65-70 nm. During this step, also the markers for alignment are created as etched patterns on the substrate's surface.

$93.6 \text{ m}^2(\text{Vs})^{-1}$ and a carrier density of $n_s = 2.77 \times 10^{15} \text{ m}^{-2}$.

The processing for the semiconducting elements is done in a repetition of the following steps for mesa etch, ohmic contacts and metal gates:

- Cleaning of the wafer's surface
- Spinning of resist (for ohmic contacts and metallic gates, a double resist stacking is used) with subsequent curing on a hot plate
- patterning using electron beam lithography (operated by T. Weimann) and developing, thereby creating a resist mask for further processing

**Figure 3.3:**

Applying metals for ohmic contacts or gates. To simplify lift-off, a double-layer positive resist is applied, cured and subsequently patterned using electron-beam lithography (a). After developing, the surface is uncovered at areas patterned by the electron-beam. Then, metal is evaporated (an alloy consisting of AuGeNi for ohmic contacts, TiAu for topgates), covering the whole chip (b). By lifting the photoresist, only the metal lines applied directly onto the substrate remain (c). In case of ohmic contacts, the eutectic alloy is annealed at 450°C to provide access to the two-dimensional electron gas (not shown).

- either etching the mesa (see Fig. 3.2) or evaporating metal (see Fig. 3.3) for ohmics or top gates (ohmic contacts are finally annealed at 450°C)
- Removing the resist

However, the fabrication of the metallic single-electron transistors varies slightly and is therefore shown in Fig. 3.4. The process deviates from the metallization applied to define the semiconducting structures and employs an additional metallic mask and angular metal evaporation [128, 129]: Here, a trilayer consisting of a copolymer (thickness of 700 nm), germanium (Ge, thickness of 30 nm) and finally a photoresist (PMMA, thickness of 160 nm) is deposited onto the sample (a). After patterning the PMMA layer using electron-beam lithography and subsequent developing, the Ge is etched using a reactive ion

3 Experimental methods

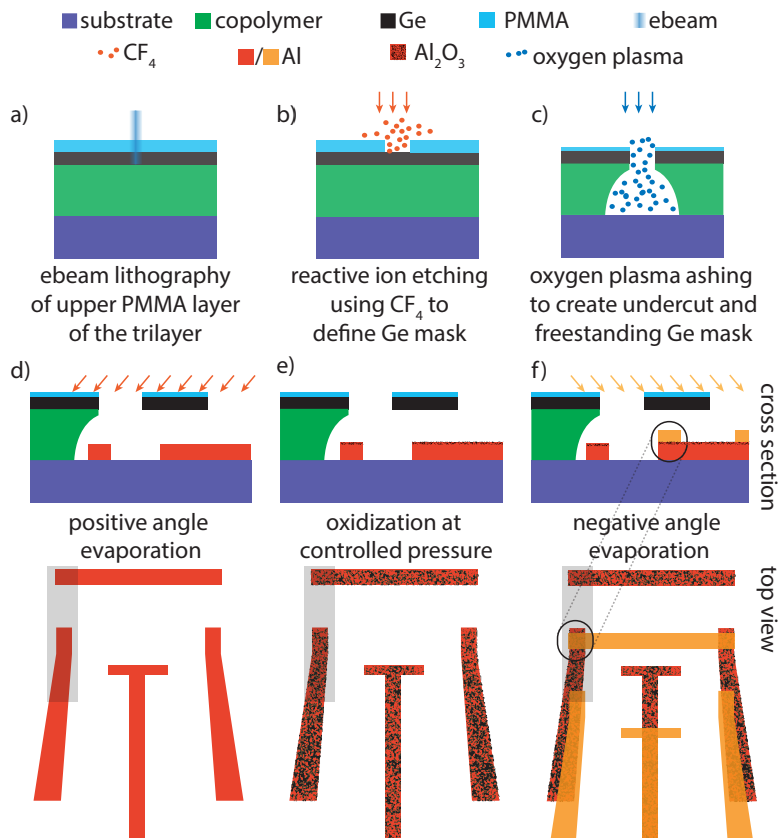


Figure 3.4:

Fabrication of single-electron transistors. First, a trilayer is created on the substrate, consisting of a copolymer (thickness of 700 nm, green), a Ge layer (thermally evaporated, 30 nm thickness, black colour) and a PMMA layer (thickness 160 nm), which is patterned using electron-beam lithography (a). Uncovered Ge is then etched using reactive ion etching (CF_4 , b). Next, the bottom copolymer (and also, the upper PMMA) are ashed using an oxygen plasma (c), thereby creating a large undercut and a free standing Ge mask. Using a two-angle evaporation technique (d,f) with intermediate oxidation (e), vertical tunnel junctions are formed. The figure shows in the bottom panels the top view and a cross-sectional view of the grey shaded area.

etching process employing a CF_4 plasma, leaving a mask for the bottom copolymer (b). This polymer is etched wherever it is not covered by Ge using an oxygen plasma (also known as "ashing"). The process creates a large undercut, yielding finally a suspended mask of Ge (c). By subsequent evaporation of Al under two different angles (d,f) with an intermediate oxidization step at controlled oxygen pressure (0.15 mbar for 15 minutes, e), the transistors are formed. A detailed description of this process can be found in e.g. [130] while the fabrication methods established at PTB including specific parameters are documented in [131].

Figure 3.5 shows the fabricated SET structure where some geometric parameters have been highlighted. The central island has a length of about $2 \mu\text{m}$ and a width of 95 nm which is marked by a . The leads have a similar width, also marked by the same letter. Therefore, the overlap between each lead and the island is $a^2 \approx 9 \times 10^{-3} \mu\text{m}^2$. Also, by comparing the position of the structure with its corresponding shadow, the offset due to the angular evaporation of Al can be estimated to $b \approx 490 \text{ nm}$.

One of the crucial issues in fabrication is the proper alignment of all steps in fabrication. Typically, crosses or squares are patterned during the first steps of fabrication to serve as a reference in alignment of the subsequent steps of lithography. This concept has been extended here to markers with so-called Penrose pattern [132]. Using this type of pattern, correlation-based analysis of the markers can be performed to yield high-accuracy alignment together with robustness against marker damage or low visibility (especially when patterning the trilayer). These markers obviously need to be processed in the first step of fabrication to guarantee alignment of the following steps and are therefore etched into the substrate during the mesa etching process.

Compared to the preceding chip P640-2-1 [43, 108], measured during my diploma thesis in Hannover (and not showing single-charge res-

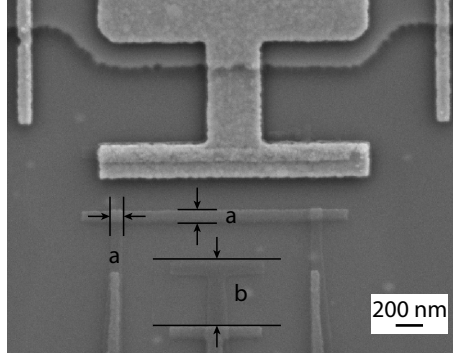


Figure 3.5: SEM image of a processed SET. The scale bar at the bottom right equals 200 nm. The overlap between leads and the central island is square-shaped and marked with the letter a , equalling $a^2 \approx (95 \text{ nm})^2$. The offset due to the two-angle evaporation, marked with b , is $b \approx 490 \text{ nm}$.

olution), not only the type of detector was changed from a quantum point contact (QPC) to the metallic SETs. Additionally, we have fabricated metallic floating gates for enhanced coupling of the potential created by the electrons stored on the nodes in the two-dimensional electron gas to the charge detectors (light area in Fig. 3.5). Using this floating gate, an enhancement in charge sensitivity has been reported in literature for different types of devices [133–136]. Alternatively, the detectors could also be directly placed onto the node, but it was unclear how robust the SET fabrication and the connection with the leads is against height variations across the etched semiconducting wire. Therefore, we chose the option with floating gates, although such floating gates are supposed to cause random switching noise [136]. Roessler et al. [136] suggest leakage currents between floating gates and top gates which are in close proximity in their work rather than leakage between electron gas and floating gates. On our chip, this effect is more unlikely

due to the large distance between the potential-inducing top gates and the floating gates. Additionally, the effect might also depend on the sample handling during the cool down, like, e.g., the speed of cooling or the application of positive bias voltages to the gates while cooling in order to reduce the density of ionized donors, leading to a more opaque barrier between topgates and 2DEG [137].

3.2 Introduction of the processed chip

The inset in Figure 3.6 presents a scanning electron microscopy image of the fully processed sample: Horizontally from left to right the semiconducting, wet-etched one-dimensional channel is shown. Light areas from top to the center correspond to metal top gates and also the floating gates on top of the node appear in the same colour, being processed in the same step of fabrication and consisting both of Ti/Au. In-between of groups of three gates each, etched semiconducting wires appear from the top which may be used as plunger gates to reduce the effective size of the node, thus adding some flexibility. Besides testing purposes, they have not been necessary for obtaining appropriate charge resolution and are therefore grounded in this thesis. From the bottom, groups of three leads, each belonging to one single-electron transistor, are visible, appearing in darker grey (representing Al) and forming the source and drain lead (left- and rightmost ones) and a local gate (central lead) to tune the island's chemical potential.

As a consequence of low yield of the metallic detectors after cleaving during the first devices, we decided to separate the chips before fabricating the metallic detectors. But on the other hand, also a minimum size of the chip is required during this fabrication process to guarantee an almost homogeneous height profile of the trilayer close to the critical elements. Thus, in total six samples of the type as shown in the inset have been fabricated onto one wafer piece of $10 \times 10 \text{ mm}^2$. The

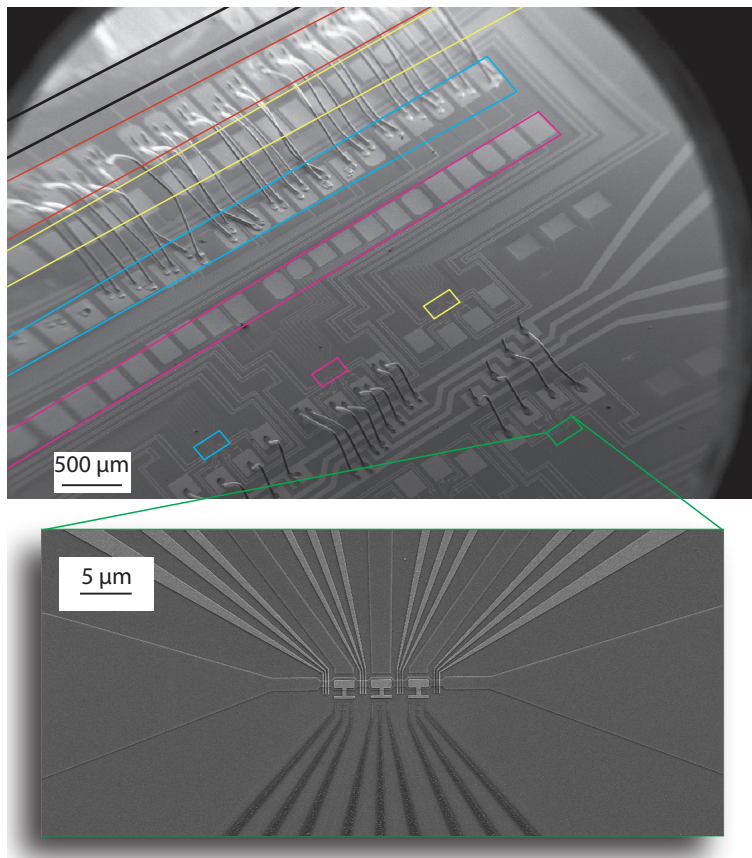


Figure 3.6:

SEM image of the processed chip. The bottom panel shows a magnification containing the sample measured. Coloured rectangles mark the rows for contacting a single sample, black corresponds to dc bonds onto the sample holder, red to the connection to one of the three samples which are colour coded appropriately. From bottom left to the right center, the rf lines to connect the entrance gates with the coaxial lines are visible. Below, the upper structure is mirrored. The sample marked by the green square has been measured.

main figure in 3.6 gives an impression of the full structure. The basic concept is to maintain a fixed connection from the external hardware onto the chip and then selectively connect the sample under investigation by a second bond wire. The layout of connections has been chosen to match the geometry of the sample holder as close as possible (see section 3.3.2). Diagonally across the center run the four rf lines necessary to drive the quantum dots dynamically. On the top, the three terminals for dc connection to each chip are visible. To minimize efforts during bonding, the connection between external pads on the sample holder and the first row of pads on the chip is held fixed for both, dc and rf signals. Then, to connect an individual sample, only direct connections have to be bonded. The outermost row of pads is wired to the rightmost chip, the intermediate row to the leftmost chip and the one closest to the center connects to the central chip. Three different widths of the semiconducting channel have been processed, ranging from $1\ \mu\text{m}$ down to $800\ \text{nm}$ (the measurements presented here are conducted using the smallest, $800\ \text{nm}$ wide channel).

In Fig. 3.7 the sample is depicted once more where the relevant elements are highlighted by appropriate colouring. The semiconducting channel (from left to right with source and drain contacts coloured green) is crossed from the top by groups of three gates each (yellow) which form serially connected dynamic quantum dots. The three dots labelled QD1, QD2 and QD4 are investigated in this thesis. Only the first two gates of each group are required to form quantum dots in-between (white ovals) and the direction of quantized charge transfer is directly given by the ordering of static and dynamic gate. Since the gates with index G1 (called entrance gate) may be dynamically driven while gates with index G2 (called exit gate) are held at static potentials, electrons are transferred from left to right. In-between, mesoscopic islands are formed which we label node 1 (red) and node 2 (blue), respectively. Using the detectors D1 and D2 (coloured accordingly) which

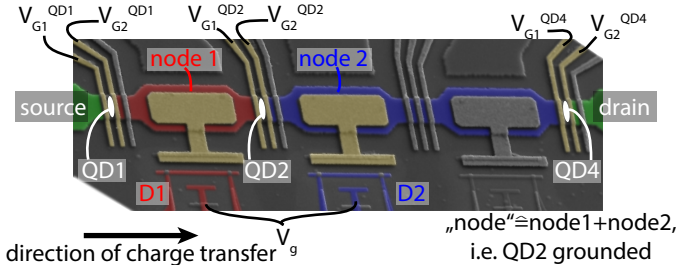


Figure 3.7:

Labelled image of the sample under investigation. It consists of a semi-conducting channel with groups of three gates each (yellow) are used to form serially connected quantum dots QD1, QD2 and QD4 (depicted by white ovals). In-between, semiconducting charge nodes 1 (red) and 2 (blue) are obtained to which charge detectors D1 (red) and D2 (blue) are coupled via floating gates (yellow), respectively. If QD2 is grounded, a large node is formed and both detectors are coupled to this node.

are capacitively coupled via floating gates (yellow) to the electrostatic potentials of the appropriate node, changes of the node's occupation number by single electrons can be monitored. If QD2 is grounded, both nodes are electrically connected and we speak in that case of "the node". The combination of three serially connected dynamic quantum dots and two detectors in-between is the minimum set in order to perform error-accounting (see chapter 6).

3.3 Low-temperature environment

To observe single-charging effects, the thermal energy $E_{\text{th}} = k_{\text{B}}T$ needs to be much lower than the energy scale set by the charging energy due to Coulomb repulsion to suppress thermally activated transport, yielding the relation $E_{\text{C}} \gg k_{\text{B}}T$ [90]. Typical charging energies

of $E_C \approx 100 \mu\text{eV}$ thus require temperatures below 1 K. Therefore, one of the aspects of experiments with single-charge devices is the creation of a low-temperature environment (typically, the operation of a single-charge transfer device at room-temperature forms an exception [138]). In this thesis, a closed-cycle or "cryogen-free" $^3\text{He}/^4\text{He}$ dilution refrigerator [139] is used to create low temperatures, fabricated by Oxford Instruments (Triton 400) achieving in minimum a base temperature of below 25 mK. Compared to conventional refrigerators, where pre-cooling of the mixture is performed using a pumped ^4He stage (1K-pot), the condensation is achieved here using a Gifford-McMahon pulse-tube cooler [140, 141] and operating at higher condensation pressures. Except of a liquid-nitrogen cold trap, no liquid gases are required for operation. Below 4 K, the basic principles of operation equal those of conventional systems: Using a counter-flow cooling system and a series of flow impedances and heat exchangers to maintain the incoming ^3He in the liquid phase, cold ^3He enters the mixing chamber in the concentrated upper phase (consisting of almost 100% pure ^3He). Due to the higher atomic mass of ^4He , a dilute phase exists below consisting of only about 6.6% ^3He with a phase boundary in-between. The transition of ^3He from the concentrated into the dilute phase gives rise to cooling due to the difference in enthalpy of the two phases [139]. This dilute phase is connected to the still which is held at about 700 mK using a resistive heater. At this temperature, only a very dilute liquid phase exists with a concentration of ^3He of about 1% but with a vapour phase consisting of more than 90% of ^3He due to the lower vapour pressure compared to ^4He at this temperature. Using a turbo molecular pump and a rotary pump, this ^3He gas is pumped and then circulated to the compressor and recondensed. A picture of the cryostat is shown in Fig. 3.8 where all shields have been removed.

During cool-down, the whole inner system is operated in vacuum

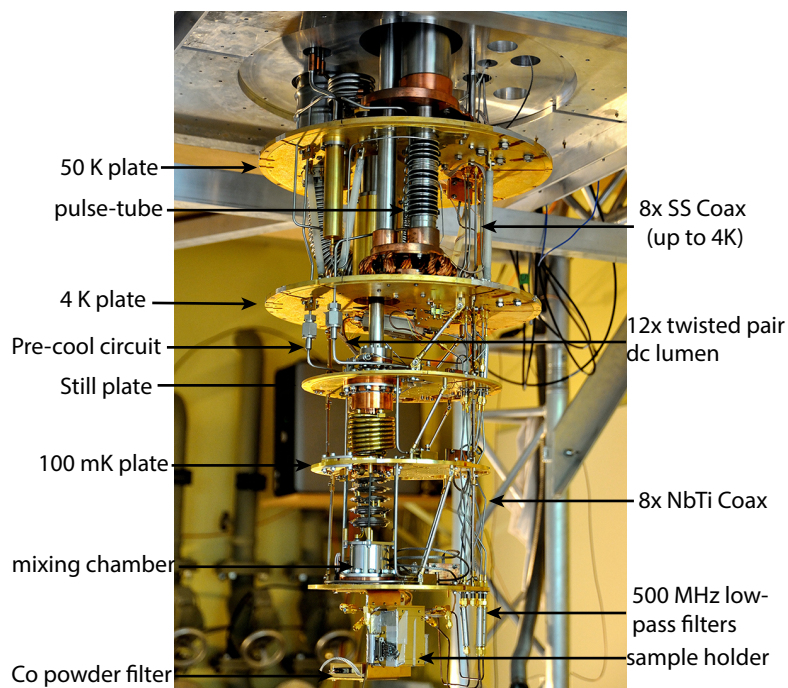


Figure 3.8:
Photography of the dry dilution cryostat with all shields removed.

at pressures below 10^{-6} mbar. Plates are labelled according to their function respective temperature, from top to bottom: 50 K plate, 4 K plate, still, 100 mK plate and mixing chamber plate where the lowest temperature of $T \leq 25$ mK is achieved and where the sample holder is mounted in the picture. The pulse-tube cooler is visible at the upper front, being connected directly via copper braids (good thermal contact

together with reduction of vibrations) to the 50 K and 4 K plate.

Also in contact with this tube is the pre-cool circuit which consists of stainless steel tubes. Inside a small amount of mixture is circulated for good thermal contact between pulse-tube cooler and all stages during cool down from room temperature to 10 K. Below this temperature, this circuit is emptied for thermal isolation.

3.3.1 Electric wiring

The cryostat offers large space for cabling and additional hardware like, e.g., cold amplifiers or filters as compared to insert systems. Dc signals are fed to the sample via a 24 wire twisted pair loom which is made of Constantan (an alloy of copper and nickel with almost constant resistivity over a wide temperature range accompanied by low thermal conductance) above 4 K and a superconducting NbTi loom for the connection further down to the sample at the mixing chamber. At every stage, the lumen is clamped between copper plates for thermal contact.

Additionally, a copper powder filter is mounted to the mixing chamber to suppress high-frequency noise [142]. In this filter, spiral wires are immersed into a mixture of copper powder and Stycast epoxy (for good thermal contact). The powder is covered by a natural oxide, thus insulating between grains and leading to high attenuation due to the skin effect because of the enormous effective surface area. Additionally, also inside the sample holder these copper powder filters are used between the external micro-d connector and the inner bond pads.

The coaxial cables for high-frequency signals are made of thin-walled stainless steel cables above 4 K. Eight of these cables are connected from the top plate to the 4 K plate of which six are directly connected down to the mixing chamber and two are equipped with low-temperature amplifiers (not used in this thesis). Between 4 K and the still, two lines

are filtered by 80 MHz low-pass filters of which one line has been used in this thesis, thus limiting the maximal driving frequency. The high-frequency connection from still to the mixing chamber is established by 0.085" NbTi coaxial cables [143]. At the mixing chamber, modified 500 MHz (≈ -3 dB) low-pass filters (Mini-circuits VLFX-400) are attached which are filled additionally with copper powder/epoxy mixture (comparable to the filters used at NIST for electron shuttling experiments [144]). Finally, copper semi-rigid coaxial cables are used to establish the connection from the mixing-chamber plate to the sample.

3.3.2 Sample holder

The chip is finally mounted to the mixing chamber using the sample holder shown in Fig. 3.9. Typically, the sample is glued onto a small copper plate using conductive silver paint which is then screwed onto the center of the sample holder. Up to eight rf signals may be connected from left and right via SMA connectors. These are then connected to the chip via bond wires. Additionally, two times 24 dc wires may be attached via the micro-d connectors visible at the bottom left and right which are fed to the top layer of the sample holder via filters made of copper powder. The corresponding bond pads are visible at the top and bottom of the top layer. Usually, to allow patching of the external dc connections to specific sample bond pads, intermediate chips containing conducting lines are employed to simplify crossings of bonds. The layout of the chip used already accounts for these geometric aspects (c.f. Fig. 3.6): The rf signals are fed from the left and right, while bond pads connecting to dc signals are positioned at the top and bottom of the chip. This allows as short bond wires as possible together with a minimization of crossings of bonds.

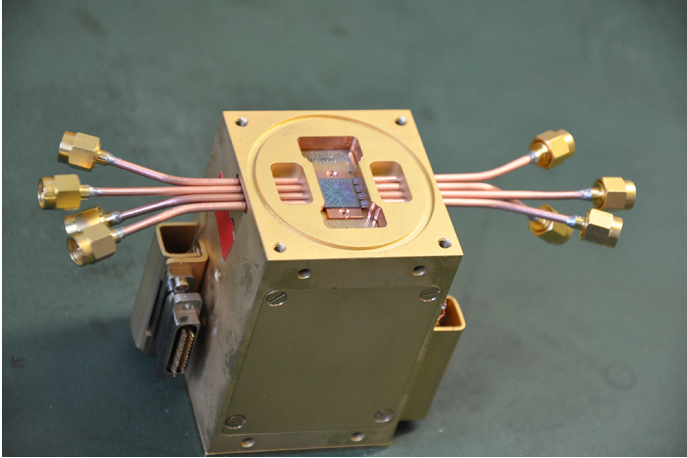


Figure 3.9:

Photography of the sample holder. The chip in the center is slightly below $10 \times 10 \text{ mm}^2$ and may not exceed this size. From left and right, two times four high-frequency semi-rigid coaxial cables may be connected via SMA connectors. Connection to the sample is obtained by directly bonding on the center pin. From top and bottom, two times 24 bond pads are placed for dc connection to the sample. By inserting straight wire chips between the bond pads and the sample, patching may be simplified (not shown).

3.4 Laboratory setup

3.4.1 Voltage sources

To generate static voltages, a modular system developed by U. Becker et al. at PTB is used which allows remote operation. The serial connection to the PC is opto-coupled to avoid ground-loops. By using two 16-bit DACs at different maximal levels it is possible to cover a voltage range of $\pm 7 \text{ V}$ with a fine resolution of $5.5 \mu\text{V}$ which corresponds to a final

resolution of 20 bit. Voltages controlling the electrostatic potentials of gates on the chip are further divided resistively by a factor of 16 which results finally in a resolution of 350 nV. Therefore, error-bars on gate voltage scales vanish compared to any symbol size. Furthermore, the system is able to generate voltages symmetrically which is employed in the application of source/drain bias voltages. Because already very small amplitudes cover the voltage range of interest, these signals are divided by a resistor ratio of 1:1751 leading to an applicable voltage of about ± 4 mV across source/drain contacts. The purpose of this reduction of voltages is the simultaneous reduction of noise from the voltage source or which is picked up between source and divider directly attached to the connector at the cryostat's top plate. If this voltage noise is of constant level, the signal-to noise ratio is strongly enhanced by choosing signals of higher amplitude with subsequent division of both, signal and noise.

These voltage sources are attached via the amplifier/divider box introduced in the following section to all static gates (exit and third gate of each dynamic quantum dot as well as the SETs' local gates) and additionally provide bias voltages for source and drain contacts.

3.4.2 Amplifiers

The current amplifiers used here are custom-built and consist of three stages as shown schematically in Fig. 3.10. As the first amplifier an OPA129 is used which acts in this circuitry as transresistance amplifier with gain set by R_F [145]. Via this stage, the current is converted to a voltage, amplified by a factor set by the feedback resistor R_F (set to $10^8 \Omega$ throughout this thesis). Because measurements are performed on both source and drain contacts of the channel, biasing is only possible via the operational amplifiers. In the second stage, the effect of this bias voltage on the current measurement is subtracted using the differ-

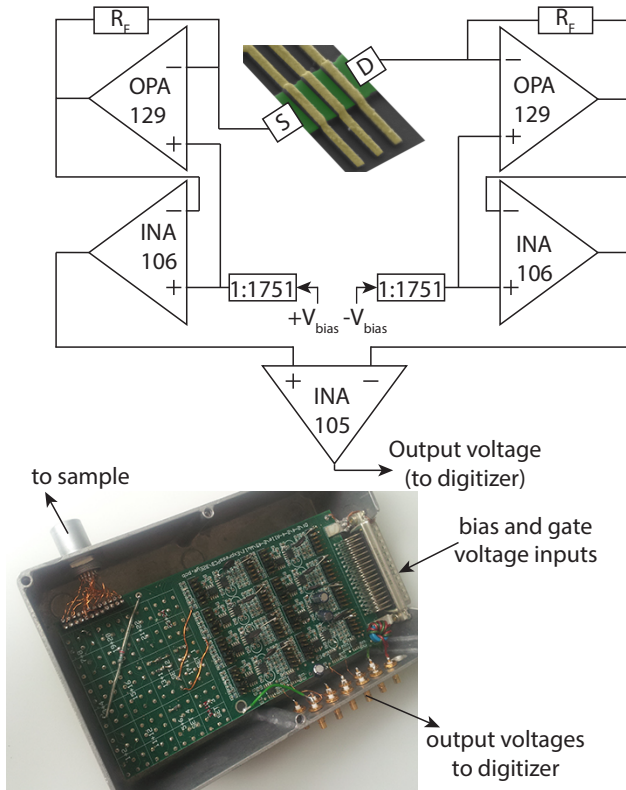


Figure 3.10:

The 3-stage current amplifier sketched as well as a picture of the board containing four amplification circuits and switches to selectively connect the sample.

ential instrumentation amplifier INA106 which additionally amplifies the difference signal by a factor of 10. Finally, the unity gain differential amplifier INA105 combines the (inverted) signals of source and drain. In summary, the amplification of this circuit equals 2×10^9 V/A. Except of the direct-current measurements of the dynamic quantum dots, the absolute precision of the amplifiers are only of minor importance in this thesis. We therefore neither employed any high-precision feedback resistors nor performed extensive calibration since the detector signals will be traced back to the signature of a single electron in the course of this thesis.

At the bottom of Fig. 3.10 the board is shown containing four separate amplifier circuits on the right hand side. Bias voltages and gate signal are input from the very right via the large D-SUB connector. Amplified signals are output via the bottom SMB connectors. The left-hand side of the board contains an array of switches to connect the board to the sample. These give the possibility to ground the sample, insert voltage dividers or series resistors. Typically, the amplifiers are connected to the sample with intermediate $150 \text{ k}\Omega$ in series to stabilize the amplification circuit when changing the input from ground to the sample by switching the intermediate connector. Also the gate voltage division by a factor of 16 is done here via these switches.

The Fisher connector at the top left of the box is directly attached to the dc port at the top-plate of the cryostat without any additional cabling. The layout of this box thus directly defines which contact of the sample needs to be attached to which dc line. Because patching outside the sample holder is only possible by re-soldering the interconnections between the Fisher connector and the board, it is necessary to consider this issue already in the sample layout or to patch during bonding. When connecting the sample to the electronics box, all switches are set to ground the sample. After this connection has been established, the switches' positions are changed to connect the signals and ampli-

fiers. The main advantage of this concept (of course, on the expense of lower flexibility) is the compactness in a rather complex environment: Assuming a three island series circuit of dynamic quantum dots, four current amplifiers (one for the semiconducting channel and three for the detectors) as well as roughly 10-15 voltage channels with filters or dividers are needed.

3.4.3 Waveform generators and digitizers

All rf signal generators and the digitizer card as well are constructed as parts of a modular system called PXI and thus are mounted into a common frame (model number NI 1065, see Fig. 3.11). To drive the quantum dots dynamically we use arbitrary waveform generators (AWGs). Although these instruments may be also used to specifically shape the waveform to either enhance the fidelity of the charge transfer by accounting for the underlying physical mechanisms in charge capture [44] or to adjust e.g. the energy at which electrons are emitted [51], the signals in this thesis are only of sinusoidal type as typically used [39, 41]. Instead, the need for of this type of instrument is implied by the fact that only single periods of a sinusoidal wave with subsequent hold of the drive at the initial/final value will be applied.

The arbitrary waveform generators provide two channels with 15 bit vertical resolution (Agilent N6030A, master) and two channels with 10 bits of vertical resolution (Agilent N6031A, slave), respectively. The sampling rate is common for both modules and equals 1.25 GS/s. The synchronization between the two modules is established by sharing the clock signal and an additional sync clock which is distributed from the master module via power splitters to the master and slave, respectively. Doing so, highest precision in timing is obtained. The start of a playback sequence is indicated between the modules by additional trigger signals. Every dynamically driven entrance gate of a QD structure on

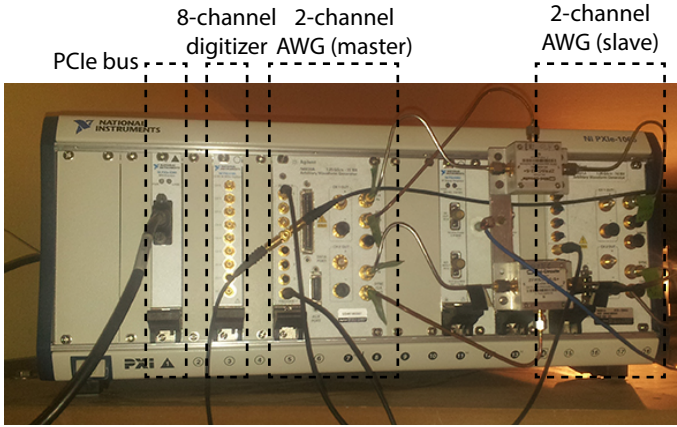


Figure 3.11: Photograph of the PXI frame equipped with digitizers and waveform generators.

the chip is attached to one channel of the arbitrary waveform generator, thereby enabling distinct control over every dynamic quantum dot in time and driving signal.

A global timebase for all modules in one frame is provided by the PXI bus system itself, enabling a stable phase between the waveform generators and the 8-channel, 12-bit digitizer card (NI 5105), sampling in maximum at 60 MS/s. The input impedance of the digitizer may be switched between 50Ω and $1 M\Omega$ and has been set here to the latter setting since only dc measurements have been conducted in this thesis. Due to limited bandwidth of the connection of about 90 MB/s to the remote PC, where further data processing and saving to disk is performed, only every tenth sampled value is transferred. Typically, the digitizer is started first and after about 50 ms, the waveform generators are triggered by software. The exact timing between the start

of sampling a waveform and the digitized measurement signals is obtained by measuring an additional marker pulse which is output at the beginning of sequence playback by the waveform generators. Thus, the timing adjustment between digitizer and waveform generators is finally performed in software during the data processing by identifying this additional marker pulse. To minimize the amount of data stored onto hard disk, the digitizer samples are reduced down to an effective sampling rate of 12 kHz by averaging of 500 points each.

All signals shown have been corrected for any dividers, amplifiers or impedance mismatch already. The signals referred to in the text and figures are always those signals applied directly to the sample.

3.4.4 Software

For remote control, we employ a heterogeneous software environment consisting of Matlab and NI Labview. The preparation of each measurement is performed in Matlab. Three different structures/arrays are created which fully describe the measurement and the physical meaning of each setting. Most evidently, a settings table (so-called pfp file) is necessary to fully describe the parameters of the next measurement job. It contains all settings of all devices at every point in time and is processed during the measurement line by line, thereby allowing to run arbitrarily nested loops, jumps in the setting parameters or the conduction of several, completely different measurements within one run.

Because we use a modular approach in the measurement software, there is no unique mapping between entries in this settings table and any physical device controlling the measurement at this point. This link is only established by a second element, which is called the pfi table and which contains a list of tuples consisting each of a (virtual) instrument address, the starting column in the array of parameters (pfp) and the number of parameters belonging to this instrument. The instrument

address does not necessarily equal any bus number or instrument number on a specific bus system, but refers to a specific driver module so that the usage of one instrument in completely different modes may be achieved by simply changing the address number in this array. When performing a measurement, the instruments are set sequentially according to their appearance in this list. Therefore, the digitizers should be the last instruments addressed since otherwise not every parameter will be set before the corresponding measurement is triggered.

The third element to describe the measurement is the so-called comment structure which is - in general - constant throughout a cool-down. This construct contains the physical description of each instrument together with a full list of interconnections between the instrument's output and a specific bond pad on the sample. Additionally, also a list of default settings is saved here which may be used at the initial generation of the settings table. With these 3 different constructs, the measurement is fully described. Finally, these elements are saved to hard disk as text files (pfi/pfp) and Matlab variables (comment structure), respectively.

After these files have been generated in Matlab, the measurement is conducted using a Labview routine. Firstly, the list of instruments (pfi table) as well as the list of parameters (pfp) is read in. Then, the pfp array is executed line by line for the instruments specified in the pfi file. The instruments' settings are applied only if parameters vary between subsequent lines, thus minimizing the time for configuration (especially important when using the waveform generators and transferring large waveforms).

Before starting a measurement, a reference string based on the current time is created. This unique identification string forms a part of the file name for a copy of all settings files as well as for the results, thereby maintaining consistency: Every resulting data is directly linked via this reference string to the corresponding parameter array and the

instrument list. Results are stored as binary raw data at a sampling rate of 12 kHz enabling thereby the repetition of software routines for the analysis. Additionally, there is a possibility to save comments regarding the measurement run at different points in time, e.g. during creation of the settings table in Matlab, before running the measurement and before quitting (in Labview). These comments are saved together with the time reference and serve as a quick overview of all measurement runs.

The processing of the resulting data is finally performed using Matlab again. Exemplary, three methods of evaluation are detailed in the following chapters, namely the continuous charging of a node by a dynamic quantum dot, the investigation of the transfer characteristics of such a dynamic quantum dot under parameter variation and finally the series operation of three dynamic dots with intermediate charge detectors.

4

Chapter 4

Conventional device characterization

In this chapter, basic characterizations of the device's individual building blocks are presented, focusing on the discussion of their functioning and the derivation of key parameters for further analysis. These include on the semiconducting part of the structure the action of the top-gates, Coulomb diamond measurements of one interconnecting node to derive its capacitance as well as the continuous charge transfer by each dynamic quantum dot separately using a cw pulse train. On the metallic side, the current flow across the detectors as a function of bias and gate is analysed, restricting the discussion mainly to deviations from conventional quantum dots resulting from tunneling of Cooper pairs. Finally, the ideal points of operation when being used as a detector are discussed.

4.1 Basic device characterization

4.1.1 Resistance during cool-down

During cooling of the device, the bias voltage applied to the source-drain leads of the semiconducting part as well as the superconducting elements is varied by about $\Delta V_{sd} \approx 140 \mu\text{V}$ to monitor the change of device resistance with temperature. The result is plotted in Fig. 4.1 for both detectors and the semiconductor channel as a function of the temperature of the mixing chamber.

For temperatures above $T = 13 \text{ K}$, the temperature is derived from the Cernox sensor, for temperatures below using the low-temperature resistance sensor based on RuO_2 . The semiconducting channel changes its resistance most strongly until the two-dimensional electron gas has fully formed, i.e. until reaching about $T \approx 60 \text{ K}$. Starting at around $1.6 \text{ M}\Omega$, the channel's resistance decreases to about $160 \text{ k}\Omega$ at below 1 K . In contrast, the metallic structures roughly maintain their room-temperature resistance (D1: $\approx 1.6 \text{ M}\Omega$, D2: $\approx 800 \text{ k}\Omega$) until the temperature of the mixing chamber drops below 1.1 K . The strong increase of the resistance is an indication that the aluminium becomes superconducting. In this phase, a band gap forms and the variation of applied voltage does not provide sufficient energy to overcome this gap, thus leading to the signature of isolation (three orders of magnitude higher resistance). The good agreement with the superconducting transition temperature from the literature is an indication of proper thermal coupling between the mixing chamber plate and the sample at this temperature range.

4.1.2 Gate-dependence of the channel's conductance

After verification of conductance of the elements at low temperatures, the next step of pre-characterization of the device under test is to deter-

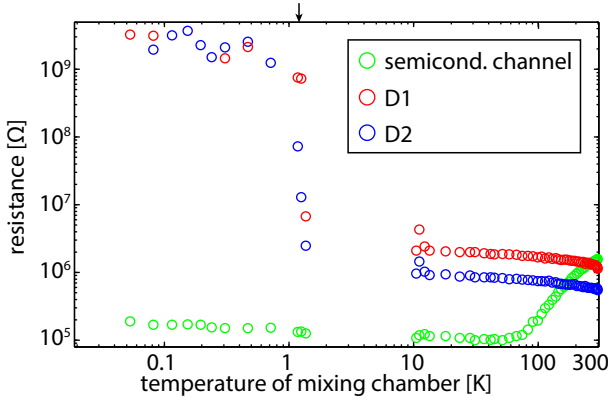


Figure 4.1:

Evolution of device resistances during cool-down. Green corresponds to the semiconducting channel, red and blue to the aluminium detectors D1 and D2, respectively. The black arrow at the top marks the transition temperature of $T = 1.14$ K of aluminium. This temperature is reached within about 18 hours when cooling down from room-temperature. The variation of source-drain potential of $\Delta V_{sd} \approx 140 \mu\text{V}$ is not sufficient to overcome the superconducting gap beyond. The two-dimensional electron gas is fully developed at about $T = 60$ K. Base temperature of $T = 25$ mK is reached after 24 hours.

mine the pinch-off voltages of the gates crossing the semiconducting channel. By applying a voltage difference between the gate and the channel's potential, the electrostatic potential of the channel can be locally modified. A barrier is formed by a gate, if the potential applied to the gate exceeds the pinch-off voltage.

A typical measurement of a gate characterization is shown in Fig. 4.2a), in this case we used the center gate (later called the exit gate) of QD1. The voltage applied to this gate is stepped from zero to -250 mV and back to zero (to check for hysteresis) and the current at fixed bias volt-

4 Conventional device characterization

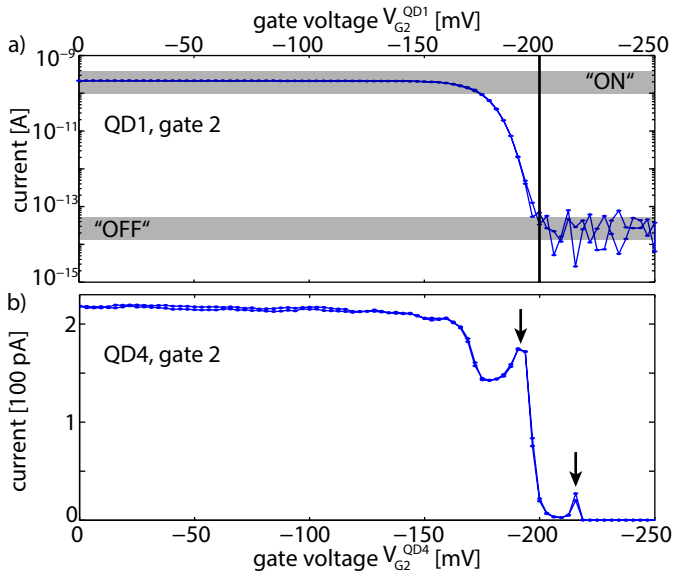


Figure 4.2:

Pinch-off of current across the semiconducting channel by applying negative potentials to the topgates. a) Conventional pinch-off modulated by Gate 2 of QD1 (back and forth). A device-specific threshold voltage (marked by the black line) modulates between "ON" and "OFF"-state. b) Pinch-off signature by gate 2 of QD4. Black arrows indicate resonances from (unintended) Coulomb-Blockade oscillations.

age is measured. None of the gates showed any hysteretic behaviour which otherwise would have been a reason to reject the sample because working points of the dots (set by the gate voltages) would not have been properly defined.

The gate acts basically as a field-effect transistor, able to switch between the "ON"-state (conducting channel) and "OFF"-state (closed channel) by variation of the applied voltage. In the transition between

these two states the barrier starts forming and is fully developed beyond the pinch-off voltage, indicated by the black vertical line in this plot.

Name of gate	Pinch-off voltage
V_{G1}^{QD1}	-213 mV
V_{G2}^{QD1}	-200 mV
V_{G3}^{QD1}	-206 mV
V_{G1}^{QD2}	-216 mV
V_{G2}^{QD2}	-212 mV
V_{G3}^{QD2}	-200 mV
V_{G1}^{QD3}	-222 mV
V_{G2}^{QD3}	none
V_{G3}^{QD3}	none
V_{G1}^{QD4}	-207 mV
V_{G2}^{QD4}	-222 mV
V_{G3}^{QD4}	none
side-gate of node 3	-172 mV

Table 4.1:

List of gates to control the semiconducting channel and their corresponding threshold-voltages to locally deplete the channel and thus suppress conduction. The pinch-off threshold voltage is defined here as that gate voltage at which the current through the channel drops below 100 fA. The bias voltage applied to the contacts equals $V_{sd} \approx 65 \mu V$.

The height of the barrier increases with more negative voltages applied, which will be discussed later (see section 5.1). Using this rather simple measurement technique, the specific shape and height of the barrier beyond pinch-off are inaccessible for experimental investigation.

Most of the measurements presented in this thesis take place in the region where the gates are in the "OFF"-state, i.e. blocking the current

driven by the voltage applied between source and drain contacts of the semiconducting channel. Therefore, all gates necessary for proper function of the device at least need to show this pinch-off signature. A list of all gates and their corresponding pinch-off voltage is given in table 4.1. Not all of the gates were electrically controllable and the gates without pinch-off signature apparently did not affect or even block the channel, i.e. most likely these ones were not connected to the room-temperature electronics. However, this might be the reason why we observe already a single-charge effect, namely the Coulomb-Blockade, in a simple one-gate sweep (Fig. 4.2b): Here, we use gate G2 of QD4 and most-likely create a quantum dot between this gate and the neighbouring, unconnected gate G3. A different explanation is a simple charge trap nearby. Both effects could only be distinguished in a stability diagram where the coupling of the gate and the charging energy of the structure (related to the dimensions of the dot) can be derived. The peak-like signatures marked by the black arrows resemble a resonance of a quantum dot's electrochemical potential (which is energetically controllable by the stepped gate voltage) with the transport window opened by the source-drain voltage.

In general, the gates do not affect the channel underneath as long as no voltages are applied. Compared to metallic nanostructures, where tunneling barriers are formed by oxidization of metal during device fabrication (and which are therefore fixed), the semiconducting devices employing tunable barriers are superior in simplicity during initial characterization and flexibility in combination of individual substructures: Not all of the gates need to work properly, as long as the semiconducting channel remains conducting at low temperatures.

In addition to the metallic top-gates, also semiconducting side-gates have been fabricated to tune the individual nodes to smaller capacitance by reducing the effective electronic area. Using the right-most side-gate, the channel could even be locally depleted by a pinch-off voltage

of ≈ -170 mV, slightly below the values of the top-gates. However, the charge-sensitivity of the detectors fabricated was even sufficiently high without this additional control parameter so that all side-gates remain grounded in the following.

4.1.3 Coulomb-blockade: Estimating capacitances

Another important parameter of the device is the charging energy of the nodes which can be estimated by performing Coulomb-Blockade measurements. There, the effect of repulsion of electrons (carrying the same charge) is employed: Without any applied voltage between source and drain contacts, electrons may only flow if an empty state on the node is energetically in resonance with the leads, otherwise current is blocked. By applying a finite voltage between the leads, a transport window is opened which becomes larger with higher voltage. A typical measurement of Coulomb-Blockade is shown in Fig. 4.3 b) while the structure and relevant parameters are depicted in Fig. 4.3 a).

The node (node 1 here, coloured in red) is formed by the left-most gates of the quantum dots QD1 and QD2, respectively (coloured yellow). The former is held fixed at $V_{G1}^{QD1} \approx -179.6$ mV while the latter is varied in a range of $V_{G1}^{QD2} \in [-167 - 184]$ mV just below the pinch-off voltage. The objective of changing the gate voltage is twofold: On the one hand, the gate forms a tunneling barrier, thus confining electrons on the node, on the other hand it tunes the electrochemical potentials of the node via capacitive coupling. The result is the typical rhombic structure centered around $V_{sd} = 0$ meV and periodically repeated along the gate axis. Dotted lines show peaks in the differential conductance indicating states of the node in resonance with the source's electrochemical potential μ_s (positive slope) and the drain's electrochemical potential μ_d (negative slope).

One diamond is sketched exemplary from which the charging energy

4 Conventional device characterization

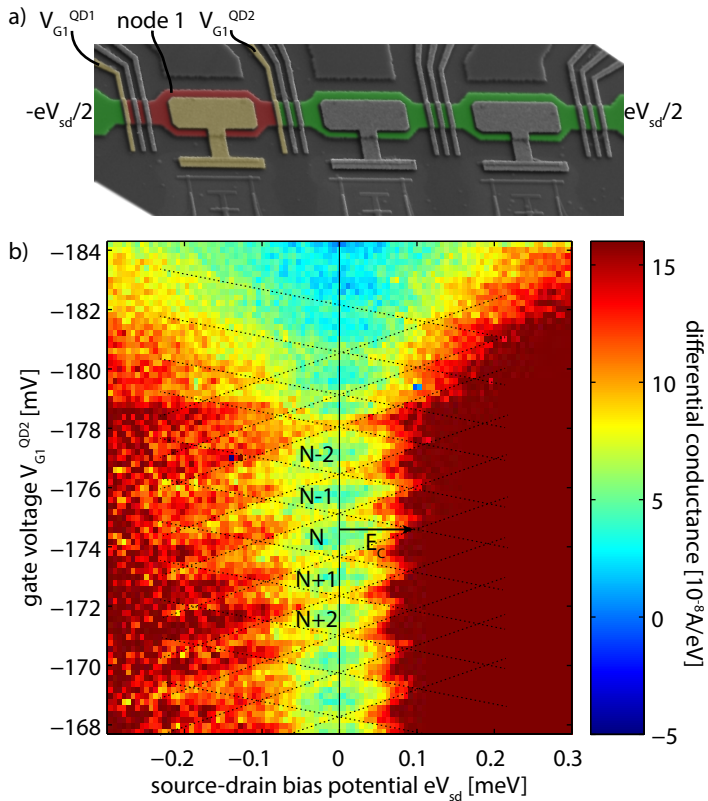


Figure 4.3:

Coulomb diamond measurement of node 1. In a), the device is sketched where the elements used are highlighted. The node 1 (red) is formed between the structures QD1 and QD2, using the entrance gates (yellow), respectively. b) The differential conductance is plotted versus the bias potential eV_{sd} and one of the gates defining the node, here gate 1 of dot QD2, controlled by voltage V_{G1}^{QD2} . As static gate, the first gate dot QD1, set to $V_{G1}^{QD1} = -179.6$ mV is chosen. The charging energy of the node E_C is estimated to $E_C \approx 100 \mu eV$.

of the node E_C can be estimated to about $E_C \approx 100 \mu\text{eV}$ (based on the assumption, that the voltage bias mainly drops across the barriers). Via $E_C = e^2/C_\Sigma$ also the total capacitance C_Σ of the node can be derived to $C_{\Sigma,\text{node1}} \approx 1.6 \text{ fF}$ which is about 10-20 times larger than in conventional quantum dots used to study single-electron effects. Although the value might appear very large, its magnitude seems to be reasonable when compared to the results obtained from simulations to investigate the precessing chip P640-2-1 studied in [108]. There, we obtained $C_\Sigma \approx 0.9 \text{ fF}$, but with a slightly smaller node and without using a floating gate on top of the node for enhanced coupling to the detector [43].

To obtain a better understanding of the implications resulting from the size of the node, one can roughly estimate of number of electrons on the node in equilibrium. The optical size of the node is known from the lithographic design and can be approximated to about $3.7 \cdot 10^{-8} \text{ cm}^2$. The electronic size, i.e. the area occupied by electrons, is reduced due to edge depletion [146] after the wet-chemical etching process by about 20%. Further using the independently determined carrier density of this wafer of $n_s = 2.77 \cdot 10^{11} \text{ cm}^{-2}$, the number of electrons on the node can be estimated to about $N_{\text{node}} \approx 1000$.

In the following experiments, the size of the node(s) will change depending on the gates used: The largest node possible is formed by using gates of QD1 on the one hand and QD4 on the other hand. In this case, the node's size should be about 3 times as large as the smallest one investigated experimentally here. Therefore, the charging energy will be reduced by a factor of 3 yielding $E_C \approx 30 \mu\text{eV}$ and $C_{\Sigma,\text{node}} \approx 4.8 \text{ fF}$. However, in a third configuration shown in this thesis, also a node will be formed between QD2 and QD4 resulting in an area twice as large as in the experiment here and thus $E_C \approx 50 \mu\text{eV}$ ($C_{\Sigma,\text{node2}} \approx 3.2 \text{ fF}$). Although the determination of these parameters is rather vague, their magnitude is relevant in order to understand effects when changing to

the regime of single-charge transfer: The number of electrons stored on the node N_{node} directly converts to an electrostatic potential using $\Delta Q = \Delta N_{\text{node}} e = C_{\Sigma} \cdot U$, i.e. the node's capacitance is the direct scaling factor between the number of electrons on the node and the resulting electrostatic potential U .

4.2 Charge transfer by the non-adiabatic dynamic QD (cw drive)

4.2.1 Finding the region of quantized-charge transfer

In this section, the results of quantized charge transfer by dynamic quantum dots are presented when being driven by continuous pulse trains, i.e. conventional characterization of the dynamic dots by direct current measurements. First, the "pump region" in the multidimensional parameter space has to be located. Therefore, we first measure the pinch-off characteristics of both gates which will later form a dynamic quantum dot without any applied rf signals. The result is shown as a color plot in Fig. 4.4 for quantum dot QD4.

Superimposed onto the pinch-off characteristic oscillations in the current through the semiconducting channel are evident which are attributed to Coulomb blockade oscillations. Here, the quantum dot formed between the two gates gives rise to an enhancement in the current whenever the dot's electrochemical potential enters the transport window opened by the applied voltage difference between source and drain lead. One of these oscillatory features is marked by a black arrow. Both gates do not only form barriers thereby creating a quantum dot, but also couple capacitively to the quantum dot's electrochemical potential. Therefore, the slope of these oscillations gives a hint on the location of the quantum dot relative to both gates: In this case, the slope is equal to 45° (keep in mind the different scaling of both

4.2 Charge transfer by the non-adiabatic dynamic QD (cw drive)

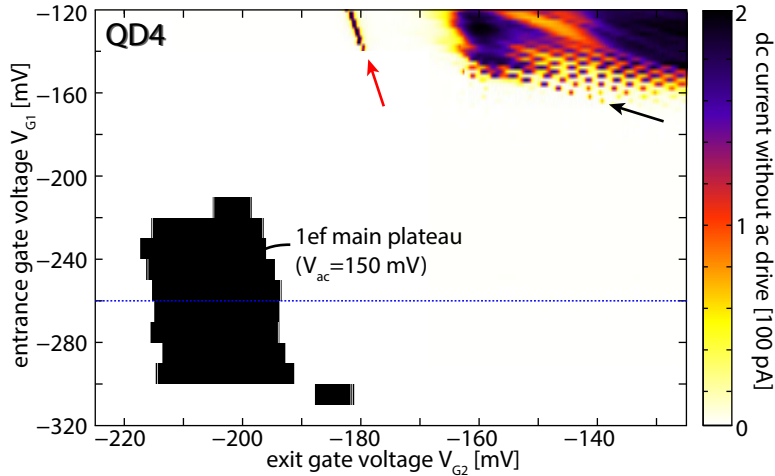


Figure 4.4:

Location of the main pumping plateau of QD4 relative to its dc characteristic without rf drive. Color shows measured current without applied ac voltage at a dc bias voltage of $V_{sd} \approx 65 \mu\text{V}$. Signatures of Coulomb Blockade Oscillations are visible (marked by black arrow). The black region in the bottom left of the plot shows the position of the $1ef_p$ -plateau (defined here as $I = (1 \pm 0.3)ef_p$) when a sine wave with amplitude $V_{ac} = 150$ mV is applied. No other plateaus were visible for this dot.

axes!) indicating equal coupling of both gates to the dot, i.e. it is indeed formed between both gates as intended. Also, a second feature (marked by a red arrow) is visible which is almost unaffected by the gate voltage V_{G1} . This line corresponds to the same feature as shown in Fig. 4.2b) and indicates another dot, formed close to gate G2 but coupled only weakly to gate G1. As discussed previously, the cause of this signature might be a dot formed between gate G2 and the uncontrolled gate G3 of QD4 but also a simple trap to the right hand side of

G2 inside the semiconducting channel is conceivable.

In order to achieve quantized charge transfer, as the next step the entrance gate voltage is set to a value slightly exceeding the single-gate pinch-off voltage (say, $V_{G1} = -225$ mV here), thereby raising the QD ground state well above the Fermi energy. The QD is empty now and current flow is strongly suppressed. Subsequently, the rf signal generator is switched on at fixed frequency and moderate amplitude. Then, the second gate (called exit gate) is swept along the blue dashed line in Fig. 4.4 and the amplitude of the oscillatory signal is increased stepwise until current flow is observed. Due to the robustness of the dynamic dots, the applied bias voltage between source and drain leads may be chosen with opposite sign to the direction of quantized current (given by the order of modulated and static gate) to distinguish between quantized and ohmic current.

The position of the resulting $1ef_p$ main plateau (defined here by $I = (1 \pm 0.3)ef_p$) is shown as the black area in Fig. 4.4 in the bottom left for an amplitude of the sinusoidal signal of $V_{ac} = 150$ mV. The frequency of the signal equals $f_p \approx 39$ MHz which corresponds to 32 points of the arbitrary waveform generator used to drive the dynamic dot (sampling at $f_s = 1.25$ GHz). This specific dot showed only one main plateau. Beyond about $I \approx 1.5ef_p$, the current increases without any quantization.

4.2.2 Investigation of the transfer characteristics (cw) of the individual dynamic QDs

In order to detail the charge-transfer mechanism obtained by applying an oscillatory signal to the entrance gate of the dynamic quantum dot QD4, a plot of the quantized current for fixed entrance gate voltage at $V_{G1} = -260$ mV (blue dashed line in Fig. 4.4) is shown in Fig. 4.5 as blue dots and line (left axis) together with the derivative of

4.2 Charge transfer by the non-adiabatic dynamic QD (cw drive)

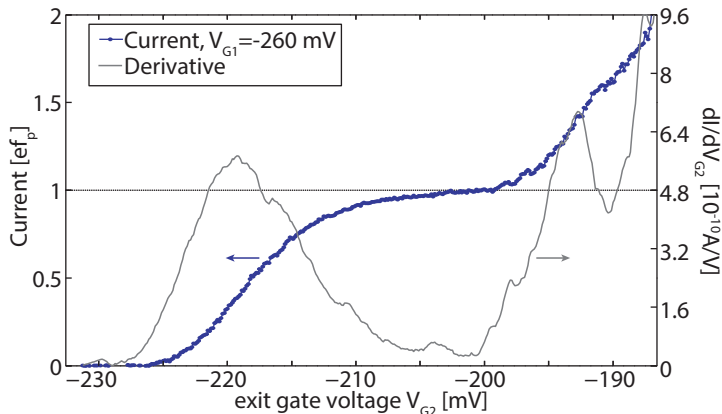


Figure 4.5:

Quantized current of QD4 at fixed entrance gate voltage $V_{G1} = -260$ mV (blue dots and line, left axis) and the corresponding derivative (grey line, right axis).

the current (grey line, right axis). The current is normalized to ef_p showing a plateau for $n_e = 1$ which corresponds to $I \approx 6.3$ pA. The derivative (grey line) reflects the asymmetric transition from $I = 0$ to $I = 1ef_p$ with a steep slope in the beginning, followed by a slow approach to $n_e = 1$, characteristic for a double-exponential shape [48]. This gives a first hint that the device obeys the decay-cascade model (see also section 2.5.2) predicting a double-exponential transition between the plateaus [34, 46, 105].

A typical two-dimensional map of the pumped current as a function of both static voltages applied to the entrance and exit gate of the dynamic quantum dot (as discussed in section 2.5.1) is shown for the dynamic quantum dot QD2 in Fig. 4.6a). Black contour lines are superimposed in steps of $0.2ef_p$.

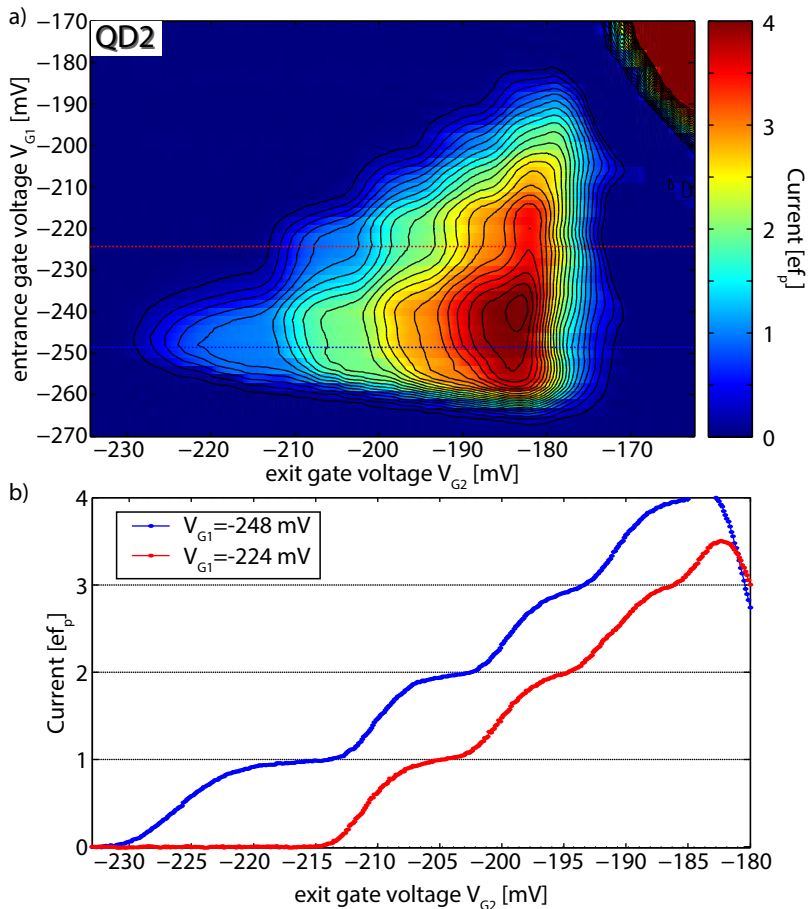


Figure 4.6:

QD2 dc current measurement with continuous pulse train, two-dimensional plot (a) and for fixed entrance gate voltage $V_{G1} = -248$ mV (across main plateaus, blue dots and line) and $V_{G1} = -224$ mV (across first side plateaus, red dots and line). Applied ac amplitude $V_{ac} = 80$ mV. Color in (a) represents current ranging from 0 to $4ef_p$, black lines show contour lines in steps of $0.2ef_p$.

4.2 Charge transfer by the non-adiabatic dynamic QD (cw drive)

The amplitude of the applied sine wave is $V_{ac} = 80$ mV. This dynamic dot shows a series of well developed plateaus (up to four) and also a number of side plateaus. Line plots for fixed gate voltage on $V_{G1} = -248$ mV (across the main plateau) and $V_{G1} = -224$ mV (across the first side plateau) are indicated by blue and red dashed lines, respectively, and shown in Fig. 4.6b). Compared to the other dots, this one shows the most regular pattern. The positions of the side plateaus in terms of gate voltage V_{G2} at electron number $n_e - 1$ equal the corresponding plateaus along the main plateau with electron number n_e .

This observation coincides very well with the expected mechanism underlying the quantized charge transfer: As discussed in chapter 2.5, the characteristic increase in current with lowered exit gate voltage is predominantly given by the loading process and the cascade of back-tunneling to the source lead. The occurrence of the side plateaus, on the other hand, can be explained by incomplete *un*loading of electrons captured on the dynamic dot. At the first side plateau, for example, n electrons are loaded onto the dynamic quantum dot in each cycle, but, due to the lowered quantum dot states (as a consequence of the lower entrance gate voltage), not all electrons are raised sufficiently high in energy to overcome the barrier formed by the exit gate during the emission part of the transfer cycle, thus reducing the number of electrons emitted to drain by 1 to $n_e - 1$. Therefore, one may conclude, that the shape of the transition is indeed given by the loading mechanism.

This is even stronger confirmed by a measurement of the dynamic dot QD1 which is shown in Fig. 4.7. In a), the quantized current is shown as a two-dimensional color plot under variation of entrance and exit gate voltages, normalized to ef_p . The frequency is the same as in the previous measurements, $f_p \approx 39$ MHz, but the amplitude is set here to $V_{ac} = 120$ mV. Black contour lines are superimposed in steps of $\Delta I = 0.2ef_p$. The main plateau region is clearly visible for this dynamic quantum dot with a series of plateaus and a very prominent

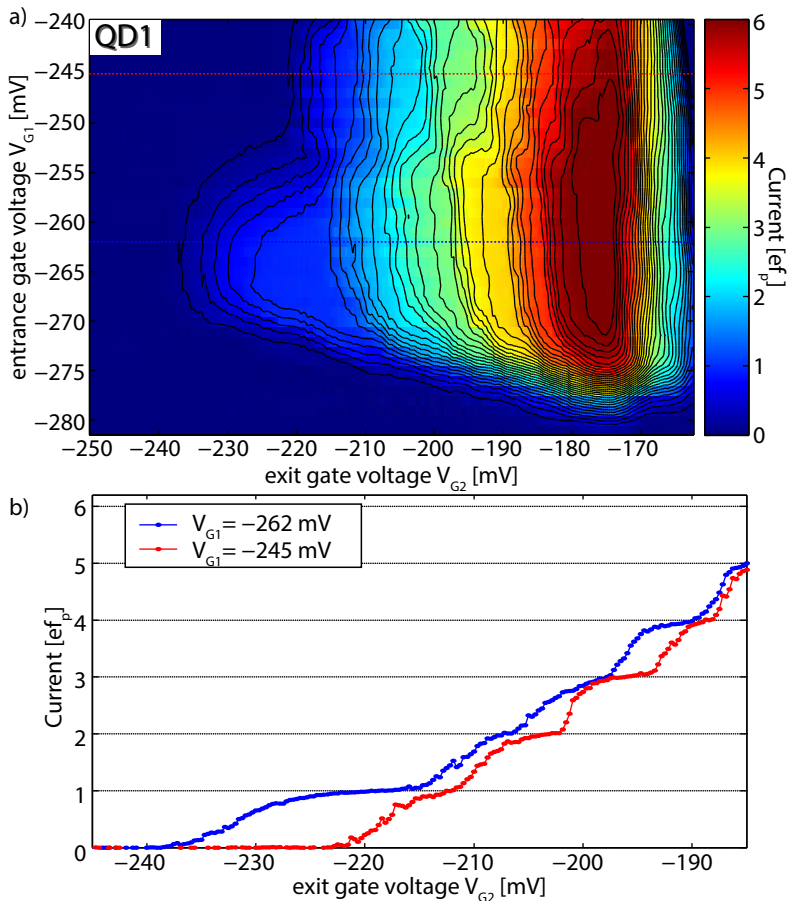


Figure 4.7:

QD1 dc current measurement with continuous driving signal, two-dimensional plot (a) and for fixed entrance gate voltage $V_{G1} = -262$ mV (across main plateaus, blue dots and line) and $V_{G1} = -245$ mV (across first side plateaus, red dots and line). Applied ac voltage $V_{ac} = 120$ mV. Color in (a) represents current ranging from 0 to $6 e f_p$, black lines show contour lines in steps of $0.2 e f_p$.

$1ef_p$ -plateau.

A line plot across this main plateau is indicated by a blue dashed line and shown as blue dots and line in Fig. 4.7b). The step-wise increase in current for fixed entrance gate voltage $V_{G1} = -262$ mV is clearly visible, although some of the plateaus are not very well developed. Additionally, a cut through the first side plateau (indicated by the dashed red line in a)) is shown by red dots and line. The position on the gate voltage axis is slightly shifted, possibly due to cross-coupling between both gates. However, the shape of each transition to a plateau n_e in the line corresponding to the main plateau agrees quite well to the equivalent transition to plateau $n_e - 1$ in the cut through the side-plateau. Since, according to theory, the line shape along this gate voltage is given by the charge capture mechanism and, moreover, the development of side plateaus is caused by insufficient unloading of captured electrons, the above-mentioned equivalence is expected. For example, the only weakly developed second main plateau is reproduced as the first side plateau. Also, the steep transition from the third to the fourth main plateau together with a comparably broad fourth main plateau are found again as the signature of the third side plateau.

4.2.3 Effect of the amplitude of the driving waveform

To conclude this section, I would like to comment more generally on the effect of the amplitude of the applied oscillatory signal. Exemplary, in Fig. 4.8 the extension of the $1ef_p$ -main plateau of QD2 for two different values of V_{ac} is shown. According to theory, the precision of single-charge transfer is unaffected by the applied voltage amplitude. Therefore, this parameter should be simply chosen such that it opens a sufficiently wide main plateau region to reduce the influence of drifts in the applied static voltage V_{G1} . For this device and setup, the applied amplitude of $V_{ac} = 80$ mV opens a main plateau with width

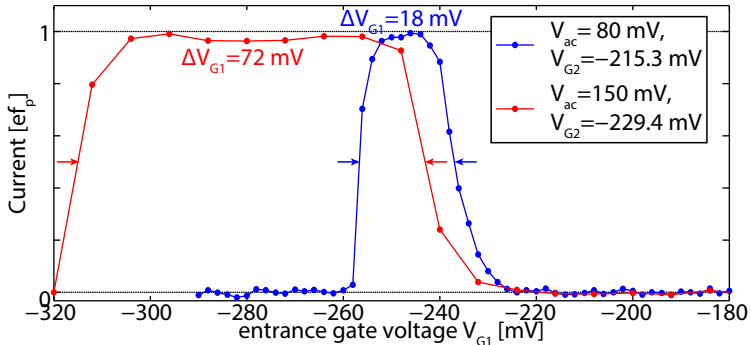


Figure 4.8:

QD2 dc current measurement with continuous rf signal, comparison of different V_{ac} . The plot shows cuts along the $n_e = 1$ main plateau for voltage amplitudes $V_{ac} = 80$ mV (blue) and $V_{ac} = 150$ mV (red), respectively. The width of the plateau is marked by arrows and defined by a current threshold of $0.5e.f_p$. The voltages applied to V_{G2} have been adjusted to compensate for inevitable cross-coupling.

$\Delta V_{G1} = 18$ mV in terms of entrance gate voltage V_{G1} . By almost doubling this parameter to $V_{ac} = 150$ mV, the width is enhanced to $\Delta V_{G1} = 72$ mV. This opens a sufficiently wide main plateau so that for all following measurements on single-charge detection this parameter has been chosen unless mentioned.

In the following section, the second building block for the following experiments, the single-electron transistor, is discussed in terms of its experimental parameters. Moreover, the section shows how the transistor is operated as an electrometer, capable of sensing individual electrons in close vicinity.

4.3 The dc-coupled single-electron transistor

4.3.1 Introduction to the superconducting SET

In this section the main characteristics of the single-electron transistors (SET), first proposed by Averin and Likharev [147], experimentally realised by Fulton and Dolan only one year later in 1987 [16] and employed here as highly-sensitive electrometers, are discussed. As shown in the experimental section 3.1, the SET is formed in a metallic system by a central node which is coupled via fixed tunneling barriers to source and drain contacts. Accessible tuning parameters of a fabricated SET are therefore the voltage applied to the contacts and an additional gating voltage applied via a capacitively coupled electrode in close vicinity. Since the system is the metallic equivalent of a quantum dot (as previously discussed), the focus is on the main differences as compared to the semiconducting implementation.

Since the transistors are made of Al and operated at low temperatures, both the leads and the central island are in the superconducting state (SSS), separated by insulating tunneling barriers made of aluminium oxide. Besides the previously discussed charging energy E_C , caused by the small island dimensions, the superconductivity adds another energy scale to the system which is the superconducting gap energy Δ_s . In Fig. 4.9, the density of states as a function of energy for a superconductor is shown which is referred to as the semiconductor model.

The energy E_f symbolises the Fermi energy, at which the condensate of Cooper pairs lies. Separated by Δ_s each from this energy, the onset of valence and conduction band is shown. The density of states diverges at these band edges [148]. While tunneling of Cooper pairs is always resonant due to the lacking degrees of freedom of these particles, the quasi-particle tunneling of electrons and holes is a threshold

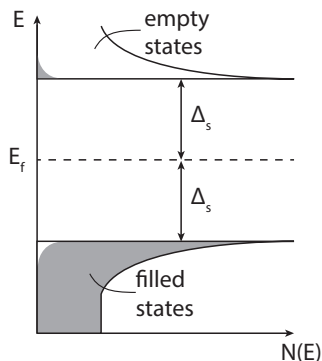


Figure 4.9:

Density of states of a superconductor in the semiconductor model. Cooper pairs form a condensate at E_f , separated from valence and conduction band by Δ_s each. States below E_f are filled, above empty. At the band edges, the density of states diverges. Additionally, thermally excited quasi-particles are depicted.

process where the particles energetically relax into the Fermi sea by the emission of photons or phonons. In order to enable quasi-particle tunneling, these have to be created by breaking a Cooper pair (consisting of 2 electrons). Due to the band gap Δ_s between the ground state of the superconducting state and the empty band for quasi-particles, this process requires an energy of $2\Delta_s$, one Δ_s for each electron. In the following discussion, the temperature is assumed to be small compared to the energy scale set by the band-gap so that thermally excited particles are negligible.

Due to the coexistence of Cooper pairs and electron- (or hole-)like quasi-particles, superconducting single-electron transistors act comparable to their normal-conducting counterparts beyond a certain threshold voltage which equals $|eV_{sd}| = \pm 4\Delta_s$. Beyond, the energy is sufficient to break Cooper pairs and to create quasi-electrons and quasi-

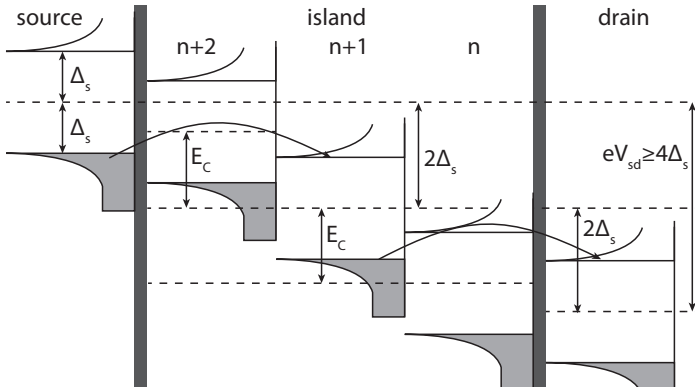


Figure 4.10:

Quasi-particle tunneling across an all superconducting double junction. The sketch involves the energetic position of the source and drain leads at an applied bias as well as the island states $n, n + 1$ and $n + 2$. These are offset by E_C each (semiconductor notation). Transport of quasi-particles is energetically allowed if the bias voltage supplies $2\Delta_s$ per junction, resulting in Giaever-tunneling [149, 150] of quasi-particles from the occupied valence band into empty states in the conduction band.

holes on both sides of the tunneling barrier. Therefore, to observe tunneling of quasi-particles across a barrier, eV_{sd} must supply an energy of $2\Delta_s$ per barrier. The processes involved are depicted in Fig. 4.10, representing the source and drain lead on the left and right hand side of the plot, respectively, as well as three charge states of the SET island differing by one charge carrier and thereby by E_C in energy. Typically, tunneling across such transistor is regarded in a sequential picture.

In order to allow tunneling by quasi-particles from source onto the island (initially being in state n), the island's conduction band in the state $n + 1$ must fall below the source's valence band. This requires, as previously mentioned, the difference in electrochemical potentials

of $2\Delta_s$. Then, with the island being in state $n + 1$, a *second* quasi-particle may tunnel from the island to drain, which again requires the energy difference $2\Delta_s$ between island and drain lead. Due to the large density of states at the edge, this contribution dominates compared to the (also possible) subsequent tunneling of the excess quasi-particle previously tunnelled onto the island. After completion of the second tunneling event, the island has returned to state n and the cycle may restart. As in conventional devices governed by Coulomb blockade, tunneling of two quasi-particles (electrons) is only allowed, if the bias voltage is further increased such that the additionally required charging energy for the second quasi-particle (in order to reach state $n + 2$) is provided. Therefore, the quasi-particle tunneling is equivalent to the normal-conducting single-electron tunneling, offset by the amount of energy required to overcome the superconducting gap. In this sense, the offset of quasi-particle tunneling in source-drain bias potential is a direct measure of the superconducting band gap Δ_s [151–154].

This is well reflected in the measured dependence of the current flowing across an SET in the all superconducting state (SSS) on its bias and local gate potential, as shown in Fig. 4.11. This device is fabricated using a similar design as compared to the detectors used as charge sensors in this thesis, but additionally, enhanced thermal coupling of the wires attached to the device provides lower electron temperatures of the system and thereby reduces effects due to thermally occupied valence and conduction band states.

Along the gate-voltage axis, the signal is periodic with periodicity of $1e$ on the SET island. The green area in the center is referred to as the gap region, tunneling is blocked here by the superconducting band gap, the current is low. Beyond the threshold of $|eV_{sd}| > \pm 4\Delta_s$, tunneling is allowed and the first charge state is inside the transport window (light blue and yellow areas, respectively). Therefore, the main parameters of the SET can be derived from this plot as indicated, like the charging

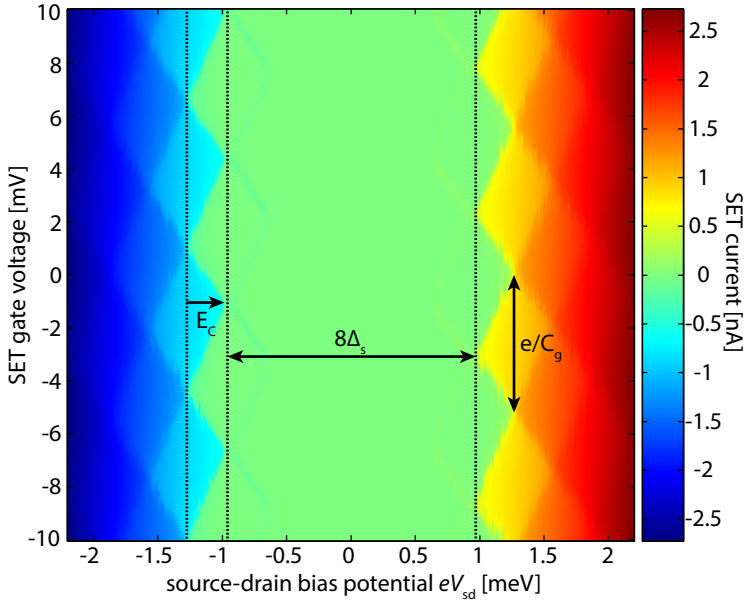


Figure 4.11:

Coulomb diamond measurement of an all superconducting SET, comparable to the structures used in this thesis as charge detectors (by courtesy of N. Ubbelohde, D. Reifert and L. Freise). The current across the SET is shown as a function of both its bias potential (x -axis) and local gate voltage (y -axis). Quasi-particle transport is suppressed in a voltage range of $|eV_{sd}| < \pm 4\Delta_s$. Since beyond the current is carried by quasi-particles, it evolves similar to the normal-conducting single-electron transistor only offset by the additional energy to break Cooper pairs into quasi-particles.

energy (given here in semiconductor notation as the spacing of energy levels on the island while in literature of metallic SETs this spacing typically corresponds to $2E_C$), the superconducting gap energy as well

4 Conventional device characterization

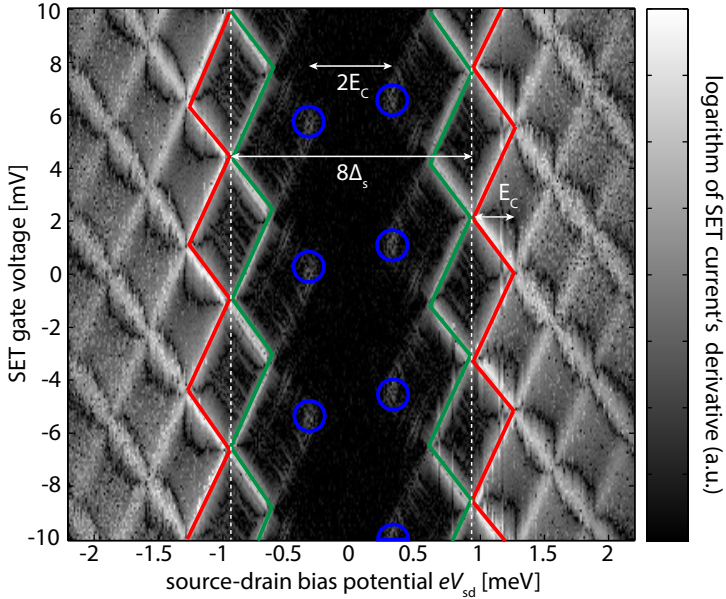


Figure 4.12:

Derivative of Coulomb diamond measurement of an all superconducting SET, same dataset as in Fig. 4.11. The grey scale is proportional to the logarithm of the derivative of the SET current along the bias axis in order to account for different amplitudes of the contributing effects. White vertical, dashed lines correspond to the onset of quasi-particle tunneling, red lines mark the lower boarder of Coulomb diamonds corresponding to quasi-particle tunneling. Green lines mark lines attributed to Josephson quasi-particle (JQP) tunneling, blue circles indicate regions where double Josephson quasi-particle (DJQP) tunneling is expected.

as the gate capacitance C_g .

However, when taking the derivative, there appear even more features, as shown in Fig. 4.12. The scaling of the grey scale is logarithmic

to account for the different amplitudes of the effects discussed in the following. Marked by red lines, the onset of quasi-particle tunneling is clearly visible with the regular pattern of Coulomb blockade beyond. Features in the sub-gap region at $|eV_{sd}| < 4\Delta_s$ cannot be explained by quasi-particle tunneling solely since the energy required for tunneling is not provided by the voltage source. Instead, transport is only possible when Cooper pairs are involved [152, 155].

The most prominent feature in this sense is marked by green lines in Fig. 4.12. This signature is attributed to the Josephson quasi-particle (JQP) cycle. As mentioned previously, tunneling of Cooper pairs requires resonance between the source and the target state on the island. Due to this condition, the effect is only observed for specific combinations of bias and gate voltage. The line shape reflects the shift in the Cooper pair resonance voltage with changes in bias and gate voltage (and is therefore parallel to the quasi-particle lines). The full cycle is sketched in Fig. 4.13a) starting with the island in state n : First a Cooper pair tunnels resonantly onto the island and remains there if a quasi-particle tunnels off the island across the opposite barrier (the charge state of the island changes after quasi-particle tunneling, thereby lifting the resonance condition with source). After both tunnel events, the island's charge state has changed from n to $n + 1$ since two elementary charges are added by the tunneling of a Cooper pair while one charge is removed due to the quasi-particle tunneling. Finally, the sequence is terminated by another tunneling event of a quasi-particle to the drain lead in this case (also the opposite direction of charge transfer is possible, as evident from Fig. 4.12).

In Fig. 4.13b), the energy diagrams of the source and drain lead as well as the island's charge states n , $n + 1$ and $n + 2$ (for Cooper pairs dashed, for quasi-particles solid) are drawn. Cooper pair and quasi-particle states with equal n differ in energy each by $E_C/2$ [156]. The

4 Conventional device characterization

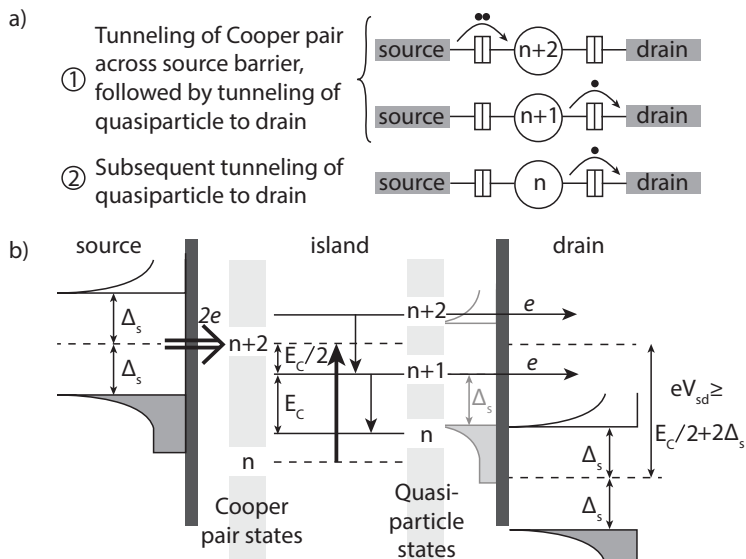


Figure 4.13:

Illustration of the Josephson-quasi-particle (JQP) cycle. a) Illustration of the cycle: First, a Cooper-pair (charge $2e$) tunnels resonantly onto the island from one lead (source in this case) with subsequent tunneling of a quasi-particle across the opposite tunneling barrier (drain here). In order to return to the initial state n , the difference in electrochemical potentials between island and drain lead of $2\Delta_s$ is required for the second quasiparticle to leave the island. b) Energy diagram depicting the states of the island involved in this charge-transfer cycle with respect to source and drain leads. The states belonging to Cooper-pairs are dashed, transitions are marked bold. Quasi-particle states are depicted by solid lines, shifted energetically by $E_C/2$ compared to Cooper pair states [156]. Due to the additionally required resonance condition with source, the $n+1$ quasi-particle state is $E_C/2$ below the source's Fermi level (dashed line). To illustrate the last tunneling event of this cycle, also the density of states for the $n+1$ quasi-particle state on the island is depicted at the right hand side.

minimum threshold voltage of this process is therefore [153, 157, 158]

$$eV_{\text{sd}} \geq E_C/2 + 2\Delta_s \quad (4.1)$$

in order to allow also the second quasi-particles to leave the island [159]. After completion, the net charge transfer across the device is $2e$, caused by the Cooper pair across the one and two quasi-particles across the other junction.

Similarly, another process is conceivable, also requiring the combination of Cooper-pair tunneling across one junction plus quasi-particle tunneling across the other. But, instead of returning to the initial state by another tunneling event of a quasi-particle, the complementary process of quasi-particle tunneling across the first junction together with a Cooper pair passing the latter junction completes the cycle [160]. This sequence (called double Josephson quasi-particle cycle, DJQP) is depicted in Fig. 4.14. Both processes require resonance with source or drain lead, respectively, and additionally the transport window to match the contributing final charge states which are n and $n+1$. Therefore, this process is not a threshold process, but occurs (periodically in e) at bias potentials $eV_{\text{sd}} = \pm E_C$ [153, 155]. These points are encircled in blue in Fig. 4.12.

In literature, there are also signatures reported showing a clear $2e$ dependence on the local gate voltage [161, 162] at bias potentials around $eV_{\text{sd}} \approx 0$ meV. In this regime, the bias voltage is too small to enable tunneling of quasi-particles. Parity effects cause an even-odd asymmetry in the system's ground-state energy [161–163] since in the odd case one electron remains unpaired on the island, causing an increase in the system's ground state energy by Δ_s (at $T = 0$). In order to obtain these features, the Josephson coupling must be large compared to the charging energy. However, due to the small tunnel junctions and the high tunnel resistance, the SETs used in this thesis are dominated by charging effects, therefore $2e$ periodic effects are not observed.

4 Conventional device characterization

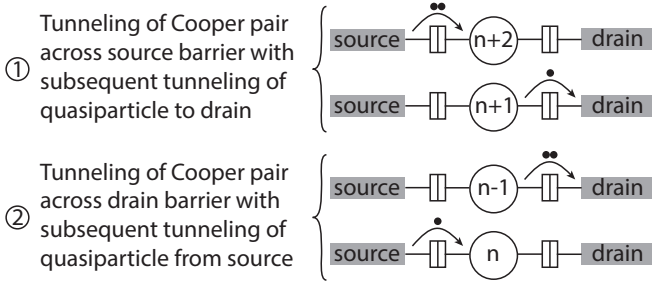


Figure 4.14:

Illustration of the double Josephson-quasi-particle cycle (DJQP). It consists of four sequential tunneling events involving Cooper pair and quasi-particle tunneling across both junctions. This requires resonance conditions with source and drain leads, respectively, which are fulfilled simultaneously only once in the (V_{sd}, V_g) -plane per period.

Turning the focus now to the SETs placed on this chip, Fig. 4.15 shows the SET current as a function of source-drain bias potential (which is symmetrically applied to both contacts) for an SET in one of the other circuits implemented on this chip (fabricated simultaneously using the same design). Additionally, the gate is modulated in this plot to illustrate the bias-dependent sensitivity of the detector, leading to the modulation envelope as a function of applied bias potential.

The superconductivity manifests itself in a large gap in transport of almost 2 meV, formed symmetrically around zero-bias. The width of this region, limited to both sides by the onset of quasi-particle tunneling, equals $8\Delta_s$ [154] with Δ_s the superconducting gap energy. This parameter is derived in comparable thin-film devices to about $200 - 300 \mu\text{eV}$ [154, 164]. In our device, the superconducting gap is estimated to equal about $\Delta_s = 225 \mu\text{eV}$. Beyond this threshold, the potential supplied by the bias voltage is sufficient to break Cooper pairs

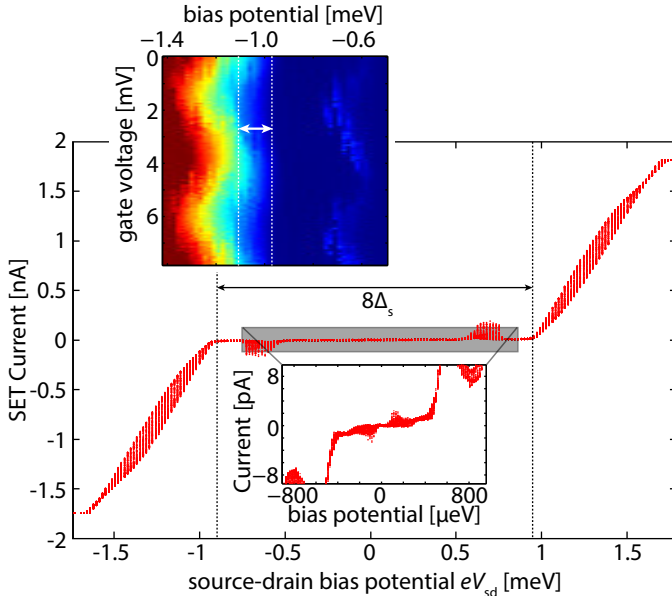


Figure 4.15:

SET modulation envelope as a function of bias voltage. For each bias voltage parameter, the SET's gate was modulated over a few periods to show the modulation amplitude. The superconducting energy gap $\Delta_s \approx 225 \mu\text{eV}$ is derived from the onset of current. Sub-gap features are visible resulting from JQP and DJQP charge cycles. Inset in the upper left shows the SET current's dependence on bias and gate potential, respectively. The double arrow marks the derived charging energy.

into quasi-particles so that finally the SET acts as a normal-conducting single-electron transistor, being dominated by Coulomb blockade. As previously discussed, also the island's charging energy can be derived from the dependence of SET current on the bias potential and gate voltage (inset in the upper left which shows the onset of quasi-particle

tunneling in the negative bias direction) and is estimated here to about $E_C \approx 150 \mu\text{eV}$ and accordingly $C_\Sigma^{\text{SET}} \approx 1 \text{ fF}$ (white double arrow in-between of both dashed lines). All measurements presented in the course of this thesis are performed in the regime of quasi-particle tunneling.

As previously discussed, also the SETs used here show features within the sub-gap region: Close to the borders, at $500 \mu\text{eV} \leq |eV_{\text{sd}}| \leq 800 \mu\text{eV}$ (see also the inset), peaks are clearly visible which are attributed to Josephson-Quasiparticle (JQP) tunneling [152, 157, 165]. Inserting the previously estimated device parameters into the threshold condition for the JQP cycle eq. (4.1), one obtains the onset of this cycle at $eV_{\text{sd}} = 525 \mu\text{eV}$ which agrees well with the range observed experimentally.

Additionally, the inset reveals another resonance feature of much smaller amplitude which is attributed to the DJQP. The observed peak position (about $150 - 200 \mu\text{eV}$, but slightly broadened) corresponds to the expectations of $\pm E_C$. However, the DJQP feature is rather small and additionally smeared out here, so that robust conclusions cannot be drawn. This broadening is most-likely caused by the elevated electron temperature in these measurements due to the large number of wires and the not yet optimized coupling to the cold plates.

4.3.2 Optimal working point of the SETs operated as charge detectors

As already mentioned above, the SETs are operated in the regime of quasi-particle tunneling, i.e. in the regime beyond the vertical dashed lines in Fig. 4.15 at $|eV_{\text{sd}}| \gtrsim 1 \text{ meV}$. The dependence of the SET current for the two detectors used in this thesis under variation of the respective local potential by the local gate for different bias potentials is shown in Fig. 4.16. From bottom to top, the bias potential is con-

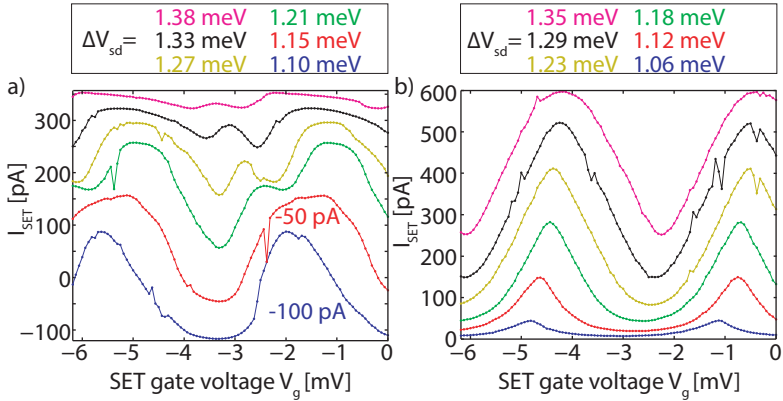


Figure 4.16:

Determination of SET's optimal working point for D1 (a) and D2 (b), respectively. The plots show the SET current modulation as a function of SET gate voltage for different SET working points set by the applied voltage difference between source and drain contact ΔV_{sd} . For D1, the lowest two traces are offset for clarity by -100 pA and -50 pA, respectively.

tinuously increased (colour-coded accordingly) and in Fig. 4.16a) the lower two traces are offset for clarity. The SETs can be used as charge detectors if this current modulation in response to changes in the local potential is large. Then, if sufficiently coupled to the object under investigation (which might be a single quantum dot or, as employed here, a mesoscopic, electrically isolated node), a change in the local potential of the SET (e.g. by an additional electron) is directly reflected by a change in the conductivity of the SET, equivalent to a change in the local gate voltage. Therefore, the response of the SET to an electron on the node to which it is capacitively coupled is determined by the slope of the SET at the actual current level. In conclusion, a steep change in current as a function of gate voltage is desirable.

The achievable modulation amplitude for detector D1 is $\Delta I \approx 200$ pA for the lowest three traces. In contrast, the response of detector D2 (Fig. 4.16b)) shows a modulation amplitude of $\Delta I \approx 370$ pA for the black trace (second from top), i.e. the modulation is almost two times as strong as for D1. The electrometers have been operated at roughly $V_{sd} = 1.1$ mV (D1) and $V_{sd} = 1.29$ mV (D2), respectively.

Also obvious is the periodicity of the response which equals about $\Delta V_g = 4$ mV for both SETs. The period reflects the change of the occupation number of the central SET island by one charge carrier. From the period observed one can derive the capacitive coupling of the SET's gate to the SET island, given by $C_g = e/\Delta V_g \approx 40$ aF, which is roughly 0.04 of the total SET's capacitance $C_{\Sigma}^{\text{SET}} = 1$ fF (as obtained from Fig. 4.15).

When operated as a charge detector, there is also a second requirement on the SET modulation as a function of the gate in addition to a steep response: This is the monotonicity for every half period (otherwise changes in the number of electrons to be monitored cannot reliably be detected) which excludes already the upper four traces for detector D1 (Fig. 4.16a)). One possible explanation of this additional resonance structure might be the coexistence of quasi-particle tunneling with JQP features above $eV_{sd} > 4\Delta_s$, as also reported in [156].

In conclusion, the working of all individual elements of the structure has been demonstrated. The parameter dependence of the dynamic quantum dots acting as single-electron source has been investigated. Moreover, the superconducting single-electron transistors have been characterized. These devices show a rich variety of features in the sub-gap region due to the (partially) coherent charge transfer resulting from the combination of quasi-particle plus Cooper-pair tunneling. However, the detectors are operated in the following only in the regime dominated by quasi-particle tunneling.



Chapter 5

Dynamic quantum dots investigated by charge detection

After the introduction of the device's components, the experimental techniques to characterize a non-adiabatic dynamic quantum dot using charge detectors are now described. Here, pulsed charge transfer and thereby continuous charging of a semiconducting node is presented, allowing to investigate several types of possible errors in such structures, like transfer errors, hold errors and detector noise.

Finally, the detailed investigation of the charge-transfer process (focusing on the charge capturing) using the counting data is presented and implications towards further optimization are described.

5.1 Non-invasive charge detection on the dynamic dot

After discussing the operation of individual building blocks of the device under investigation, this section covers the first measurement using a combination of several parts of the structure. Here, the continuous charging of a charge node, acting like a capacitor, by a dynamic quantum dot is shown. This experiment represents one of the simplest approaches to investigate the compound device and is therefore chosen as the most suitable introductory experiment. Additionally, the flexibility of the device, which is given by the possibility to switch each gate in the semiconducting part between conducting and insulating, may be demonstrated here.

This initial experiment should demonstrate three main aspects:

- We transfer an integer number of electrons unidirectionally by applying a single pulse to the entrance gate of the dynamic dot.
- We are able to resolve the outcome of the transfer process on the single-charge level using the single-electron detectors.
- We are able to hold the transferred electrons on the node.

The device configuration, used in this introductory paragraph, is shown in Fig. 5.1. The dynamic quantum dot used here is formed between the two left-most gates in the structure (coloured in yellow) and is indicated by the white oval. The dot is connected on the left hand side to the source lead acting as a reservoir of electrons, on the right hand side to the charge node, coloured in purple. This charge node is formed between the dynamic dot and the yellow-coloured gate labelled "barrier" on the right hand side of the structure. All other, uncoloured gates are grounded and therefore do not affect the circuit.

5.1 Non-invasive charge detection on the dynamic dot

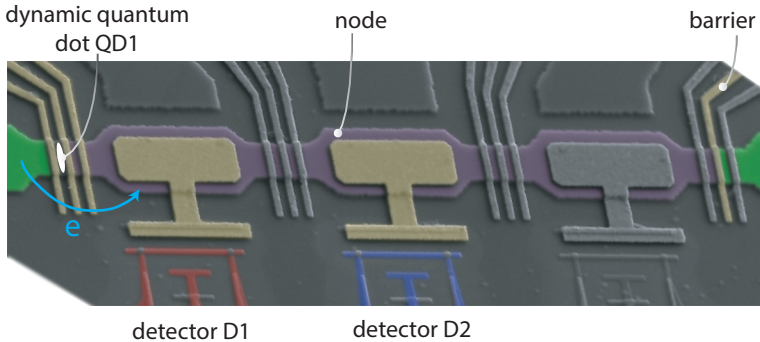


Figure 5.1:

Circuitry used for continuous node-charging. The left-most dynamic quantum dot (white oval with control gates coloured in yellow) is set to transfer approximately one electron per pulse from the source lead (green) to the large common node (purple) which is observed by detectors D1 (red) and D2 (blue) simultaneously. On the opposite side, the node is separated from the drain lead (green) by a static barrier formed by the second, dc-coupled control gate of the rightmost dot V_{G2}^{QD4} . Un-coloured gates are grounded and do not affect the 2DEG underneath.

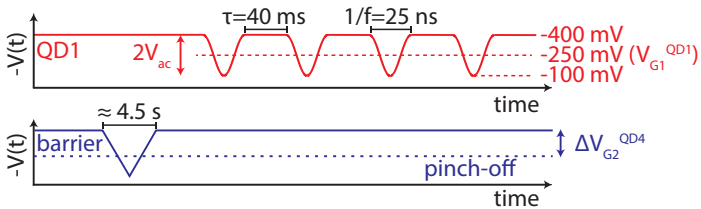


Figure 5.2:

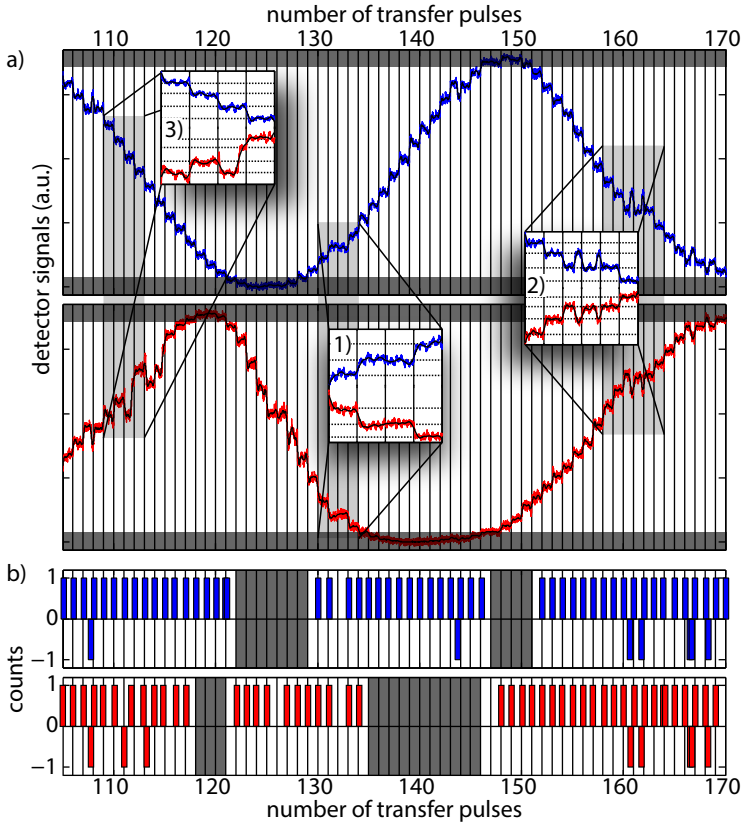
Gate-voltage patterns for continuous node charging on the entrance gate of the dynamic quantum dot (upper, red curve) and the static gate defining the charge node to the right (lower, blue curve). Curves are offset and independently scaled for clarity.

The direction of transferred electrons by the dynamic quantum dot is indicated by the cyan arrow with the symbol e and is given by the order of the ac-driven gate G1, called the "entrance gate", and the static dc gate G2 ("exit gate"), as explained in chapter 2.5. If the dynamic dot is suitably tuned by choosing proper voltages on the gates V_{G1}^{QD1} and V_{G2}^{QD1} , respectively, one should be able to transfer exactly one electron per pulse applied to the ac gate. Here, we apply the static voltages $V_{G1}^{QD1} = -250$ mV and $V_{G2}^{QD1} = -170$ mV. The pulse for transferring an electron is superimposed onto the static voltage at the entrance gate and consists of a single sinusoidal period phase-shifted by $\varphi = -\pi/2$ and of amplitude $V_{ac} = 150$ mV with the final value hold up to the next pulse. Doing so, we increase the barrier formed by the gate between two pulses to reduce the probability of unwanted tunneling events onto/from the node. In total, V_{G1}^{QD1} equals -400 mV between the pulses while the pinch-off voltage of this gate solely is about $V_{G1}^{QD1} = -210$ mV. Using this kind of superposition of dc voltage and pulse, the full charge-transfer process (see section 2.5.1) is completed within one pulse (i.e., highest equivalence between pulsed and continuous drive of the dynamic quantum dot) and the delay between pulses τ will not affect the transfer process. Therefore, we are able to choose the delay between two pulses τ arbitrarily and select a value much larger than the bandwidth of our detectors, i.e. $\tau \gg 1/\Gamma_d$, enabling us to resolve the outcome of each pump pulse with our detectors. As it will turn out, the value chosen for the exit gate voltage leads to about one electron on average being captured and transferred per cycle to the node. The dependence of the number of electrons captured on this control voltage will be discussed in more detail experimentally in the subsequent sections 5.1.3 and 5.2. Initially, we will operate the dynamic quantum dot at constant control parameters and will only change the height of the barrier. This allows to investigate the capability of our circuitry to hold electrons on the node as a function of the

barrier height.

The resulting pulse pattern on the entrance gate of the dynamic dot is shown in the upper trace (red line) in Fig. 5.2. After an initial waiting time a series of pulses, each delayed by $\tau = 40$ ms, is applied. Since we transfer electrons only unidirectionally, we thereby charge the node following the dynamic quantum dot and thus create an electrostatic potential acting oppositely to the transfer process, i.e. the higher the number of electrons on the node, the lower the probability of successful charge transfer. This effect is known as mesoscopic feedback and is discussed in sections 2.6.1 and 7 theoretically and experimentally. Additionally, also the signals applied to the gate forming the barrier on the opposite side of the node (blue line) is depicted in the graph: The barrier is energetically lowered below the pinch-off voltage to equilibrate the electrochemical potential of the node with the one of the drain lead and then raised again. Doing so, the initial conditions on the node are comparable at every repetition of the experiment. Afterwards, the digitizer is triggered to record the detector time-traces and the series of pulses onto the entrance gate of the dynamic dot is started. This scheme is repeated under variation of the height of the node's barrier to drain, controlled by V_{G2}^{QD4} . The formation of a barrier sets in if the applied voltage exceeds the pinch-off voltage (which in turn depends on the local potentials and might be affected by the conditions of cooling the sample [137]). Therefore, the barrier height will be given in the following as ΔV_{G2}^{QD4} which is the excess voltage beyond pinch-off as shown in Fig. 5.2.

In Fig. 5.3a) a section of the resulting detector time-traces is shown with the x-axis rescaled in order to match with the timing of pulses. The upper panel reflects the detector labelled D2, the lower one the detector D1. Each vertical black line corresponds to a transfer pulse. Since none of the intermediate gates across the semiconducting channel is used, both detectors are coupled to the same node and therefore should


Figure 5.3:

Evaluation of continuous node-charging by the dynamic quantum dot QD1, tuned to operate at approximately $1e.f_p$. The right barrier of the node is formed by QD4's exit gate, thus both detectors D1 and D2 couple to the same node. a) Resulting detector signals for detector D1 (lower panel, red) and D2 (upper panel, blue). Each transfer pulse is indicated by a vertical black line. The grey-shaded areas at the top and bottom of each panel mark insensitive regions. The insets illustrate 1) a missing cycle event, 2) two subsequent hold errors, i.e. electrons leaking from the node through the barriers to source or drain, respectively, and 3) a detector error of D1 caused by a charge trap nearby. b) Evaluated counting signals derived from a).

observe the same signal. One clearly observes the discrete change in detector current in response to the change in the node's electrochemical potential due to the addition of electrons (in case of successful charge transfer). Between the pulses, the detector signals typically remain constant. Moreover, also the periodic response function of the SETs during the continuous charging of the node is maintained as well, being comparable to the traces shown in Fig. 4.16.

This is the signature of single-charge transfer by the pulsed dynamic quantum dot and, since one clearly observes the steps in the SET signal, also of single-charge resolution of the detectors. Since the detector response is periodic, the response to an extra electron is a function of the actual working point of the SET: The largest step is found at the vertical center while the response vanishes at the extrema of the SET signal. To account for this, we omit the upper and lower 6% of the response in the following analysis because the response cannot be evaluated with high significance. This is symbolized by the dark-grey areas at the top and the bottom of each panel.

With respect to the time-scales of the measurement, the transfer of an electron onto the node represents an instantaneous change in the potential of the SET. Therefore, the analysis of the SET's response in time to such an event gives a proper estimate of the bandwidth of our detectors. In the limit of infinite bandwidth, the response would immediately follow the local potential in a step-like fashion. However, a finite bandwidth causes an exponential convergence to the final value on a characteristic time-scale. Taking the time interval corresponding to a response in the interval of 10%-90% of the final signal (equal to about $\tau_{10 \rightarrow 90} = 1.5$ ms) and defining the bandwidth as the inverse of this time-scale, we obtain $\Gamma_d \approx 1/\tau_{10 \rightarrow 90} \approx 600$ Hz.

Finally, not only the amplitude of the detector's response varies as a function of the point of operation, but also the direction of the response changes over one period. However, since the dynamic quan-

tum dot is comparably robust against a bias voltage on drain (i.e., the node), we are able to distinguish between surplus and missing electrons by taking the direction of the jump following a transfer pulse as a reference. For example, detector D2 (blue) falls between pulses 105 and 125 steadily with every additional pulse (transferred electron), i.e. we are on the falling edge. Between pulses 125 and 148, any additional electron transferred by the dynamic dot leads to a positive response (rising edge).

The insets in Fig. 5.3 explain three scenarios that will be investigated in the evaluation of the time-traces. For illustrative purposes, the levels occupied by the detectors are indicated as dashed horizontal lines.

Firstly, in order to address the question how precisely the dynamic quantum dot transfers electrons onto the node, the inset 1) clarifies what is called a "missing cycle" event, i.e. a pulse at which no electron has been transferred. This is reflected here by constant detector signals of D1 and D2 before and after the pulse in question. Therefore, a measurement scheme like the continuous charging allows to determine the transfer fidelity, i.e. the ratio of successful charge transfer events to the total number of transfer pulses onto the gate. Moreover, one could also evaluate the height of the detector response in order to extract errors in which more than one electron has been transferred. Initially, however, we will limit the number of charge carriers transferred per cycle to in maximum one by proper tuning of the dynamic quantum dot.

Additionally, electrons might leave the node unintentionally, either via the dynamic dot to the source, or via the barrier to drain. The signature of these so-called "hold errors" is shown in inset 2): After the second and third successful transfer pulse, respectively, the detector states both change to indicate an additional electron on the node. But, they do not remain constant until the next pulse and switch back to the previously occupied state instead. The "hold errors" are based on the quantum mechanical effect of tunneling which is of stochastic nature.

This can be seen directly in the inset: The life-time of the electron on the node until it leaves to one of the leads is not deterministic and also, after these two subsequent hold errors, the node may be further charged with additional electrons. However, the probability of hold errors rises with the number of electrons stored on the node (equivalent to a smaller effective barrier).

Finally, also so-called "detector errors" may be distinguished in this device configuration. As explained above, both detectors observe the same node and should yield the same results: The inset 3) shows a monotonously falling detector D2 indicating successful charge transfer by the dynamic dot onto the node remaining in the same state in-between, i.e. no hold errors. However, detector D1 switches shortly after the second pulse to a state indicating a lower electron number on the node and, before the next pulse, back to the state expected for successful charge transfer. This is most-probably the signature of a local two-level charge trap (potentially inside the oxide barrier of the single-electron transistor itself) which couples asymmetrically to both detectors. Thus, by using more than one detector per island, one can eliminate this type of error by performing correlation measurements.

Fig. 5.3b) contains the evaluated counts derived from the time-trace in a) using the algorithm described in the next section, the upper panel (blue bars) corresponds to detector D2, the lower one (red bars) to detector D1. Each bar with positive value indicates a surplus electron on the charge node, while bars with negative value resemble electrons lost from the node. In contrast to usual counting experiments on quantum dots, the counting signal corresponding to additional electrons on the node is very regular, since the addition of electrons is clocked by the pulses applied to the dynamic dot. The "missing cycle" event at pulse 132 (see also inset 1)) is characterized by a lacking bar in both detector counting traces, because no electron has been transferred to the node during this cycle. Also the two subsequent "hold errors" (be-

fore pulses 161 and 162 and in inset 2)) appear in the counting signals of both detectors (another one may be found between pulses 107 and 108). Oppositely, "detector errors" appear only in the counting signal of detector D1 (between pulses 111-112 (inset 3)) and 113-115, respectively).

Besides the correlation measurements for enhanced detection accuracy, the coupling of several detectors to the same island has another advantage that can be directly seen in Fig. 5.3b): The counting signal of each detector is interrupted by regions of insensitivity (coloured in dark grey in the counting signal) whenever the detector's working point is close to one of the extrema. But the relative phase between the two detectors may be adjusted such that one of them always remains sensitive as shown in the figure. This may be accomplished by applying a small voltage signal to the tuning gate of one of the detectors. Doing so, the counting measurements on the node may be performed quasi-continuously using e.g. detector D2 extended by D1 in case of D2 being insensitive. This concept can be regarded as an alternative to applying active feedback to the SET (stabilizing it on a sensitive working point using the SET's gate in a feedback loop). Here, the measurement system is kept simple but, on the other hand, higher demands on the device fabrication are added, e.g. in terms of yield or reproducibility.

5.1.1 Data analysis

In this section, I would like to point out the more general aspects of the analysis of the counting signals and give an illustrative description of the algorithm to derive the counts shown in Fig. 5.3b). This is done exemplarily for the trace plotted in Fig. 5.4a) of detector D2.

After loading files describing the measurement conditions and extracting parameters like, e.g., the pulse pattern, delays between pulses or the number of repetitions, we first search generally for changes in the

SET time traces indicating changes in the node's potential, separately for both detectors D1 and D2. To this end, we use the derivative of the detectors' time-traces, apply a second-order Savitzky-Golay filter [166] whose smoothing window corresponds to about 20 ms (roughly half of the delay between consecutive pulses). Peak-finding is then performed, i.e. we search for local maxima of the derivative within an interval of a quarter of the smoothing window (about 5 ms). The function finally returns the positions and the values (peak-height) of the extrema found. The result is indicated in Fig. 5.4b) by the red squares.

Afterwards, the time traces are split into intervals, interrupted by insensitivities of the detectors at which the current through the SET is extremal, i.e. where it falls into the light grey bands already illustrated in Fig. 5.4a) at the top and bottom of the graph. To determine whether the SET operates on the rising or falling edge in-between, we take profit of our knowledge about timing and unidirectionality of single-electron transfer by the dynamic quantum dot. Maxima found in a certain time interval around the expected pulse (dominated by the finite bandwidth of the detector and the additional broadening due to the smoothing filter) are most likely the signature of an additional electron on the node. Since the response cannot switch between rising or falling edge without passing a minimum or maximum, all measurements between two regions of insensitivity belong to the same rising or falling edge. Therefore, the slope is given by the sign of the dominating extrema found close to the transfer pulses. In the illustration in Fig. 5.4b), we can conclude from these considerations that the SET operates in the time intervals 50-60 and 83-103 on the rising edge while in the other two intervals 60-83 and 103-120 the falling edge is occupied as sketched in Fig.5.4c). To simplify the consecutive analysis, the peak values found are finally multiplied by the appropriate slope such that peaks corresponding to an addition of electrons on the node have positive sign and vice versa.

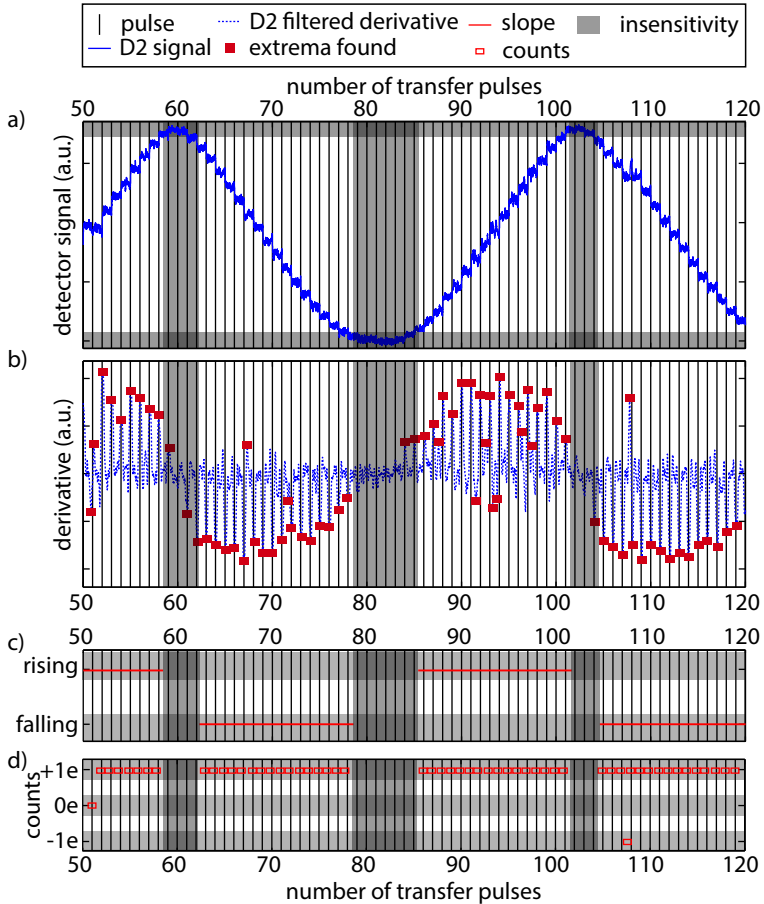

Figure 5.4:

Illustration of evaluation of continuous node-charging. a) The raw detector signal for D2 as a series of transfer pulses is applied to QD1. b) Smoothed derivative and derived maxima (without further processing). c) Extraction of slope and sensitivity of the detector from the signature of change in SET current in response to the transfer of an electron onto the node. d) Final counting analysis indicating successful charge transfer, transfer errors and hold errors.

Next, the decision is made whether a peak is regarded as the signature of a change in the number of electrons on the node. To this end each peak height is compared to the average of the adjacent maxima resulting from electron transfer onto the node (identified by their timing). The result of this analysis is shown in Fig. 5.4d). The comparison of the resulting counts with the extrema shown in b) evidences the working of the algorithm: As an example, the first two extrema found are identified as noise, yielding a transfer error signature (zero counts at this pulse). The same result is obtained for the maximum after transfer pulse 67 as well as in the interval 83-103 for the three peaks with opposite sign compared to the signature of transferred electrons.

In contrast, the extremum at around pulse 108 is indeed classified as a hold error due to the comparable amplitude of the response in agreement with the raw data in a): Just before the next pulse, the detector switches back to the previous state (the number of carriers on the node is reduced by one as a consequence of a hold error) and then, after the pulse and a successful charge transfer (increasing the number of carriers on the node again), occupies the same state again.

Finally, statistical analysis can be performed based on the counting data, in which initially the counts are classified according to their occurrence in time and their sign (indicating a surplus or missing electron). As discussed above, additional electrons at points in time close to the transfer pulse are regarded as successful transfer events. If the signature is missing, a transfer error is assumed (e.g., as happened at pulse 51 of the illustration in Fig. 5.4). Negative counts are always regarded as hold errors, i.e. interpreted as electrons tunneling off the island.

5.1.2 Results

The first question to address in this analysis is how well the dynamic dot operates in pulsed mode. The answer comprises of two aspects:

First, are we able to control the transfer of single electrons in time? And second, what is the transfer fidelity given as the ratio of successful transfer counts and the total number of pulses applied?

Transfer fidelity of the dynamic quantum dot

Aspect one is addressed in Fig. 5.5a) presenting the deviation of an observed transfer event from the timing of the transfer pulse. The pulsed transfer works as expected, showing a narrow distribution in time around the center pulse. To obtain quantitative results, a gaussian distribution (orange line) is optimized to fit the data, yielding a delay in time by 1.5 ms due to the finite detector bandwidth and a width (2σ) of about ± 4 ms which is well within the filter window of the Savitzky-Golay smoothing filter (about 5 ms), used in the analysis of the peaks. Only a few counts are found outside the interval $[-10, 10]$ ms which are most-likely related to erroneous counts. Therefore, one can conclude that the pulsed operation of the dynamic quantum dot allows precise control of electron transfer in time.

The dynamic dot's transfer fidelity is analysed here only as a function of the number of electrons stored on the node with fixed point of operation set by V_{G2}^{QD1} . The node's capability of holding electrons in turn depends on the effective height ΔV_{G2}^{QD4} of the right barrier to the drain lead (given as the difference of applied voltage to pinch-off voltage) which is depicted as a function of filenumber in the bottom of Fig. 5.5b). The analysis is interrupted after the observation of the fifth hold-error which might appear arbitrarily at this point but will be justified hereafter. Counting data is obtained from the signal of D2 which is extended by D1 whenever the former is insensitive. The evaluation (shown in Fig. 5.5b)) where red corresponds to successful transfer, black to missing cycle errors and grey to insensitivity or the end of the analysis, yields a transfer fidelity of $P_1 = 0.915\%$ (9749 events in total). Additionally, no significant increase with increasing

5.1 Non-invasive charge detection on the dynamic dot

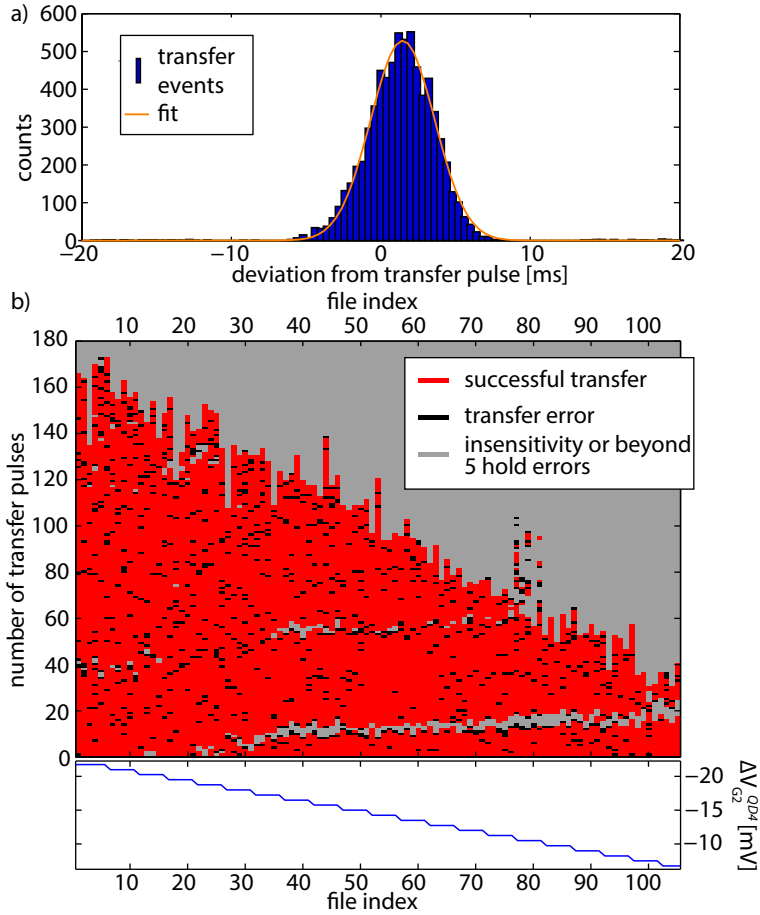


Figure 5.5:

Transfer fidelity of the dynamic quantum dot QD1 for combined detectors. a) Timing analysis: Delay of transfer events detected on the node from the applied transfer pulses (blue bars). A gaussian fit (orange line) is superimposed. b) Map of successful charge transfer (red) and transfer errors (missed cycles, black). Grey points mark insensitivities (both detectors are at their respective extremas) or the end of evaluation after the fifth hold error. Effective barrier height at the bottom panel.

number of electrons on the node is observed.

Analysis of hold errors and barrier characterisation

As the next aspect in the analysis, the occurrence of hold-errors is addressed. To investigate the most-likely source of leakage and to justify the choice of five hold-errors in the previous evaluation, the occurrence of hold-errors as a function of the number of pulses as well as the height of the barrier to drain is investigated. The data is taken here from detector D2 only in order to avoid false-counts related to detector errors in D1 caused by fluctuating charge traps. First, to emphasize the stochastic nature of this leakage, the timing of hold-errors, given relative to the preceding transfer pulse, is shown in Fig. 5.6a) as a histogram (red bars). Additionally, the distribution of transfer events in time is superimposed. The transfer events define a window for the observation of hold errors, since the addition by successful charge transfer and the - within the bandwidth of the detectors - simultaneous removal of an electron due to leakage exactly cancel each other, leading to the signature of a missing cycle event (the node's charge state remains constant). Only if the charge transfer fails, a hold-error can be detected around the timing of a transfer pulse (i.e., with a probability of $1 - P_1 = 0.085$) leading to the observed reduction of counts in this interval.

We account for the random occurrence of hold errors by repeating the pulse sequence for each effective barrier height ΔV_{G2}^{QD4} , defined as the excess voltage beyond pinch-off, for five times (left-most data point: six times), as depicted at the bottom of Fig. 5.6b). The resulting, cumulative occurrence of hold errors as a function of both, the number of transfer pulses (proportional to the number of electrons stored on the node) and the file index (equivalent drain barrier height), is shown in Fig. 5.6b). Colour codes the number of cumulative hold errors for each pulse sequence, ranging from dark blue (zero hold errors) to dark red (eight hold errors). White regions mark either insensitivities of the SET

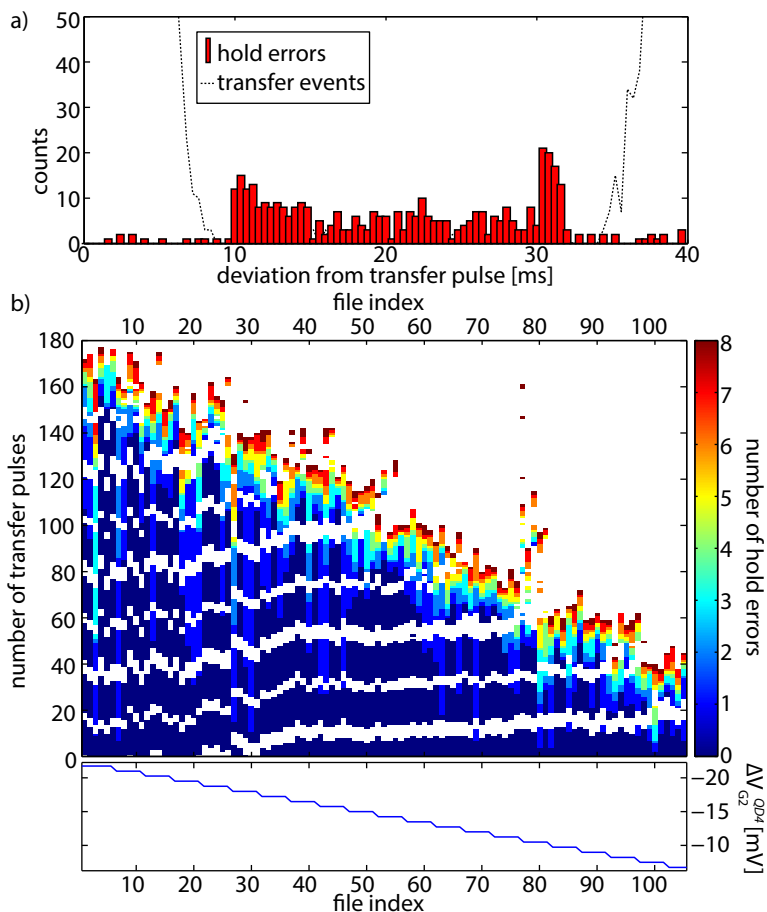


Figure 5.6:

Analysis of hold errors. a) Occurrence of hold errors in time, relative to the previous transfer pulse. The dashed line marks the distribution of transfer events. b) Evolution of hold errors with the number of transfer pulses for detector D2 only. Colour codes the number of hold errors detected so far. The x-axis corresponds to the number of measurement and thereby is related to the barrier height (plotted at the bottom panel). White areas correspond to insensitivity or the excess of eight hold errors.

(only detector D2 is analysed) or the end of analysis for the specific pulse sequence (after the eighth hold error). The effective barrier is reduced from left to right as displayed in the bottom panel and, as clearly evident from the colour plot, thereby the number of electrons which can be stored on the node also decreases. Apparently, there is a certain threshold in the number of electrons that can be safely stored on the node for a given barrier height while in excess of this value the probability of hold errors drastically increases.

In order to quantify the number of electrons that can be stored on the node as a function of effective barrier voltage $\Delta V_{G2}^{QD^4}$, we have extracted from Fig. 5.6 the pulse index at which the fifth hold error was detected. Then, by counting the number of electrons transferred until this point from Fig. 5.5, we obtain the number of electrons stored on the node for each repetition of the continuous-charging experiment. The result is plotted versus $\Delta V_{G2}^{QD^4}$ in Fig. 5.7 as blue dots together with a linear fit (orange line).

As expected, the data clearly suggests that the capability of the node to store electrons indeed depends strongly on the barrier formed by the voltage applied to the barrier gate. The linear dependence, even to relatively high numbers of electrons stored on the node, is a clear indication that the initial assumption of leakage across the drain barrier is valid. Additionally, this result suggests that the dynamic quantum dot is robust against leakage. Otherwise, a deviation from this linear dependence for large numbers of electrons on the node is expected. From the fitted slope $\alpha_V = -7.3 \text{ mV}^{-1}$, one can extract the factor $\alpha_{V \rightarrow E}$ which converts the applied effective gate voltage $\Delta V_{G2}^{QD^4}$ into an energy height of the barrier when considering additionally the charging energy of the node (derived to about $E_C \approx 30 \text{ } \mu\text{eV}$):

$$\alpha_{V \rightarrow E} = E_C \alpha_V, \quad (5.1)$$

yielding $\alpha_{V \rightarrow E} \approx 0.22 \text{ meV/mV}$.

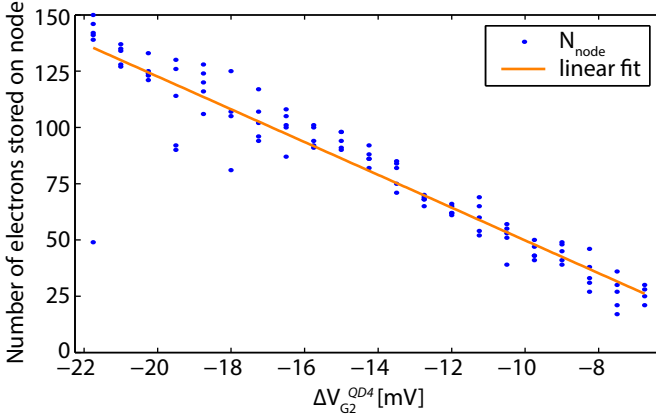


Figure 5.7:

Number of electrons stored on the node (blue dots) when the fifth hold error is detected, plotted as a function of the effective barrier height. A linear fit $N_{\text{node}}(\Delta V_{\text{G2}}^{\text{QD4}}) = \alpha_V \cdot (\Delta V_{\text{G2}}^{\text{QD4}} + V_0)$ is indicated by the orange line with fitting parameters $\alpha_V = -7.3 \text{ mV}^{-1}$, $V_0 = 3.2 \text{ mV}$.

Moreover, the offset voltage V_0 obtained from the fit yields an insulating barrier only for $\Delta V_{\text{G2}}^{\text{QD4}} \lesssim -3 \text{ mV}$ for the limit $N_{\text{node}} = 0$ electrons stored on the node, indicating that tunneling of electrons via this barrier is suppressed just 3 mV beyond the pinch-off voltage. Naively, one might expect $V_0 = 0$, i.e. the voltage corresponding to pinch-off of the underlying channel equals the beginning ability of the node to hold electrons. However, regarding the uncertainties in the fit parameters and the rather rough estimation of the pinch-off voltage the agreement is quite well. Additionally, these two values are obtained under differing measurement conditions: The pinch-off voltage was defined as the gate voltage at which the current is lower than 100 fA (which corresponds to about 600,000 electrons per second) while in the pulsed measurement the hold-capability of the node is

analysed for times larger than the pulse delay of $\tau = 40$ ms (i.e. less than 25 electrons per second). Finally, there is an intrinsic effect in the charge transfer mechanism which should enable tunneling already for voltages with $\Delta V_{G2}^{QD4} < 0$: Electrons are emitted at rather high energies (of the order of 60 meV in [51]) and therefore, after emission, a cascade of electron-electron scattering events sets in (being the dominant scattering effect at low temperatures without a magnetic field), distributing the excess energy among the electrons on the node. The efficiency of this process depends strongly on the energy of the participants and reduces dramatically for low energies of a few meV [167], thereby leading to a high probability of electrons being able to tunnel already before reaching the pinch-off limit due to this excess energy. Since the coupling to the phonon bath is rather weak at low temperatures, this continuous emission of electrons with such an excess energy leads to an effective increase in temperature of the electrons stored on the node and thereby to an enhanced probability of tunneling.

Enhancement of detection efficiency using two detectors

Comparing the two two-dimensional plots Fig. 5.5 and Fig. 5.6, one can already directly see the enhanced detection efficiency in the former plot due to the extension of detector D2 by D1 in case of insensitivity. More quantitatively, the detection efficiency, defined here as the fraction of observations in the sensitive range is only 0.637 for detector D1 and 0.762 for detector D2, respectively. The extension of D2 by the counting signal of D1 in case of insensitivity leads to an average coverage of 0.948 with only a single adjustment of the relative phase between the two detectors prior to the start of the measurement. This evaluation is shown in plot 5.8 as a function of barrier gate voltage with the average values indicated by the arrows at the left axis. Red bars correspond to D1, blue ones to D2 and the combination of both is represented by green bars.

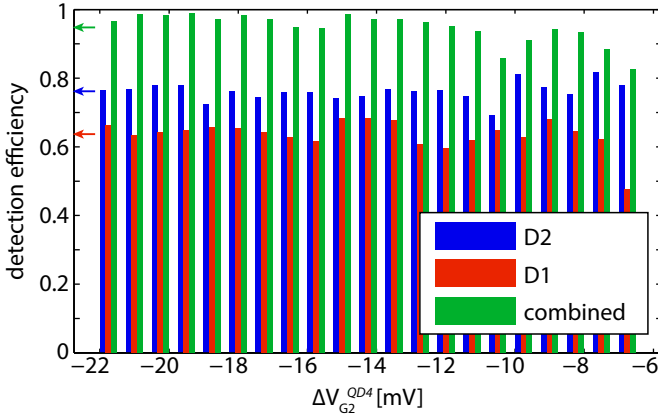


Figure 5.8:

Detection efficiency for individual detectors (D1: red, D2: blue) and the combination of both (green). The mean detection efficiencies of 0.637 (D1), 0.762 (D2) and 0.948 (combination) are indicated by the arrows.

Summary

In summary, we have shown the ability of controlled charge transfer by a pulsed dynamic quantum dot on the level of single electrons. Moreover, the node is capable of holding even large numbers of electrons (more than 150) for sufficiently long time scales provided the electrostatically defined barriers are raised adequately. The combination of several detectors observing the same node can be either used to enhance the dynamic range of detection (by applying an appropriate phase-shift between the detectors) or to increase the fidelity of counting by allowing to distinguish between electron signals and local charge fluctuations in correlation measurements.

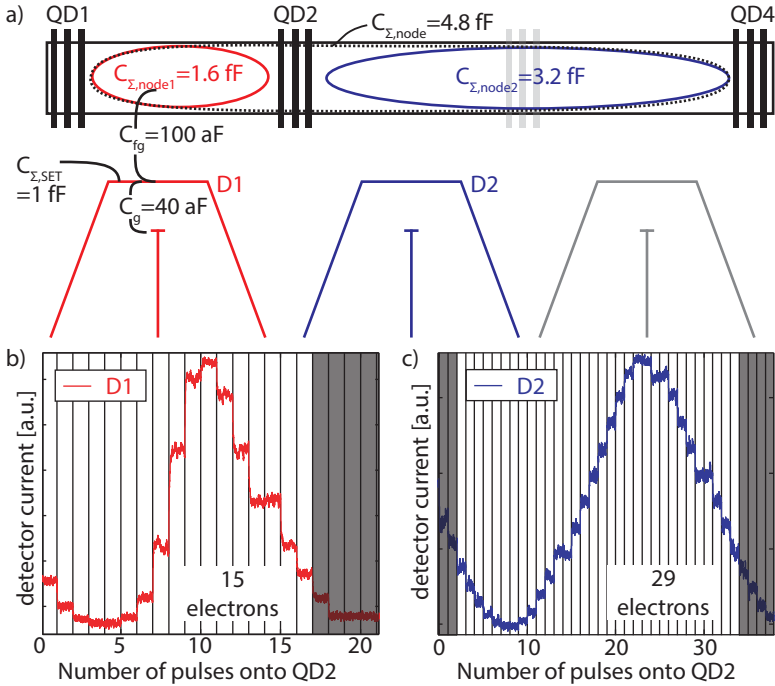
5.1.3 Continuous charging experiments beyond barrier characterization

Besides the previously presented results mainly concentrating on the action of the barrier, there are some other device characteristics which may be deduced from the analysis of continuously charging the node by the dynamic quantum dot.

Analysis of coupling capacitances

In previous sections, we have already derived the intrinsic capacitances of the individual elements, as depicted in the sketch in Fig. 5.9. Due to the single-charge resolution of the detector and the ability of the dynamic quantum dot to transfer a large number of electrons onto the node, we are able to investigate the coupling capacitance C_{fg} of electrons on the node via the floating gate to the corresponding SET. The potential formed by an electron on the node depends on the node's size, which again is tunable by the top-gates forming the dynamic quantum dots. For the smallest node, node 1 between QD1 and QD2, we had already experimentally estimated in direct transport measurements (see section 4.1.3) a capacitance of $C_{\Sigma}^{\text{node1}} = e^2/E_C \approx 1.6$ fF. Geometric arguments lead to capacitances $C_{\Sigma}^{\text{node2}} \approx 3.2$ fF for the node 2 between QD2 and QD4 (twice as large as node 1) as well as $C_{\Sigma}^{\text{node}} \approx 4.8$ fF for the largest node possible between QD1 and QD4 with QD2 grounded (three times as large as node 1), as depicted in Fig. 5.9.

With a coupling capacitance C_{fg} between the node and the corresponding detector (expected to be equal for both SETs due to the same geometry of the floating gate), the influence of an electron on the semiconducting node onto the electrochemical potential of the SET is given by $e^2/C_{\Sigma}^{\text{node}} \cdot C_{\text{fg}}/C_{\Sigma}^{\text{SET}}$. Therefore, the SET response (change in SET current or, equivalent, SET period) should scale inversely with the capacitance of the node.


Figure 5.9:

Analysis of coupling capacitances. a) Schematic of the device and depiction of parameters discussed in the main text. The capacitance of the semiconducting nodes can be tuned by top-gates. b) and c) SET response when operating QD2 to transfer electrons from node 1 to node 2 in order to obtain the SET response to the change in the nodes' potential (two independent measurements for D1 (b) and D2 (c), respectively).

For the largest node with capacitance C_{Σ}^{node} between QD1 and QD4, we previously obtained a SET period (change in the occupation of the SET island by one electron) in terms of electrons on the node of 42 (see, e.g., Fig. 5.4) which corresponds to a potential of the node of

about 1.3 meV. The geometric approximation of the node's charging energy is confirmed by operating QD2 as a dynamic dot, dividing the large node into the smaller nodes 1 and 2, each separated from the leads by potentials induced to QD1 and QD4 top-gates, respectively. In this configuration, we obtain a SET period of 15 electrons on node 1 and 29 electrons on node 2 as shown in Fig. 5.9b) and c), respectively. Because the potential U caused by the additional electrons on the node is absolutely known ($U = N_{\text{node}}e^2/C_{\Sigma}^{\text{node}}$ with N_{node} the number of electrons on the node), we directly obtain also the cross-capacitance $C_{\text{fg}} = e^2/U = 100$ aF.

This number is of reasonable order of magnitude, being equivalent to about 10% of the SET's overall capacitance C_{Σ}^{SET} (as derived in section 4.3), given as the sum of all capacitances $C_{\Sigma}^{\text{SET}} = C_{\text{fg}} + C_g + C_s + C_d$ with C_s, C_d the capacitances attributed to the oxide tunneling barriers to source and drain lead, respectively. Typically, the latter two capacitances are the dominating contributors to the overall capacitance, making it favourable to reduce the junction size in order to obtain a lower capacitance and thereby higher charging energies. Concerning structures coupled with floating gates, even higher relative coupling (up to 38%) has been demonstrated in an experiment in which two coupled quantum dots in an all-etched semiconducting system have been investigated [134]. Compared to the local gate capacitance $C_g = 40$ aF which is placed at about the same distance to the SET island, the capacitive coupling is more than twice as large, potentially due to difference in shape.

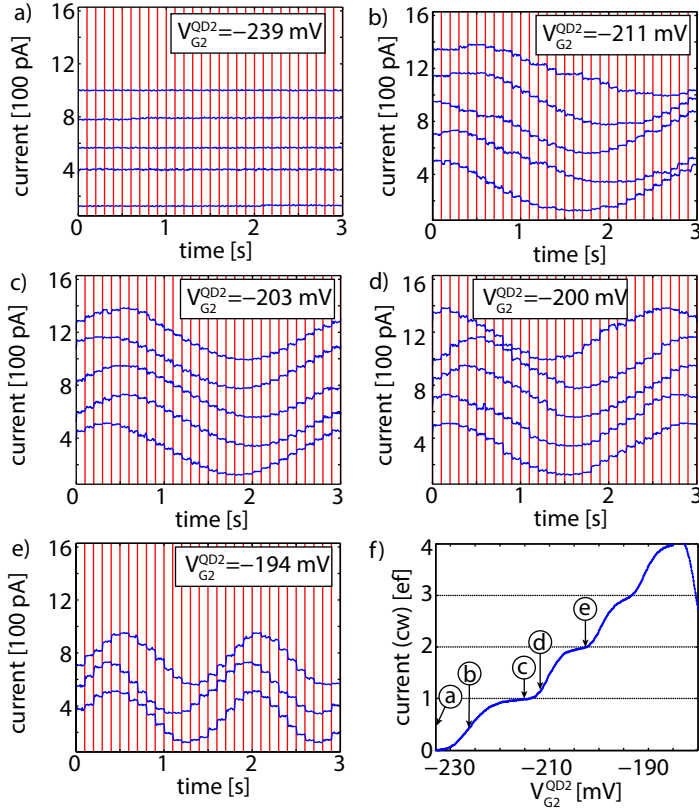
Changing the number of transferred electrons per cycle

Until now, the point of operation has been fixed such that in maximum one electron has been transferred per cycle. Here, the modification of the working point by variation of the exit gate voltage, analysed

by electron counting, is introduced. QD2 is used as clocked electron source to transfer electrons from an open reservoir (QD1 grounded) onto the charge node 2 (secluded by applying a large, negative voltage onto the second gate of QD4). Only detector D2 is strongly coupled to this node. The outcome of this experiment is shown in Fig. 5.10.

At the bottom right (panel f)), the direct-current characterization (with continuous rf drive) of the gate dependence is shown as a reference. Comparing absolute gate voltages in both measurements, we observe characteristic features in the pulsed experiment at slightly more positive control gate voltages. This is a hint for the nominally static gate being also modulated slightly by the cw signal due to cross-coupling which needs to be compensated for in the cw measurement by applying more negative gate voltages. However, the points with equal average number of transferred electrons per cycle as in the panels a)-e) are labelled accordingly. Each panel contains up to five repetitions of the same measurement conditions with the individual traces offset for clarity.

If the control gate voltage V_{G2}^{QD2} is tuned very negatively, electron transfer is completely blocked and the detector signal remains constant before and after the application of pulses onto the dynamic dot (a). Panel (b) corresponds to the transition to the first plateau where on average $\langle n_e \rangle \approx 0.5$ electrons per cycle have been transferred (same evaluation as shown later at the preliminary analysis of fast triple transfer in Fig. 7.10). When the control gate voltage is tuned more positive, almost perfect single-charge transfer is obtained (c). Restricted to the sensitive regions of the SET, no transfer error is monitored, i.e. the dynamic quantum dot is operated on the $n_e = 1$ plateau. At panel (d), however, the transfer probability of $n_e = 2$ electrons per cycle becomes significant. This is reflected in the SET traces by partly doubling the response which yields on average $\langle n_e \rangle = 1.1$ transferred electrons per cycle. Finally, at point e), the dynamic quantum dot is operated


Figure 5.10:

Detector responses to continuous loading by QD2 from an open source reservoir at different exit gate voltages V_{G2}^{QD2} representing the transfer of $n_e = 0$ (a), $n_e \approx 0.5$ (b), $n_e \approx 1$ (c), $n_e \approx 1.1$ (d) and $n_e \approx 2$ (e). Additionally, the cw measurement is shown indicating the equivalent working points set by the control gate voltages in (a)-(e). The x-axis is shifted towards more negative voltages, possibly due to cross-coupling of the cw signal onto the static control gate voltage. All traces in one graph are repetitions of the same measurement conditions and are vertically offset each for clarity.

5.2 Microscopic insight into dynamics of single-electron capture

on the $n_e = 2$ -plateau which is found at a gate-voltage distance to the first plateau of about 9 mV (comparable to the distance obtained by the cw measurement shown in panel (f)). The doubling in the number of transferred carriers is most-easily seen by comparing the number of periods of the time-traces corresponding to single- (c) and double- (e) charge transfer, respectively.

In conclusion, the control over the number of electrons transferred by the dynamic quantum dot in pulsed mode has been demonstrated, verified by single-charge detection. Moreover, the gate-dependence of transfer probabilities is found to agree with the behaviour expected from cw measurements (please compare to the contradictory results at the end of chapter 5.2). However, a well-founded quantitative analysis is hard to accomplish with this measurement scheme, due to possible back-action of the accumulated potential onto the dynamic quantum dot and, if strongly charged, the chance of occurrence of hold errors (see, e.g., uppermost traces in panel (c) and (d)).

5.2 Microscopic insight into dynamics of single-electron capture

After the introductory discussion of the functioning of the single-electron circuitry, in this section the qualitative and quantitative characterisation of the dynamic quantum dot by single-electron counting is presented. The parameter dependence will be first restricted to the exit gate voltage, similarly to the preceding analysis (presented in Fig. 5.10). To minimize the interaction of the electrostatic potential built up by the charge carriers stored on the node with the dynamic quantum dot, a specific pulse scheme is used, as discussed right after the basic measurement depiction. This enables us to study the interplay of individual transfer probabilities for different occupation numbers n of the dy-

dynamic dot quantitatively and with reduced uncertainty as compared to the previous experiment.

The active elements are depicted in Fig. 5.11a) and highlighted by colors: The dynamic quantum dot under investigation is QD1, formed by static voltages applied to the entrance and exit gate (labelled V_{G1}^{QD1} and V_{G2}^{QD1} , respectively). The direction of charge transfer is from the source lead onto the node (left to right in this image), given by the order of driven (entrance) and static (exit) gate. All signals applied to the entrance gate will remain fixed, unless mentioned: The static offset is set to $V_{G1}^{QD1} = -250$ mV, the waveform superimposed to enable pulsed single-charge transfer equals the one of previous measurements with $f_p \approx 39$ MHz, $V_{ac} = 150$ mV and containing only a single shifted cosine-shaped period which is held at the minimum voltage (i.e., highest barrier possible) to enhance the capability of the pump to localize electrons on the node. To define the node on the opposite side, we use a single gate of QD4 to form a barrier. Up to this point, the measurement conditions equal those from section 5.1.

But, instead of using the dc-coupled exit gate of QD4 as done previously, we employ the QD4's entrance gate allowing also a pulsed drain barrier. The waveform is equal to the one applied to QD1, the static offset is slightly smaller ($V_{G1}^{QD4} = -240$ mV), but there is another - more important - difference in the action of this barrier compared to the working of QD1: The following exit gate is grounded, i.e. $V_{G2}^{QD4} = 0$ mV. This changes the effect of a pulse applied to V_{G1}^{QD4} completely: Charge transfer is not suppressed any more across QD4 whenever the barrier is below pinch-off, thus leading to an equilibration of potentials on the node and the drain lead. Additionally, this process is expected to happen stochastically, i.e. the direction as well as the number of transferred electrons will be randomly distributed around an equilibrium value given by the difference in electrochemical potentials μ_{node} of the node and μ_d of the drain lead.

5.2 Microscopic insight into dynamics of single-electron capture

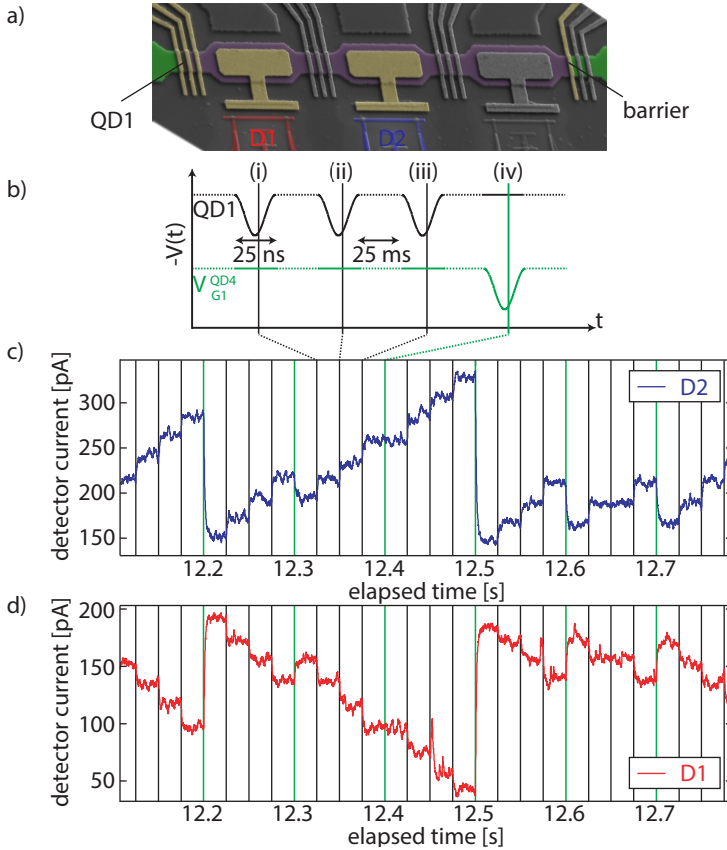


Figure 5.11:

Setup and raw detector signals at pulsed electron transfer with intermediate reset. a) SEM image of the device with active elements colored. b) Pulse sequence showing the three transfer pulses (black) applied to QD1 (while the barrier is held high) and the subsequent reset pulse (lowering the barrier shortly). Pulses are delayed each by $\tau = 25\text{ ms}$. c) and d) detector current signals for single-electron transfer ($V_{G2}^{QD1} = -197.5\text{ mV}$) for detectors D2 (c, blue trace) and D1 (d, red trace), respectively.

To enable a continuous measurement without the limitations discussed in the previous section, we apply the following pulse sequence to the device (see Fig. 5.11b): First, the dynamic quantum dot is triggered three times (upper, black line) to transfer an integer number of electrons onto the node during each pulse, followed by a subsequent reset of the node's charge state using a pulse applied to the barrier gate (green line). Each pulse lasts about 25 ns, the delay between pulses is chosen to $\tau = 25$ ms. Together with the superimposed shifted cosine pulse, the applied voltage of the barrier equals $V_{G1}^{QD4} - V_{ac} = -390$ mV (thereby strongly exceeding the pinch-off threshold) and is reduced only during the pulse to $V_{G1}^{QD4} + V_{ac} = -90$ mV which is in the conducting regime below pinch-off.

The result is a step-like change of the node's charge at every pulse while remaining constant in-between as shown in Fig. 5.11c) and d) for both detectors D2 (blue) and D1 (red), respectively. As indicated in the SEM picture (Fig. 5.11a), both detectors are coupled again to the same node. In the exemplary timetraces in c) and d), both measure on opposite edges of the detectors' response functions, leading to a contrary response to an additional electron on the node: An additional electron on the node reduces the current across detector D1, while the same event is indicated by a rising current across detector D2. But, as a consequence of the unidirectional charge transfer of the dynamic quantum dot, this effect can be compensated for in the data evaluation. Vertical lines mark points in time at which pulses were applied to the sample, the color coding reflects the gate which was pulsed: The green lines belong to the barrier gate (i.e., marking a reset pulse), while black ones correspond to pulses applied to the dynamic quantum dot (i.e., marking transfer pulses). The difference of one electron on the node causes on average a change in detector current for D2 of about $\Delta I \approx 20$ pA and $\Delta I \approx 16.5$ pA for detector D1, respectively.

The working point of the dynamic quantum dot, tunable by the ap-

5.2 Microscopic insight into dynamics of single-electron capture

plied static voltage V_{G2}^{QD1} , has been set in this example to $V_{G2}^{QD1} = -197.5$ mV. This corresponds to the transition between $n_e = 0$ and $n_e = 1$ electrons per cycle (as it will turn out later in the analysis) with $P_1^{QD1} > 0.9$, i.e. a high probability to transfer one electron per cycle onto the node. The occurrence of transfer events involving more than one electron per cycle is very unlikely at these conditions. At all transfer events (black lines) in Fig. 5.11c,d) exactly one electron has been transferred, except for the one at $t = 12.65$ s, where both detectors remain constant before and after the pulse: No electron has been transferred. In contrast, the outcome of a reset pulse appears to be random as expected: At 12.3 s, the node's occupation is reduced by one electron, remains constant after the following reset pulse (at 12.4 s) and finally is reduced by eight electrons at the pulse at 12.5 s. This behaviour will be discussed later in this chapter, but let us first focus on the transfer properties of the dynamic quantum dot and how transfer probabilities are extracted from the detector current signals.

5.2.1 Data evaluation

The evaluation is based on the fact that only discrete states are occupied on the node. This allows to perform a binning of the detector signal, resulting in a histogram as shown in Fig. 5.12 for both detectors D2 (blue,a) and D1 (red,b), respectively, over almost half a minute (275 sequence periods) of the time-traces shown in Fig.5.11c),d). A necessary prerequisite is sufficient stability of the detectors; drifts in the background potentials for example would smear these levels out and appropriate identification becomes impossible. Random redistribution of the initial state of each sequence period by the reset pulse leads to a broad occupation of the charge states to be detected.

Identified maxima (the levels of occupation of the node) are indicated by green dots, minima by yellow dots. The peak-detection algo-

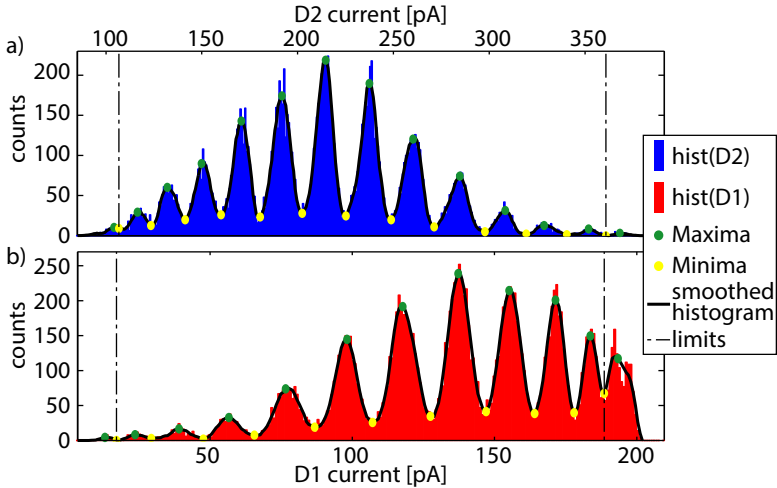


Figure 5.12:

Histograms for level detection derived from pulsed electron transfer with intermediate reset. After smoothing (black line), maxima (green dots) and minima (yellow dots) are detected from which the limits are derived.

rithm operates on the smoothed histogram, filtered by a second-order Savitzky-Golay-filter (black line). From this procedure, we also define the limits of detector current values by the first and last minimum found and disregard detector currents beyond. Although this approach possibly reduces the number of events evaluated without any need (as for D2 in this example), it also prevents from erroneous level assignment due to e.g. too small occupancy during the measurement or too small distance between neighbouring levels (as for D1 for the highest current level). A proper distribution of the initial states of each sequence period is ensured by the stochastic nature of the reset pulse. The analysis yields 12 levels for D2 and 10 levels for D1 within the

5.2 Microscopic insight into dynamics of single-electron capture

limits at these specific working points of the two detectors.

After this level-detection, each interval between two pulses can be attributed to a specific charge state of the node. Then, by simply taking the difference in states between a final and an initial state, we obtain our counting signal, i.e. the number of electrons transferred. Additionally, also the absolute difference between initial and final state relative to the distance of the maxima is evaluated to correct for possible misattributions if one or both of the participating states are close to a minimum. As an example, if electron transfer fails but the initial state is close to a minimum (due to, e.g., small drifts in the background charges or in the voltage sources), then there is a small chance that the final state is attributed to the neighbouring state (e.g., due to noise), although the absolute difference of both states (given by the difference of corresponding mean values) is much smaller than the difference in the maxima. Finally, by performing correlation between counting signals derived from both detectors (as discussed in the following), the fidelity of the counting signal is further enhanced.

A larger interval of the timetraces of Fig. 5.11, together with the rotated histograms (to match the current axis) are plotted in Fig. 5.13a) (detector D2) and e) (detector D1). The levels (maxima) obtained are indicated by horizontal lines, light-grey areas mark the insensitive regions. The derived counting signals are plotted in b) and d) for D2 and D1, respectively. Detector D2 is sensitive throughout the interval shown here, but D1 occupies at three different times states beyond the upper sensitivity limit. An outcome of a transfer event is not considered due to insensitivity if either the initial or the final state is beyond the limit.

As only mean values of the detector signals between two pulses are evaluated, the analysis is unable to access events like, e.g., hold-errors (see section 5.1). However, the barriers confining the node are sufficiently high on both sides of the node so that unintended electron

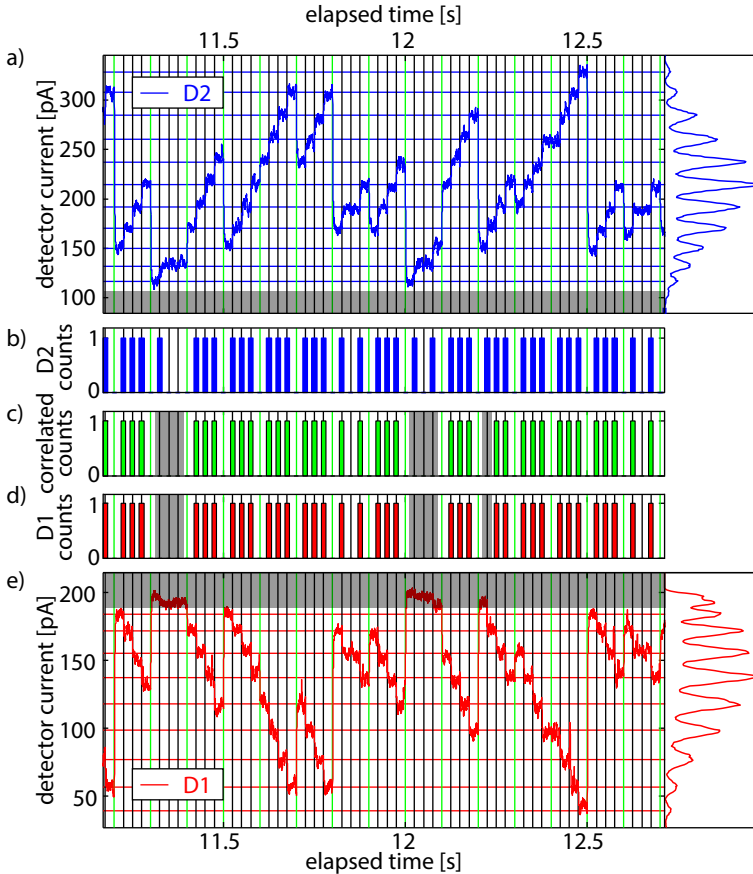


Figure 5.13:

Counting signals derived from pulsed electron transfer with intermediate reset for $P_1 > 0.9$ at exit gate voltage $V_{G2}^{QD1} = -197.5$ mV. Detector current signal of D2 (a) and D1 (e) together with occupation levels of the node (horizontal lines) found by algorithm via histogram (to the right). Grey areas mark detector insensitivities. Resulting counts derived for D2 (b) and D1 (d), respectively together with correlated counts for both detectors (c).

5.2 Microscopic insight into dynamics of single-electron capture

tunneling is strongly suppressed: For the largest effective barrier applied, the number of electrons stored on the node was about 150 before a significant increase in the occurrence of hold errors is observed (see Fig. 5.7). Additionally, the barrier exceeds the respective pinch-off voltage by $\Delta V_{G1}^{QD4} \approx -150$ mV, while the maximum number of electrons to detect is $N_{\text{node}} \approx 20$ (given by the maximum number of states between both limits of the SET response).

Finally, since both detectors are coupled to the same node, we are able to perform a correlation analysis of both detectors' counting signals to eliminate additional sources of errors. These mainly are switching noise caused by two-level charge traps of which especially detector D1 is affected (see for example Fig. 5.13d) at $t = 12.45$ s or $t = 12.57$ s) or errors in the level detection algorithm leading to missed/surplus levels in one of the detectors.

The working points of the SETs are not only affected by the charge on the semiconducting nodes, but also by cross-capacitive coupling to the gate used to tune the dynamic quantum dot, redistribution of background charges or long-time drifts. In order to reduce the probability that one or both of the SETs are insensitive throughout a measurement for a specific quantum dot gate voltage, 20 separate time-traces are taken with variation of the local SET gates for each exit gate voltage of the quantum dot. The variation covers about 70% of the SET period, as shown in Fig. 5.14. Dots and lines represent the typical SET response to their local gates as a reference (D2: blue, panel a) and D1: red, panel b)) without triggering the dynamic quantum dot in the semiconductor channel. Indicated by the black scale bar is the range of variation of SET gate voltages for each dynamic quantum dot setting.

Additionally, open circles mark the change in SET working points by variations of the local gate voltages while operating the dynamic quantum dot at one fixed gate voltage ($V_{G2}^{QD1} = -197.5$ mV, as used in the traces shown in Figs. 5.11-5.13). The SET working points are

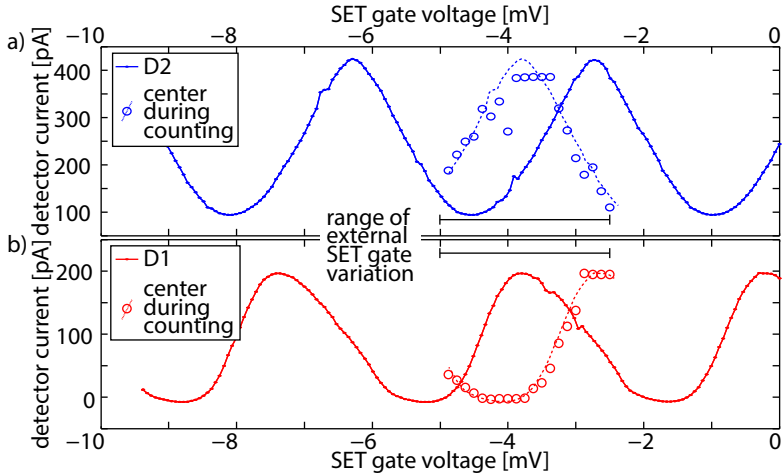


Figure 5.14:

Gate dependence of SET current (before pulsed charge transfer) for detector D2 (a, blue dots and line) and D1 (b, red dots and line), respectively. Additionally, open circles mark the SET working points under variation during pulsed charge transfer at $V_{G2}^{QD1} = -197.5$ mV. The dashed lines show the corresponding detector response, shifted in SET gate voltage, as guide to the eye.

defined here as the SET state with highest occupation, i.e. the overall maximum of the histogram obtained during evaluation. Dashed lines reflect shifted corresponding SETs' response functions (as guides to the eye), accounting for cross-capacitive shifts resulting from asymmetric coupling of the detectors to V_{G2}^{QD1} .

As an alternative solution for stabilizing the detectors on the edge, one could compensate the shift in the detector's working point due to cross-coupling with the dynamic quantum dot's gate voltage by the local SET gates. However, also drifts in the background charges might cause a change in the detector's local potential which cannot be com-

pensated for without the usage of active feedback. Due to the long measurement time of about 24 hours, this effect might not be negligible.

5.2.2 Counting statistics of charge transfer by a dynamic quantum dot

For each exit gate voltage of the dynamic quantum dot and each SET gate voltage a measurement of 279 sequence periods (containing 279 reset pulses and 837 transfer pulses) is taken, equalling about 30 s in time. Due to the variation of the SET working points in 20 steps, in summary 10 minutes of data per exit gate setting of the dynamic quantum dot are obtained, containing each 16740 transfer pulses. The analysis is performed for each exit gate / local SET gate setting, but the results presented in the following contain only traces in which both detectors have been sufficiently sensitive (at least for 30% of the sequence). Additionally, at least 150 events in which both detectors equal in the resulting counts are necessary for a time-trace to be considered in the analysis (which corresponds to about 18% of all transfer events). This criterion prevents traces in which for example the level detection has failed from distorting the statistical analysis.

Employing the methods discussed in this section, we are able to directly access the full probability distribution of single-charge transfer by the dynamic quantum dot QD1 under variation of its working point as shown in Fig. 5.15. Here, the probabilities for the transfer of $n_e = 0 \dots 4$ electrons per cycle derived by counting are shown for exit gate voltages ranging from $V_{G2}^{QD1} = -230$ mV to $V_{G2}^{QD1} = -164.5$ mV. For most negative parameter values, the exit barrier is highest and the transfer of electrons is expected to be blocked: Because the dot's energy level is well above the Fermi energy of the source lead when the tunneling barrier to source is lowest, electrons are not cap-

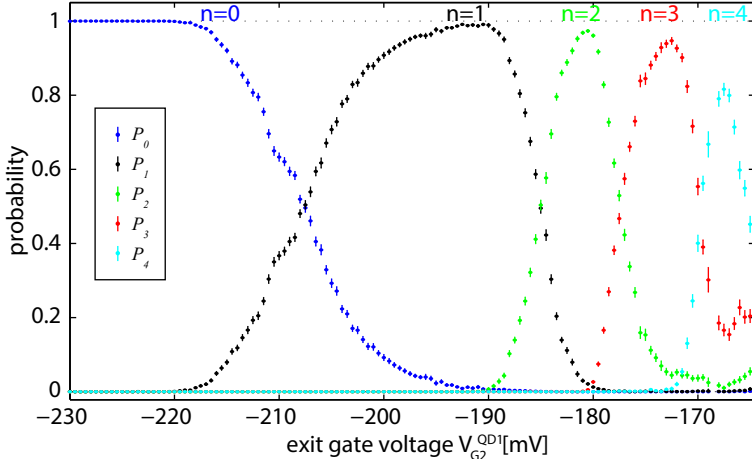


Figure 5.15:

Exit gate dependence of the probability distribution obtained for the analysis of single-charge transfer. The vertical lines correspond to the interval of confidence. Graph shows the probabilities P_n corresponding to transfer of $n_e = 0$ (blue), $n_e = 1$ (black), $n_e = 2$ (green), $n_e = 3$ (red) and $n_e = 4$ (cyan) electrons per transfer pulse. The fidelity of single-charge transfer for $n_e = 1$ is $P_1 = 0.991$, reaches $P_2 = 0.973$ as the upper limit and is still above 0.8 in maximum for $n_e = 4$.

tured onto the dot during the initialization phase so that no electrons are left on the dot to be unloaded to drain. I.e., one expects $P_0 = 1$ (blue dots) (and thus $P_n = 0 \forall n > 0$) for the most-negative parameters as reflected by the measurement.

At values $V_{G2}^{QD1} > -220$ mV, single-electron capture becomes energetically allowed by the now sufficiently lowered ground state energy of the dynamic quantum dot thus leading to an increase of P_1 (black dots) while $P_0 + P_1 = 1$ holds, i.e. in this regime charge transfer of more than one electron per cycle is very unlikely and is not observed.

5.2 Microscopic insight into dynamics of single-electron capture

The interval of $V_{G2}^{QD1} \in [-200 \dots -188]$ mV represents the $n_e = 1$ main plateau with $P_1 > 0.9$, i.e. high probability to transfer exactly one electron per transfer pulse.

Although the quality of quantization of the dynamic dot used here is rather low in terms of plateau length, the presented measurement scheme is able to address one of the most-frequently raised questions in single-charge transfer devices: What is ultimate accuracy in transferring one electron per cycle? A similar approach to investigate the transfer accuracy of a metallic single-electron pump has been demonstrated by Keller et al. [25]. However, they employed so-called single-electron shuttling (transferring one electron back and forth by the same pump). This might lead to different results compared to the unidirectional charge transfer mode used to generate a quantized current if the probability distributions do not equal for both transfer directions.

The counting analysis yields in maximum a probability of precise single-charge transfer $P_1 = 0.991$ for $V_{G2}^{QD1} = -190.5$ mV, thus at the end of the plateau as predicted by theory. This is also the exit gate voltage setting at which $P_2 = 0.0018$ (green dots) exceeds the value of 10^{-3} for the first time while all other probabilities including transfer of $n_e > 2$ are still negligible. Therefore, one may conclude that the assumption made to analyse the charge transfer mechanism using noise measurements [168] have been valid, namely that at the $1ef_p$ -plateau only transfer events involving $n_e \in [0, 1, 2]$ contribute to the current.

The following transfer probabilities of $n_e = 2, 3, 4$ achieve in maximum $P_2 = 0.973$ (at $V_{G2}^{QD1} = -180.5$ mV), $P_3 = 0.947$ (at $V_{G2}^{QD1} = -172.5$ mV) and $P_4 = 0.818$ (at $V_{G2}^{QD1} = -167.5$ mV). Thus, the distance between the maxima in terms of gate voltage decreases monotonously in terms of exit gate voltage. Apparently, also the accuracy of quantization is reduced with higher number of electrons n_e transferred per cycle.

But, it is further worth noting that the detection scheme and the underlying algorithm is limited to a small number of transferred carriers per cycle only, resulting from the limited number of detectable states per detector (16 for detector D2, 13 for detector D1). In consequence, this leads to a comparably small detection efficiency of events involving a high number of transferred electrons n_e per cycle: A series of perfect transfer of, say, $n_e = 5$ electrons per cycle will not be completely detectable since D1 is only able to resolve 13 electrons, but with the current pulse scheme with three transfer pulses per cycle in total 16 different levels are necessary (which is detectable by D2 only in optimal conditions, either).

This example demonstrates that for large n_e the probability of detection decreases thus leading to an relatively higher number of events involving smaller n_e in the evaluated counting signal. This might be an explanation of the fact that P_2 and P_3 do not go down to zero after reaching their respective maxima. In this regime, the assumption of equality in detection of different numbers of electrons n_e transferred per cycle is not valid any more and thus also the normalization to obtain the probabilities from the series of individual counts is not perfectly justified any more. However, also reduced quantization of the dynamic quantum dot at high numbers of electrons transferred cannot be ruled out.

The reduced detection efficiency can also be observed in the analysis of the number of correlated events as a function of the working point of the dynamic quantum dot, set by the exit gate voltage V_{G2}^{QD1} , as shown in Fig. 5.16. Although this quantity is additionally a function of the relative phase between both detectors (correlated events may only be found if both detectors are sensitive at the same time), there is a clear drop at about $V_{G2}^{QD1} = -175$ mV beyond which the mean number of correlated events ($\overline{N}_{\text{corr}} = 2876$) is below half of the global mean ($\overline{N}_{\text{corr}} = 5948$ events). Limited to the range of exit gate volt-

5.2 Microscopic insight into dynamics of single-electron capture

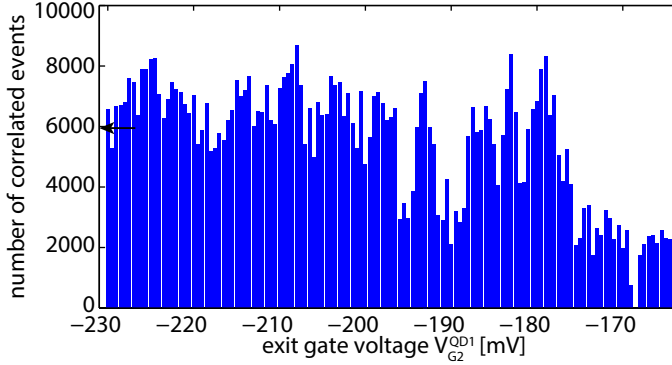


Figure 5.16:

Number of correlated events per working point. The black arrow corresponds to the geometrical mean (5948 events) over all gate voltages, if limited to exit gate voltages $V_{G2}^{QD1} \leq -180.5$ mV (maximum of P_2) the average number of correlated events equals 6620. In total, 16740 pulses are applied at each exit gate setting.

ages $V_{G2}^{QD1} \leq -180.5$ mV (which corresponds to the position of the maximum of P_2), the mean number of correlated events equals $\bar{N}_{\text{corr}} = 6620$. Compared to the number of transfer pulses applied for each parameter setting, this corresponds to a ratio between transfer pulses and events used to evaluate the counting statistics of about 0.4.

From the probability distributions (Fig. 5.15), one can obtain again the average current output of the dynamic quantum dot by summing up all probabilities multiplied by the corresponding number of electrons transferred: $I = ef_p \cdot \sum_{n_e} P_{n_e} n_e$. The result of this calculation is shown in Fig. 5.17.

The derived current, normalized to ef_p and plotted as black dots and line, shows the expected step-like increase in current as a function of exit gate voltage V_{G2}^{QD1} . But, since we have access to the individual

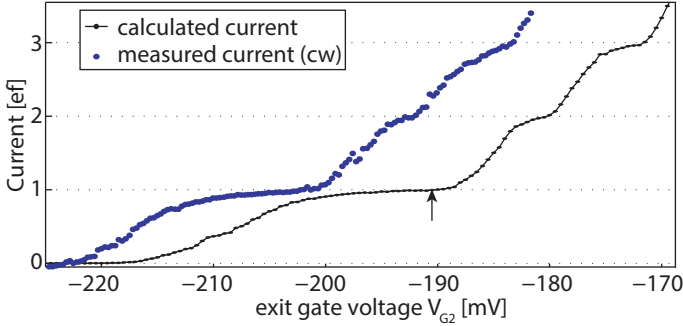


Figure 5.17:

Calculated current derived from counting data of QD1 (black dots and lines) in comparison to measured current with continuous pulse train applied (blue dots). Direct-current data (cw drive) is shifted towards more positive gate voltages on the exit gate voltage axis. The black arrow marks the position of the maximum of P_1 .

transfer probabilities, we are able to identify the point of maximum precision in single-electron transfer which is marked by the black arrow and, as predicted by theory [46], is located towards the end of the plateau in close proximity to the transition to the $2ef_p$ -plateau. As a proof of consistency, also a direct current measurement obtained by continuous pulsing is shown as blue dots. The position of the data is shifted in gate voltage towards more positive gate voltages to compensate partly for the effect of cross-coupling of the pulse signal onto the exit gate but is not fully compensated for clarity.

Essentially, both traces - although obtained using completely different characterization methods - qualitatively agree very well, showing a wide plateau for single-charge transfer ($n_e = 1$), a rather weak plateau for $n_e = 2$ and a wider plateau for $n_e = 3$ but containing a finite slope. The main difference in both traces can be found in the transition be-

5.2 Microscopic insight into dynamics of single-electron capture

tween zero and $1ef_p$. Equalling for $I > 0.5ef_p$, there is an offset (clearly visible in Fig. 5.15) in the gate dependence for the counting data, yielding a slightly broader transition from 0 to $1ef_p$ as compared to the cw data. Most probably, this results from a change in the local potential of the dynamic dot during the measurement as it did not appear in a repetition of this experiment. In summary, the counting data is consistent with the direct current measurement, indicating that the properties of the dynamic quantum dot are preserved in pulsed single-electron transfer and, secondly, that the algorithm to extract the data does not strongly bias the result (for sufficiently small $n_e \leq 3$, at least).

Analysis of the reset pulse

Until now, the result of the reset pulse has been excluded completely from the analysis, simply stating that it equilibrates the node's electrochemical potential μ_{node} with the one of the drain lead μ_d . In the following, this will be analysed in more detail: In principle, we are able to perform the same analysis as shown for the transfer pulses also for the action of the reset pulse. However, a correlation between both detectors and over several SET working points does not yield a reasonable result due to the change by a large number of electrons on the node. Therefore, the analysis is restricted to detector D2 only as well as to individual settings of V_g and V_{G2}^{QD1} . These restriction lead to a rather weak statistical base containing only 279 events.

Figure 5.18 shows the difference in the occupation number of the node after the reset pulse for two different exit gate voltages of the dynamic quantum dot as a histogram. The first graph (a, green bars) contains the analysis at $V_{G2}^{QD1} = -197.5$ mV (same timetrace as used for Figs. 5.11-5.13). The dynamic quantum dot is operated here at the transition between zero and single-charge transfer, resulting in (at maximum) three electrons transferred onto the node between two reset pulses. First thing to notice is that the reset pulse indeed acts not uni-

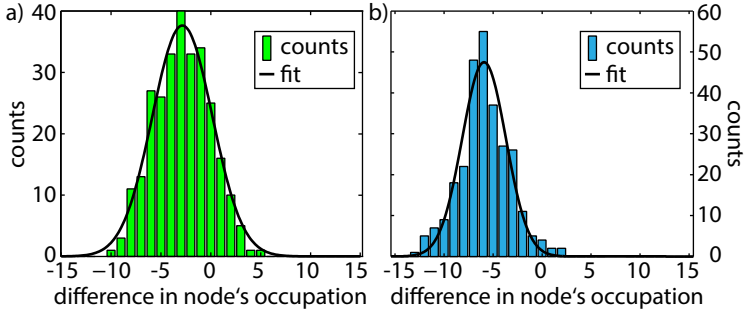


Figure 5.18:

Histograms of change of node's electron number due to reset pulse at $V_{G2}^{QD1} = -197.5$ mV (a, green bars) and $V_{G2}^{QD1} = -180$ mV (b, blue bars), respectively. Additionally, fits to gaussian distribution are superimposed (black lines).

directionally: Although the center of the distribution is negative (i.e., most likely electrons are removed from the node by a reset pulse), there also appear events where electrons are added to the node by the reset pulse.

To proceed to the quantitative analysis we perform a fit to a non-centred, non-normalized gaussian distribution

$$y(N_{\text{node}}) = A \cdot \exp\left(-\frac{(N_{\text{node}} - N_0)^2}{2\sigma^2}\right).$$

The resulting amplitude A is only of minor importance, being related mainly to the number of reset events. But the center of the distribution N_0 gives an expectation value for the mean number of electrons removed from the island due to the reset pulse. The fitted value of $N_0 = -2.85$ corresponds well to the average number of electrons transferred per period at this working point $\bar{n}_e = 3 \cdot \sum_n P_n \cdot n = 3 \cdot (0.056 \cdot (0) + 0.944 \cdot (1) + 0 \cdot (2)) \approx 2.83$ derived from the evaluation of transfer pulses. Thus, the distribution of node's change in occupation

5.2 Microscopic insight into dynamics of single-electron capture

number following a reset pulse contains basically the same information as the direct current measurement yielding in both cases the average number of electrons transferred per cycle without access to individual transfer rates. The third parameter to fully describe the normal distribution is the width of the distribution, in this case $\sigma = 4.3$. In about 96% of all reset pulses, the change of the node's charge carrier causes a change in electrons on the node within an interval of $N_0 \pm 2\sigma = [-11.4, 5.7]$.

For comparison, a similar evaluation has been performed for a second setting of the QD's exit gate voltage with $V_{G2}^{QD1} = -180$ mV (blue bars). At this working point, the transfer probabilities are shifted towards the second plateau: $P_{n=(0\dots4)} = (0, 0.014, 0.958, 0.028, 0)$, i.e. most-probably two electrons are transferred per pulse accompanied by almost equal contributions of a few percent of one or three electrons, resulting in on average $\bar{n}_e = 6.04$ surplus electrons on the node between two subsequent reset pulses. The expected shift in the distribution compared to Fig. 5.18a) is reflected by the corresponding fit ($N_0 = -5.9$). In this example, the discrepancy is slightly larger but agrees well within the confidence bounds of the fit with \bar{n}_e . The variance $\sigma = 3.2$ is comparable to the one for a).

Since the random redistribution predominantly measures the Fermi distribution of the drain lead, the variance can be used as an indicator of the electron temperature in this lead. The width of the Fermi distribution, approximated by $4k_B T$, equals an energy range of about $2\sigma E_C$, yielding a temperature of $T \approx 700$ mK. However, due to the limited statistical basis and the uncertainties in the estimation of E_C , this value should be considered only as an order of magnitude.

5.2.3 Detailed analysis of the capture mechanism

After this general discussion of the pulsed charge-transfer experiment, a detailed analysis of the single-electron capture mechanism based on the

counting data is presented in the following section. As discussed previously, the charge transfer cycle consists mainly of three different phases which are the initialization of the quantum dot with a large number of electrons when the barrier to the source lead is low, followed by the capture process when this barrier is raised again and back-tunneling to source sets in for all carriers above a certain energy (determined mainly by the value of the exit gate voltage) and finally the emission process to the drain lead. In consequence, the chance of successful charge transfer is given by the product of all three probabilities attributed to each of the processes.

Given a sufficiently large voltage amplitude of the pulse V_{ac} , the barrier to source is lifted completely so that occupation of the dynamic dot by electrons from source during the initialization is always maintained. On the opposite part of the period (during the emission process), a sufficiently large amplitude always guarantees that all electrons on the dot are also emitted to drain. These two boundaries limit the main plateau on the entrance-gate axis. The other way round, if one ensures operation of the dynamic dot on the main plateau (i.e., within the parameter range marked by the magenta and brown lines in Fig. 2.13), these two processes occur with probabilities equal to one. Finally, by counting electrons transferred by the dynamic dot to the node, we therefore directly access the probability distribution of the third process involved in single-charge transfer in our device, namely the dynamic charge capture process during the rise of the source barrier. The operation of the dynamic quantum dot within this regime can be ensured also by counting (see Fig. 5.20).

As outlined in section 2.5.2, there are basically two models of charge capture discussed in literature [35, 46, 48] which are the grand-canonical (thermal) limit and the rate-driven (decay cascade) limit. These can be distinguished due to their differing dependence on external control parameters (see also Fig. 2.16) leading to either exponential de-

5.2 Microscopic insight into dynamics of single-electron capture

pendence on the control-gate voltage V_{G2} in the grand-canonical limit (see eq. (2.47)) or double-exponential dependence in case of the decay-cascade limit (see eq. (2.48)). Fig. 5.19a) shows a zoom-in into the data presented in Fig. 5.15, focusing on the $n_e = 1$ -plateau and including in this part only the transitions $0 \leftrightarrow 1$ and $1 \leftrightarrow 2$ by restricting the parameter range to $V_{G2} < -186$ mV.

Because the conclusions drawn in the following are based on an elaborate data analysis, I will detail first how the data is extracted from the counting signal and how it is then further processed. For each gate-voltage setting, we obtain the number $M_n(V_{G2})$ of successful capture and transfer events of $n_e = 0 \dots 4$ electrons and the total number of events $\overline{N}_{\text{corr}}(V_{G2})$ which has been discussed already in Fig. 5.16. As an estimator of the underlying (unknown) probability distribution which obeys binomial statistics we use by definition the ratio

$$P_n(V_{G2}) = M_n(V_{G2}) / \overline{N}_{\text{corr}}(V_{G2}). \quad (5.2)$$

We further estimate the interval of confidence for each data point using the principle of maximal likelihood and the quantile function of the binomial distribution. This interval contains the range of probabilities in conformity within a 95% confidence interval with the observed outcome \overline{P}_n . On the other hand, the observed outcome is unlikely in case of the unknown probability distribution lying outside this interval. These estimators and their attributed interval of confidence are displayed as black dots and lines, respectively, in Fig. 5.19.

Additionally, solid lines mark the best fit for the thermal (red) and the athermal limit (black) to equations [(2.43),(2.47)] and [(2.45),(2.48)], respectively. These have been obtained by standard least-squares optimization of the data weighted by the interval of confidence. As fit parameters we use the sets $\{\alpha_{\mu,n}, \Delta_{\mu,n}\}$ and $\{\alpha_{X,n}, \Delta_{X,n}\}$. The values of maximal likelihood are given in table 5.1 together with estimations of errors of the fit parameters. These are obtained by fitting 500 sets of

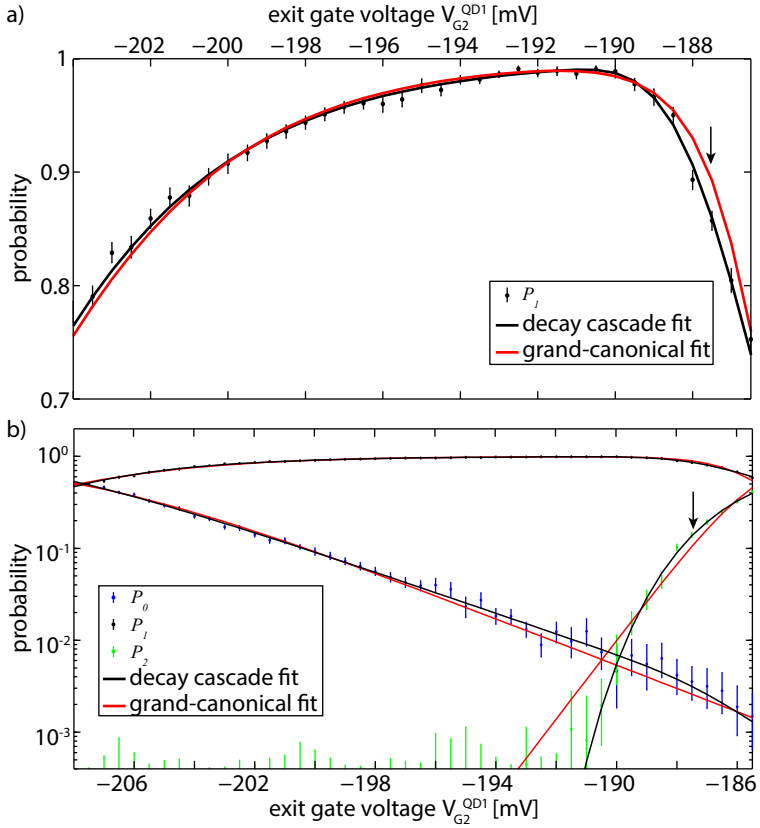


Figure 5.19:

Comparison between thermal and athermal modelling of counting data. a) Measured probability of single-electron transfer P_1 as function of the control parameter V_{G_2} (black dots) and interval of confidence as black lines (95%). Additionally, solid lines represent the best optimization for the thermal (red) and the athermal model (black), respectively. b) Probabilities P_0 (blue), P_1 (black) and P_2 (green) as function of V_{G_2} on logarithmic scale together with the corresponding fits to the thermal (red) and athermal model (black).

5.2 Microscopic insight into dynamics of single-electron capture

	$\alpha_{\mu/X,1}$ /mV ⁻¹	$\alpha_{\mu/X,2}$ /mV ⁻¹	$\Delta_{\mu/X,1}$	$\Delta_{\mu/X,2}$
Thermal	-0.293 ±0.003	-0.983 ±0.023	-60.8 ±0.6	-182.1 ±4.2
Athermal	0.261 ±0.003	0.385 ±0.009	-54.5 ±0.6	-71.5 ±1.6

Table 5.1: Best fit parameters.

synthetic data for both models separately in a Monte-Carlo approach. Synthetic data is drawn from binomial distributions with success probabilities taken from the best-fit model and the total number of events equalling those in the experiment for each gate voltage setting V_{G2} .

Returning to Fig. 5.19, the resulting fits for the thermal and athermal model agree well for $V_{G2} < -190$ mV, but there is a large discrepancy for the thermal fit for more positive gate voltages as indicated by the arrow. This is even further emphasized in Fig. 5.19b) which contains the plot of probabilities P_0 , P_1 and P_2 on a logarithmic scale. Here, the deviation in the same parameter range in case of the grand-canonical case is evident for P_2 where the data shows an exponential dependence on the logarithmic scale while the thermal model predicts a linear characteristic. In contrast, the athermal limit is capable of reproducing the experimental data very well. Moreover, also the uncertainties in the fitting parameters are much larger in the thermal limit compared to the decay cascade model, thereby leading to the conclusion that the dynamic quantum dot at these experimental conditions operates in the decay-cascade limit.

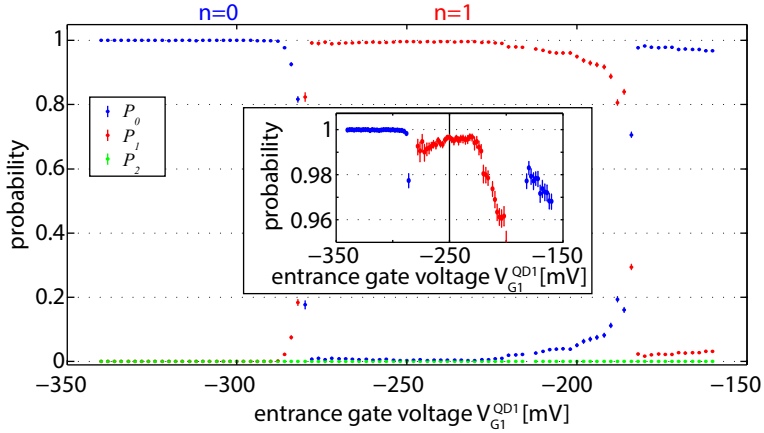
The classification of the driving principle of single-electron capture in such a dynamic quantum dot paves also the route towards strategies of optimization: If the dynamic quantum dot is operated in the

thermal limit, further lowering of the leads' electron temperature will simultaneously enhance the precision of electron capture. In contrast, in the regime dominated by the decay-cascade mechanism a further reduction in temperature will not lead to a more precise operation which has been indeed observed in surface-acoustic wave driven dots [31]. Previously, this saturation of transfer precision as a function of temperature has been attributed to thermal heating of the electron gas [31, 169]. Therefore, this observation alone is insufficient to distinguish both regimes of operation.

The thermal limit may be reached by reducing the plunger-action of the modulated gate. This could be achieved e.g. by applying a compensation signal to the typically unmodulated exit gate during the dot's initialization phase (interval b-c) in Fig. 2.11). In contrast, when operated in the athermal limit, the precision of initialization is achieved by increased separation of decay cascade steps X_n/X_{n-1} . This is accomplished either by enlarged decay rate ratios $\Gamma_n(t)/\Gamma_{n-1}(t)$ [46] or by large energy separation of neighbouring states. In the latter case, the ratio can be large even if $\Gamma_n(t) \approx \Gamma_{n-1}(t)$ due to the differing decoupling times t_{n-1}^b and t_n^b , respectively, at which the integrated decay-cascade rates X_n are evaluated.

5.2.4 Analysis of entrance-gate voltage dependence by counting

Until now, the entrance gate offset voltage has been fixed and was assumed to enable charge transfer on the main plateau. To prove this assumption and to show the robustness in terms of gate voltage range we perform also a single-electron counting measurement with the exit gate voltage fixed (defining the number of carriers captured on the dynamic quantum dot and thus the number of carriers transferred per cycle in maximum) while varying the entrance gate voltage offset. From


Figure 5.20:

Results from counting under variation of entrance barrier voltage with fixed exit gate voltage to operate at $n_e = 1$ on the main plateau.

this single line sweep, one can directly derive the location of the main plateau as evident from Fig. 2.14: The maximum number of electrons transferred is found when tuning the entrance gate voltage offset from blocking (most negative) towards more positive values - supposing a sufficiently high oscillatory amplitude V_{ac} . The resulting distributions of transfer probabilities are shown in Fig. 5.20 together with an inset focusing on the range of probabilities $P_n > 0.95$. Due to changes in the local potentials, the point of highest P_1 had changed in exit gate voltage towards $V_{G2}^{QD1} = -178$ mV as determined by a quick characterization with interchanged parameters in advance to the measurements presented here. The maximum number of electrons transferred in this graph equals $n_e = 1$ while $P_n < 0.001$ holds $\forall n > 1$. For entrance gate voltages $V_{G1}^{QD1} < -288$ mV, any charge transfer is blocked because the high barrier formed by the entrance gate

is not sufficiently lowered, thus preventing electrons from tunneling onto the dynamic quantum dot during the initialization phase. The main plateau, if defined by $P_1 > 0.99$ (see also the inset), extends over $-278 \text{ mV} \leq V_{G1}^{QD1} \leq -222 \text{ mV}$. The black vertical line in the inset marks the value at which all previous measurements have been conducted and which equals the center of the plateau. For even more positive entrance gate voltages, the probability to transfer one electron drops again but does not reach exactly zero, most probably passing across the (at this setting of V_{G2}^{QD1} just rising to the) first side plateau. The data has been obtained using in total 21540 transfer pulses per entrance gate parameter.

5.2.5 Qualification of dots QD2 and QD4 by counting

To conclude this chapter, lastly the counting data obtained for the other two dynamic quantum dots used on this sample is presented. For details of the nomenclature, please refer to Fig. 3.7. The probability distributions are plotted in Fig. 5.21 as a function of exit gate voltage V_{G2} for QD2 (a) and QD4 (b), respectively. Generally, both resemble the probability distribution for QD1 discussed already in detail in this chapter.

It is quite instructive to compare the distributions to the direct current measurements, which are plotted here as insets for both dynamic quantum dots, respectively. Using the cw drive, only one plateau had been found for QD4, beyond the current seemed to approach the $2ef_p$ -plateau first, but for $I \gtrsim 1.5ef_p$ quantization breaks down. In Fig. 5.21b) this behaviour is exactly reflected: The plateau for $n_e = 1$ reaches its maximum of $P_1 = 0.992$ at $V_{G2}^{QD4} = -191.5 \text{ mV}$ (the shift of the position of the plateau in terms of V_{G2}^{QD4} can be again explained by cross-coupling of the cw-signal onto the exit gate), followed by a subsequent increase of P_2 (equivalent to the transition from $1ef_p$ towards

5.2 Microscopic insight into dynamics of single-electron capture

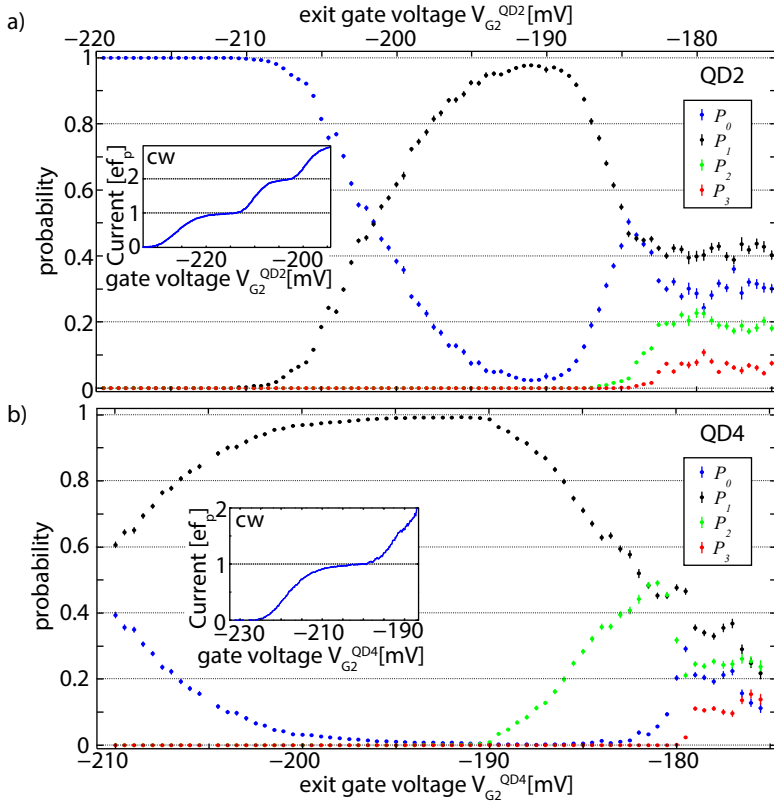


Figure 5.21:

Probability distributions of charge transfer derived by counting for QD2 (a) and QD4 (b). Plotted are the probability distributions for $n_e = 0 \dots 3$ as a function of the respective exit gate voltage V_{G2} . The insets show the gate-dependence of the current using a cw drive. While QD4 (b) behaves comparable to QD1 (cf. Fig. 5.15), but limited to a $n_e = 1$ plateau only (as expected from the cw measurements, see inset), QD2 (a) behaves differently: After a weakly developed $n_e = 1$ -plateau, the probability P_0 increases again and probabilities $P_n > 0$ involving $n > 1$ are observed only in the unquantized regime - in contradiction to the cw measurements (inset).

$2ef_p$ in the cw measurements).

But, quantization breaks down at about $V_{G2}^{QD4} = -181.5$ mV with $P_{n=(1,2)} \approx 0.5$ (corresponding to an equivalent number of $n_e = 1.5$ electrons per transfer cycle on average). Thus, the measurement conforms well with the cw measurements (inset). To obtain this data, we use the entrance gate of QD1 as a pulsed barrier (the exactly inverse of the previous measurements), loading electrons *from* the node to the drain lead. Static offsets have been set for both pulsed gates to $V_{G1}^{QD1, QD4} = -240$ mV, modulation amplitude has been chosen again to $V_{ac} = 150$ mV. The algorithm did not need any adjustments except of the change in active components (which pulse corresponds to the dynamic dot, which one to the barrier). The working points of the SETs have been set to 20 different values for each exit gate voltage parameter. In summary, 51540 transfer pulses are applied at each gate setting, all pulses are delayed by $\tau = 25$ ms each.

For QD2, small adjustments to the algorithm have been made to acknowledge the smaller nodes to which the detectors are coupled, using the entrance gates of both QD1 and QD4 as pulsed barriers. This results in a higher response of the detectors to electrons on the appropriate nodes. Again, 20 SET working points per exit gate voltage have been chosen, leading to 104940 transfer events per exit gate setting. Comparing QD2 (Fig. 5.21(a)) to its cw trace (Fig. 4.6 and as inset), there is a discrepancy in the number of plateaus observed. While the latter one shows up to four plateaus, the probability distribution derived by counting represents only a significant plateau for $n_e = 1$ followed by an increase in P_0 again. Additionally, the maximum value of $P_1 = 0.976$ is significantly lower than the maxima for P_1 obtained for the other two dynamic quantum dots. The origin of this deviation is subject to further investigations. But, one possible explanation might be the circumstance that the dynamic quantum dot QD2 is operated between two small nodes (quasi-zero-dimensional source and drain reservoirs)

5.2 Microscopic insight into dynamics of single-electron capture

which might drastically affect the transfer characteristics compared to the loading (which is the critical part of the transfer cycle) from a one- or two-dimensional reservoir. On the other hand, also QD4 is operated here using a mesoscopic reservoir as the source, but this source reservoir consists of the full node between QD1 and QD4 and therefore, the effect should be about 3 times smaller as compared to QD2. Additionally, when loading from a secluded reservoir, every transfer event causes a change in the source's electrochemical potential, which, under consideration of the mesoscopic feedback, might strongly affect the transfer probabilities (this effect should also be three times smaller for QD4), as observed and discussed already in section 5.1.3. This feature is not only limited to this specific set of data, but can also be observed in, e.g., Fig. 5.9b), where the continually growing positive potential at the source lead causes a rapid reduction of the transfer probability after the successful transfer of about 16 electrons.

Certainly, the amplitude of the pulse is sufficient to unload all electrons captured on the dot during the emission part. This is also confirmed by the measurements of continuous loading the node by QD2 (Fig. 5.10). In that experiment the drain reservoir equals the one used here, but the source reservoir is open (QD1 being grounded) instead. Therefore, the increase in P_0 for $V_{G2}^{QD2} > -190$ mV as well as the rather low maximal value in P_1 might be explained by a modification of the dynamics of back-tunneling during capture of electrons due to the small, secluded source reservoir.

5.2.6 Summary

In summary, non-adiabatic single-electron quantum dots have been investigated by single-charge detection. Using this method, the precision of single-charge capture could be assessed, yielding a probability of $P_1 > 0.99$ for two of the three dots (without the application of a

magnetic field). Additionally, the full probability distribution of charge capture has been obtained allowing to examine the underlying physical mechanisms by comparison with theoretical models. The charge-capturing process can be described in these devices using a generalized "decay cascade model" from which we predicted routes towards increased transfer fidelity. Furthermore, deviations from the expected transfer characteristics of a dynamic quantum dot have been found when operated with finite source reservoir which deserves further investigation.



The self-referenced current source

In this chapter the operation of the self-referenced current source is discussed. This is a device generating a current based on the triggered transfer of single electrons (like conventional "electron pumps") combined with the intrinsic monitoring of transfer errors. Doing so, the uncertainty of the current output may be reduced by several orders of magnitude as will be demonstrated in this chapter. In the first demonstration experiment of this concept - conceived theoretically by Michael Wulf [62] - three single-electron pumps are connected serially with two intermediate charge detectors capable of monitoring deviations from the nominally quantized current on the level of single electrons. After the basic depiction of the measurement conditions, the algorithm used for the extraction of counting signals from the detector traces will be presented. Lastly, the results concerning error correction and the increase of fidelity of the output current will be discussed.

6.1 Introduction to series pumping and error accounting

Before going into details of the measurement and the results derived, this section gives an introduction to the underlying concept and competing concepts.

The basic motivation of this work is fundamental metrology with the aim of redefining the electric base unit in the SI, the Ampere. Due to the increased ability of single-electron control over the last 25 years, several systems have been established in which electrons are *actively* manipulated to generate a quantized current with amplitude $I = \langle n_e \rangle e f_p$ where e is the elementary charge, f_p an external driving frequency of the charge-transfer process and $\langle n_e \rangle$ the *average* number of carriers in each transfer cycle. The development started with adiabatically operating pumps and turnstiles [17, 18, 20] using both metallic systems with tunneling barriers formed by oxidization as well as semiconducting systems with local control using metallic topgates (similar to the dynamic quantum dots in this thesis).

Until now, the experiments conducted by Keller et al [25, 26] still set the benchmark in experimentally demonstrated precision of the quantized current sources. Using a seven-junction pump, they reported an uncertainty in the output current of 15 parts in 10^9 (15 ppb). The disadvantage of all adiabatic devices is the fact that always a trade-off is necessary between proper charge confinement for high precision (resulting in a high tunneling resistance R_T) and high-speed operation for large output currents (requiring a low tunneling resistance for reduction of the $R_T C$ time constant which determines on which time scale the systems is able to follow the energetically favourable state). This finally limits the speed in high precision devices to about 10^7 cycles per second, resulting in a current in case of single-charge transfer of $I \approx 2$ pA which is at least two orders of magnitude below the requirements for a

practical single-electron quantum current standard.

The recently developed non-adiabatic single-electron pump [38] is able to overcome this limitation in operation speed by employing dynamic barriers and thus strongly reducing the tunneling times. Moreover, the electric control is comparatively simple employing two gates only of which just one is driven by a radio-frequency signal [39]. Additionally, these devices show robustness against parameter variation [41] and recently, the accuracy of quantization could be demonstrated to be lower than 1.2 ppm [44]. But there is still a weak link in determining first the accuracy of a quantum current source and then using its current in some experiment which is the assumption that the source does not change its precision in-between. In contrast to Josephson [22] and quantum Hall effect [21], which both are robust as macroscopic quantum effects, a single-electron device is based on manipulating single charges at a high rate and is therefore highly sensitive to, e.g., changes in background charges which might lead to deviations in the accuracy of single-charge transfer.

As an alternative concept, the *passive* real-time counting of electrons [56] passing a constriction has been proposed, either using a double quantum dot and employing so-called bidirectional counting [59] (in which a detector is asymmetrically coupled to both dots and thereby the direction of tunneling events may be determined) or a chain of metallic islands (50 in the studies presented) through which a current I is biased and the electrons flow as solitons (which are electrons located on one island but with a repelling potential spread over several islands) [58]. In these concepts, the technical limitation is shifted towards the bandwidth of the detectors which necessarily must be much larger than the typical time-scale of electron tunneling events in order to observe or exclude the occurrence of faster events to avoid the influence of the finite detector's bandwidth [89] onto the counting statistics. Using a reflectometry technique to read out the detector's state called

RF-SET, a bandwidth in excess of 10^8 Hz at a high charge sensitivity of $< 10^{-4} e/\sqrt{\text{Hz}}$ has been demonstrated [57], but even with this advanced concept a current of only a few pA might be realized when the tunneling rates are limited to, say, 10 MHz.

Motivated by the work of Keller et al [25] and their key idea of counting errors instead of individual transferred electrons during the characterization of the 7-junction electron pump, M. Wulf proposed the so-called error-accounting scheme [62]. In this concept, not only one clocked electron source is operated for quantized-current generation but a number of devices in a series arrangement with charge detectors in-between. Due to the few control parameters of the dynamic quantum dot compared to an e.g. 7-junction adiabatic pump, this type of device is just made for complex circuits. The implementation in such circuits has been demonstrated in series [43] or parallel arrangements for higher current outputs [42, 170]. The key difference of this concept compared to the device characterization by Keller is the circumstance that the error accounting is performed *during* generation of a quantized current while in the experiments by Keller the characterization of the device (using a so-called "shuttle mode" transferring one electron back and forth) and the current output are performed sequentially. In between, a cryogenic needle switch has to be switched to change from one mode of operation to the other and severe efforts have been put in trying to verify consistent behaviour of the device in the two different modes [27, 119, 144]. In contrast, using the error accounting scheme and a series arrangement of pumps, there are no two different steps for device characterization and quantized current generation: Rather deviations from the perfect operation are measured *online*.

The individual pump structures are separated by interconnecting charge nodes whose spatial extensions are large compared to the pump structures. The respective number of electrons stored on these nodes can be assessed by capacitively coupled charge detectors. If the pumps are

operated synchronously and the number of transferred electrons equals for all pumps, the inflow of carriers onto the node equals the outflow. Thus, the average number of electrons on the node, as the difference of incoming and outgoing electrons, remains constant. Only if the number of electrons transferred by the pumps neighbouring the node deviates (i.e., one is failing in transferring exactly one electron by missing a cycle or adding a surplus electron onto the node), the node's charge state changes.

In this way, only the much less-frequent transfer errors need to be resolved in time instead of all electrons passing the node. Because the tunneling barriers are defined electrostatically, the nodes may be well isolated from each other by high barriers to prevent leakage of electrons in-between. The two aspects which are the triggered single-electron transfer (limiting the frequency of counting events in maximum to the driving frequency) and the necessity of only detecting the less-frequent transfer errors strongly relax the requirements on the detector's bandwidth: E.g., considering a driving frequency of $f_p = 1$ GHz and a moderate error rate of 10^{-5} of the pump, the time-scale of errors to be detected is on average of $\approx 10^{-4}$ s.

The main difficulty in the error accounting scheme is the attribution of error signals to specific pumps and types of errors, since only the change of the node's charge state within the detector's bandwidth is directly accessed. As an example, let us define the output current of the device as the number of electrons passing the last pump in a chain of three pumps. Assuming now a deviation of the second node's charge by +1 electron, this might result either from a consecutive error of the first two pumps transferring each a surplus electron within the observation time (in this case, the output current equals the number of transfer pulses within this time interval) or by the third pump missing a cycle (reducing the number of electrons transferred by one).

This example illustrates two basic relations: Firstly, the resulting un-

certainty after accounting reduces for a comparably high ratio of detector bandwidth to error rates Γ_{err} , given as the product of pumping frequency and error probability, i.e. $\Gamma_{\text{err}} = f_p(1 - P_1)$. Secondly, the uncertainty scales exponentially with the number of pumps in series (in the given example extended to five pumps in series, the first explanation would now require failure of four pumps within the detector's characteristic time-scale). The general equation for reduction of uncertainty in a series of N_{ser} pumps states [62]

$$u_c \approx \frac{2N_{\text{ser}}!}{\left(\frac{N_{\text{ser}}+1}{2}\right)! \left(\frac{N_{\text{ser}}-1}{2}\right)!} (\Gamma_{\text{err}}/\Gamma_d)^{\frac{N_{\text{ser}}-1}{2}} (1 - P_1) \quad (6.1)$$

with P_1 the average probability of all pumps to transfer exactly one electron per cycle, Γ_d the detector's bandwidth and f_p the pumping frequency. In the case of $N_{\text{ser}} = 3$ as used in this thesis eq. (6.1) simplifies to $u_c \approx 6(1 - P_1)^2 \cdot f_p/\Gamma_d$. This relation will be discussed in more detail in section 6.4 following the description of the measurements.

6.2 Description of the measurement

The device is shown as a SEM micrograph in Fig. 6.1 and the individual elements are labelled accordingly. As mentioned, we will operate in the following experiment three dynamic quantum dots connected in series as pumps which are labelled QD1, QD2 and QD4, respectively. To account for this, all gates forming the pumps are coloured in yellow in the figure. The additional quantum dot structure fabricated and located between QD2 and QD4 (uncoloured) is grounded and does not affect the electron system underneath. As in the previous experiments, only the first two of the three gates of each dynamic quantum dot are used in the experiment with the third one held at ground potential. The entrance gate (left-most one of each dynamic quantum dot) is

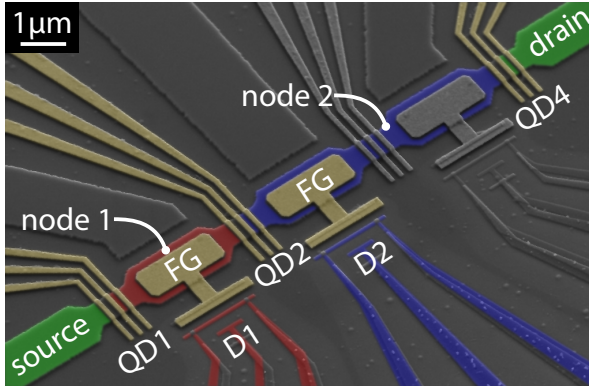


Figure 6.1:

False-colored SEM image of the device operated as self-referenced current source. The three dynamic quantum dots operated are colored in yellow and labelled QD1, QD2 and QD4, respectively. Charge detectors D1 and D2 are capacitively coupled via gates with floating potentials (FG) to the charge nodes 1 and 2 interconnecting the quantum dots.

connected directly to one of the output channels of the arbitrary waveform generator while the second (exit) gate is tuned by a static voltage source. The interconnecting nodes 1 and 2 are coloured red and blue, respectively. The dynamic quantum dots transfer electrons from source via the two nodes to drain, with the direction of charge transfer given by the order of driven (entrance) and static (exit) gate.

The charge transfer is monitored using the two charge detectors D1 (coloured red) and D2 (coloured blue). Both are coupled each to their respective node using a floating top gate (coloured yellow and labelled FG). Since structure QD2 is used, both nodes are separated from each other and the charge states may differ.

Because each dynamic quantum dot is controlled by a separate channel of the arbitrary waveform generator, we are able to trigger a transfer

event by a specific dynamic quantum dot at will. To gain some additional information about the actual sensitivity of the detectors and also of the transfer characteristics of the dynamic quantum dots, we employ a slightly more complex pulse pattern than just the simultaneous operation which is sketched in Fig. 6.2a). The pattern consists of two parts, which we refer to as the marker sequence (pulses (i)-(iii)) where the dynamic dots are triggered one by one, and the series operation (pulses (iv)-(v)). All pulses are delayed by $\tau = 20$ ms which is about ten times larger than the detectors' bandwidth to ensure safe detection of the outcome of the previous pulse by the detectors. The expected detector signals are schematically shown in Fig. 6.2b) together with the two charge states involved for both detectors.

When pulsed sequentially and under the assumption of perfect single-charge transfer, QD1 will first transfer one electron from the source reservoir to node 1 by pulse (i), leading to a step-response in detector D1 ($d_1 \rightarrow d_1 + 1$). Since D2 is coupled mainly to node 2, its state remains constant at state d_2 . When triggering QD2 (pulse (ii)), one electron is shuttled from node 1 to node 2. This leads to a simultaneous, step-like response in both detectors indicating the same difference in number of electrons on the node but with opposite sign: The total number of charge carriers on node 1 will be reduced by one electron (reflected by $d_1 + 1 \rightarrow d_1$), while the number of electrons on node 2 will be increased by one (showed by $d_2 \rightarrow d_2 + 1$). Lastly, by triggering QD3 (pulse (iii)), one electron is then transferred unidirectionally from node 2 to the drain reservoir, reducing the number of electrons on node 2 which is indicated by a step in detector D2 ($d_2 + 1 \rightarrow d_2$). At the end of the sequence and under the condition of perfect charge transfer as assumed here, both detectors return to their initial states $d_{(1/2)}$ indicating that both nodes hold the same number of electrons as at the beginning of the pulse sequence. In total, one electron has been transferred during this sequence from the source reservoir to drain. Due

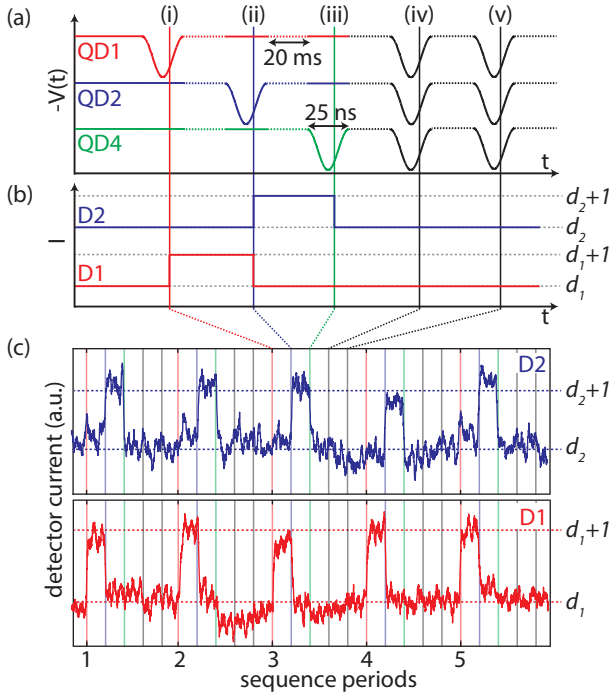


Figure 6.2:

Pulse pattern, expected detector signals and raw detector signals in ideal series charge transfer. (a) The voltages applied to the individual pumps are sketched. The pulses (i)-(iii) constitute the so-called marker sequence, transferring one electron sequentially through the structure. All dynamic quantum dots are driven simultaneously at the pulses (iv)-(v). The pulses contain a single period of a shifted cosine pulse at $f_p = 39$ MHz, the delay is $\tau = 20$ ms each. (b) Expected detector signals of the detectors D1 and D2, respectively, during the pulse sequence in (a). The marker sequence leads to a step-like response while, in ideal series operation without transfer errors, the detector signals remain constant. (c) Raw detector signals of D1 (lower graph) and D2 (upper graph) during ideal series charge transfer over 5 periods of the sequence shown in (a). Vertical dashed lines indicate the two detector states $d_{(1/2)}$, $d_{(1/2)} + 1$ as guides to the eyes.

to the large, electrostatically defined barriers, the number of carriers is expected to remain constant between the pulses, i.e. tunneling across dynamic dots is forbidden between the pulses.

The following series operation consisting of pulses (iv) and (v) equals the scheme discussed in the context of error accounting at the beginning of this chapter, which is the simultaneous operation of dynamic dots with detectors at the interconnecting nodes measuring the error signals. Here, the pulse pattern is extended by an intermediate delay between the pulses of $\tau = 20$ ms as well in order to enable the detectors to measure the nodes' charge state in-between. If all dynamic dots transfer exactly one electron per pulse, the number of incoming and outgoing electrons on the nodes equal, leading to constant detector states before and after the pulse. Figure 6.2c) contains the measured detector time-traces for the pulse pattern depicted above for precise single-charge transfer by all three dynamic dots over an interval of five periods. The two charge states $d_{(1/2)}, d_{(1/2)} + 1$ are well separated and indicated by the horizontal dashed lines. The upper, blue trace corresponds to the response of detector D2, the lower, red one to the response of detector D1. Vertical lines symbolize the pulses (i)-(v) with the colour code chosen in the same way as the neighbouring node to the right of the dynamic dot triggered to which electrons are transferred. Black lines mark the simultaneous pulses (iv) and (v). In summary, during one sequence period consisting of the marker sequence (with a duration of 60 ms) and two series pulses with intermediate delays (taking 40 ms) and under the assumption of precise single-electron transfer, 3 electrons have passed QD4 to drain within 100 ms, i.e. we expect 30 electrons to be transferred to drain per second, limiting the current based on single-charge transfer to $I = 30e \text{ s}^{-1} = 4.806 \times 10^{-18}$ A.

Before starting with the analysis concerning the improvement of transfer fidelity by error accounting, let us focus on how deviations in the expected detector signals may be interpreted as specific transfer errors.

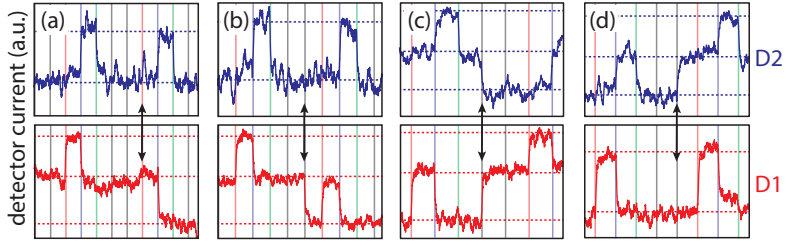


Figure 6.3:

Raw detector signals indicating errors in series charge transfer. The black double arrow marks the point at which the error occurs, all errors are of the type "missing cycle". (a) Failure of quantum dot QD1 in single operation during the marker sequence. (b) Error by QD1 in series operation. (c) Error by QD2 in series operation. (d) Error by QD4 in series operation.

The simplest case is the occurrence of a transfer error during the marker sequence: Since only one dynamic dot is triggered, the resulting change in the detector signal directly reflects the number of electrons transferred. If, as exemplary shown in Fig. 6.3a), the detector states remain constant after triggering QD1 (for a properly working dot QD1 we expect the number of charge carriers on node 1 to increase by 1), this type of signature is attributed to a missed cycle by QD1 (i.e., no electron has been transferred). The pulse under discussion is marked by a black double arrow. By the following pulse, triggering QD2 (blue vertical line), an electron is transferred from node 1 to node 2, leading to a drop in the baseline of detector D1.

In series operation, the attribution of errors is slightly more complicated and demands correlation of both detectors for proper interpretation. Consider the situation depicted in Fig. 6.3b) as an example, marked by the black double arrow. Taking D1 as the only source of information, one can only state that node 1 contains one electron less after the second series pulse (the sign of the occupation difference can

be obtained from the marker sequence as discussed later). This may be caused either by QD1 failing to transfer an electron or by QD2 moving two electrons from node 1 to node 2 and QD1 operating properly. But with both detectors, this uncertainty can be lifted: If the latter was the case, one would expect to observe detector D2 to indicate a surplus electron on node 2 (two electrons would be moved by QD2 onto the node while only one electron is removed by QD4 leaving one excess electron on the node). But in the case depicted in b), detector D2 remains constant before and after the pulse from which we deduce that most likely QD1 missed a transfer cycle.

Similarly, also errors by the other two dynamic quantum dots may be deduced from the detector signals. In Fig. 6.3c) a missing-cycle event is shown during series operation by QD2: Detector D1 indicates a surplus electron on node 1 while D2 reflects a missing electron (at the series pulse marked by black double arrow). Thus, the baseline of both detectors shifts by one electron, for D1 upwards (plus one electron) and for D2 downwards (minus one electron). Likewise, a missing-cycle event of QD4 only affects the charge state of node 2 with the number of carriers on node 1 remaining constant before and after the pulse (comparable to b) for QD1). This is illustrated in the example in Fig. 6.3d).

6.3 Details of the counting algorithm

After this basic description of the underlying principles of the measurement, the counting algorithm is detailed which converts the detector signals into electrons transferred across the device.

In advance of the specific analysis of detector time traces, we perform a self-consistent calibration of our detectors in terms of electrons on the node. In this step, we use only the detector responses during the marker sequence. Based on the assumption of only unidirectional

charge transfer (which is fulfilled in the regime of all dynamic quantum dots transferring about one electron per pulse), we obtain two informations from each pulse: These are the polarity of the response and the amplitude. Obviously, the response at a specific working point of the detector (being, e.g., dependent on the edge of the detector's response, the applied bias voltage across the detector and the capacitive coupling to the node) is directly given as the difference in the detector current before and after the pulse. Moreover, also the information about the edge of the detector's response is encoded (by triggering the dynamic dot QD1 for example, we only increase the number of electrons on the node 1). To clarify this, the main result of this analysis is shown in Fig. 6.4. To keep the following explanation as simple as possible, only half of the SET period is discussed which we refer to as the rising edge (hatched region). The analysis for the opposite edge of the SET is done accordingly.

In a) and c), the detector currents in response to changes of the appropriate local gate voltage are shown demonstrating once more the periodicity of the response. Horizontal dashed lines indicate limits of sensitivity derived by the counting algorithm and discussed later in this chapter. The hatched region in plots a) and c) mark the area which we refer to as the rising edge of the SET since an additional electron on the node (carrying a negative potential) will lead to an increase in detector current (positive response). From the exact knowledge of timing of pulses, we know a priori which pulses trigger a specific dynamic quantum dot and thereby lead to an enhancement or reduction of the number of charge carriers on each node. E.g., triggering QD1 (QD4) will only enhance (reduce) the number of electrons stored on node 1 (node 2) while QD2 will reduce the number of electrons on node 1 and increase the number of electrons on node 2.

We therefore evaluate the responses of both detectors ΔI for pulses relevant for the corresponding node separately as a function of the ini-

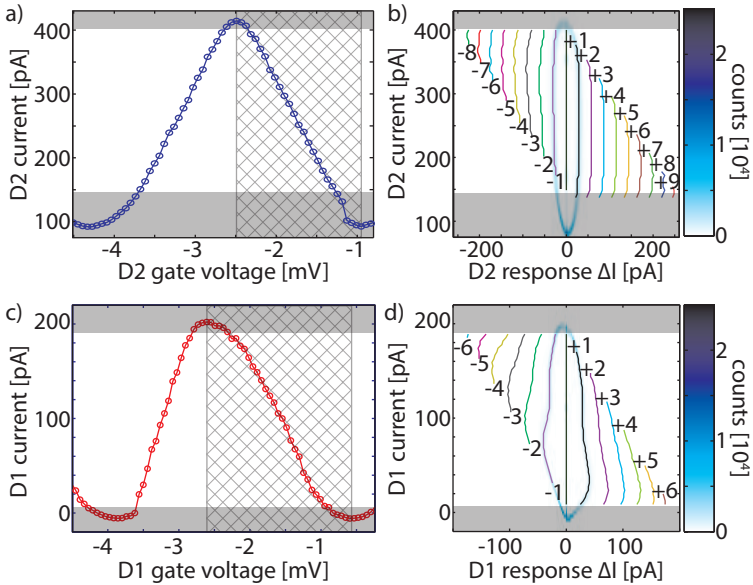


Figure 6.4:

Evaluation of the SETs' response to the marker sequence. In a) and c), the detector currents in response to variation of the local gates for fixed bias voltages are shown for D2 (a, blue dots and line) and D1 (c, red dots and line), respectively. The shaded regions mark what is referred to as the rising edge (positive response to negatively charged electrons on the node). For SET working points within this region, the marker sequence is evaluated and a histogram of the detector response ΔI (difference of detector current before and after the pulse) as a function of SET current before the pulse (which we refer to as the working point of the SET) is performed. Panels on the right hand side show the frequency distribution of (response, working point)-pairs for single electron transfer for D2 (b) and D1 (d), respectively. Negative response corresponds to a reduction of electrons on the node, a positive one to an enhancement. Only pulses directly affecting the charge state of the node have been taken into account. Due to the setting of the dynamic quantum dots, the main maxima reflect the transfer of ± 1 electron onto/off the node. Lines in vertical direction indicate the extrapolated detector response for a larger deviation in electron number on the node based on the maxima found for single-electron transfer. Grey shaded areas (top and bottom) mark in all plots the limits of sensitivity (details discussed in the text).

tial working point (i.e. SET current) before the pulse. The result is a two-dimensional frequency distribution for pairs of (SET response, SET working point) with the dominating maximum for a response unequal zero corresponding to the signature of ± 1 electron on the node which is presented in panels b) for detector D2 and d) for detector D1. Dark color indicates a large number of counts (of the order of 20000 events), white to zero counts. The y-axis reflects the SET working point (same axis as the y-axis in a) and c), respectively), the x-axis the response (i.e. difference in SET current before and after a pulse ΔI) derived from the analysis. The weak, additional maximum at zero response is visible, indicating transfer errors by the dynamic quantum dots. A negative response for the rising edge of the detector indicates a reduction of electrons on the node, a positive one an increase in electrons on the node.

The next step in detector calibration consists of a detection of maxima in the SET response (i.e. finding the response for ± 1 electron on the node) for each working point. From this information, a prediction of the SET response for an arbitrary number of up to ± 9 electrons on the node is performed which is indicated by the lines in vertical direction. Taking as an example detector D2 and an initial working point of $I = 200$ pA, the response for one additional electron on the node equals about $\Delta I \approx 29$ pA, leading to a final state of the detector at $I = 229$ pA. We may then start at this point to find the response for another electron on the node (which is again $\Delta I \approx 29$ pA) to predict a detector's response equalling $\Delta I \approx 58$ pA of D2 starting initially at $I = 200$ pA to two electrons transferred onto the node 2. On the rising edge of the SET's response function, the number of detectable electrons on node 2 reduces with increasing initial working point. Under optimal conditions, a change of 9 electrons on node 2 may be detected by D2. The detectable number of electrons on node 1 by D1 is limited to 6 due to the higher response to an electron on the node (lower

capacitance of the node 1).

The key idea here is that the detectors' response is intrinsically validated and is independent of, e.g., amplifier gain or other technical aspects. Using our approach, it is similarly possible to use, e.g., the whole node (thereby reducing the response to one electron due to the higher node's capacitance) or change the sequence pattern but still the detector response may be characterized by analysing the impact of an surplus or missing electron on the node on the corresponding detector(s).

Secondly, also the contributing dynamic quantum dots are fully characterized by obtaining their respective transfer probability distributions in the same mode of operation as during current generation. Finally, the comparison between the individual transfer characteristics and the observed detector patterns in series operation may also be used to determine drifts in the operation of the dynamic quantum dots on long time scales.

Using this approach, we obtain for both detectors D1 and D2 and for both edges of SET response separate reference tables containing the SET current levels before any charge transfer together with the response to a change of electrons on the node of up to ± 9 . We now compare the time traces with the prediction from the reference tables to convert the detector signals into a sequence of electrons transferred between source, the nodes, and drain based on the mean detector currents between each pulse.

The evaluation is exemplary shown in Fig. 6.5 containing in a) the two raw detector signals D2 (blue trace, upper panel) and D1 (red trace, lower panel) together with the color-coded pulse pattern as vertical lines. Additionally, the detector levels indicating distinct charge states of the corresponding nodes are depicted as horizontal dashed lines as guides to the eye. All dynamic quantum dots are tuned to transfer approximately one electron per transfer pulse. Both detectors occupy four different states within this window corresponding to 22 periods

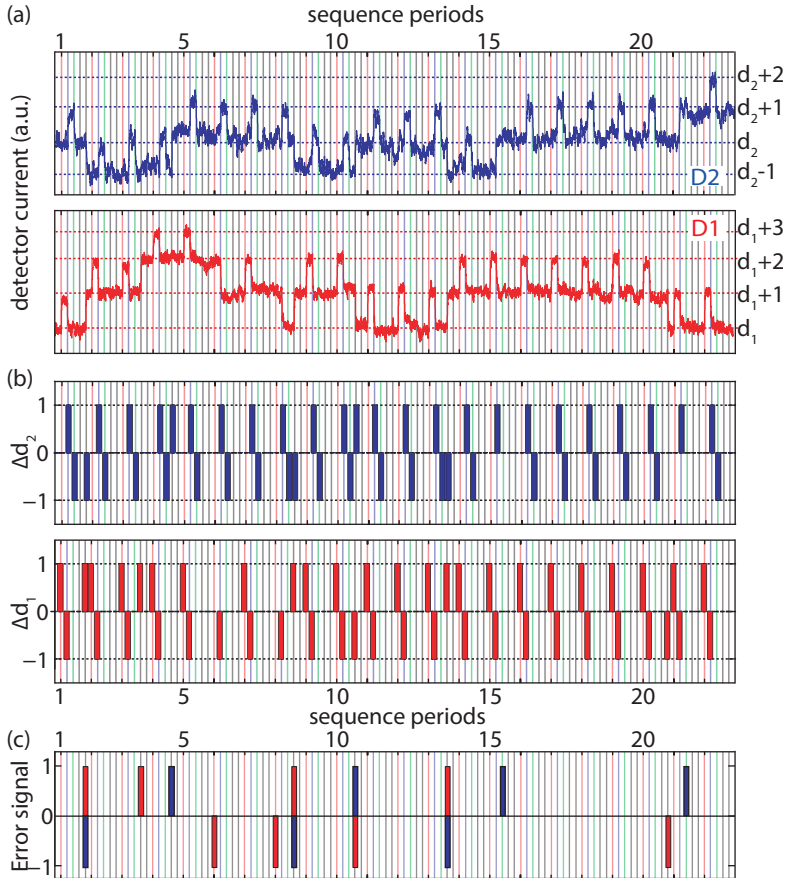


Figure 6.5:

Raw detector traces (a) together with derived counting (b) and error signals (c) for a time interval of 22 periods equalling 2.2 s. Data attributed to detector D2 is coloured in blue while the corresponding data for detector D1 is encoded in red. Details are given in the text.

of the pulse pattern (equalling a time interval of 2.2 s). In perfect operation, only two states are occupied (due to the signature of single-electron shuttling during the marker sequence, c.f. Fig. 6.2), but erroneous charge transfer deviating from one electron per cycle by any of the dynamic dots leads to a change in the two states involved. Panel b) contains the evaluated counts for detector D2 (blue, upper panel) and D1 (red, lower panel), respectively.

The horizontal lines indicating the different states of occupation might suggest that also an evaluation using the algorithm based on level detection is suitable for the extraction of counts (as used to characterize the individual dynamic quantum dots). But, there is an important difference underlying the two types of measurement: In the characterization of the single dynamic dot, intermediate reset pulses lead to a stabilization of the nodes' charge states around an equilibrium value given by the potential of the leads. In contrast, the detector signals may vary over several periods of the SET response in series operation of the dynamic quantum dots. Compare in this context also the cross-coupling from charge on node 1 to detector D2 and vice versa (see, e.g., Fig. 7.1). This makes the level detection and attribution impossible since one main requirement is that the detectors remain on the same edge of the response. In contrast, the charge on the nodes in series operation is an independent parameter given predominantly by the difference in working points of the dynamic quantum dots. However, the algorithm presented in this section is able to analyse the former type of measurement leading to the same results, yielding a strong indication for the integrity of the analysis.

By comparison of the counting traces in Fig. 6.5b) with the expected pattern of detector response (given by the pulse sequence), one can easily derive the error signals for both detectors. For D1, one expects the sequence $(+1, -1, 0, 0, 0)$, corresponding to the sequential transfer of the marker electron, then removal of the surplus electron from

node 2 by triggering QD4 which is not monitored by D1, and finally followed by two series pulses during which the in- and outflow of electrons onto/from the node equal. For D2, similar considerations yield the counting sequence $(0, +1, -1, 0, 0)$.

The error signal, shown in Fig. 6.5c) for both detectors and colour-coded correspondingly, is then obtained by subtraction of the expected signal from the derived counting signal. Overall, the number of electrons on node 1 remains constant on average over the time interval chosen, while at the end of the time window node 2 contains one surplus electron. The analysis reveals two errors caused by QD1 and another two by QD4, respectively, during the marker sequence, all of the type "missing-cycle" (QD1 in periods 6 and 8, QD4 in periods 15 and 22) while QD2 operates perfectly throughout all marker sequences. Additionally, there are seven errors in series operation within this time window (periods 1, 3, 4, 8, 10, 13 and 20). The details of attribution of series errors to certain scenarios of single-electron transfer is discussed in the following section after discussing an additional property of the marker sequence.

6.4 Results and discussions

The main advantage of the marker sequence compared to the series operation is that the outcome of each pulse is immediately attributed to the dynamic dot triggered - without any further analysis or uncertainties (assuming, that the detectors do not count erroneously). Therefore, for a specific point of operation, the full transfer probability distribution of each dynamic quantum dot can be derived - with maximal certainty. For each setting of working points, time traces of 10 minutes are taken, containing 5970 sequence periods and thus also the same number of individual pulses per dynamic quantum dot as marker events. After rejection of sequences in which the corresponding detector was

insensitive, one obtains, e.g., for the setting used for the time trace of Fig. 6.5 in total 4151 events for QD1, 4480 events for QD2 and 1333 events for QD4. QD2 holds an exceptional position interconnecting the two nodes and therefore being observed by two detectors. The two detectors are evaluated independently in this step and their results are averaged. In this example, detector D2 is sensitive only for about a quarter of the series of pulses, leading to a small number of detectable events for QD4 while the outcome of pulses applied to QD2 is still detectable by evaluation of D1. Please note that the algorithm for the following analysis has been refined in comparison to Ref. [63], leading mainly to differing time intervals by changing the limits of sensitivity. Due to the now slightly differing data sets, the absolute numbers in this section may differ slightly while the main results remain valid.

6.4.1 Error accounting

Since only a finite time-trace containing in maximum 5970 events is evaluated (in the case of detectors being always sensitive), there might be a chance that unlikely events are missed. Therefore, we set the number of counts for all events not being observed in the time-traces to one. Finally, the number of counted events for each QD and electron number transferred is divided by the sum of all events obtained for this QD, leading to the probability distributions in Fig. 6.6a). The number of electrons transferred per cycle by each QD is limited in the evaluation to 3 in maximum (the dynamic quantum dots are all tuned to transfer approximately one electron, therefore the transfer probabilities from $n_e > 2$ are typically negligible, cf. the characterization of an individual dynamic dot in section 5.2).

Obviously, the highest transfer probability for each dynamic quantum dot is for $n_e = 1$ as expected (red section), i.e. the charge transfer is indeed dominated by single-electron transfer: $P_1^{QD_i} > 0.9 \forall i$,

$i = 1, 2, 4$. The dynamic dots QD1 and QD4 are set to operate at the transition $n_e = 0 \leftrightarrow 1$ electron per cycle, i.e. if any of the two causes an error it is most-likely of the type "missing cycle", i.e. no electron is transferred. This is in good agreement with the observations from the error current in Fig. 6.5c) where both dynamic dots missed to transfer an electron at two marker pulses each. In contrast, QD2 deviates in the opposite direction by transferring two electrons with probability $P_2^{QD2} = 1.6\%$, according to the analysis. Its probability to transfer zero electrons is rather low (about $P_0^{QD2} = 0.3\%$). For none of the dynamic quantum dots a transfer event of three electrons has been observed, so that the probability attributed to this case equals the inverse of the total number of marker events for this specific QD at this setting of operation. For QD1, also the transfer of two electrons has not been observed experimentally within the time trace at this setting.

Although the transfer probabilities are comparable, they do not equal. Since charge conservation holds, the number of electrons on the node accumulated throughout the time-trace equals the difference between incoming and outgoing electrons. QD1 adds on average 0.94 electrons per cycle onto node 1, while QD2 removes 1.01 electrons onto node 2, from which QD4 transfers 0.97 electrons per pulse. In summary, this action leads to a positively charged node 1 and an oppositely charged node 2. In the long-term limit, all QDs should equal in the number of carriers transferred since the nodes may not be arbitrarily charged (see also the discussion about mesoscopic feedback in chapter 7), but apparently this limit is not yet reached within the measurement time. QD2's point of operation is changed most-frequently in this dataset, while operation of QD1 is varied in an outer loop and QD4's control gate voltages are held constant. The charge states of the nodes are not equilibrated between two subsequent settings.

In the discussion so far the observation of constant detector signals

6 The self-referenced current source

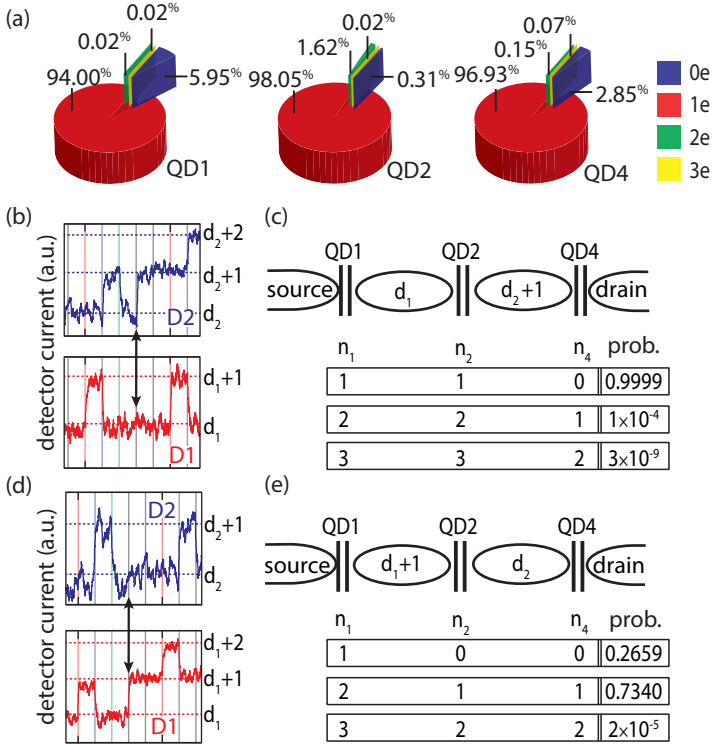


Figure 6.6: Exemplary demonstration of error accounting. Pie charts in a) symbolize the average transfer probability distributions of the dynamic quantum dots QD1, QD2 and QD4 (from left to right) at the specific operation point (same data set as plotted in Fig. 6.5) as derived from the analysis of marker pulses. In b), a detail of the trace in Fig. 6.5 containing the sequence period 4 is shown where an additional electron is detected on node 2 during series operation, accompanied by a schematic containing different scenarios of realization and the corresponding probabilities in c). In d) and e), the same as in b) and c) is shown for sequence period 3 where an additional electron on node 1 is identified during series operation.

in simultaneous operation has been attributed to perfect single-charge transfer by all dynamic quantum dots. But imagine that none of the dynamic quantum dots transferred an electron at the same pulse: The resulting detector signals are the same as in single-charge transfer by all dynamic dots (both detectors remain in the same state before and after the pulse), but in this case no electron has been transferred. This example illustrates that in fact one needs to answer the question: "Which is the most-likely scenario of charge transfer by the dynamic quantum dots that is in accordance with the observations by the detectors?"

Due to the knowledge of the individual transfer probability distributions of all dynamic QDs contributing in series charge transfer, one may attribute probabilities to each of the scenarios compatible with the detector signals. Coming back to the initial example and considering the actual points of operations (cf. Fig. 6.6), it is quite fair to state that for this working point the conclusion of perfect charge transfer from constant detector signals is valid: The probability for all pumps failing equals $P_0^{QD1} \cdot P_0^{QD2} \cdot P_0^{QD4} / \left(\sum_n \prod_i P_n^{QDi} \right) = 6 \cdot 10^{-6}$, i.e. statistically in only six of one million cases all pumps will fail simultaneously, while in 99.9994% all pumps transfer exactly one electron. The transfer probability of simultaneously two electrons by all pumps during a series pulse is already of the order of 10^{-9} .

As an illustration how the analysis is conducted for a time-trace like the one shown in Fig. 6.5, two situations are chosen exemplary with the first one taken from sequence period 4 (shown again in detail in Fig. 6.6b). During the first pulse in series operation, the detector D2 changes its charge state from d_2 to $d_2 + 1$, indicating a surplus electron on node 2, while detector D1 remains in charge state d_1 . This situation is depicted schematically again in Fig. 6.6c) together with different scenarios of realization. From the measurement one can only state directly that QD4 has transferred one electron less than the other

two dynamic dots QD1 and QD2 (which both transferred the same number of electrons during this pulse). Therefore, limiting the possibilities to charge transfer with $n_e^{QD_i} \geq 0 \forall i = 1, 2, 4$ and the conformity with the detector signals, one obtains the following scenarios: $(n_e^{QD1}, n_e^{QD2}, n_e^{QD4}) \in \{(1, 1, 0), (2, 2, 1), (3, 3, 2)\}$.

The likeliness of each scenario is then related to the product of the probabilities describing the corresponding charge transfer by each dynamic quantum dot. Because the sum of probabilities for each QD is normalized to one, also the sum of all combinations of all probabilities for the three dynamic quantum dots equals one. But since we consider here only a small subset of combinations (reduced due to the additional information from the detector signals), these probabilities have to be renormalized by the sum of all conceivable probabilities which then results in the probability of each scenario. For the exemplary case here, the first scenario including only a single quantum dot failing (with QD4 transferring no electron at this pulse) is the most likely one with probability of 0.9999. The process underlying the scenario with second-largest probability involves erroneous charge transfer by already two dynamic quantum dots with likeliness of 10^{-4} . The third-order failure process with $(n_e^{QD1}, n_e^{QD2}, n_e^{QD4}) = (3, 3, 2)$ is very unlikely with an attributed probability of the order of 10^{-9} . To summarize, although the attribution of this type of detector signals indicating a transfer error is accomplished with high certainty, the small chance of misattribution slightly broadens the probability distribution (resembling a growing lack of knowledge) of the number of charge carriers transferred in the time interval.

As a second example, sequence period 3 is chosen whose raw signals are depicted in Fig. 6.6d). At the first series pulse, marked by the black double arrow, detector D2 (blue) remains in state d_2 , while D1 (red) changes from d_1 to $d_1 + 1$, indicating a surplus electron on node 1. Figure 6.6e) contains again the sketch of the situation experimen-

tally observed together with the table containing the charge transfer scenarios $(n_e^{QD1}, n_e^{QD2}, n_e^{QD4}) \in \{(1, 0, 0), (2, 1, 1), (3, 2, 2)\}$ and their respective probabilities. While the last-mentioned scenario involving erroneous charge transfer by all three pumps is unlikely again, the probabilities for other two cases are of comparable magnitude. A detector signature as in this case leads to a strong broadening of the probability distribution over the number of charge carriers due to the high chance of misattribution. Therefore, signatures of this type should be reduced in order to obtain a high certainty in the number of electrons transferred. This may be either achieved by tuning the dynamic quantum dots equally to the transition $0 \rightarrow 1$ (the transfer probability distributions of the dynamic quantum dot are very asymmetric, cf. section 5.2) so that the transfer of two or more electrons per cycle becomes very unlikely or by increasing the number of dots in series.

6.4.2 Counting the number of transferred electrons

We now may use the error-accounting scheme to identify the number of electrons transferred across the device. The device's output current is defined here by the number of electrons emitted via QD4 to drain. Let us first assume the "bare" operation of the dynamic quantum dot QD4, i.e. without the serially connected quantum dots QD1 and QD2 and thus without the ability to verify the success of charge transfer. One would then expect a negative deviation of the number of transferred electrons from the ideal transfer of exactly one electron per cycle because missing cycle events are the dominant source of errors at the actual working point. The resulting probability distribution of transferred electrons as a function of the number of pulses may be calculated using the experimentally derived transfer probabilities during the marker sequence.

Figure 6.7 shows the evolution of the simulated probability distribu-

tion as a function of number of pulses as a colour plot for the bare quantum dot QD4. For higher visibility, the deviation from ideal charge transfer with $n_e^{QD4} = 1$ per cycle is plotted. Black colour corresponds to a probability of one and evolves via blue to white (probability of zero). Initially, the number of transferred electrons is well known, but quickly the exact number becomes uncertain. After 402 pulses, the maximum of the probability distribution has dropped down to 0.111 at 392 electrons transferred, i.e. most-probably one expects a deviation of 10 electrons. The variance of the distribution is $\sigma = 3.6$. In 96.2% of all realizations, the number of electrons transferred after 402 pulses N_e will be within the interval $N_e \in [385 \dots 399]$, i.e. we expect within this interval of confidence a deviation of $[-17 \dots -3]$ electrons.

These findings can now be compared to the results of error accounting of the same time-trace. We chose for the analysis the longest time interval in which both detectors remained sensitive at these specific working points of the three dynamic quantum dots. The result of the error accounting analysis is superimposed as black dots onto the evolution of the transfer probability distribution of the bare quantum dot QD4. Again, the deviation from perfect single-charge transfer by QD4 is plotted as black circles marking the position of maximum of the probability distribution. Vertical dashed lines mark the occurrence of transfer errors (black) and one event (red) resembling the second type of error with non-unique attribution.

The analysis yields three transfer errors (of type missing cycle) during marker pulses at positions labelled $(m0)$. Additionally, five errors of the same type of error during series operation have been detected, labelled $(s0)$. All these types lead to a deviation from the nominal number of transferred electrons for perfect single-charge transfer by -1 each. This is reflected by a step in the trace in negative direction at each event of this type. At pulse 249 (labelled $(s1)$, coloured orange), a different type

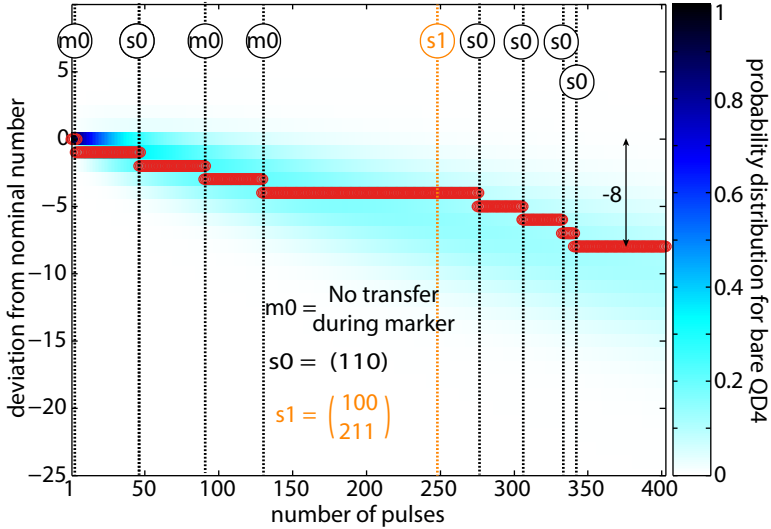


Figure 6.7:

Exemplary evolution of probabilities in time. The x-axis represents the number of transfer pulses, while the y-axis gives the deviation in transferred electrons across QD4 to drain from single-charge transfer per cycle. As a colour plot, the evolution of the simulated probability distribution for the "bare" QD4 without accounting is shown, based on the analysis of the marker sequence. Black corresponds to a probability of 1, white to 0. After 402 pulses, the maximum equals 0.111 for a deviation of -10 electrons. Superimposed by red dots is the maximum after each pulse, derived from the error accounting analysis. Steps correspond to detected transfer errors and are labelled accordingly and explained in the text. Most probably, the deviation after accounting from optimal charge transfer equals -8 .

of transfer error occurs which cannot be attributed uniquely. But, no step is shown since the most-likely scenario (underlined) explaining the signature observed involves the transfer of one electron by QD4. Before

this pulse, the maximum of the probability distribution indicated a deviation of -4 electrons with probability of 0.998 which reduces as a consequence of this signature and the uncertainties in attribution by the ratio of the both probabilities to about 0.733 .

Finally, the error accounting indicates a deviation of -8 electrons after 402 transfer pulses. For comparison, Fig. 6.8a) contains the two final probability distributions for the single dynamic quantum dot QD4 (grey) and the self-referenced current source with error accounting (blue). After accounting, the number of electrons emitted to drain is with confidence of 0.998 in the interval $n_e^{QD4} \in [393, 394]$. Moreover, the standard deviation equals $\sigma = 0.4$ which corresponds to a reduction of uncertainty compared to the single dynamic quantum dot by a factor of 9 . The result from error accounting lies well within the 96% interval of confidence of the expected probability distribution of QD4 operated individually. This meets expectations since the derived probability distribution based on error accounting is just a specific realization of the operation of the "bare" QD4 (equal to a specific random walk), but this fact can be regarded as a clear indication of consistency of the analysis.

For comparison, Fig. 6.8b) shows the probability distributions for a different setting of gate voltages controlling the dynamic quantum dots. At this specific working point, the longest error-free time interval contained 30 sequence periods, i.e. 90 electrons have been transferred to drain without any failure by any dynamic dot. In the sequence with longest continuous sensitivity of both detectors, only unique errors have been observed and therefore, the attribution of detector signals to specific error scenarios can be fulfilled with high fidelity. Within the time interval of $\Delta t = 17.9$ s (corresponding to 537 pulses onto QD4), two missed-cycle events by QD4 during the marker sequence and 7 missed-cycle events by QD4 during series operation have been observed. This corresponds to a deviation of -9 electrons from the

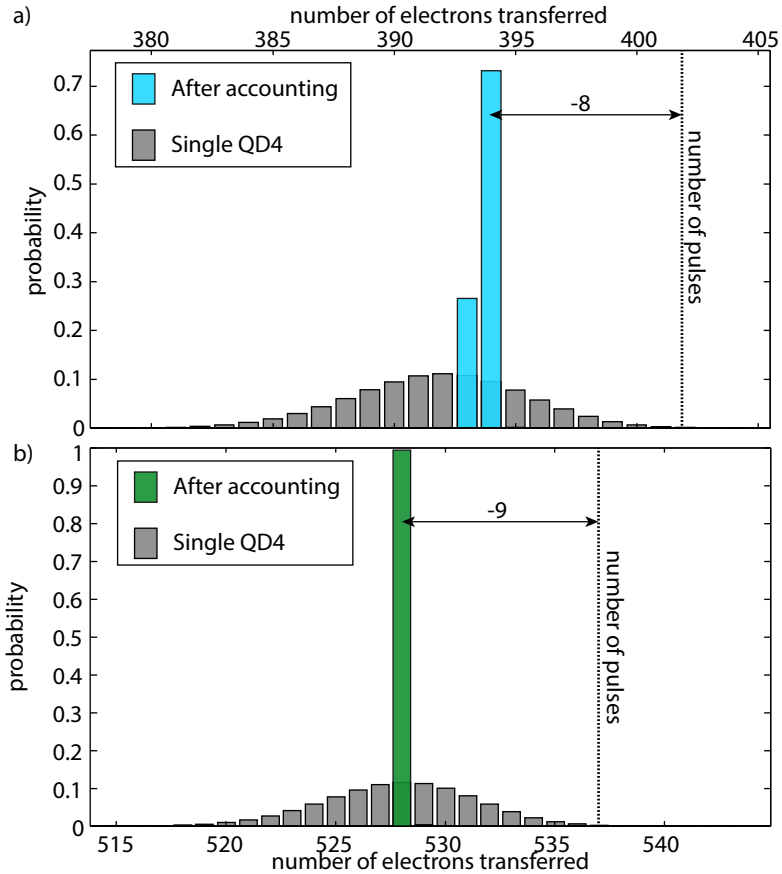


Figure 6.8:

Comparison of the resulting probability distributions after accounting to the calculated probability distributions for the bare QD4 at different points of operation. a) Final probability distributions for the same data set as in Fig 6.7 for the single QD4 (grey) and after accounting (blue). One non-unique scenario leads to a significant broadening of the probability distribution after accounting. In b), only uniquely attributable errors were observed during accounting (green). Based on the standard deviation, the uncertainty has been reduced by a factor of almost 50 compared to the single operation of QD4 (grey).

number of transfer pulses, as reflected by the maximum of the probability distribution after accounting. Thus, the analysis yields a number of 528 electrons transferred with a confidence of 0.995. The standard deviation, given by the square-root of the variance of the distribution, equals $\sigma = 0.073$. Compared to the standard deviation of the bare QD4, this resembles an improvement by a factor of about 50.

Since electric current is defined as the ratio of transferred carriers to the time interval of observation times the elementary charge e , the average output current of this device equals

$$I_c = \frac{n_e^{QD4}}{\Delta t} e = \frac{528}{17.9 \text{ s}} 1.602 \times 10^{-19} \text{ C} = 4.726 \times 10^{-18} \text{ A}.$$

Moreover, the 2σ uncertainty of this current can be calculated to $u(I_c) = \frac{2\sigma e}{\Delta t} = 1.3 \times 10^{-21} \text{ A}$ which corresponds to a relative uncertainty of $u_c = 2.7 \times 10^{-4}$ which is more than two orders of magnitude lower than PTB's actual calibration capabilities at current levels of the order of 1 fA. Currently, the charging of a capacitor is used in this low-current regime. Using such a "conventional method", an expanded uncertainty of 60000 $\mu\text{A}/\text{A}$ has been reported [Entry of the dc current calibration and measurement capabilities at PTB in the BIPM database, 171].

As an outlook and to evaluate the technical limits of the error accounting scheme, we assume a circuit of five serially connected dynamic dots and four intermediate detectors. Using the RF-SET technology, the time-resolution of the detectors can be easily reduced to 20 μs (Schoelkopf et al. reported a detector's bandwidth of up to 100 MHz [57]). Using further a transfer frequency of $f_p = 1 \text{ GHz}$ together with a transfer error probability of $|1 - P_1| \approx 1 \cdot 10^{-6}$ as experimentally demonstrated [44], a very low relative uncertainty of $u_c < 10^{-8}$ seems feasible at a current level of $I = 160 \text{ pA}$ (operating only in series with a preceding characterization of the individual dynamic dots using only the marker sequence). This would enable a vali-

dated primary realization of the redefined electrical base unit Ampere. Such device further allows a direct closure of the quantum metrological triangle [65, 66] to test the validity of electrical quantum metrology.

There is an intrinsic feature of the device of extraordinarily fascination to me which is the possibility to directly investigate deviations from the expected transfer characteristics or drifts during the current generation. Because the statistics of the observed transfer errors in series operation are just a specific realization of the previously characterized individual transfer probabilities, the results should therefore lie well within the confidence intervals obtained from the device characterization during the marker sequence. Any strong deviation from the interval of confidence is then a clear indication that there is some fault in either the preceding characterization or the series current generation and therefore the measurement should be rejected. This is contrary to the typically performed measurements in metrology where a characterization is only possible before and after the measurement.

6.5 Conclusion

To conclude, we have demonstrated the first clocked quantum current source whose output is intrinsically validated by error accounting. The statistical analysis has been presented yielding a relative uncertainty of the order of $u_c \approx 3 \cdot 10^{-4}$. Within the aA-current range (i.e. $I \approx 10^{-18}$ A), the method presented here advances the conventional, currently available techniques in calibration at PTB by two orders of magnitude. Although the current level at this first experimental realization has been rather low, the perspectives for up-scaling in terms of output current together with lowering of the uncertainty at the same time are very promising. Using such a primary realization of the redefined Ampere, the long pursued goal in electrical quantum metrology, the "quantum metrological triangle", seems feasible. This experiment

might lead to either a proper basement of electrical quantum metrology (if the experiment yields the expected results) or very exciting new insights into physics on the fundamental scale.



Series operation: Feedback and MHz repetition rates

This chapter concludes the presentation of experimental results on the series operation of dynamic quantum dots. While we focused in the previous chapter on time traces at fixed external control settings of the dots, we will initially investigate here the dependence of transfer fidelity on external control parameters in the series circuitry as well as the role of charge feedback. Another aspect discussed in this chapter is the single-charge transfer with reduced waiting time between consecutive pulses, transferring electrons in the MHz-regime and thereby addressing mainly the effect of hot electrons on the following dynamic quantum dot.

7.1 Introduction to feedback during series operation

When dynamic quantum dots are operated in series, every difference in the number of electrons transferred by the adjacent dots leads to an accumulation/reduction in the number of electrons located on the interconnecting node, depending on the sign of the error. Since electrons carry the elementary charge $-e$, this directly leads to the formation of an electrostatic potential $U = -e^2/C_{\Sigma}^{\text{node}}$ with C_{Σ}^{node} the overall capacitance of the node. It is this potential that forms the basis of all measurements presented because this quantity is detected by the capacitively coupled electrometers. However, there is a second effect of this potential since it simultaneously acts back onto the dynamic quantum dots as discussed in section 2.6.1 and Refs. [43, 108]. As an illustrative introduction to this effect, let us discuss the operation of two serially connected dynamic quantum dots which transfer electrons from an open reservoir to an enclosed drain node. With this configuration we mimic the extreme scenario of series operation of three dynamic quantum dots in which the first two dots are set to transfer about one electron per cycle each and the third one completely blocks electron transfer. The barrier is that high in this example that tunneling of electrons is fully suppressed.

The result of such a measurement is shown in Fig. 7.1 with both dynamic dots initially tuned to transfer about one electron per pulse. Vertical lines correspond to the pulse applied to QD1 (red) and QD2 (blue), respectively. Detector D1 monitors the interconnecting node between QD1 and QD2 (red trace, lower panel) and D2 the drain lead where the potential is continually increased (blue trace, upper panel). For details of this nomenclature, please see Fig. 3.7. D1 reflects the sequential transfer of electrons by the two dynamic quantum dots and switches typically between two states, numbered accordingly. Each

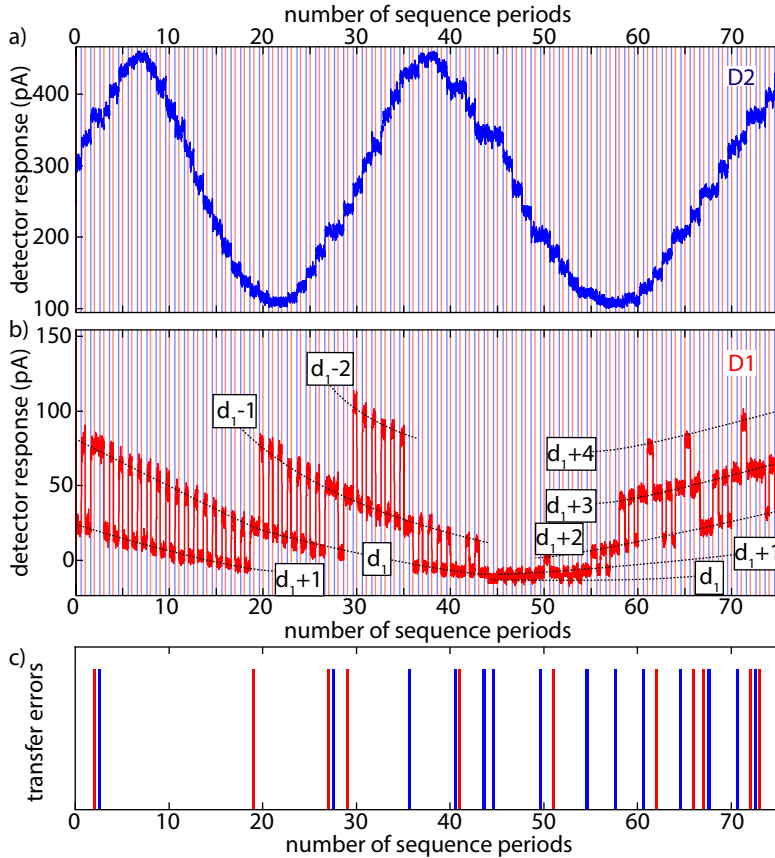


Figure 7.1:

Introductory example of feedback in series operation of dynamic quantum dots. a) and b) present the detector signals, vertical lines indicate the pulses applied. Dashed lines symbolise the different charge states of node 1. In c), the occurrence of transfer errors is indicated, color codes the corresponding dynamic quantum dot (red: QD1, blue: QD2).

transfer error results in a change of the contributing charge states. The drift observed results from the potential on node 2 and is a direct consequence of the cross-capacitive coupling of electrons on node 2 onto detector D1. About 20 electrons on node 2 cause the same signal on D1 as a single electron on node 1. D2 shows the characteristics of continuous charging of the node (comparable to the measurements shown in e.g. Fig. 5.3) because no electrons are transferred from this node to the drain lead. The number of electrons on node 2 is only changed by the preceding dot QD2 and remains constant in-between. A transfer error is reflected by a constant detector signal before and after a pulse applied to QD2 (blue vertical line) and occurs, e.g., in periods 3, 28, 36 and 41. The occurrence of errors is depicted in Fig. 7.1c), colour-coded for QD1 (red) and QD2 (blue), respectively. As intended, the measurement indicates that we increasingly charge the drain node and thereby create a negative electrostatic potential. As a result, the transfer fidelity of QD2 reduces with increasing potential at drain: While only three transfer errors are observed during the first 35 periods, the fidelity reduces to about 60% after about 55 periods.

This behaviour is also reflected in the states involved in charge transfer on node 1: While initially the first node is charged more positively (the lower state changes from $d_1 \rightarrow d_1 - 2$ until sequence period 35) due to the lower transfer fidelity of QD1, the steady reduction in transfer probability of QD2 afterwards leads to a more negative potential on node 1 ($d_1 + 4$ in maximum). Finally, this potential also affects the action of QD1, leading to an overall reduction of transfer fidelity after about 60 electrons transferred onto node 2. Moreover, this example also demonstrates quite nicely the correlation of cause-and-action: The continuously more negatively charged node 2 reduces first the transfer probability of QD2, leading to an increase of electrons on node 1 as long as QD1 maintains its transfer rates. But finally, this increasing negative potential on node 1 causes the reduction of transfer fidelity of

QD1 beyond period 65.

7.2 Parameter dependence of transfer fidelity in series operation

After this introductory example, the discussion of feedback is extended to the case of three working dynamic quantum dots in series. Here, the external conditions equal roughly the device configuration of the experiments discussed in chapter 6, but the pulse pattern is restricted only to the part referred to as the marker sequence. The advantage of omitting the simultaneous series pulses in this case is that the attribution of detector signals indicating transfer errors is unique. In Fig. 7.2 a) and b) the resulting detector signals as well as the derived counting signals in series operation are sketched for the case of perfect transfer fidelity with one electron being transferred per pulse and quantum dot.

Transfer pulses are indicated in this section again by vertical lines; colour codes the respective quantum dot triggered (red: QD1, blue: QD2, green: QD4). The detectors measure again the changes in the number of electrons on node 1 (D1, red) and node 2 (D2, blue), respectively. In Fig 7.2 c) and d), a series of transfer errors is depicted, leading finally to the reduction of the overall number of transferred electrons by one: In period 2, QD1 misses a transfer cycle, resulting in a decreased number of electrons on node 1 by one. The charge state of this node returns to the previous value during period 3 (missing cycle by QD2), leading simultaneously to a reduction in the number of electrons on node 2. Finally, in period 4, both charge nodes obtain their initial value since QD4 misses to transfer an electron. Since only one dynamic quantum dot is triggered at a time, we are able to directly determine the number of electrons on the nodes whenever the corresponding detector is sensitive.

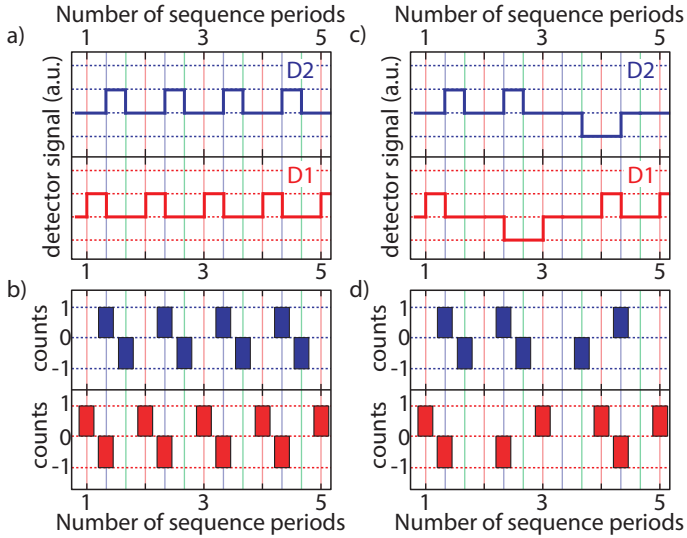


Figure 7.2:

Sketched detector signals (a) and corresponding counting signals (b) in sequential-transfer mode without transfer errors. The vertical lines indicate the color-coded transfer pulses for QD1 (red), QD2 (blue) and QD4 (green), respectively. (c) and (d) demonstrate consecutive transfer errors (missing cycle) for QD1 (second period), QD2 (third period) and QD4 (fourth period), resulting in one missing electron as compared to optimal single-charge transfer.

Real measurement data is shown in Fig. 7.3 a) for both detectors (D1 in red, lower panel and D2 in blue, upper panel) together with the evaluated counting signal in panel b). As previously, by statistical analysis of the transfer events, the full probability distributions for all dynamic quantum dots is obtained. Horizontal dashed lines indicate different charge states on the nodes as guides to the eyes. The evaluation of data however is not directly based on these levels, but is performed using the

7.2 Parameter dependence of transfer fidelity in series operation

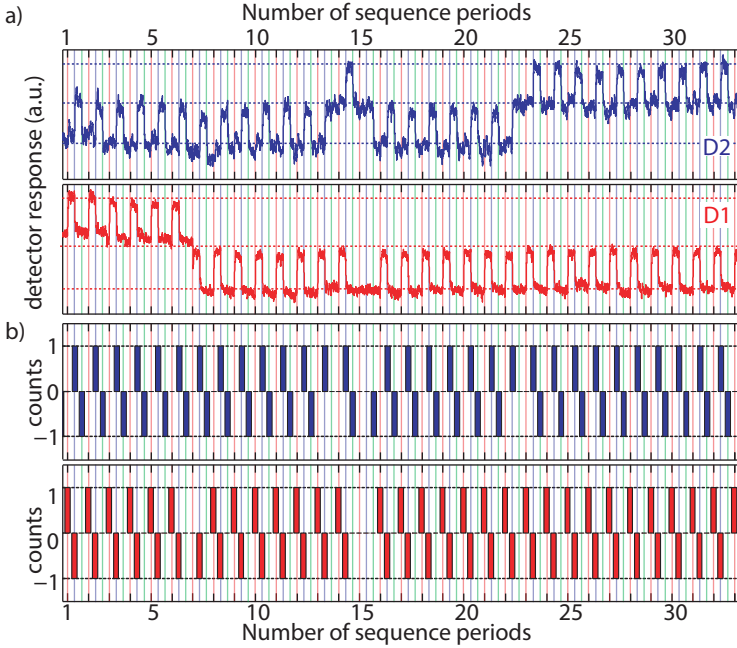


Figure 7.3:

Detector signals (a) and corresponding counting signals (b) in sequential transfer mode. QD4 is operated here at $V_{G2}^{QD4} = -176.3$ mV.

algorithm discussed in chapter 6.3. The main advantage of this type of algorithm compared to the level detection used to qualify the individual pump with equilibrated charge nodes (see section 5.2.1) within this context is the robustness against crosstalk-effects (as observed for, e.g., the introductory example in Fig. 7.1). At this specific point of operation, only zero and single-electron transfer events are observed. The rather regular patterns indicate an average probability of $P_1^{QDi} \lesssim 1$ for all dynamic quantum dots $i = 1, 2, 4$. During the 32 periods shown,

QD1 misses two cycles, QD2 one and QD4 again two cycles. Moreover, by summing the number of counts for each node, we additionally gain information about the change in the number of carriers located on each node. Within the interval displayed, the number of electrons is reduced on node 1 by one electron and is increased by one on node 2.

Setting a specific working point of the dynamic quantum dots is complicated here since there are basically two types of tuning parameters defining the transfer characteristics of each dynamic quantum dot: These are, as previously, on the one hand the control gate voltages (essentially the voltage applied to the exit gate G2, provided the operation on the main plateau) and on the other hand the potentials on the nodes which cannot be controlled externally. The control gate voltages are set as follows: QD1's exit-gate voltage is set to $V_{G2}^{QD1} = -190$ mV, QD2 to $V_{G2}^{QD2} = -200$ mV and QD4's exit-gate voltage V_{G2}^{QD4} is varied from -175 mV (operating in the open regime, thus transferring a large number of electrons per cycle) to -225 mV (fully blocking). As a reference for the specific parameter dependence of this dynamic dot, see Fig. 5.21 (please note that in order to obtain this figure only transfer events for $n_e \leq 3$ have been evaluated). Between two gate-voltage settings, the node's potential is held constant, a new gate-voltage setting is applied and the next time trace is taken. While setting new parameters, the measurement of the detector signals is interrupted. The statistical base, given by the number of transfer events per parameter setting, is (in maximum) only 450 periods per control gate setting of QD4, leading to a comparably large statistical uncertainty. Possible insensitivities of the detectors will further reduce the number of events detectable.

7.2.1 Evaluation of transfer probabilities

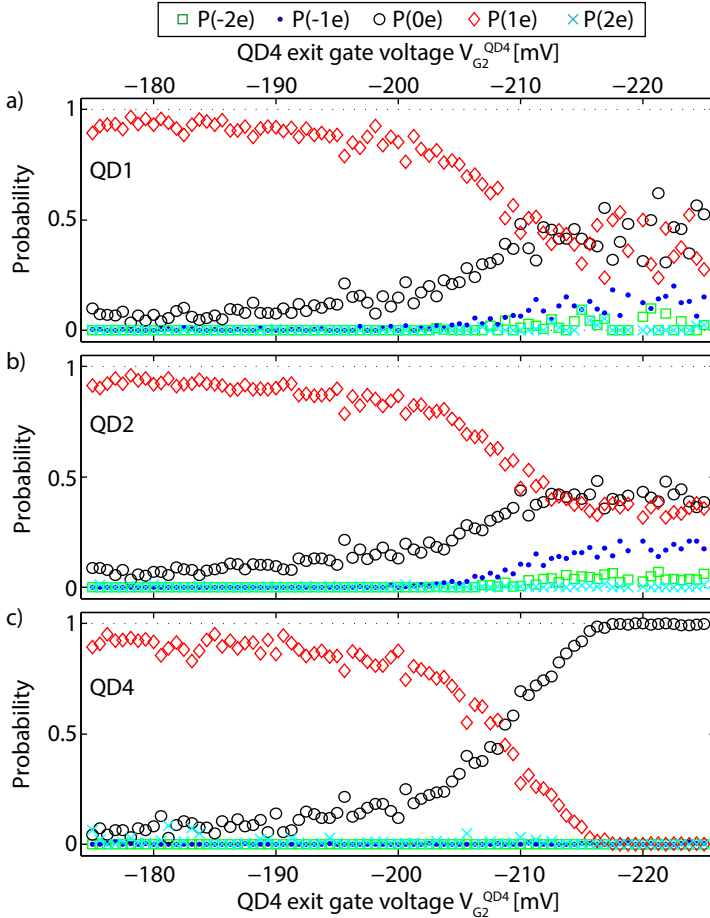
The resulting number of electrons transferred per cycle is predominantly given by the setting of QD1 which loads electrons from an open

7.2 Parameter dependence of transfer fidelity in series operation

source reservoir at constant electrochemical potential and is therefore the most robust quantum dot in this serial arrangement. Its operation point is set here to transfer about one electron per cycle as derived from Fig. 5.15 (neglecting here cross-coupling effects from the gate-voltages tuning neighbouring dynamic quantum dots). QD2 is nominally tuned to about $n_e^{QD2} \approx 0.6e$ per cycle. Finally, QD4 is set, as already mentioned above, to the open, unquantized regime (see Fig. 5.21) where this dot transfers a large number of electrons per cycle.

However, the initial guess of transfer rates from the working of the individual quantum dots (without a considerable number of excess charge carriers on the nodes) can only be regarded as a starting point to understand the series operation in the long-time limit: When the dynamic quantum dots are operated serially, the possible charge accumulation on both nodes is an additional, relevant tuning parameter of the transfer rates of the neighbouring quantum dots. This charge accumulation, resulting from any momentary difference in transfer rates, forms an electrostatic potential on the node influencing the charge transfer by both adjoining dynamic quantum dots. The asymmetry in this so-called mesoscopic charge feedback [43], acting much more strongly onto the subsequent than onto the preceding dynamic dot (in the direction of charge transfer) as discussed in section 2.6.1, will finally lead to an equilibration of transfer rates.

This expectation of asymmetric charge feedback is already confirmed in the raw-data trace in Fig. 7.3 where all dynamic dots transfer about one electron per cycle although the setting of QD4's control gate voltage - based on the individual characterization - suggests a larger number of electrons $n_e \gtrsim 2$ transferred per cycle across QD4. The detailed parameter dependence of transfer probabilities of P_n^{QDi} , ($n = -2 \dots 2$) for all dynamic quantum dots $i = 1, 2, 4$ as a function of QD4's control gate voltage V_{G2}^{QD4} is displayed in Fig. 7.4 for QD1 (a), QD2 (b) and QD4 (c), respectively, on linear scale.


Figure 7.4:

Evaluation of transfer probabilities in series operation (sequential-transfer mode) as a function of working point of QD4. The transfer probabilities are shown for QD1 (a), QD2 (b) and QD4 (c), respectively, as a function of QD4's control gate voltage $V_{G_2}^{QD4}$. The voltages to control QD1 and QD2 are fixed at nominally about $1e$ per cycle (QD1) and $0.6e$ per cycle (QD2), while $V_{G_2}^{QD4}$ is stepped from -175 mV (operating in the open, unquantized regime) towards fully blocking at -225 mV.

7.2 Parameter dependence of transfer fidelity in series operation

Over a wide parameter range (with $V_{G2}^{QD4} \gtrsim -200$ mV), the main contributing process is the transfer of one electron per pulse, i.e. $n_e = 1$. This conforms with the expectation of device operation, being dominated by the dynamic quantum dot QD1 which is set to operate close to perfect single-charge transfer. Moreover, the transfer probabilities of all dynamic quantum dots equal on a coarse scale as one might expect since every deviation causes a charge built-up on the node, thereby leading to a convergence of transfer rates of adjacent dynamic quantum dots. But, the probability of precise single-charge transfer P_1 reaches only about 0.9 for all the quantum dots QD1, QD2 and QD4, respectively, most-likely due to the setting of QD2 which effectively reduces the transfer probability of QD1 by feedback via node 1. The effect of QD4's exit gate is rather weak for voltages $V_{G2}^{QD4} \gtrsim -200$ mV, but dominates the transfer probabilities of all serially connected dots beyond when quenching the charge transfer by the increased barrier formed, as apparent in Fig. 7.4c). At QD4's gate voltages $V_{G2}^{QD4} \lesssim -215$ mV the charge transfer by QD4 is completely suppressed. This strongly affects the working of QD1 and QD2 via charge feedback, leading to a reduction in the probability P_1 to transfer one electron per cycle and increasing P_0 . Details of the resulting behaviour of the dots QD1 and QD2 in this regime (referred to as the break-down of unidirectional charge transfer) will be discussed in section 7.2.3. Another subtle feature in this analysis is the initial convergence of charge-transfer probabilities of the dynamic quantum dots, leading to a rising single-charge transfer probability for all quantum dots in the parameter range -175 mV $\leq V_{G2}^{QD4} < -178$ mV.

7.2.2 Evaluation of charge built-up on the node

Since we perform single-electron charge detection, one obvious approach towards a more detailed analysis of the observed behaviour of

the series of dynamic quantum dots is to analyse the charge built-up on the node. Since the electrochemical potentials of both nodes are not reset between two different gate-voltage settings by equilibration with the leads, the cumulative number of surplus/missing electrons derived by counting has to be examined. The resulting dependence of these quantities on the gate voltage V_{G2}^{QD4} tuning the operation of QD4 is shown in Fig. 7.5a) (red, open circles for node 1 and blue, open squares for node 2). The grey-shaded region for most negative voltages of V_{G2}^{QD4} will be excluded from further analysis since here the algorithm, being based on the assumption that electrons are predominantly transferred unidirectionally, possibly fails.

The just mentioned initial convergence of transfer probabilities for most positive gate voltages is one of the features apparent in this graph: Since the largest deviation of adjacent dynamic quantum dots is between QD2 (transferring on average below one electron per pulse) and QD4 (operating initially in the open, unquantized regime), the number of electrons on the interconnecting node 2 is reduced much stronger than on node 1. As further expected, the reduction in the number of electrons transferred by QD4 by continually applying a more negative gate voltage onto the exit gate leads to an increase in the number of electrons stored on the nodes.

One possible source of error in this analysis is caused by the circumstance that the detectors are not able to monitor the change of the nodes' charge states continuously. However, regions of insensitivity can be corrected for by the information about the slope of the detectors before and after the insensitivity: If in both cases the detector operates on the, e.g., rising edge, then the charge state of the corresponding node has been re-obtained. In contrast, when the edge is opposite after the time the detector was insensitive, then a certain number of electrons must have been added/removed to/from the node in order to achieve the new detector state. This number can be estimated from the com-

7.2 Parameter dependence of transfer fidelity in series operation

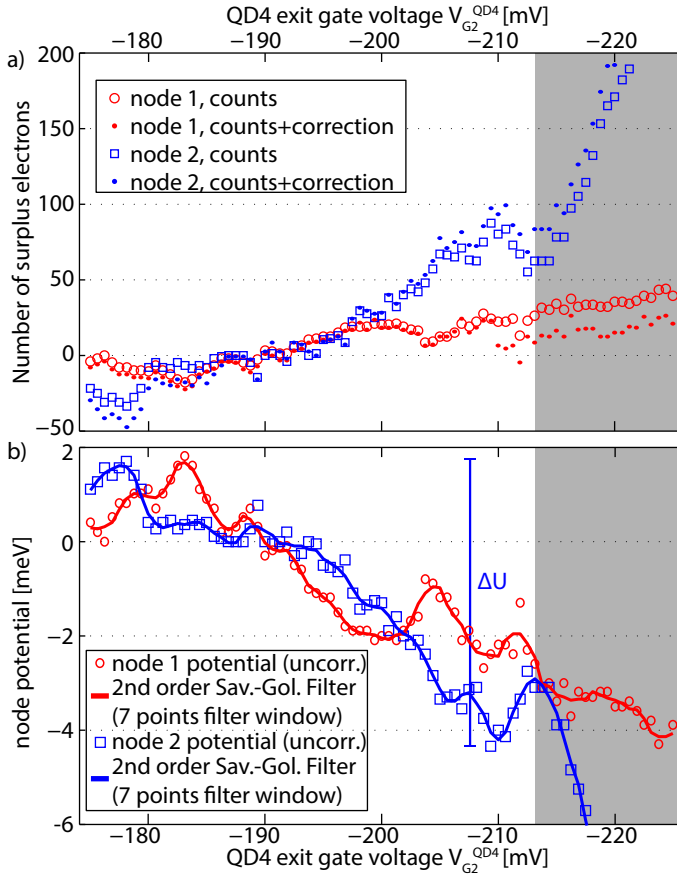


Figure 7.5:

Evaluation of charge accumulation on the nodes in series operation (sequential-transfer mode). Same dataset and x-axis as in Fig. 7.4. a) The number of additional charge carriers (based on the counting data) on node 1 is shown as red open circles, the number of surplus electrons on node 2 as blue open squares. Corrected values including additionally the number of electrons to pass regions of insensitivity are displayed by dots. b) Resulting potentials on both nodes (based on the direct counting data), calculated using the node's capacitances derived in section 5.1.3.

parison of the SET current in response to an electron on the node with the response to its local gate voltage. The result of this analysis is indicated by the dots in Fig. 7.5a) coloured in red (node 1) and blue (node 2), respectively. Qualitatively, the same behaviour is obtained as for the uncorrected data while the absolute difference in the two sets of data provides an estimator of the possible error.

Using the capacitances of the nodes derived in section 5.1.3, the number of surplus or missing electrons (without considering here the correction of insensitivity) is converted directly into a potential on the node as shown in Fig. 7.5b). Additionally, smoothed data is shown by the solid lines in red (node 1) and blue (node 2), respectively. The potentials derived are of almost equal amplitude for both nodes, ranging from $U \approx +2$ meV to $U \approx -4$ meV. If additionally the correction of insensitive regions is considered (not shown), one obtains a modulation of the node's potentials of about $\Delta U \approx 7.5$ meV.

This value agrees well with a comparable measurement (shown in Fig. 7.6) of the series operation of QD1 and QD4 (with QD2 grounded) driven by continuous-wave signals (frequency $f_p = 39$ MHz as in pulsed mode, but without any intermediate delay between pulses) with the large interconnecting node, whose charge state is monitored by detector D2. QD1 is set here again to transfer about one electron per cycle (confirmed by current measurements on the semiconducting channel) while in a) the point of operation of QD4 is varied using both, entrance- and exit-gate voltages.

Since the repetition rate is much higher than the detector's bandwidth, single-charge resolution cannot be obtained by the detectors. However, the average charge state of the node can be derived. A large plateau in the current is obtained (not shown) corresponding to the transfer of one electron per cycle by both dynamic quantum dots, marked by the white, dashed polygon. This is accomplished by continuously charging the node in order to compensate for the change in the control-

7.2 Parameter dependence of transfer fidelity in series operation

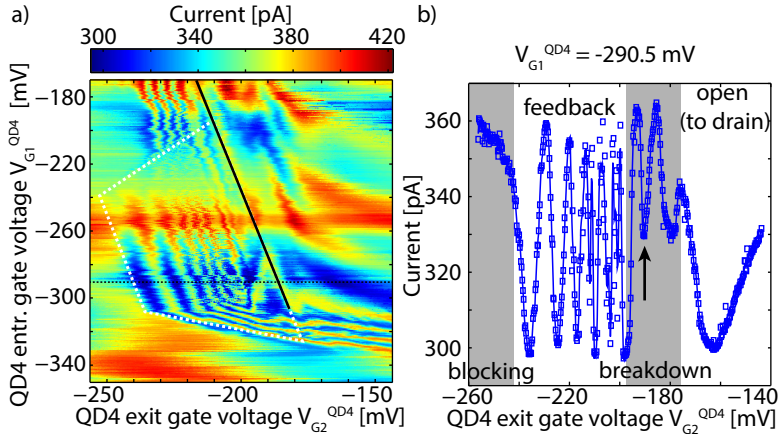


Figure 7.6:

Mesoscopic feedback using QD1 and QD4 with cw drive. a) QD1 is set to transfer about one electron per cycle while the working point of QD4 using both entrance and exit gate voltages. The signal shown is the current across detector D2. b) Single trace for fixed entrance-gate voltage of QD4 with $V_{G1}^{QD4} = -290.5$ mV. About 6.25 periods are passed from blocking ($V_{G2}^{QD4} = -260$ mV) to breakdown of quantized-charge transfer ($V_{G2}^{QD4} \approx -190.5$ mV), marked by the black arrow.

gate voltages of QD4, leading to the periodic response of the SET within the white, dashed polygon. The region of break-down of unidirectional charge transfer is indicated by the black solid line. Due to capacitive cross-coupling of the modulation signal applied to the dots onto the detector, the amplitude of the detector's response changes, but its periodicity, given by the capacitive coupling between detector and node via the floating gate, should be maintained in terms of the node's potential/ number of electrons on the node.

In b), the detector current across D2 as a function of the exit-gate voltage of QD4 is shown for fixed QD1 and $V_{G1}^{QD4} = -290.5$ mV

(dashed line in a)). Four different regions can be identified, which are blocked transfer for most-negative gate-voltages, followed towards more positive voltages by feedback-driven single-charge transfer (i.e., operating within the white dashed polygon in a)), the consecutive break-down of directionality of charge transfer (black solid line in a)) and finally the open regime where no static barrier is formed between the node and the drain lead (since the entrance gate is continually lowered below pinch-off during each cycle). Although the exact voltage at which break-down occurs is not determinable with certainty, we define it at the point where the phase of the SET is reversed (marked by the black arrow). This value yields about 6.25 periods of the SET from blocking until break-down. In turn, this number can be converted into a difference of the electrostatic potentials of $\Delta U \approx 8.5$ meV using the periodicity of the SET in terms of electrons on this node (see Fig. 5.4) and the charging energy of this node derived in section 4.1.3. This value agrees well with the previously obtained $\Delta U \approx 6 - 7.5$ meV for the pulsed counting measurement, thereby confirming the integrity of the counting measurement and the corresponding analysis.

7.2.3 Break-down of unidirectional charge transfer

Finally, returning to the pulsed operation, the break-down of unidirectional, quantized charge transfer by QD1 and QD2 beyond voltages $V_{G2}^{QD4} \lesssim -200$ mV is discussed using the transfer probabilities (already depicted in Fig. 7.4), but for clarity on a logarithmic scale as shown in Fig. 7.7.

In the range $V_{G2}^{QD4} \gtrsim -200$ mV, all dynamic quantum dots show only a reduction in single-charge transfer probability when the gate voltage is tuned more negative, leading to an increase of missing-cycle events, i.e. P_0 increases for all dots. Concentrating first on QD4, a further reduction in gate voltage beyond $V_{G2}^{QD4} \approx -200$ mV leads

7.2 Parameter dependence of transfer fidelity in series operation

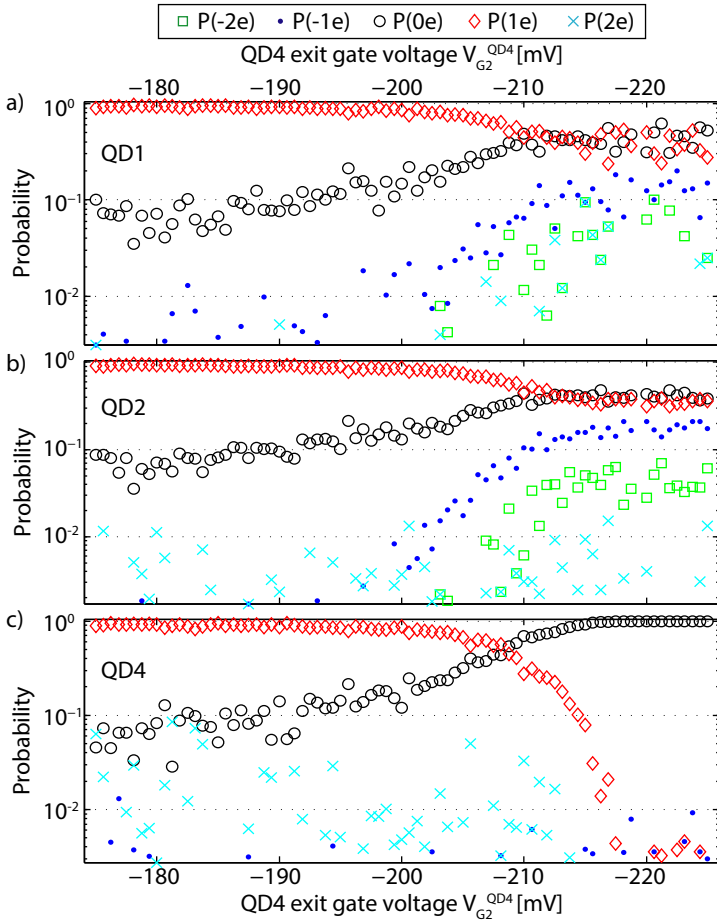


Figure 7.7:

Evaluation of transfer probabilities in series operation (sequential-transfer mode) as a function of working point of QD4 on logarithmic scale. Other conditions equal to Fig. 7.4.

finally to a full suppression of charge transfer across the dynamic dot, i.e. $P_0^{QD4} \approx 1$ while $P_n \approx 0 \forall n \neq 0$. This conforms with expectations since the barrier formed underneath the exit gate is energetically increased and thereby tunneling is completely suppressed.

But how are the other two serially connected dynamic quantum dots affected by this blocking of charge transfer? There are two scenarios conceivable: Either the emission of electrons to drain is simply blocked, leading to the same characteristic in QD1 and QD2 as observed for QD4, i.e. $P_0 \rightarrow 1$. Or the exit barrier, causing unidirectional charge transfer for an unbiased dynamic quantum dot, will be too small to suppress back-tunneling if the modulated entrance barrier is lowered below pinch-off during the loading phase of the charge-transfer cycle (phase (b) in Fig. 2.11). This question could not be addressed in the previously conducted measurements without single-charge resolution [43, 108] since the average charge state of the node (which is monitored by the detector) remains constant in both cases, as also obvious from Fig. 7.6.

However, using single-charge detection we are able to discriminate both scenarios resolving the outcome of each transfer pulse: As a consequence of the blocking dot QD4, also QD1 and QD2 show an increase in P_0 , i.e. the number of missing-cycle events rises. But, as an additional effect supporting the second scenario, also the direction of quantized charge transfer is not maintained any more which manifests itself by an increase of backward-transfer events including single- and double-electron loss from drain to source during a pulse. Due to the large number of electrons stored on the nodes (effectively reducing the exit barriers), the dynamic quantum dots can be overcome, leading finally to the break-down of unidirectional charge transfer. The time traces of the detectors reflect constant node potentials when none of the adjacent dots is triggered due to the large entrance barrier of all dynamic quantum dots between the pulses. Only during a pulse, the

entrance barrier is lowered below pinch-off, leading to the possibility of electron back-flow across the comparably small exit barrier. However, this effect requires a large difference in electrochemical potentials of source and drain lead.

This observation has strong impact onto the operation of the self-referenced current source (chapter 6): The regime of comparably large bias between appropriate source and drain reservoirs has to be avoided since one of the main assumptions in error attribution and accounting is the unidirectionality of charge transfer (see, e.g., Fig. 6.6). This requires well characterization of the individual quantum dots and operation of all dots at almost equal transfer probabilities in order to avoid too large bias conditions.

7.2.4 Summary

To conclude this section, we have analysed the operation of three dynamic quantum dots in series under variation of the transfer probabilities of the last quantum dot QD₄, achieved by tuning its exit gate voltage. The feedback mechanism stabilizing the three dots due to charge accumulation is resolved and discussed. Finally, also the breakdown of unidirectional charge transfer by the dynamic quantum dots against a large bias potential is observed, evidenced by counting.

7.3 Series operation of dynamic QDs with MHz repetition rate

As the last experimental aspect in series operation of two dynamic quantum dots (QD1 and QD2), the transfer of electrons with reduced delay between pulses is discussed. Possible deviations from measurements with slow repetition rates might be expected if relaxation processes do not equilibrate the electron reservoirs before the next transfer pulse is

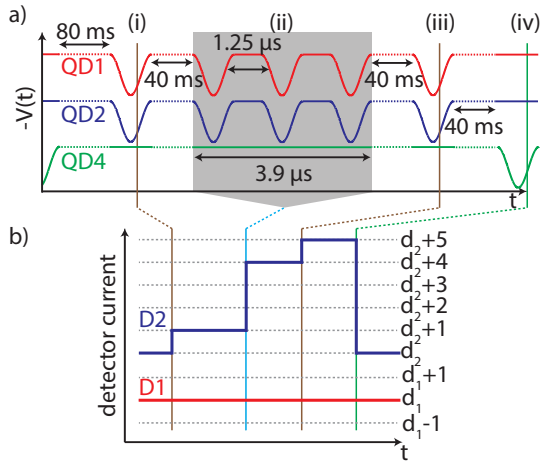


Figure 7.8: Pulse pattern used in series charge transfer of two dynamic quantum dots with MHz repetition rate.

applied. Due to the relatively high emission energy of electrons to drain, "hot" electrons will predominantly influence the capturing process of the subsequent dynamic quantum dot (phase © in Fig. 2.11). Therefore, the discussion focuses on the transfer statistics of QD2, whose source node equals the drain node of QD1 (node 1; for detailed description of the elements discussed here see Fig. 3.7).

Both dynamic quantum dots are always triggered simultaneously in this section. The measurement signal, as discussed above, is formed by the number of electrons emitted by QD2. In order to enable continuous measurements while also being able to observe the outcome of the pulse sequence, we use the entrance gate of QD4 again as pulsed barrier, as introduced already in section 5.2. The resulting pulse pattern is shown in Fig. 7.8a).

After an initial waiting time of $\tau = 80$ ms, QD1 and QD2 are triggered once (pulse (i), marked by a brown vertical line in the following). After a delay of $\tau = 40$ ms, three simultaneous pulses, delayed by about $1.25 \mu\text{s}$ each, are applied to both quantum dots which is far below the time resolution of our detectors (labelled (ii), blue vertical line). After further $\tau = 40$ ms, a single pulse is applied to QD1 and QD2 again (pulse (iii), brown). Pulses (i) and (iii) allow on the one hand to determine the individual transfer probability distribution of QD2 at low repetition rates and, on the other hand, to verify the operation of the detectors on the same edge during the full sequence. Finally, the sequence is concluded with the reset pulse (labelled (iv), coloured in green).

Additionally, the expected detector signals are depicted in Fig. 7.8b) for both detectors and perfect single-charge transfer per applied pulse. Since the number of electrons transferred by QD1 and QD2 equal and the charge state of this node is not affected by the reset pulse, detector D1 is expected to remain constant. However, the detector D2 (monitoring the output of QD2 onto node 2) should indicate the sequential addition of one (pulse (i)), three (ii) and one (iii) electrons and finally a reset of this node's charge state at pulse (iv).

Fig. 7.9a) shows the resulting measurement signals for D1 (red, lower panel) and D2 (blue, upper panel) together with the derived counting signal in panel b) for detector D2. Horizontal lines indicate the different charge states, encircled numbers indicate MHz-pulses where the number of electrons transferred per cycle by the dynamic quantum dots deviates from $n_e = 1$. Beginning at a more general perspective without going into details, D2 shows specific jumps in response to pulse applied to the dynamic dots while D1 remains mainly constant and only rarely changes its current level (e.g., at points marked by ① and ②), as expected from Fig. 7.8. Additionally, one observes a small variation in D1, reflecting the changes in the potential of node 2 due to cross-

capacitive coupling. Since this variation tends towards a reduction in detector current during a sequence period (and we simultaneously add electrons to node 2), one can deduce that this detector operates on the falling edge (an additional electron leads to a reduction in current).

Taking this time trace, let us discuss the occurrence of transfer errors which are observed in this example only during the fast series pulses marked by the vertical blue line. At ①, QD2 transfers only 2 electrons during the three fast pulses, simultaneously leading to a jump in detector D1 indicating a surplus electron on node 1 (since QD1 transfers exactly 3 electrons as intended). At position ②, the previous charge state on node 1 is regained due to a missing cycle by QD1. Another type of error is observed at the two positions indicated by ③ where both dynamic quantum dots miss one of the three fast cycles each, so that node 1's charge state remains constant but only two electrons are transferred to node 2. At the end of the interval shown (marked by ①) QD2 misses one cycle while QD1 operates properly as in period 18. The counting data is obtained using the algorithm employed throughout this thesis for the analysis of series charge transfer (see section 6.3 for details.) The algorithm works well even for large changes in the number of electrons on the node, as observed following the reset pulses although its reference table is based on the change of the node's occupation number by a single electron. Small deviations in this reference (e.g., due to the binning) linearly increase with increasing number of electrons to detect, thereby enhancing the probability of false counts for large changes in the number of electrons on the node especially if one or both contributing states are close to the extrema of the SET response. One such erroneous count occurs at the reset pulse during period 18, where the counting algorithm detects a change in the node's occupation by -8 electrons while the initial and the final state differ only by 7 states. However, the reset pulse will not be investigated further in this analysis.

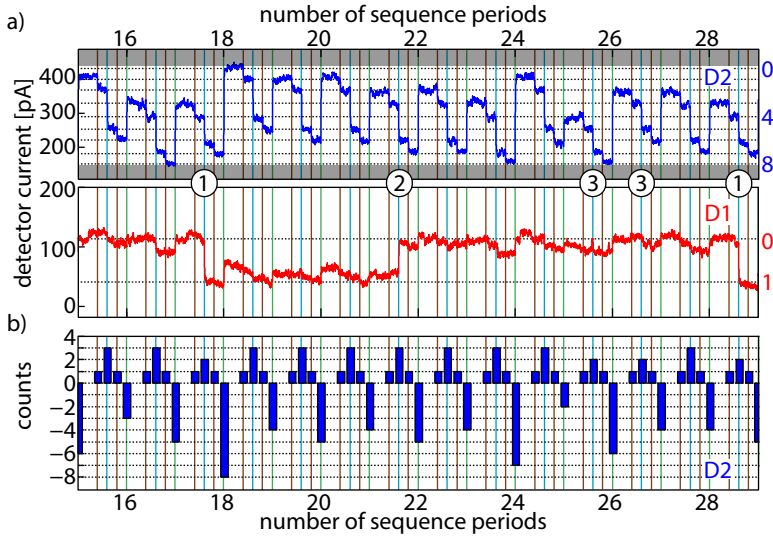


Figure 7.9:

Time trace of series charge transfer of two dynamic quantum dots with MHz repetition rate over a time interval of 14 sequence periods. Real measurement signals (a) for D1 (red, lower panel) and D2 (blue, upper panel) as well as derived counts (b) for D2. Vertical lines indicate pulses applied to the gates as discussed in the main text. Horizontal lines represent charge states of the nodes as guide to the eyes.

Without using the counted signal, one can already obtain a first hint whether to expect deviations in transfer fidelities by comparing the detector responses for the single and the fast triple pulses which is shown as a histogram in Fig. 7.10. The detector D2's response is almost linearly at this working point, resulting in an accumulation of counts at around $\Delta I = 32.6$ pA corresponding to single-charge transfer for the single pulses (i, blue) and (iii, red) and another distribution around $\Delta I \approx 100$ pA for the triple pulses (iii, green). Any deviations would

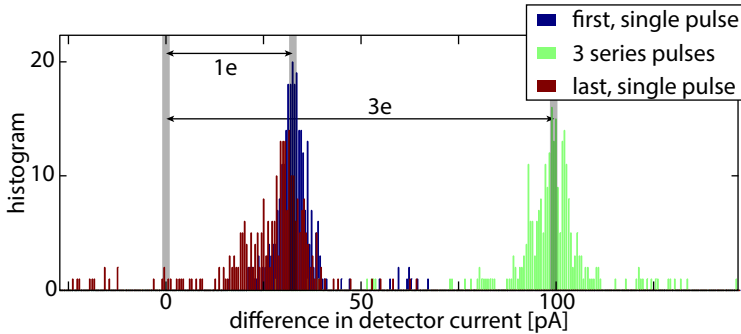


Figure 7.10:

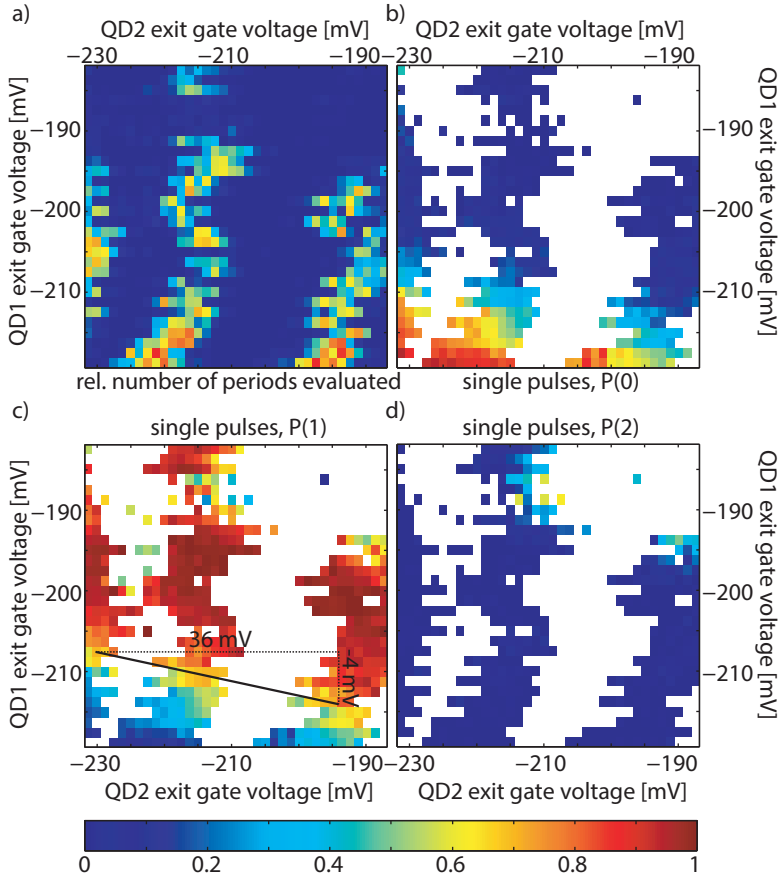
Histogram of difference in detector D2 current in response to pulses. Grey areas mark zero or the center of the distributions. $1e$ corresponds here to a difference in detector current of 32.6 pA, $3e$ to 100 pA.

lead either to a reduction or an increase in the number of electrons transferred during the series pulses, i.e. instead of an accumulation of events indicating three-electron transfer, peaks around $\Delta I \approx 65$ pA (two-electron transfer) or $\Delta I \approx 133$ pA (four-electron transfer) would appear. However, the data does not show any significant deviations between the two different repetition rates. Negative differences, observed mainly for the last pulses in this data-set, indicate a crossing from positive to negative edge of the detector's response. This emphasizes the impact of the initial and final marker pulses as a measure at which edge the SET is operating: Only sequences at which the detector's operation point is maintained on the same edge will be considered in the following. In any other cases, the detection algorithm would fail since it cannot detect events across different SET edges. Due to the limited number of electrons observable on each detector's edge and the comparably large number of electrons to detect (5 at perfect single-charge transfer), this necessary restriction reduces the usable amount of data

drastically.

The result of this restriction is shown in Fig. 7.11a), displaying the relative number of periods used in the evaluation as a function of both control gates defining the serially connected quantum dots QD1 and QD2, V_{G2}^{QD1} (y-axis) and V_{G2}^{QD2} (x-axis), respectively. In total, the measurement covers 279 sequence periods per gate setting. Blue reflects low sensitivity of this detector while red corresponds to highest sensitivity. A clear modulation of sensitivity, reflecting the effect of gate variation on the electrochemical potential of the detector due to capacitive cross-coupling, can be observed. Due to the position of the detector on the chip relative to the gates under variation, the influence of V_{G2}^{QD2} is much stronger since this gate is much closer to the detector (equal to higher capacitive coupling).

Figs. 7.11b)-d) display the transfer probabilities P_n^{QD2} of QD2 in series operation, considering only the single pulses (i) and (iii), for $n_e^{QD2} = 0 \dots 2$ electrons per cycle. As expected, the series circuit blocks electron transfer when both quantum dot gates are set to most negative values (bottom left), as shown in b). On the opposite range of parameters, both dynamic quantum dots are energetically lowered which enhances the probability of transferring a larger quantity of electrons per cycle, as reflected by the rising probability of transferring two electrons per cycle across QD2 (top right in d). In the intermediate regime, both dynamic quantum dots are locked to transfer about one electron per cycle, yielding a wide plateau with high probability of P_1^{QD2} (c). As sketched in this figure, the feedback mechanism stabilizing the serially connected acts asymmetrically as a function of both control parameters which is observed in the transition region from zero- to single-charge transfer. To quantify this effect, we analyse the position of $P_1^{QD2} = 0.7$ as a function of both gate voltages. If QD2's control gate voltage V_{G2}^{QD2} is changed by 36 mV, only a change in


Figure 7.11:

Two-dimensional plot of relevant dimensions characterising the charge transfer by the single pulses (i) and (iii) under variation of the working points of QD1 and QD2, controlled by $V_{G_2}^{QD1}$ (y-axis) and $V_{G_2}^{QD2}$ (x-axis), respectively. Panel (a) shows the normalized number of detectable sequence periods, thereby indicating regions of sensitivity as well as the cross-coupling of QD control gates and the SET D2. Panels (b), (c) and (d) depict the probabilities of QD2 transferring $n_e^{QD2} = 0 \dots 2$ electrons per cycle, based on the single pulses (i) and (iii).

V_{G2}^{QD1} of -4 mV is required in order to maintain the same output of electrons across QD2. While therefore QD2 responds immediately to variations of V_{G2}^{QD1} , the effect of its local tuning gate on the number of electrons transferred is comparably weak, yielding a ratio of about 9. In summary, the subsequent quantum dot QD2 is mainly controlled by the number of electrons transferred by QD1 (set by V_{G2}^{QD1}) due to charge feedback instead of the voltage applied to its control gate V_{G2}^{QD2} . This asymmetry is in good agreement with the simulation of feedback by applying static potentials to either source or drain of a single dynamic quantum dot (see section 2.6.1) where a ratio of about 10 has been obtained for the effect of these bias conditions onto the number of electrons transferred by the dot.

Finally, the focus is turned to the fidelity of the three subsequent series pulses (ii) in comparison to the previously discussed single-electron transfer probability (Fig. 7.11c). The probability of observing a change in the charge state of node 2 after pulse-sequence element (ii) of three electrons (equalling perfect single-charge transfer per pulse by QD2) is shown in Fig. 7.12a).

Again, a wide plateau in the center of the plot reflects the stabilized single-charge transfer across QD2 reaching values close to one in the plateau region. But, in order to allow detailed comparison of this data with the results obtained from the single-charge transfer characteristics by pulses (i) and (iii), the latter need to be scaled appropriately: The outcome of sequence element (ii) involves three subsequent, independent single pulses. Therefore, the single-charge transfer probability derived from pulses (i) and (iii) is shown again in Fig. 7.12b), but after raising the data to the power of 3. The resulting compression of the transition region from zero- to single-charge transfer as compared to Fig. 7.11c) agrees well with the experimentally determined probability by analysing the triple pulses in Fig. 7.12a). Therefore, at least at these repetition rates, the subsequent dynamic quantum dot is not affected

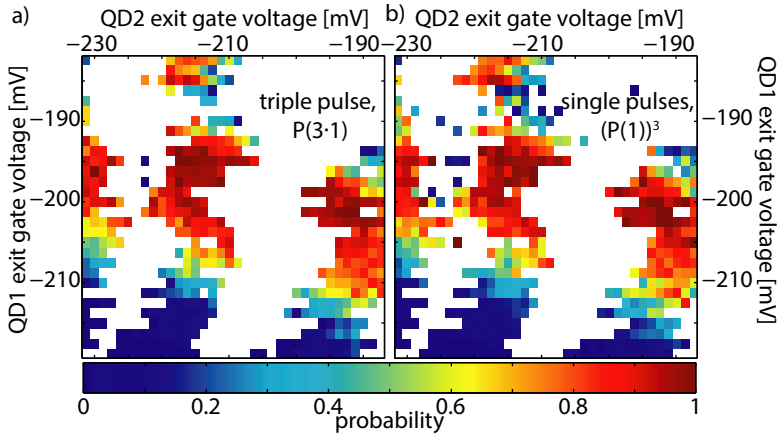


Figure 7.12:

Comparison of success probability of three frequent pulses (a) labelled (ii) in sketch 7.8 with the appropriately scaled single transfer probability (b).

by the emission of hot electrons onto its source node by the preceding dynamic quantum dot.

In summary, we may conclude that the detectors remain stable even after applying several pulses to the dynamic quantum dots with higher repetition rates in the MHz-regime. Secondly, the charge detection algorithm yields reasonable results even for higher numbers of electrons transferred although being based only on the response to single electrons. Lastly, potential heating effects due to limited relaxation processes of emitted hot electrons do not influence the characteristics of subsequent dynamic quantum dots at these conditions (comparably low repetition rate, only few fast-transfer events). Additionally, also the asymmetry of mesoscopic charge feedback could be resolved where the output of a series of two dynamic quantum dots is predominantly controlled by the setting of the first quantum dot.



Summary and outlook

In this thesis, dynamic quantum dots, capable of transferring electrons on-demand and one by one, have been investigated on the fundamental level of individual transfer events. To this end, such electron sources have been combined on-chip with highly-sensitive electrometers yielding single-electron resolution.

The dynamic quantum dots are formed in a two-dimensional electron gas located in an AlGaAs/GaAs wafer 90 nm below the surface. Using appropriate fabrication, a small wire is obtained whose electrostatic potential is locally controlled by metallic top-gates, where groups of three gates each form a dynamic quantum dot. In-between, metallic single-electron detectors are placed, using a shadow-evaporation technique.

The objectives pursued with this approach are two-fold: On the one hand, this arrangement allows the characterisation of a single dynamic quantum dot on the level of individual charge-transfer events. This includes the achievable transfer fidelity which is the key property of every single-electron source (in this case, $P_1 > 0.99$ for two of three dynamic

quantum dots) as well as its dependence on variations of external control parameters. After the introduction of the device's individual building blocks using conventional direct-current measurements and high repetition rates, measurements on the non-adiabatic dynamic quantum dot with single-charge resolution are presented. These cover the pulsed operation mode with arbitrarily large delays between subsequent pulses as well as the demonstration of robustness of the single-electron source against electrostatic potentials in the drain node. This part of the thesis concludes with the detailed investigation of the charge-capture mechanism, analysed by counting. By comparison of the full charge-transfer distribution with theoretical models, two limits of charge capture, namely the grand-canonical and the decay-cascade limit, can be distinguished and strategies for further optimization depending on the capture mechanism are derived.

The second direction of research presented in this thesis covers the realization of a self-referenced single-electron current source. This is a device generating a quantized current when driven by a periodic driving signal, as in conventional single-electron current sources, but in addition allows to monitor deviations from the quantized current level, caused, e.g., by rare missed transfer cycles or the unintended transfer of more than one electron per cycle. Thereby, the accuracy of the output current can be verified simultaneously with the generation of this quantized current. Moreover, errors can be accounted for during a precision experiment while previously the verification and generation of quantized currents have been two separate, sequential steps.

This device is realized here by serially connecting three dynamic quantum dots with single-electron detectors monitoring the charge state of the interconnecting node: In perfect operation, the number of incoming and outgoing electrons equal, leading to constant detector signals. Only in case of deviations from single-charge transfer, a surplus or missing electron remains on the node which leads to a signal in the corre-

sponding detector. As shown in this thesis, the most-likely source of error can be derived by performing correlation analysis of the detector signals. The minimal set of elements, consisting of three dynamic quantum dots with two intermediate detectors, is realized, but being operated only at low repetition rates yielding a current of about $I \approx 4.8$ aA. However, this combination of sources and detectors allows a reduction of the uncertainty in the number of transferred electrons by a factor of about 50 as compared to a single dynamic quantum dot without charge detection circuitry.

Finally, the interactions of dynamic quantum dots in a series circuitry are investigated, caused by electrostatic potentials formed on the interconnecting nodes. Using single-electron counting data, the number of electrons located on the nodes is assessed under variation of the control parameter determining the number of electrons transferred across the last dynamic quantum dot. Lastly, the effect of heating in a series circuit by the emission of hot electrons on the following dynamic quantum dot is addressed. To this end, the transfer fidelity obtained for single-charge transfer by one pulse is compared to the fast transfer of three electrons by three pulses, delayed by about $\tau \approx 1.25 \mu\text{s}$ each. Potential deviations are not observed, thereby opening the path towards higher repetition rates by either enhanced transfer fidelity of the dynamic quantum dots (e.g., by operating in a magnetic field) or higher detector bandwidth (by implementing the detectors in a resonant circuit).

When discussing directions of further research, the most obvious point is the current limitation in observation time due to insensitivities of the detectors. The continuous measurement of the nodes' charge states can be either achieved by increasing the number of detectors per node, operated with an appropriate phase such that at least one of the detectors remains sensitive, or by implementing a feedback circuit stabilizing the detectors at the point of highest sensitivity using an elec-

trostatic potential applied to the detector's local gate electrode. The observable then becomes this feedback signal instead of the currently used detector current.

However, there are a number of obstacles which need to be passed when moving to higher current levels and which cannot be solved that easily: As an example, the operation of dynamic quantum dots in a magnetic field for enhanced transfer fidelity simultaneously leads to a lowering in the scattering rates, potentially resulting in an increase of the error rates of subsequent dynamic quantum dots, or, more serious, to leakage across the barrier formed by the following quantum dot. As a potential remedy, the fabrication of a floating Ohmic contact on the node, leading to an increase in the number of scatterers and a better coupling to the phonon bath, is conceivable.

Another issue might be too large cross-coupling between detectors and the (then continuous) driving signals applied to the gates of the dynamic quantum dots in order to achieve clocked single-electron transfer. Here, suitable shielding needs to be developed in order to minimize cross-coupling while simultaneously keeping the node's capacitance small to maintain single-charge resolution of the detectors. Also, the amplitude necessary to drive the dynamic quantum dots could potentially be reduced by optimized design or drive.

Thinking about further optimizations of the dynamic quantum dots, alternative driving signals might also be an option: Specifically shaped driving waveforms, which account for the underlying physical mechanisms in charge capture and transfer, might lead to more precise functioning even at increased repetition rates. Additionally, a modulation of both gates (in order to tune the dynamic quantum dot to the grand-canonical regime) has been proposed. Whether this direction is suitable in series circuits is not clear yet since it potentially leads to a reduction in robustness of the dynamic quantum dot and it therefore remains an open question which needs to be addressed in the near future.

Bibliography

- [1] J. C. Maxwell, *The scientific papers*, edited by W. D. Niven, Vol. 2 (University Press (Cambridge), 1890) (see p. 1).
- [2] J. C. Maxwell, *A treatise on electricity and magnetism*, Vol. 1 (Clarendon Press (Oxford), 1873) (see p. 2).
- [3] M. Planck, “Ueber irreversible Strahlungsvorgänge”, *Annalen der Physik* **306**, 69 (1900) (see p. 2).
- [4] BIPM, *Le Système international d’unités - The International System of Units*, 8th edition (2006) (see pp. 2 sqq.).
- [5] I. M. Mills, P. J. Mohr, T. J. Quinn, B. N. Taylor, and E. R. Williams, “Redefinition of the kilogram, ampere, kelvin and mole: a proposed approach to implementing CIPM recommendation 1 (CI-2005)”, *Metrologia* **43**, 227 (2006) (see pp. 2, 4).
- [6] G. Girard, “The Third Periodic Verification of National Prototypes of the Kilogram (1988-1992)”, *Metrologia* **31**, 317 (1994) (see p. 3).
- [7] R. Davis, “The SI unit of mass”, *Metrologia* **40**, 299 (2003) (see p. 3).
- [8] CCEM, “Draft mise en pratique for the ampere and other electric units in the International System of Units (SI)”, <http://www.bipm.org/cc/CCEM/Allowed/26/CCEM-09-05.pdf> (2009) (see p. 4).

- [9] BIPM, “Draft of 9th SI Brochure”, (2013) (see p. 4).
- [10] I. M. Mills, P. J. Mohr, T. J. Quinn, B. N. Taylor, and E. R. Williams, “Adapting the International System of Units to the twenty-first century”, *Philosophical Transactions of the Royal Society A: Mathematical, Physical and Engineering Sciences* **369**, 3907 (2011) (see p. 4).
- [11] J. Miller, T. P. Hill, and A. Censullo, “Unresolved concerns about the ”new SI””, *Accreditation and Quality Assurance* **16**, 657 (2011) (see p. 4).
- [12] T. P. Hill, J. Miller, and A. C. Censullo, “Towards a better definition of the kilogram”, *Metrologia* **48**, 83 (2011) (see p. 4).
- [13] P. J. Mohr, B. N. Taylor, and D. B. Newell, “CODATA recommended values of the fundamental physical constants: 2010”, *Review of Modern Physics* **84**, 1527 (2012) (see p. 4).
- [14] C. Tamm, N. Huntemann, B. Lipphardt, V. Gerginov, N. Nemitz, M. Kazda, S. Weyers, and E. Peik, “Cs-based optical frequency measurement using cross-linked optical and microwave oscillators”, *Physical Review A* **89**, 023820 (2014) (see p. 4).
- [15] R. A. Millikan, “On the Elementary Electrical Charge and the Avogadro Constant”, *Physical Review* **2**, 109 (1913) (see p. 5).
- [16] T. A. Fulton and G. J. Dolan, “Observation of Single-Electron Charging Effects in Small Tunnel Junctions”, *Physical Review Letters* **59**, 109 (1987) (see pp. 5, 29, 107).
- [17] L. J. Geerligs, V. F. Anderegg, P. A. M. Holweg, J. E. Mooij, H. Pothier, D. Estève, C. Urbina, and M. H. Devoret, “Frequency-Locked Turnstile Device for Single Electrons”, *Physical Review Letters* **64**, 2691 (1990) (see pp. 5, 29, 178).

-
- [18] L. P. Kouwenhoven, A. T. Johnson, N. C. van der Vaart, C. J. P. M. Harmans, and C. T. Foxon, “Quantized Current in a Quantum-Dot Turnstile Using Oscillating Tunnel Barriers”, *Physical Review Letters* **67**, 1626 (1991) (see pp. 5, 29 sq., 32, 178).
- [19] M. H. Devoret, D. Esteve, and C. Urbina, “Single-electron transfer in metallic nanostructures”, *Nature* **360**, 547 (1992) (see pp. 5, 29 sq.).
- [20] H. Pothier, P. Lafarge, C. Urbina, D. Esteve, and M. H. Devoret, “Single-Electron Pump Based on Charging Effects”, *Europhysics Letters* **17**, 249 (1992) (see pp. 5, 33, 178).
- [21] K. v. Klitzing, G. Dorda, and M. Pepper, “New Method for High-Accuracy Determination of the Fine-Structure Constant Based on Quantized Hall Resistance”, *Physical Review Letters* **45**, 494 (1980) (see pp. 5, 179).
- [22] B. D. Josephson, “Possible new effects in superconductive tunnelling”, *Physics Letters* **1**, 251 (1962) (see pp. 5, 179).
- [23] S. Shapiro, “Josephson Currents in Superconducting Tunneling: The Effect of Microwaves and Other Observations”, *Physical Review Letters* **11**, 80 (1963) (see p. 5).
- [24] N. Feltin and F. Piquemal, “Determination of the elementary charge and the quantum metrological triangle experiment”, *The European Physical Journal Special Topics* **172**, 267 (2009) (see p. 5).
- [25] M. W. Keller, J. M. Martinis, N. M. Zimmerman, and A. H. Steinbach, “Accuracy of electron counting using a 7-junction electron pump”, *Applied Physics Letters* **69**, 1804 (1996) (see pp. 6, 8, 34 sq., 159, 178, 180).

- [26] M. W. Keller, A. L. Eichenberger, J. M. Martinis, and N. M. Zimmerman, “A Capacitance Standard Based on Counting Electrons”, *Science* **285**, 1706 (1999) (see pp. 6, 178).
- [27] M. W. Keller, N. M. Zimmerman, and A. L. Eichenberger, “Uncertainty budget for the NIST electron counting capacitance standard, ECCS-1”, *Metrologia* **44**, 505 (2007) (see pp. 6, 180).
- [28] J. M. Shilton, V. I. Talyanskii, M. Pepper, D. A. Ritchie, J. E. F. Frost, C. J. B. Ford, C. G. Smith, and G. A. C. Jones, “High-frequency single-electron transport in a quasi-one-dimensional GaAs channel induced by surface acoustic waves”, *Journal of Physics: Condensed Matter* **8**, L531 (1996) (see p. 6).
- [29] V. I. Talyanskii, J. M. Shilton, M. Pepper, C. G. Smith, C. J. B. Ford, E. H. Linfield, D. A. Ritchie, and G. A. C. Jones, “Single-electron transport in a one-dimensional channel by high-frequency surface acoustic waves”, *Physical Review B* **56**, 15180 (1997) (see p. 6).
- [30] P. Utko, J. B. Hansen, P. E. Lindelof, C. B. Sørensen, and K. Gloos, “Single-Electron Transport Driven by Surface Acoustic Waves: Moving Quantum Dots Versus Short Barriers”, *Journal of Low Temperature Physics* **146**, 607 (2007) (see p. 6).
- [31] T. J. B. M. Janssen and A. Hartland, “Recent Measurements of Single Electron Transport of Surface Acoustic Wave Devices at the NPL”, *IEEE Transactions on Instrumentation and Measurement* **50**, 227 (2001) (see pp. 6, 170).
- [32] L. Nevou, V. Liverini, P. Friedli, F. Castellano, A. Bismuto, H. Sigg, F. Gramm, E. Müller, and J. Faist, “Current quantization in an optically driven electron pump based on self-assembled quantum dots”, *Nature Physics* **7**, 423 (2011) (see p. 6).

-
- [33] J. P. Pekola, J. J. Vartiainen, M. Möttönen, O.-P. Saira, M. Meschke, and D. V. Averin, “Hybrid single-electron transistor as a source of quantized electric current”, *Nature Physics* **4**, 120 (2008) (see p. 6).
- [34] A. Fujiwara, K. Nishiguchi, and Y. Ono, “Nanoampere charge pump by single-electron ratchet using silicon nanowire metal-oxide-semiconductor field-effect transistor”, *Applied Physics Letters* **92**, 042102, 042102 (2008) (see pp. 6, 53, 101).
- [35] G. Yamahata, K. Nishiguchi, and A. Fujiwara, “Accuracy evaluation of single-electron shuttle transfer in Si nanowire metal-oxide-semiconductor field-effect transistors”, *Applied Physics Letters* **98**, 222104 (2011) (see pp. 6, 166).
- [36] A. Rossi, T. Tantt, K. Y. Tan, I. Iisakka, R. Zhao, K. W. Chan, G. C. Tettamanzi, S. Rogge, A. S. Dzurak, and M. Möttönen, “An Accurate Single-Electron Pump Based on a Highly Tunable Silicon Quantum Dot”, *Nano Letters* **14**, 3405 (2014) (see p. 6).
- [37] G. C. Tettamanzi, R. Wacquez, and S. Rogge, “Charge pumping through a single donor atom”, *New Journal of Physics* **16**, 063036 (2014) (see p. 6).
- [38] M. D. Blumenthal, B. Kaestner, L. Li, S. Giblin, T. J. B. M. Janssen, M. Pepper, D. Anderson, G. Jones, and D. A. Ritchie, “Gigahertz quantized charge pumping”, *Nature Physics* **3**, 343 (2007) (see pp. 6, 179).
- [39] B. Kaestner, V. Kashcheyevs, S. Amakawa, M. D. Blumenthal, L. Li, T. J. B. M. Janssen, G. Hein, K. Pierz, T. Weimann, U. Siegner, and H. W. Schumacher, “Single-parameter nonadiabatic quantized charge pumping”, *Physical Review B* **77**, 153301 (2008) (see pp. 6, 83, 179).

- [40] J. P. Pekola, O.-P. Saira, V. F. Maisi, A. Kemppinen, M. Möttönen, Y. A. Pashkin, and D. V. Averin, “Single-electron current sources: Toward a refined definition of the ampere”, *Reviews of Modern Physics* **85**, 1421 (2013) (see p. 6).
- [41] B. Kaestner, V. Kashcheyevs, G. Hein, K. Pierz, U. Siegner, and H. W. Schumacher, “Robust single-parameter quantized charge pumping”, *Applied Physics Letters* **92**, 192106 (2008) (see pp. 6, 47, 83, 179).
- [42] P. Mirovsky, B. Kaestner, C. Leicht, A. C. Welker, T. Weimann, K. Pierz, and H. W. Schumacher, “Synchronized single electron emission from dynamical quantum dots”, *Applied Physics Letters* **97**, 252104 (2010) (see pp. 6, 180).
- [43] L. Fricke, F. Hohls, N. Ubbelohde, B. Kaestner, V. Kashcheyevs, C. Leicht, P. Mirovsky, K. Pierz, H. W. Schumacher, and R. J. Haug, “Quantized current source with mesoscopic feedback”, *Physical Review B* **83**, 193306 (2011) (see pp. 6, 9, 53, 55 sqq., 69, 97, 180, 210, 217, 226).
- [44] S. P. Giblin, M. Kataoka, J. D. Fletcher, P. See, T. J. B. M. Janssen, J. P. Griffiths, G. A. C. Jones, I. Farrer, and D. A. Ritchie, “Towards a quantum representation of the ampere using single electron pumps”, *Nature Communications* **3**, 930 (2012) (see pp. 6, 42, 47, 83, 179, 206).
- [45] N. M. Zimmerman, E. Hourdakis, Y. Ono, A. Fujiwara, and Y. Takahashi, “Error mechanisms and rates in tunable-barrier single-electron turnstiles and charge-coupled devices”, *Journal of Applied Physics* **96**, 5254 (2004) (see pp. 6, 34).
- [46] V. Kashcheyevs and B. Kaestner, “Universal Decay Cascade Model for Dynamic Quantum Dot Initialization”, *Physical Re-*

- view Letters **104**, 186805 (2010) (see pp. 6, 47, 52, 101, 162, 166, 170).
- [47] L. Fricke, M. Wulf, B. Kaestner, V. Kashcheyevs, J. Timoshenko, P. Nazarov, F. Hohls, P. Mirovsky, B. Mackrodt, R. Dolata, T. Weimann, K. Pierz, and H. W. Schumacher, “Counting Statistics for Electron Capture in a Dynamic Quantum Dot”, *Physical Review Letters* **110**, 126803 (2013) (see pp. 6, 47 sq., 53).
- [48] G. Yamahata, K. Nishiguchi, and A. Fujiwara, “Accuracy evaluation and mechanism crossover of single-electron transfer in Si tunable-barrier turnstiles”, *Physical Review B* **89**, 165302 (2014) (see pp. 6, 47, 101, 166).
- [49] J. D. Fletcher, P. See, H. Howe, M. Pepper, S. P. Giblin, J. P. Griffiths, G. A. C. Jones, I. Farrer, D. A. Ritchie, T. J. B. M. Janssen, and et al., “Clock-Controlled Emission of Single-Electron Wave Packets in a Solid-State Circuit”, *Physical Review Letters* **111**, 216807 (2013) (see pp. 7, 53).
- [50] E. Bocquillon, V. Freulon, J.-M. Berroir, P. Degiovanni, B. Placais, A. Cavanna, Y. Jin, and G. Feve, “Coherence and Indistinguishability of Single Electrons Emitted by Independent Sources”, *Science* **339**, 1054 (2013) (see p. 7).
- [51] N. Ubbelohde, F. Hohls, V. Kashcheyevs, T. Wagner, L. Fricke, B. Kaestner, K. Pierz, H. W. Schumacher, and R. J. Haug, “Partitioning of on-demand electron pairs”, accepted for publication in *Nature Nanotechnology*, arXiv, 1404.0030 (2014) (see pp. 7, 53, 83, 140).
- [52] L. J. Geerligs, S. M. Verbrugh, P. Hadley, J. E. Mooij, H. Pothier, P. Lafarge, C. Urbina, D. Estève, and M. H. Devoret, “Sin-

- gle Cooper pair pump”, *Zeitschrift für Physik B - Condensed Matter* **85**, 349 (1991) (see p. 7).
- [53] F. Hoehne, Y. A. Pashkin, O. V. Astafiev, M. Möttönen, J. P. Pekola, and J. Tsai, “Coherent superconducting quantum pump”, *Physical Review B* **85**, 140504 (2012) (see p. 7).
- [54] S. Gasparinetti, P. Solinas, Y. Yoon, and J. P. Pekola, “Single Cooper-pair pumping in the adiabatic limit and beyond”, *Phys. Rev. B* **86**, 060502(R) (2012) (see p. 7).
- [55] M. Field, C. G. Smith, M. Pepper, D. A. Ritchie, J. E. F. Frost, G. A. C. Jones, and D. G. Hasko, “Measurements of Coulomb Blockade with a Noninvasive Voltage Probe”, *Physical Review Letters* **70**, 1311 (1993) (see p. 7).
- [56] W. Lu, Z. Ji, L. Pfeiffer, K. W. West, and A. J. Rimberg, “Real-time detection of electron tunnelling in a quantum dot”, *Nature* **423**, 422 (2003) (see pp. 7, 179).
- [57] R. J. Schoelkopf, P. Wahlgren, A. A. Kozhevnikov, P. Delsing, and D. E. Prober, “The Radio-Frequency Single-Electron Transistor (RF-SET): A Fast and Ultrasensitive Electrometer”, *Science* **280**, 1238 (1998) (see pp. 7, 180, 206).
- [58] J. Bylander, T. Duty, and P. Delsing, “Current measurement by real-time counting of single electrons”, *Nature* **434**, 361 (2005) (see pp. 7, 179).
- [59] T. Fujisawa, T. Hayashi, R. Tomita, and Y. Hirayama, “Bidirectional Counting of Single Electrons”, *Science* **312**, 1634 (2006) (see pp. 7, 179).
- [60] R. Schleser, E. Ruh, T. Ihn, K. Ensslin, D. C. Driscoll, and A. C. Gossard, “Time-resolved detection of individual electrons in a quantum dot”, *Applied Physics Letters* **85**, 2005 (2004) (see p. 7).

-
- [61] S. Gustavsson, R. Leturcq, B. Simovic, R. Schleser, T. Ihn, P. Studerus, and K. Ensslin, “Counting Statistics of Single Electron Transport in a Quantum Dot”, *Physical Review Letters* **96**, 076605 (2006) (see p. 7).
- [62] M. Wulf, “Error accounting algorithm for electron counting experiments”, *Physical Review B* **87**, 035312 (2013) (see pp. 7, 177, 180, 182).
- [63] L. Fricke, M. Wulf, B. Kaestner, F. Hohls, P. Mirovsky, B. Mackrodt, R. Dolata, T. Weimann, K. Pierz, U. Siegner, and H. W. Schumacher, “Self-Referenced Single-Electron Quantized Current Source”, *Physical Review Letters* **112**, 226803 (2014) (see pp. 8, 196).
- [64] T. Brandes, “Feedback Control of Quantum Transport”, *Physical Review Letters* **105**, 060602 (2010) (see pp. 9, 56).
- [65] K. Likharev and A. Zorin, “Theory of the Bloch-Wave Oscillations in Small Josephson Junctions”, English, *Journal of Low Temperature Physics* **59**, 347 (1985) (see pp. 9, 59, 207).
- [66] H. Scherer and B. Camarota, “Quantum metrology triangle experiments: a status review”, *Measurement Science and Technology* **23**, 124010 (2012) (see pp. 9, 59, 61, 207).
- [67] T. Ihn, *Semiconductor Nanostructures* (University Press (Oxford), 2010) (see pp. 11 sq.).
- [68] S. Datta, *Electronic Transport in Mesoscopic Systems* (University Press (Cambridge), 1995) (see pp. 12, 15, 18).
- [69] T. Ando, A. B. Fowler, and F. Stern, “Electronic properties of two-dimensional systems”, *Reviews of Modern Physics* **54**, 437 (1982) (see p. 12).

- [70] D. K. Ferry, S. M. Goodnick, and J. Bird, *Transport in Nanostructures*, 2nd edition (University Press (Cambridge), 2009) (see pp. 13, 21).
- [71] A. B. Fowler, F. F. Fang, W. E. Howard, and P. J. Stiles, “Magneto-Oscillatory Conductance in Silicon Surfaces”, *Physical Review Letters* **16**, 901 (1966) (see p. 13).
- [72] J. H. Davies, *The Physics of Low-dimensional Semiconductors: An Introduction* (University Press (Cambridge), 2009) (see pp. 15, 64).
- [73] B. Weber, S. Mahapatra, H. Ryu, S. Lee, A. Fuhrer, T. C. G. Reusch, D. L. Thompson, W. C. T. Lee, G. Klimeck, L. C. L. Hollenberg, and M. Y. Simmons, “Ohm’s Law Survives to the Atomic Scale”, *Science* **335**, 64 (2012) (see p. 17).
- [74] B. J. van Wees, H. van Houten, C. W. J. Beenakker, J. G. Williamson, L. P. Kouwenhoven, D. van der Marel, and C. T. Foxon, “Quantized Conductance of Point Contacts in a Two-Dimensional Electron Gas”, *Physical Review Letters* **60**, 848 (1988) (see p. 18).
- [75] D. A. Wharam, T. J. Thornton, R. Newbury, M. Pepper, H. Ahmed, J. E. F. Frost, D. G. Hasko, D. C. Peacock, D. A. Ritchie, and G. A. C. Jones, “One-dimensional transport and the quantisation of the ballistic resistance”, *Journal of Physics C: Solid State Physics* **21**, L209 (1988) (see p. 18).
- [76] R. Landauer, “Spatial Variation of Currents and Fields Due to Localized Scatterers in Metallic Conduction”, *IBM Journal of Research and Development* **1**, 223 (1957) (see p. 18).
- [77] R. Landauer, “Conductance determined by transmission: probes and quantised constriction resistance”, *Journal of Physics: Condensed Matter* **1**, 8099 (1989) (see p. 18).

-
- [78] M. Büttiker, “Four-Terminal Phase-Coherent Conductance”, *Physical Review Letters* **57**, 1761 (1986) (see p. 18).
- [79] Y. Imry and R. Landauer, “Conductance viewed as transmission”, *Reviews of Modern Physics* **71**, 306 (1999) (see p. 18).
- [80] S. Gasiorowicz, *Quantenphysik*, 9th, revised and extended edition (Oldenbourg Verlag, 2005) (see p. 19).
- [81] S. Tarucha, D. G. Austing, T. Honda, R. J. van der Hage, and L. P. Kouwenhoven, “Shell Filling and Spin Effects in a Few Electron Quantum Dot”, *Physical Review Letters* **77**, 3613 (1996) (see p. 21).
- [82] L. P. Kouwenhoven, D. G. Austing, and S. Tarucha, “Few-electron quantum dots”, *Reports on Progress in Physics* **64**, 701 (2001) (see pp. 21, 23).
- [83] J. von Delft and D. C. Ralph, “Spectroscopy of discrete energy levels in ultrasmall metallic grains”, *Physics Reports* **345**, 61 (2001) (see p. 21).
- [84] C. W. J. Beenakker, “Theory of Coulomb-blockade oscillations in the conductance of a quantum dot”, *Physical Review B* **44**, 1646 (1991) (see p. 21).
- [85] M. A. Kastner, “The single-electron transistor”, *Reviews of Modern Physics* **64**, 849 (1992) (see p. 21).
- [86] L. P. Kouwenhoven, C. M. Marcus, P. L. McEuen, S. Tarucha, R. M. Westervelt, and N. S. Wingreen, “Electron transport in quantum dots”, in *Mesoscopic electron transport* (Springer, 1997), pp. 105–214 (see pp. 21, 24).
- [87] S. Datta, *Quantum Transport: Atom to Transistor* (University Press (Cambridge), 2005) (see p. 25).

- [88] M. C. Rogge, “Einzel-, Doppel- und Dreifachquantenpunkte im Transport”, PhD thesis (Gottfried Wilhelm Leibniz Universität Hannover, 2008) (see p. 27).
- [89] C. Fricke, “Der Quantenpunktkontakt als Ladungsdetektor in der Transportspektroskopie”, PhD thesis (Gottfried Wilhelm Leibniz Universität, Hannover, 2008) (see pp. 27, 179).
- [90] K. Flensberg, A. A. Odintsov, F. Liefrink, and P. Teunissen, “Towards single-electron metrology”, *International Journal of Modern Physics B* **13**, 2651 (1999) (see pp. 29, 34, 59, 74).
- [91] L. P. Kouwenhoven, A. T. Johnson, N. C. Vaart, A. Enden, C. J. P. M. Harmans, and C. T. Foxon, “Quantized current in a quantum dot turnstile”, *Zeitschrift für Physik B - Condensed Matter* **85**, 381 (1991) (see p. 32).
- [92] X. Jehl, B. Voisin, T. Charron, P. Clapera, S. Ray, B. Roche, M. Sanquer, S. Djordjevic, L. Devoille, R. Wacquez, and et al., “Hybrid Metal-Semiconductor Electron Pump for Quantum Metrology”, *Physical Review X* **3**, 021012 (2013) (see p. 32).
- [93] S. Lotkhov, S. Bogoslovsky, A. Zorin, and J. Niemeyer, “The single electron R-pump: First experiment”, *Conference on Precision Electromagnetic Measurements (CPEM), Conference Digest*, 319 (2000) (see p. 34).
- [94] B. Steck, A. Gonzalez-Cano, N. Feltin, L. Devoille, F. Piquemal, S. Lotkhov, and A. B. Zorin, “Characterization and metrological investigation of an R-pump with driving frequencies up to 100 MHz”, *Metrologia* **45**, 482 (2008) (see p. 34).
- [95] M. Seo, Y.-H. Ahn, Y. Oh, Y. Chung, S. Ryu, H.-S. Sim, I.-H. Lee, M.-H. Bae, and N. Kim, “Improvement of electron pump accuracy by a potential-shape-tunable quantum dot pump”, *Physical Review B* **90**, 085307 (2014) (see p. 36).

-
- [96] Y. Nagamune, H. Sakaki, L. P. Kouwenhoven, L. C. Mur, C. J. P. M. Harmans, J. Motohisa, and H. Noge, “Single electron transport and current quantization in a novel quantum dot structure”, *Applied Physics Letters* **64**, 2379 (1994) (see p. 38).
- [97] M. Kataoka, J. D. Fletcher, P. See, S. P. Giblin, T. J. B. M. Janssen, J. P. Griffiths, G. A. C. Jones, I. Farrer, and D. A. Ritchie, “Tunable Nonadiabatic Excitation in a Single-Electron Quantum Dot”, *Physical Review Letters* **106**, 126801 (2011) (see pp. 42, 48).
- [98] S. J. Wright, M. D. Blumenthal, G. Gumbs, A. L. Thorn, M. Pepper, T. J. B. M. Janssen, S. N. Holmes, D. Anderson, G. A. C. Jones, C. A. Nicoll, and D. A. Ritchie, “Enhanced current quantization in high-frequency electron pumps in a perpendicular magnetic field”, *Physical Review B* **78**, 233311 (2008) (see p. 44).
- [99] B. Kaestner, C. Leicht, V. Kashcheyevs, K. Pierz, U. Siegner, and H. W. Schumacher, “Single-parameter quantized charge pumping in high magnetic fields”, *Applied Physics Letters* **94**, 012106 (2009) (see p. 44).
- [100] S. J. Wright, “Quantised charge pumping in a perpendicular magnetic field”, PhD thesis (University of Cambridge, 2010) (see pp. 44, 66).
- [101] S. J. Wright, A. L. Thorn, M. D. Blumenthal, S. P. Giblin, M. Pepper, T. J. B. M. Janssen, M. Kataoka, J. D. Fletcher, G. A. C. Jones, C. A. Nicoll, and et al., “Single- and few-electron dynamic quantum dots in a perpendicular magnetic field”, *Journal of Applied Physics* **109**, 102422 (2011) (see p. 44).

- [102] C. Leicht, P. Mirovsky, B. Kaestner, F. Hohls, V. Kashcheyevs, E. V. Kurganova, U. Zeitler, T. Weimann, K. Pierz, and H. W. Schumacher, “Generation of energy selective excitations in quantum Hall edge states”, *Semiconductor Science and Technology* **26**, 055010 (2011) (see p. 44).
- [103] J. D. Fletcher, M. Kataoka, S. P. Giblin, S. Park, H.-S. Sim, P. See, D. A. Ritchie, J. P. Griffiths, G. A. C. Jones, H. E. Beere, and T. J. B. M. Janssen, “Stabilization of single-electron pumps by high magnetic fields”, *Physical Review B* **86**, 155311 (2012) (see p. 44).
- [104] C. Leicht, “Nicht-adiabatische Halbleitereinzelelektronenpumpe unter Magnetfeldeinfluss”, PhD thesis (Gottfried Wilhelm Leibniz Universität Hannover, 2013) (see pp. 44, 64, 66).
- [105] V. Kashcheyevs and J. Timoshenko, “Quantum Fluctuations and Coherence in High-Precision Single-Electron Capture”, *Physical Review Letters* **109**, 216801 (2012) (see pp. 47, 52, 101).
- [106] C. W. J. Beenakker and H. van Houten, “Quantum Transport in Semiconductor Nanostructures”, *Solid State Physics* **44**, 1 (1991) (see pp. 48 sq.).
- [107] V. Kashcheyevs and J. Timoshenko, “Modeling of a tunable-barrier non-adiabatic electron pump beyond the decay cascade model”, *Conference on Precision Electromagnetic Measurements (CPEM), Conference Digest (preprint)* (2014) (see p. 52).
- [108] L. Fricke, “Ladungsdetektion an sequentiellen, nicht-adiabatischen Einzel-Elektronen-Pumpen”, Diploma thesis (Gottfried Wilhelm Leibniz Universität Hannover, 2010) (see pp. 55, 69, 97, 210, 226).

- [109] B. M. Wood and S. Solve, “A review of Josephson comparison results”, *Metrologia* **46**, R13 (2009) (see p. 58).
- [110] J.-S. Tsai, A. K. Jain, and J. Lukens, “High-Precision Test of the Universality of the Josephson Voltage-Frequency Relation”, *Physical Review Letters* **51**, 316 (1983) (see p. 58).
- [111] A. K. Jain, J. E. Lukens, and J.-S. Tsai, “Test for Relativistic Gravitational Effects on Charged Particles”, *Physical Review Letters* **58**, 1165 (1987) (see p. 58).
- [112] F. Delahaye, T. J. Witt, E. Pesel, B. Schumacher, and P. Warnecke, “Comparison of quantum Hall effect resistance standards of the PTB and the BIPM”, *Metrologia* **34**, 211 (1997) (see p. 59).
- [113] BIPM, *Key comparison BIPM.EM-K12*, http://kcdb.bipm.org/AppendixB/appbresults/BIPM.EM-K12/BIPM.EM-K12_RH_Jul14.pdf (see p. 59).
- [114] F. Schopfer and W. Poirier, “Quantum resistance standard accuracy close to the zero-dissipation state”, *Journal of Applied Physics* **114**, 064508 (2013) (see p. 59).
- [115] T. J. B. M. Janssen, N. E. Fletcher, R. Goebel, J. M. Williams, A. Tzalenchuk, R. Yakimova, S. Kubatkin, S. Lara-Avila, and V. I. Fal'ko, “Graphene, universality of the quantum Hall effect and redefinition of the SI system”, *New Journal of Physics* **13**, 093026 (2011) (see p. 59).
- [116] A. Penin, “Quantum Hall effect in quantum electrodynamics”, *Physical Review B* **79**, 113303 (2009) (see p. 59).
- [117] B. N. Taylor and T. J. Witt, “New International Electrical Reference Standards Based on the Josephson and Quantum Hall Effects”, *Metrologia* **26**, 47 (1989) (see p. 59).

- [118] P. Mohr and B. Taylor, “CODATA recommended values of the fundamental physical constants: 1998”, *Rev. Mod. Phys.* **72**, 351 (2000) (see p. 59).
- [119] M. W. Keller, “Standards of Current and Capacitance based on Single-Electron Tunneling Devices”, in *Proceedings of fermi school cxlvi: ”recent advances in metrology and fundamental constants”* (2001) (see pp. 59, 180).
- [120] F. Piquemal and G. Genevès, “Argument for a direct realization of the quantum metrological triangle”, *Metrologia* **37**, 207 (2000) (see pp. 59, 61).
- [121] B. P. Kibble, “Atomic masses and fundamental constants 5”, in, edited by A. H. W. J. H. Sanders (Plenum Press (New York), 1976) Chap. A measurement of the gyromagnetic ratio of the proton by the strong field method, pp. 545–551 (see p. 61).
- [122] M. Stock, “The watt balance: determination of the Planck constant and redefinition of the kilogram”, *Philosophical Transactions of the Royal Society A: Mathematical, Physical and Engineering Sciences* **369**, 3936 (2011) (see p. 61).
- [123] F. Hohls, A. C. Welker, C. Leicht, L. Fricke, B. Kaestner, P. Mirovsky, A. Müller, K. Pierz, U. Siegner, and H. W. Schumacher, “Semiconductor Quantized Voltage Source”, *Physical Review Letters* **109**, 056802 (2012) (see p. 61).
- [124] T. Heinzel, *Mesoscopic Electronics in Solid State Nanostructures*, 2nd, revised edition (Wiley VCH, 2007) (see p. 64).
- [125] S. M. Sze and M. K. Lee, *Semiconductor Devices: Physics and Technology*, 3rd edition (John Wiley & Sons (New York), 2012) (see p. 64).
- [126] G. Snider, *One-dimensional Poisson and Schrödinger solver*, <https://www3.nd.edu/~gsnider/> (see p. 65).

-
- [127] C. Lu, Z. H. and Lagarde, E. Sacher, J. F. Currie, and A. Yelon, “A surface analytical study of GaAs(100) cleaning procedures”, *Journal of Vacuum Science and Technology A* **7**, 646 (1989) (see p. 66).
- [128] J. Niemeyer, “Eine einfache Methode zur Herstellung kleinster Josephson-Elemente”, *PTB-Mitteilungen* **84**, 251 (1974) (see p. 67).
- [129] G. J. Dolan, “Offset masks for lift-off photoprocessing”, *Applied Physics Letters* **31**, 337 (1977) (see p. 67).
- [130] G. Dolan and J. Dunsmuir, “Very small ($\gtrsim 20$ nm) lithographic wires, dots, rings, and tunnel junctions”, *Physica B: Condensed Matter* **152**, 7 (1988) (see p. 69).
- [131] T. Klaffs, “Experimente zur Potential- und Stromverteilung in Quanten-Hall-Systemen mit Einzelelektron-Transistoren”, PhD thesis (Technische Universität Carolo-Wilhelmina, Braunschweig, 2004) (see p. 69).
- [132] K. Docherty, “Improvements to the alignment process in electron-beam lithography”, PhD thesis (University of Glasgow, 2010) (see p. 69).
- [133] I. H. Chan, P. Fallahi, R. M. Westervelt, K. D. Maranowski, and A. C. Gossard, “Capacitively coupled quantum dots as a single-electron switch”, *Physica E: Low-dimensional Systems and Nanostructures* **17**, 584 (2003) (see p. 70).
- [134] A. Hübel, J. Weis, W. Dietsche, and K. v. Klitzing, “Two laterally arranged quantum dot systems with strong capacitive interdot coupling”, *Applied Physics Letters* **91**, 102101 (2007) (see pp. 70, 144).

- [135] H. O. H. Churchill, A. J. Bestwick, J. W. Harlow, F. Kuemmeth, D. Marcos, C. H. Stwertka, S. K. Watson, and C. M. Marcus, “Electron-nuclear interaction in ^{13}C nanotube double quantum dots”, *Nature Physics* **5**, 321 (2009) (see p. 70).
- [136] C. Roessler, T. Kraehenmann, S. Baer, T. Ihn, K. Ensslin, C. Reichl, and W. Wegscheider, “Tunable charge detectors for semiconductor quantum circuits”, *New Journal of Physics* **15**, 033011 (2013) (see p. 70).
- [137] M. Pioro-Ladrière, J. H. Davies, A. R. Long, A. S. Sachrajda, L. Gaudreau, P. Zawadzki, J. Lapointe, J. Gupta, Z. Wasilewski, and S. Studenikin, “Origin of switching noise in $\text{GaAs-Al}_x\text{Ga}_{1-x}\text{As}$ lateral gated devices”, *Physical Review B* **72**, 115331 (2005) (see pp. 71, 125).
- [138] K. Nishiguchi, A. Fujiwara, Y. Ono, H. Inokawa, and Y. Takahashi, “Room-temperature-operating data processing circuit based on single-electron transfer and detection with metal-oxide-semiconductor field-effect transistor technology”, *Applied Physics Letters* **88**, 183101, 183101 (2006) (see p. 75).
- [139] F. Pobell, *Matter and Methods at Low Temperatures*, 3rd edition (Springer, 2007) (see p. 75).
- [140] A. T. A. M. de Waele, “Pulse-tube refrigerators: principle, recent developments, and prospects”, *Physica B: Condensed Matter* **280**, 479 (2000) (see p. 75).
- [141] A. T. A. M. de Waele, “Basic Operation of Cryocoolers and Related Thermal Machines”, *Journal of Low Temperature Physics* **164**, 179 (2011) (see p. 75).

-
- [142] J. Martinis, M. Devoret, and J. Clarke, “Experimental tests for the quantum behavior of a macroscopic degree of freedom: The phase difference across a Josephson junction”, *Physical Review B* **35**, 4682 (1987) (see p. 77).
- [143] Keycom, *NbTi cables*, <http://www.keycom.co.jp/eproducts/upj/upj7/page.htm> (see p. 78).
- [144] M. W. Keller, “Practical aspects of counting electrons with a single-electron tunneling pump”, *The European Physical Journal Special Topics* **172**, 297 (2009) (see pp. 78, 180).
- [145] P. Horowitz and W. Hill, *The Art of Electronics*, 2nd edition (University Press (Cambridge), 1989) (see p. 80).
- [146] K. K. Choi, D. C. Tsui, and K. Alavi, “Experimental determination of the edge depletion width of the two-dimensional electron gas in GaAs/Al_xGa_{1-x}As”, *Applied Physics Letters* **50**, 110 (1987) (see p. 97).
- [147] D. V. Averin and K. K. Likharev, “Coulomb Blockade of Single-Electron Tunneling, and Coherent Oscillations in Small Tunnel Junctions”, *Journal of Low Temperature Physics* **62**, 345 (1986) (see p. 107).
- [148] M. Tinkham, *Introduction to Superconductivity*, 2nd edition (McGraw-Hill (New York), 1996) (see p. 107).
- [149] I. Giaever, “Electron Tunneling Between Two Superconductors”, *Physical Review Letters* **5**, 464 (1960) (see p. 109).
- [150] I. Giaever, *Nobel Lecture: Electron Tunneling and Superconductivity*, Nobel Media AB, (1973) http://www.nobelprize.org/nobel_prizes/physics/laureates/1973/giaever-lecture.html (see p. 109).

- [151] A. M. van den Brink, A. A. Odintsov, P. A. Bobbert, and G. Schön, “Coherent Cooper pair tunneling in systems of Josephson junctions: Effects of quasiparticle tunneling and of the electromagnetic environment”, *Zeitschrift für Physik B - Condensed Matter* **85**, 459 (1991) (see p. 110).
- [152] M. Tuominen, J. Hergenrother, T. Tighe, and M. Tinkham, “Single-electron tunneling transistors incorporating Cooper pair processes”, *IEEE Trans. Appl. Supercond.* **3**, 1972 (1993) (see pp. 110, 113, 118).
- [153] B. A. Turek, “Precision Measurements with the Single Electron Transistor: Noise and Backaction in the Normal and Superconducting state”, PhD thesis (Yale University, 2007) (see pp. 110, 115).
- [154] J. H. Love, “Resolved dynamics of single electron tunneling using the RF-SET”, PhD thesis (Yale University, 2007) (see pp. 110, 116).
- [155] P. Hadley, E. Delvigne, E. H. Visscher, S. Lähteenmäki, and J. E. Mooij, “ $3e$ tunnelling processes in a superconducting single-electron tunneling transistor”, *Physical Review B* **58**, 15317 (1998) (see pp. 113, 115).
- [156] Y. Nakamura, T. Sakamoto, and J.-S. Tsai, “Study of Josephson-Quasiparticle Cycles in Superconducting Single-Electron Transistors”, *Japanese Journal of Applied Physics* **34**, 4562 (1995) (see pp. 113 sq., 120).
- [157] T. Fulton, P. Gammel, D. Bishop, L. Dunkleberger, and G. Dolan, “Observation of Combined Josephson and Charging Effects in Small Tunnel Junction Circuits”, *Physical Review Letters* **63**, 1307 (1989) (see pp. 115, 118).

-
- [158] N. A. Court, “Quasiparticle Dynamics in a Single Cooper-Pair Transistor”, PhD thesis (University of New South Wales, 2008) (see p. 115).
- [159] A. J. Manninen, Y. A. Pashkin, A. N. Korotkov, and J. P. Pekola, “Observation of thermally excited charge transport modes in a superconducting single-electron transistor”, *Europhysics Letters* **39**, 305 (1997) (see p. 115).
- [160] A. Clerk, S. Girvin, A. Nguyen, and A. Stone, “Resonant Cooper-Pair Tunneling: Quantum Noise and Measurement Characteristics”, *Physical Review Letters* **89**, 176804 (2002) (see p. 115).
- [161] M. T. Tuominen, J. M. Hergenrother, T. S. Tighe, and M. Tinkham, “Experimental evidence for parity-based $2e$ periodicity in a superconducting single-electron tunneling transistor”, *Physical Review Letters* **69**, 1997 (1992) (see p. 115).
- [162] J. Lu, J. Hergenrother, and M. Tinkham, “Magnetic-field-induced crossover from $2e$ to e periodicity in the superconducting single-electron transistor”, *Physical Review B* **53**, 3543 (1996) (see p. 115).
- [163] D. Averin and K. Likharev, “Possible Applications of the Single Charge Tunneling”, in *Single charge tunneling*, Vol. 294, edited by H. Grabert and M. H. Devoret, NATO ASI Series (Springer US, 1992), pp. 311–332 (see p. 115).
- [164] N. A. Court, A. J. Ferguson, and R. G. Clark, “Energy gap measurement of nanostructured aluminium thin films for single Cooper-pair devices”, *Superconductor Science and Technology* **21**, 015013 (2008) (see p. 116).

- [165] A. M. van den Brink, G. Schön, and L. J. Geerligs, “Combined Single-Electron and Coherent-Cooper-Pair Tunneling in Voltage-Biased Josephson Junctions”, *Physical Review Letters* **67**, 3030 (1991) (see p. 118).
- [166] A. Savitzky and M. J. E. Golay, “Smoothing and Differentiation of Data by Simplified Least Squares Procedures”, *Analytical Chemistry* **36**, 1627 (1964) (see p. 131).
- [167] D. Taubert, G. J. Schinner, C. Tomaras, H. P. Tranitz, W. Wegscheider, and S. Ludwig, “An electron jet pump: The Venturi effect of a Fermi liquid”, *Journal of Applied Physics* **109**, 102412 (2011) (see p. 140).
- [168] N. Maire, F. Hohls, B. Kaestner, K. Pierz, H. W. Schumacher, and R. J. Haug, “Noise measurement of a quantized charge pump”, *Applied Physics Letters* **92**, 082112 (2008) (see p. 159).
- [169] P. Utko, P. E. Lindelof, and K. Gloos, “Heating in single-electron pumps driven by surface acoustic waves”, *Applied Physics Letters* **88**, 202113 (2006) (see p. 170).
- [170] S. J. Wright, M. D. Blumenthal, M. Pepper, D. Anderson, G. A. C. Jones, C. A. Nicoll, and D. A. Ritchie, “Parallel quantized charge pumping”, *Physical Review B* **80**, 113303 (2009) (see p. 180).
- [171] <http://kcdb.bipm.org/appendixC/cmcInformation.asp?cmc=453150601&Branch=EM/DC&Service=EM/DC.3&SService=&IService=&menu=EM> (see p. 206).

Curriculum vitae

Name:	Lukas Fricke
Date of birth:	16.09.1985
Place of birth:	Celle
Nationality:	German
1992 - 1996	Grundschule Eicklingen
1996 - 1998	Orientierungsstufe Burgstraße, Celle
1998 - 2005	Gymnasium Ernestinum, Celle
05.2005	Abitur
10.2005 - 05.2010	Studies of physics, Gottfried Wilhelm Leibniz University Hanover
05.2009 - 05.2010	Diploma thesis at the Institute of solid state physics, supervised by Prof. Dr. Rolf J. Haug and entitled "Ladungsdetektion an sequentiellen, nicht-adiabatischen Einzel-Elektronen-Pumpen"
05.2010	Diplom
05.2010 - 08.2010	Scientific staff at the Institute of solid state physics at Leibniz University Hanover
09.2010 - 12.2014	Preparation of this PhD-thesis at the Physikalisch-Technische Bundesanstalt (PTB), Braunschweig
06.2014	Awarded the "Helmholtz-Preis" for "A self-referenced single-electron quantized current source" jointly with B. Kaestner, F. Hohls, R. Dolata and H.W. Schumacher

List of publications

This work has been published in parts in the following publications:

- M. Wulf, L. Fricke, F. Hohls, B. Kaestner, R. Dolata, P. Mirovsky, K. Pierz, T. Weimann, and H. W. Schumacher, “Series operation of single-electron sources with charge detection”, Proceedings of the Conference on Precision Electromagnetic Measurements (CPEM), 246 (2012)
- L. Fricke, M. Wulf, B. Kaestner, V. Kashcheyevs, J. Timoshenko, P. Nazarov, F. Hohls, P. Mirovsky, B. Mackrodt, R. Dolata, T. Weimann, K. Pierz, and H. W. Schumacher, “Counting Statistics for Electron Capture in a Dynamic Quantum Dot”, Physical Review Letters **110**, 126803 (2013)
- L. Fricke, M. Wulf, B. Kaestner, F. Hohls, P. Mirovsky, B. Mackrodt, R. Dolata, T. Weimann, K. Pierz, U. Siegner, and H. W. Schumacher, “Self-referenced Single-Electron Quantized Current Source”, Physical Review Letters **112**, 226803 (2014)

Other publications:

- C. Fricke, F. Hohls, N. Sethubalasubramanian, L. Fricke, and R. J. Haug, “High-order cumulants in the counting statistics of asymmetric quantum dots”, Applied Physics Letters **96**, 202103 (2010)
- *Based on the data of my diploma thesis:* L. Fricke, F. Hohls, N. Ubbelohde, B. Kaestner, V. Kashcheyevs, C. Leicht, P. Mirovsky, K. Pierz, H. W. Schumacher, and R. J. Haug, “Quantized current source with mesoscopic feedback”, Physical Review B **83**, 193306 (2011)

- C. Fricke, F. Hohls, N. Sethubalasubramanian, L. Fricke, and R. J. Haug, “Transport through a quantum dot analyzed by electron counting”, AIP Conference Proceedings **1399**, 305 (2011)
- L. Fricke, S. Serrano-Guisan, and H. W. Schumacher, “Parameter dependence of resonant spin torque magnetization reversal”, Physica B **407**, 1153 (2012)
- F. Hohls, A. C. Welker, C. Leicht, L. Fricke, B. Kaestner, P. Mirovsky, A. Müller, K. Pierz, U. Siegner, and H. W. Schumacher, “Semiconductor Quantized Voltage Source”, Physical Review Letters **109**, 056802 (2012)
- P. Mirovsky, L. Fricke, F. Hohls, B. Kaestner, C. Leicht, K. Pierz, J. Melcher, and H. W. Schumacher, “Towards quantized current arbitrary waveform synthesis”, Journal of Applied Physics **113**, 213704 (2013)
- N. Ubbelohde, F. Hohls, V. Kashcheyevs, T. Wagner, L. Fricke, B. Kaestner, K. Pierz, H. W. Schumacher, and R. J. Haug, “Partitioning of on-demand electron pairs”, accepted for publication in Nature Nanotechnology, arXiv, 1404.0030 (2014)

Invited talk:

- IXth Rencontres du Vietnam: Nanophysics: From fundamentals to applications (2013)

Danksagung

An dieser Stelle möchte ich Allen, die mich bei dieser Arbeit unterstützt haben, danken:

Ohne den persönlichen Einsatz und Enthusiasmus von Hans Werner Schumacher, in dessen Fachbereich diese Arbeit entstanden ist, wäre wohl beispielsweise der Helmholtz-Preis nicht unserer Gruppe zugesprochen worden. Auch die vielen Diskussionen über die wichtigste Nebensache der Welt (auch wenn diese in Zeiten, in denen Dortmund tabellarisch sogar hinter Wolfsburg rangiert, schwer fallen) trugen zu einem angenehmen Arbeitsklima bei.

Großer Dank geht auch an Frank Hohls, der diese Arbeit immer unterstützend begleitet hat, jederzeit für offene Fragen zur Verfügung stand, Korrekturen gewälzt und dankenswerterweise die Prüfung dieser Arbeit übernommen hat.

Professor Rolf Haug möchte ich für die Prüfung der Arbeit danken sowie für vielfältige Diskussionen, sei es über physikalische Inhalte oder allgemeiner über gutes, wissenschaftliches Arbeiten.

Slava Kashcheyevs, Bernd Kästner, Pavel Nazarov und Janis Timoshenko haben die theoretische Beschreibung von dynamischen Quantenpunkten (weiter-)entwickelt und auf diese Weise eine weitergehende Interpretation der Messdaten ermöglicht.

In technischen Fragen konnte ich mich immer auf die guten Ratschläge und tatkräftige Hilfe von Peter Duda, Uli Becker, Holger Marx und Sascha Droste verlassen, vielen Dank!

In Sachen Reinraum und Probenherstellung sei Philipp Mirovsky, Bernd Kästner, Peter Hinze, Thomas Weimann, Brigitte Mackrodt und Ralf Dolata gedankt sowie für das Wafermaterial Holger Marx und Klaus Pierz.

Für die gute Stimmung im Büro einschließlich ausgiebiger Diskussionen zeichnete sich eine wechselnde Belegschaft verantwortlich, na-

mentlich (in chronologischer Reihenfolge) Florian Bergmann, Patryk Krzysieczko, Alexander Fernandez Scarioni, Cédric Neuville, Mattias Kruskopf und Niels Ubbelohde.

Vielen Anderen aus der Arbeitsgruppe gebührt weiterer Dank, sei es beispielsweise für organisatorische Unterstützung (Christine) oder auch die Sicherstellung der Versorgung mit Kaffee sowie die Idee, mal Fallschirmspringen zu gehen (Birgit). Unvergessen werden auch die Carrera-Abende bei Holger bleiben. Für die nette Atmosphäre in der Arbeitsgruppe insgesamt seid ihr alle verantwortlich, Danke Euch allen!

Die Vielzahl der erzielten Ergebnisse wäre ohne Michael Wulf nicht denkbar gewesen, der hier an der PTB das Labor maßgeblich aufgebaut und mit mir zusammen die Messungen durchgeführt hat. Sein unerwarteter, viel zu früher Abschied hat eine riesengroße Lücke hinterlassen, sowohl fachlich als auch menschlich. Es stimmt mich traurig, dass ich Dir nicht mehr persönlich "Danke" sagen kann.

Ohne meine Familie und Freunde, die mich jederzeit unterstützt haben, hätte ich es nicht bis hierher geschafft! Besonderer Dank für Ihre Rücksichtnahme und auch die unglaubliche Energie, mit der sie mir den Rücken frei hält und mich gleichzeitig voranbringt, gilt Christina. Vielen Dank für Alles!